UNIVERSITY OF READING
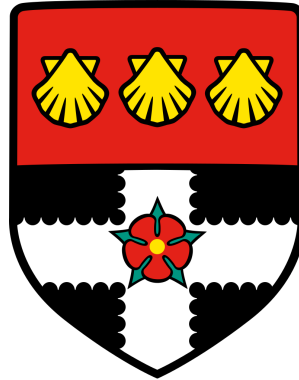
Department of Meteorology

DETECTION OF THE TEMPERATURE RESPONSES TO STRATOSPHERIC SULPHATE AEROSOL GEOENGINEERING

Yuen Tung Eunice Lo

A thesis submitted for the degree of Doctor of Philosophy

October 2017

Declaration

I confirm that this is my own work and the use of all material from other sources has been properly and fully acknowledged.

<div align="right">

Yuen Tung Eunice Lo

October 2017

</div>

Acknowledgements

I would like to express my sincere gratitude to my supervisors, Andrew Charlton-Perez, Ellie Highwood and Fraser Lott, for their continuous support and guidance throughout my PhD. Their collective expertise has contributed greatly to this work. I would also like to thank my monitoring committee members, Keith Shine, Ed Hawkins and Chris Merchant, for monitoring my progress twice yearly and giving valuable suggestions to my research.

This research made use of existing detection and attribution algorithms and climate model outputs. I would like to thank the Climate Monitoring and Attribution Team in the UK Met Office and Yang Feng in Environment Canada for their advice on detection and attribution, and on the Environment Canada's Optimal Fingerprint code.

I acknowledge the World Climate Research Programme's Working Group on Coupled Modelling, which is responsible for CMIP, and I thank the climate modeling groups for producing and making available their model output. For CMIP the U.S. Department of Energy's Program for Climate Model Diagnosis and Intercomparison provides coordinating support and led development of software infrastructure in partnership with the Global Organization for Earth System Science Portals.

I thank all participants of the Geoengineering Model Intercomparison Project and their model development teams, CLIVAR/WCRP Working Group on Coupled Modeling for endorsing GeoMIP, and the scientists managing the Earth System Grid data nodes who have assisted with making GeoMIP output available.

Finishing this PhD would have been extremely difficult without the scholarship from the Fong Shu Fook Tong Foundation during the first year of my PhD and the studentship offered by the University of Reading from my second year onwards. I am also grateful for the resourceful

Abstract

Stratospheric sulphate aerosol injection has been proposed as a potential way to cool the climate and alleviate some of the adverse impacts of climate change. Both prudent climate policy-making and successful geoengineering monitoring would require robust knowledge of the detectability of the geoengineering effects amid other externally forced changes and internal variability.

The first part of this thesis investigates how we could detect the global-mean cooling effect of 5 Tg yr^{-1} SO$_2$ injection with optimal fingerprint total least squares techniques in a climate model. Both the classical technique that assumes unforced variability as the null hypothesis and a non-stationary alternative could be applied to detect the global-mean cooling response within 10 years of geoengineering. However, the detectability of the geoengineering signal would depend on the filtering technique used for distinguishing the forced signals from climate noise.

The second part of this thesis identifies the best spatial scales on Earth's surface for geoengineering detection in temperature within 10 years of hypothetical deployment. The global scale would give the highest chance of early geoengineering detection, followed by the Northern Hemisphere and the Northern mid-latitudes. Detection of the geoengineering effect in other latitudinal bands and smaller regions would likely (>50% of the studied cases) take longer than 10 years.

Compared to surface temperatures, using the vertical temperature structure that includes the tropospheric cooling and tropical lower stratospheric warming effects of the sulphate aerosols would increase the geoengineering detectability during the first 10 years of implementation on the global, hemispheric and tropical scales. Minimising the upper stratospheric (above 30 hPa)

contribution to the vertical temperature structure could further improve the geoengineering detectability in the Tropics by 12.5%.

These results suggest the possibility of efficient geoengineering monitoring with optimal fingerprint detection techniques, especially if the vertical temperature structure is included in the detection diagnostic.

Table of contents

List of figures

List of tables

List of tables

Nomenclature

Acronyms / Abbreviations

ACE-FTS   Atmospheric Chemistry Experiment Fourier Transform Spectrometer

ALA   Alaska

AMSU-A   The Advanced Microwave Sounding Unit-A

AMZ   Amazon

AR5   Fifth Assessment Report

BDC   Brewer-Dobson circulation

CALIPSO   Cloud-Aerosol Lidar and Infrared Pathfinder Satellite Observation

CDR   Carbon Dioxide Removal

CMIP5   The Coupled Model Intercomparison Project Phase 5

CNA   Central North America

CO_2 Carbon dioxide

ECOF   Environment Canada's Optimal Fingerprint package

ENA   East North America

ENSO   El Niño/Southern Oscillation

EOF   Empirical orthogonal function

ERF   Effective radiative forcing

ESGF   Earth System Grid Federation

ESM   Earth system model

GeoMIP   The Geoengineering Model Intercomparison Project

GISTEMP   GISS Surface Temperature Analysis

GOMOS   Global Ozone Monitoring by Occultation of Stars

Nomenclature

H_2SO_4	Sulphuric acid
HadCRUT4	Hadley Centre-Climatic Research Unit Version 4
INDC	Intended Nationally Determined Contribution
IPCC	Intergovernmental Panel on Climate Change
ITCZ	Inter-tropical convergence zone
MAESTRO	Measurement of Aerosol Extinction in the Stratosphere and Troposphere Retrieved by Occultation
MED	Mediterranean
NDVI	Normalized Difference Vegetation Index
NEU	North Europe
NTP*	Pacific Islands region
OLS	Ordinary least squares
OSIRIS	Optical Spectrograph and InfraRed Imaging System
QBO	Quasi-biennial oscillation
RCP	Representative Concentration Pathway
ROF	Regularised optimal fingerprint
SAF	Southern Africa
SAGE III	Stratospheric Aerosol and Gas Experiment III
SAI	Sulphate aerosol injection
SAS	South Asia
SAT	Near-surface air temperature
SBDART	Santa Barbara DISORT Atmospheric Radiative Transfer
SEA	Southeast Asia
SNR	Signal-to-noise ratio
SO_2	Sulphur dioxide
SOCRATES	Suite Of Community RAdiative Transfer codes based on Edwards and Slingo
SPICE	Stratospheric Particle Injection for Climate Engineering
SRM	Solar Radiation Management

SSWs	Stratospheric sudden warming events
TCR	Transient climate response
TLS	Total least squares
TOA	Top-of-atmosphere
ToE	Time of emergence
UNFCCC	United Nations Convention on Climate Change
USD	US dollar
UV	Ultraviolet
WMO	World Meteorological Organisation
WNA	West North America

Chapter 1

Introduction

1.1   Geoengineering: motivation for research

As of June 2017, Earth's globally-averaged, combined land and ocean surface temperature is 0.75 °C above the average temperature between 1961–1990 (Figure 1.1). This makes 2017 so far the third warmest year since 1850. According to the Hadley Centre-Climatic Research Unit Version 4 (HadCRUT4) dataset (Morice et al., 2012) from which Figure 1.1 was produced, the warmest and second warmest years in history were 2016 and 2015, respectively. Other datasets such as those from NASA's Goddard Institute for Space Studies (Schmidt, 2017) and the National Oceanic and Atmospheric Administration (NOAA National Centers for Environmental information, 2017) indicate the same.

Figure 1.1 shows a warming trend since the start of the 20th century. The observed warming, both globally and regionally, has been repeatedly attributed to the combination of natural and anthropogenic sources, with the latter being dominated by human emissions of greenhouse gases (Bindoff et al., 2013; Stott, 2003; Stott et al., 2001; Tett et al., 2002). Anthropogenic climate change has increased the likelihood of historical extreme weather events. These include the extreme floods in England and Wales in 2000 (Pall et al., 2011), the drought in the South
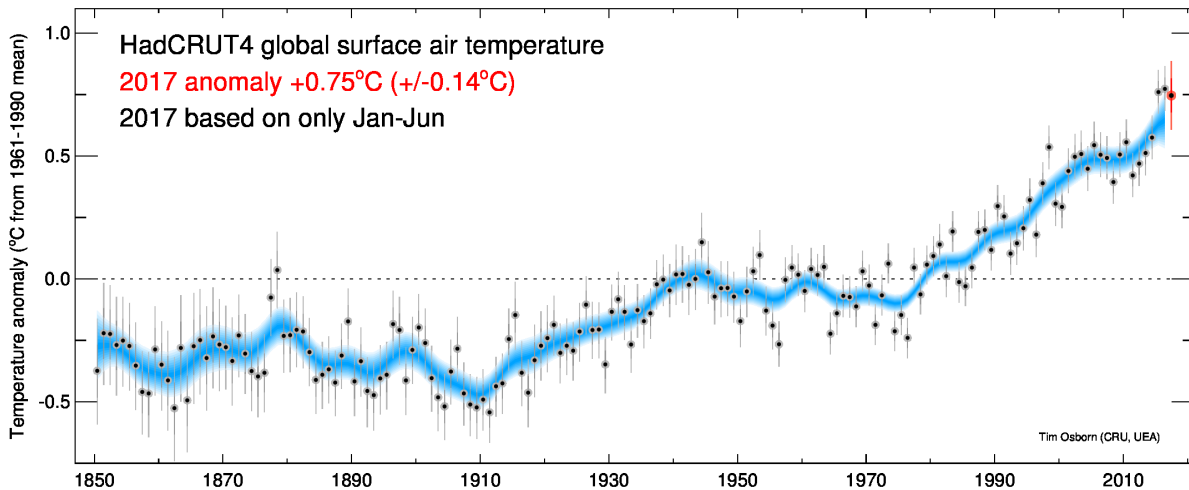
Figure 1.1 Figure taken from Osborn (2017) showing the annual-mean global-mean surface temperature anomaly time series from 1850 to 2017, with respect to the 1961–1990 mean. The black dots indicate the temperature anomalies, the thick grey lines denote $\pm$ 1 standard deviation from the mean values, and the thin grey lines represent the 95% confidence interval of the anomalies. The blue line and shading show the decadally-smoothed values and their uncertainties estimated from the respective 95% confidence interval. The creator of this figure, Tim Osborn of the Climate Research Unit of the University of East Anglia, generated this figure from the HadCRUT4 dataset (Morice et al., 2012).

Amazon region in 2010 (Shiogama et al., 2013), the unusually hot summer in Southern Europe in 2012 (Wilcox et al., 2017), the heatwaves in Eastern China in 2013 (Sun et al., 2014), the intense rainfall in Southeast China in 2015 (Burke et al., 2016), etc. Extreme events like these can be deadly. Mitchell et al. (2016) demonstrated that anthropogenic climate change had increased the risk of human mortality during the 2003 European heatwaves by $\sim 70\%$ in Central Paris and $\sim 20\%$ in London.

Global-mean surface temperature is projected to rise rapidly in the future if no effort were made to mitigate greenhouse gas emissions (Alexander et al., 2013). The intensity, frequency and duration of extreme events such as heatwaves (Meehl and Tebaldi, 2004) and droughts (Cook et al., 2014) are projected to increase in various regions over the 21$^{\text{st}}$ century in a such a 'business as usual' warming scenario. In the face of the threat of climate change, Parties to the United Nations Framework Convention on Climate Change (UNFCCC) codified a goal to "keep a global temperature rise this century well below 2 °C above pre-industrial levels and to pursue efforts to limit the temperature increase even further to 1.5 °C" in the Paris Agreement in 2015 (United Nations Framework Convention on Climate Change, 2017).

Following the Paris Agreement, countries submitted Intended Nationally Determined Contributions (INDCs) that outlined their intended 2020–2030 policies for addressing climate change. Although these INDCs included intended national action for both avoiding and adapting to climate change, they had a main focus on greenhouse gas emission reductions. By assuming that all of the countries that had submitted an unconditional INDC fully and successfully implement their intended mitigation action, Rogelj et al. (2016) estimated a reduction of about 4 Gt of annual carbon dioxide (CO_2) equivalent emissions by 2030, compared to the median current-policy scenario (which was estimated with the most recent global greenhouse gas emission estimates and implemented national climate policies). However, despite these intended emission cuts and the assumption that the post-2030 greenhouse gas mitigation effort remains similar to those stated in the INDCs, Rogelj et al. (2016) estimated a median warming of 2.6–3.1 °C by 2100, relative to the pre-industrial levels (1850–1900). This range is well above the 1.5 °C and 2 °C targets set in the Paris Agreement.

In two more recent studies (du Pont et al., 2017; Pan et al., 2017), countries' (I)NDCs, where NDCs are INDCs that have been ratified, were compared to the allowed greenhouse gas emissions allocated to different countries through principles of equity for achieving the Paris Agreement targets. Although du Pont et al. (2017) based their study on global cost-optimal scenarios that would deliver the Paris Agreement goals, whereas Pan et al. (2017) used RCP2.6 (Vuuren et al., 2011) as their 2 °C scenario, both studies concluded that most countries, in particular China, fell short of their equitable share of mitigation contribution for meeting the 2 °C target, not to mention the more ambitious 1.5 °C target. This, again, highlights the need for additional efforts, in mitigation and potentially otherwise, in order to meet the desired climate goals of the Paris Agreement.

Geoengineering, also known as 'climate engineering' or 'climate intervention', refers to a "broad set of methods and technologies that aim to deliberately alter the climate system in order to alleviate the impacts of climate change" (Edenhofer et al., 2012). Proposed geoengineering methods fall into two main categories, one that aims at lowering Earth's surface temperature by reducing the amount of solar radiation absorbed in the climate system, or
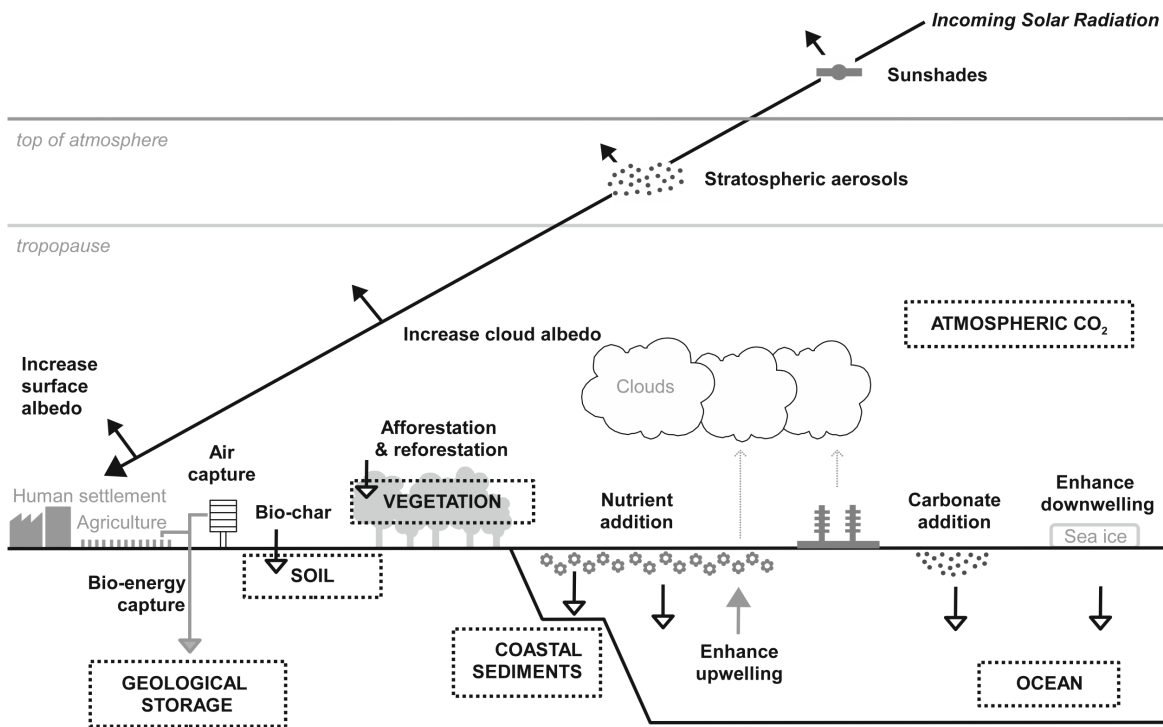
Figure 1.2 Figure taken from Vaughan and Lenton (2011), illustrating the most discussed SRM and CDR techniques. Reprinted by permission from Springer Nature Terms and Conditions for RightsLink Permissions Springer Customer Service Centre GmbH: Springer Climatic Change A review of climate geoengineering proposals, Naomi E. Vaughan and Timothy M. Lenton, ©Springer Science+Business Media B.V. 2011 (2011).

Original figure caption: Schematic overview of the climate geoengineering proposals reviewed. *Black arrowheads* indicate short wave radiation, *white arrowheads* indicate enhancement of natural flows of carbon, *grey downward arrow* indicates engineered flow of carbon, *grey upward arrow* indicates engineered flow of water, *dotted vertical arrows* illustrate sources of cloud condensation nuclei and dashed boxes indicate carbon stores. Not to scale

Solar Radiation Management (SRM); and the other that aims at lowering atmospheric CO_2 concentration by increasing net carbon sinks, or Carbon Dioxide Removal (CDR). SRM techniques include deliberate injections of reflective materials such as stratospheric aerosols into the upper atmosphere, marine cloud brightening, crop albedo enhancement, etc. (National Research Council, 2015b); whereas CDR techniques include large-scale afforestation, ocean iron fertilisation, carbon capture and storage, etc. (National Research Council, 2015a). Figure 1.2 provides an overview of the most discussed SRM and CDR techniques to date.

In particular, stratospheric sulphate aerosol injection (SAI)[1] has been widely discussed as a potential way of limiting global surface temperature rise because of its analogy with large volcanic eruptions (e.g. the 1991 Mount Pinatubo eruption), and its potentially high effectiveness, affordability and feasibility. SAI involves deliberate injections of sulphate aerosols or their precursors into the stratosphere to increase Earth's albedo, and thereby reduce the amount of solar radiation reaching the surface. The aerosols are designed to be injected into the stratosphere because they have a much longer lifetime in the stratosphere (about a year) than in the troposphere (a few days) (Rasch et al., 2008b). A longer lifetime means aerosols injected into the equatorial stratosphere can be transported poleward by the Brewer-Dobson circulation (BDC) and zonally through zonal flows in the stratosphere to a greater extent, and less frequent injections would be required to maintain a desirable aerosol mass burden (Rasch et al., 2008b).

Nevertheless, continual replenishment of the aerosols would be needed to keep cooling the climate because aerosols coagulate and eventually settle out of the stratosphere by gravity. Sudden cessation of SAI would result in rapid changes in climate toward the unperturbed state that is much warmer. This is commonly know as the 'termination effect', and it is expected to be more difficult to adapt to than climate change without any geoengineering (Shepherd, 2009). Wigley (2006) simulated sequential Mount Pinatubo eruptions every 1, 2, and 4 years, and all of their simulations showed that the global-mean surface cooling effect of increased levels of stratospheric sulphate aerosols would vanish rapidly once the aerosol injections stop. Similarly, Jones et al. (2013) demonstrated in climate models that sudden termination of SRM after 50 years of implementation designed to offset 1% increase in CO_2 concentrations per year would result in rapid rise in global-mean temperature, and faster increase in global-mean precipitation and decline in sea-ice cover than would have been experienced without geoengineering.

---

[1]In the geoengineering literature, the more general term 'stratospheric aerosol injection', which could involve the use of other types of aerosols such as titania, soot and limestone, is sometimes abbreviated as SAI as well. This thesis solely refers to 'sulphate aerosol injection' as SAI. SAI in this thesis is equivalent to 'stratospheric sulphate injection', or SSI, that has sometimes been used in the literature.

Introduction

As mentioned above, SAI has been much researched partly because of its natural analogue—large volcanic eruptions. In 1991, Mount Pinatubo in the Philippines erupted 20 Tg of sulphur dioxide gas (SO_2) into the stratosphere (Bluth et al., 1992). Through a series of photochemical reactions, the gas was oxidised to sulphuric acid (H_2SO_4) (McKeen et al., 1984), which subsequently condensed to form sulphate aerosols. Sulphate aerosols are highly reflective in the ultraviolet and visible regions of the electromagnetic spectrum. As a result of reduced incoming solar radiation (insolation) following the eruption, the globally averaged surface temperature dropped by $\sim 0.5\,°C$ in 1992 (Parker et al., 1996).

Crutzen (2006) called for active scientific research of stratospheric sulphate aerosol geo-engineering in view of the lack of progress in greenhouse gas mitigation, although the idea of mimicking volcanic eruptions to cool the Earth's surface dates back to Budyko (1977). Since Crutzen (2006), research has accelerated to explore the potential benefits, side effects, costs, feasibility, societal impacts and ethical implications of sulphate aerosol geoengineering.

The cooling efficiency of sulphate aerosol geoengineering depends on the size, composition and amount of the aerosol particles, as well as their injection height and location. Using information from the Mount Pinatubo eruption, Crutzen (2006) found that 1 Tg of sulphur could offset $0.75\,\mathrm{W\,m^{-2}}$ of radiative forcing, which is defined as the net change in downward radiative flux at the tropopause after stratospheric temperatures adjust to reach a new radiative equilibrium as a response to some perturbation to the Earth system (Myhre et al., 2013). Indeed, state-of-the-art climate models agree that $5\,\mathrm{Tg\,yr^{-1}}$ SO_2 injection into the tropical lower stratosphere would offset $\sim 0.4\,°C$ of the warming in a Representative Concentration Pathway where radiative forcing stabilises at $4.5\,\mathrm{W\,m^{-2}}$ by 2100, i.e. RCP4.5 (Thomson et al., 2011), within a few years of geoengineering implementation (please see Figure 2.2 in Section 2.2.1). Reduced insolation and surface temperatures would reduce the frequency of extreme hot and precipitation (floods and droughts) events, lower the rate of sea-level rise due to thermal expansion of water, and increase inorganic carbon storage in the oceans (Irvine et al., 2016).

McClellan et al. (2012) estimated an annual cost of 1–3 billion USD for delivering 1 Tg of sulphur (or equivalent albedo modification materials) to 20–30 km by aircrafts specifically designed for geoengineering. Delivering 5 Tg of the material to the same altitude range would cost 2–8 billion USD annually. These estimations included research, development, testing and evaluation costs of the aircrafts, fuel costs and personnel costs for flying operations, maintenance and logistics, but they are unlikely to be complete (Ferraro, 2013). Nevertheless, McClellan et al. (2012) concluded that the basic technology for delivering several teragrams of reflective materials into the stratosphere already existed, and that the associated costs would likely be less than 1% of the costs of greenhouse gas mitigation or climate damages.

Shepherd (2009) assessed the effectiveness, timeliness, affordability and safety of various SRM and CDR techniques. SAI scored high in the first three criteria but low in safety. Indeed, injecting large amounts of sulphate aerosols into the stratosphere could bring additional, unintended effects to human health and the climate system. For example, exposure to increased amounts of sulphate aerosols could cause adverse respiratory, cardiovascular, dermal and other effects to the human body (Effiong and Neitzel, 2016). Under the scenario that employed SAI to cool the globe by 1 °C, Eastham (2015) estimated that ~ 25000 additional premature deaths would happen in 2040, mainly due to exposure to the injected sulphate aerosols.

For the climate system, modelling studies showed that injecting 5 Tg yr^{-1} SO$_2$ into the tropical stratosphere or 3 Tg yr^{-1} SO$_2$ into the Arctic stratosphere would weaken Asian and African summer monsoons (Robock et al., 2008), stratospheric heating caused by geoengineering sulphate aerosols would weaken the tropical overturning circulation (Ferraro et al., 2014), and enhanced heterogeneous reactions on the aerosols would deplete stratospheric ozone at high latitudes (Pitari et al., 2014; Tilmes et al., 2009). A more detailed overview of the projected climate responses to SAI can be found in Section 1.2.

The knowledge that SAI could feasibly and inexpensively complement greenhouse gas mitigation in cooling the climate but that it might pose novel risks to climate and society has been the main motivation of inter-disciplinary research in this area. Only through research

can we improve our understanding of SAI and its impacts on the climate system, ecosystems, human societies and behaviour, etc. The 'arm the future' argument states that researching geoengineering today might give us the additional option to adapt to climate change and to geoengineer (if we choose to), which could be a lesser evil than having no choice but to adapt to dangerous climate change (Betz, 2012).

1.2 Projected climate responses to sulphate aerosol injection (SAI)

Much research has been done in climate models to better our understanding of the potential climate responses to SAI. This section provides an overview of the projected responses to SAI in various aspects of the Earth system, as found in the geoengineering literature. As mentioned in Section 1.1, the climate impacts of SAI would be contingent on the aerosol properties, as well as the aerosol injection rate, location and height. Different climate models also simulate different responses, even in the same SAI scenario (as demonstrated in the next paragraph). Therefore, apart from this section, the global-mean and grid-scale temperature and precipitation responses to SAI in the scenario that is used in this thesis (G4, please refer to Section 2.2.1) and simulated by the climate models that are included in this thesis (please also refer to Section 2.2.1) will be detailed in Sections 2.2.1.1 and 2.2.1.2.

Using the UK Met Office's HadGEM2 model (Bellouin et al., 2011b) and the Goddard Institute for Space Studies' ModelE (Schmidt et al., 2014), Jones et al. (2010) showed that 5 Tg yr^{-1} of SO$_2$ injection into the lower stratosphere could reduce global-mean near-surface temperature by 0.74 and 0.47 K over the first decade of implementation, respectively, compared to the baseline A1B warming scenario (Nakicenovic et al., 2000). However, surface temperature responses to SAI was found to be spatially inhomogeneous in either model. Cooling would generally be stronger in the Northern high latitudes, and over land than over ocean (Jones et al., 2010). Spatially inhomogeneous surface temperature changes were also found in other SRM

experiments where incoming solar radiation was reduced to balance the radiative forcing of increased CO_2 concentrations (e.g. Irvine et al. (2016); Robock (2014)). This highlights the potentially spatially inhomogeneous benefits and harms of SAI and SRM.

In two recent studies, Kravitz et al. (2017) and MacMartin et al. (2017) demonstrated that the globally averaged surface temperature, the North-South inter-hemispheric surface temperature gradient, and the Equator to Pole surface temperature gradient could simultaneously be kept at their respective 2020 levels, if time-varying amounts of SO_2 were injected at 4 locations along $180\,^\circ$ in longitude, throughout 2020–2099 against an RCP8.5 warming scenario (Riahi et al., 2011). They concluded that multiple climate objectives could be met simultaneously by controlling SAI year by year using a feedback mechanism, while acknowledging that temperature residuals were still present in their results.

Temperature extremes are also projected to change unevenly across the globe in the event of SAI. Aswathy et al. (2015) reported in their multi-model study that the spatial pattern of extreme temperature changes would be similar to that of the mean temperature changes mentioned earlier in this section, in a scenario where SO_2 was gradually injected into the tropical lower stratosphere from 2020 to 2070 to keep the globally averaged planetary temperature nearly constant at the 2020 level in RCP4.5. However, extreme high temperatures would rise less than the mean temperature, whereas extreme low temperatures would rise more than the mean in the Northern middle to high latitudes (Aswathy et al., 2015).

Apart from temperature, various studies have looked at the hydrological impacts of SAI. In the same experiment above, Aswathy et al. (2015) projected a global reduction of 0.046 mm day^{-1} in precipitation over 2040–2069, relative to the baseline RCP4.5 climate during the same period. Part of this reduction could be linked to the global-mean surface cooling caused by the injected sulphate aerosols during the same period (-0.47 K, Aswathy et al. (2015)). However, in addition to the negative temperature-dependent effect of stratospheric sulphate aerosols on global-mean precipitation, Ferraro and Griffiths (2016) estimated $\sim 0.2\%$ decrease in global-mean precipitation mainly due to increased downward infrared radiation emission

by the aerosol layer, in a scenario where 5 Tg yr^{-1} of SO_2 was injected into the tropical lower stratosphere between 2020 and 2070. Nevertheless, as with temperature changes, mean (Robock et al., 2008) and extreme high precipitation changes (Aswathy et al., 2015) are both expected to vary substantially across different regions if SAI were implemented.

For the Arctic cryosphere, Berdahl et al. (2014) estimated an increase in March and September Arctic sea ice extents, and Northern Hemisphere spring (April to June) snow cover extent over the period 2020–2070, relative to RCP4.5, if increasing amounts (to keep RCP4.5 top-of-atmosphere (TOA) net radiative forcing at the 2020 level) or 5 Tg yr^{-1} of SO_2 were injected into the tropical lower stratosphere on top of RCP4.5 during this 50-year period. However, a majority of the climate models Berdahl et al. (2014) used still simulated a decline in September Arctic sea ice extent and Northern Hemisphere spring snow extent throughout 2020–2070, in spite of SAI deployment.

In high-mountain Asia, glacier volume loss could lead to 15.5 mm of sea-level rise over 2010–2069 in the mid-range, RCP4.5 warming scenario (Zhao et al., 2017). This amount of sea-level rise could be reduced to 9 or 9.8 mm, if SO_2 were injected gradually or constantly into the tropical lower stratosphere as described in the previous paragraph, respectively (Zhao et al., 2017). In the same, constant SAI scenario over in the Atlantic, Moore et al. (2015) estimated a 50% reduction in the number of storm surge events as big as that caused by the 2005 Katrina hurricane, primarily due to cooling of the tropical Atlantic by SAI.

In the stratosphere where the amount of sulphate aerosols would be increased in the event of SAI, ozone concentrations are expected to change. One of the main ways through which SAI affects stratospheric ozone concentrations is that the geoengineering sulphate aerosols provide additional surface area for heterogeneous reactions to occur. This tends to suppress the NO_x ozone-depletion cycle, but accelerate the HO_x and ClO_x ozone-depleting cycles (Lary, 1997; Pitari et al., 2014; Prather, 1992). Since these cycles dominate at different latitudes and altitudes, Pitari et al. (2014) simulated an increase in stratospheric ozone in low to middle latitudes, and a decrease in stratospheric ozone in the polar regions, relative to RCP4.5, in

scenarios where SAI was implemented gradually or constantly to reduce the level of warming in RCP4.5.

In the same, constant (5 Tg yr^{-1}) SAI experiment mentioned above, Pitari et al. (2014) estimated a global-mean reduction of 1.1–2.1 DU of stratospheric ozone 20–30 years into SAI deployment. In another SAI experiment where 2 Tg yr^{-1} of sulphur was injected into the stratosphere between 2020 and 2050, Tilmes et al. (2009) simulated a delay of ~ 30 years in the recovery of the Antarctic ozone hole. This could lead to increased ultraviolet exposure in the polar regions (Pitari et al., 2014). SAI-induced stratospheric ozone reductions would also lead to a decrease in tropospheric ozone concentrations (Xia et al., 2017), posing implications on human health and crop growth.

Elevated stratospheric sulphate aerosol levels not only affect stratospheric chemistry but also radiative transfer and dynamics. Stratospheric sulphate aerosols absorb solar near-infrared and terrestrial longwave radiation, radiatively warming the tropical lower stratosphere (Ferraro et al., 2011). Even if SO_2 were injected into the lower stratosphere at latitudes up to 30 ° North or South of the Equator, Richter et al. (2017) showed that the lower stratosphere would still primarily warm between 30 °S and 30 °N. Such warming would enhance tropical upwelling of the Brewer-Dobson circulation (BDC) (Aquila et al., 2014; Ferraro et al., 2015), and consequently slow down or shut down the quasi-biennial oscillation (QBO), depending on the SO_2 injection rate, as found in various equatorial or tropical SAI experiments (Aquila et al., 2014; Niemeier and Schmidt, 2017; Richter et al., 2017).

The BDC is characterised by tropical upwelling of tropospheric air into the stratosphere, where it is then transported upward and poleward before downwelling in the extra-tropics (Butchart, 2014). The BDC is projected to strengthen under elevated greenhouse gas concentrations (Butchart et al., 2006; Garcia and Randel, 2008; Hardiman et al., 2014). The projected strengthening of the BDC due to SAI and greenhouse gases is expected to affect transport and thus the distribution of stratospheric ozone, water vapour and sulphate aerosols (Ferraro et al., 2015).

Introduction

The QBO is the quasi-periodic oscillation of equatorial zonal wind between easterlies and westerlies (Baldwin et al., 2001). Niemeier and Schmidt (2017) suggested that a slowed or lost QBO would also reduce meridional transport of the stratospheric geoengineering sulphate aerosols out of the Tropics, and thus decrease the SAI radiative forcing efficiency.

Because of the potential warming of the tropical lower stratosphere due to the geoengineering sulphate aerosols, an increased meridional temperature gradient in the lower stratosphere and, thus, intensified stratospheric polar vortices are expected in the event of SAI (Ferraro et al., 2015; Tilmes et al., 2009). This could have a range of implications on the climate system, including a reduction in column ozone in high latitudes due to lower polar temperatures (Tilmes et al., 2009), a decrease in stratospheric sudden warming events (SSWs) (Ferraro et al., 2015), and the poleward shift of eddy-driven midlatitude tropospheric jets in winter (Ferraro et al., 2015).

Furthermore, a warmer tropical lower stratosphere as a result of SAI means a higher cold point temperature, which would lead to an increase in water vapour entry into the tropical stratosphere from the troposphere below (Mote et al., 1996). An increase in stratospheric water vapour mixing ratio would further warm the stratosphere (Jones et al., 2016) and deplete stratospheric ozone via the HO_x cycle (Heckendorn et al., 2009).

Last but not least, SAI would increase the ratio of diffuse to direct radiation through the scattering of solar radiation (Irvine et al., 2016). Diffuse light penetrates canopies and reaches leaf surfaces more easily, enhancing photosynthesis rate (Kravitz et al., 2012). Assuming no nutrient limitation, 5 Tg yr^{-1} and 8 Tg yr^{-1} SO_2 injection could lead to a boost in global gross primary productivity by 1.6 (Ito, 2017) and 3.8 Gt C yr^{-1} (Xia et al., 2016), respectively. As noted by Kravitz et al. (2012), however, increased diffuse to direct radiation ratio could whiten the sky and reduce solar power generation.

A majority of SAI research to date, including all of those mentioned in this section, has been done with computer simulations of the climate system. The Geoengineering Model Intercomparison Project (GeoMIP) (Kravitz et al., 2011) was developed to standardise hy-

pothetical geoengineering experiments so they could be conducted across different climate models (please see Section 2.2 for details). However, even the most sophisticated climate models lack complete and accurate representation of climate processes, feedbacks, aerosol microphysics, stratospheric chemistry and stratospheric dynamics, particularly at small scales.

This has prompted some researchers to propose field experiments. The Stratospheric Particle Injection for Climate Engineering (SPICE) project was commissioned by Research Councils UK in 2010 (Pidgeon et al., 2013). Part of the SPICE proposal was a 1 km 'pipe and balloon' test bed that aimed at observing the movements of the pipe and water-filled balloon under different wind conditions. This project was eventually cancelled due to concerns surrounding potential commercialisation of the non-patented pipe technology. Subsequently, Keith et al. (2014) proposed a range of SRM field experiments in 2014, and work to turn these proposed tests into reality is under way (Harvard University Center for the Environment, 2017).

Deliberate human intervention to the climate system, be it in the form of computational research, field experiments or deployment, has been a topic of controversy because of its social and ethical implications. Manipulating temperatures through the injection of reflective stratospheric sulphate aerosols has sparked particular concerns because of its potentially transboundary yet inhomogeneous physical impacts and its inability to address the root of the climate change problem—elevated CO_2 concentrations. The following section outlines the inevitable ethical and governing challenges in relation to SAI and the wider geoengineering research and deployment.

1.3 Ethical and governing challenges

1.3.1 A slippery slope

Geoengineering research could be a slippery slope towards geoengineering deployment (Hulme, 2012). Once research on geoengineering gains momentum, ultimate deployment of the technol-

ogy might become inevitable to some researchers and investors. This could pressure climate policymakers into choosing the option that involves geoengineering in the future, even if research outcomes showed that it was not the most desirable option. This plausible scenario would then not be one where we choose the lesser evil among different options (Betz, 2012), as the 'arm the future' argument optimistically suggests (Section 1.1).

The slippery slope argument is further complicated by field experiment proposals. This is because the line between a geoengineering field experiment of considerable scale and deployment could be extremely blurry. Adding to the concern that geoengineering research would eventually lead to deployment, large-scale field experiments could be indistinguishable from deployment to start with.

Lenferna et al. (2017) attempted to distinguish SAI field experiments from full-scale deployment by their supposedly different purposes (learning about the effectiveness and risks of geoengineering with field experiments versus achieving a certain climate goal with deployment), and by the time and spatial scales they span and the radiative forcing they introduce (field experiments spanning shorter and smaller scales and imposing a smaller radiative forcing on the climate system than deployment). However, differentiating between large-scale field experiments and deployment remains challenging because their purposes could overlap, and the detection of some climate responses to SAI, such as the regional responses and precipitation changes, amid natural variability would be difficult without a large-scale field experiment that is similar to deployment (Lenferna et al., 2017).

1.3.2 Distributive, procedural and intergenerational justice

Just like the impacts of climate change, the benefits and harms of geoengineering field experiments and deployment are likely to be geographically inhomogeneous. As mentioned in Section 1.2, uneven spatial distributions of mean and extreme temperature and precipitation

changes due to global geoengineering sulphate aerosol coverage are projected by climate models.

Furthermore, injections of SO_2 into the tropical or Arctic stratosphere would disrupt Asian and African summer monsoons (Robock et al., 2008), whereas SAI in the Northern Hemisphere or Southern Hemisphere alone could induce drought or greening in the Sahel region (Haywood et al., 2013). These examples suggest that both global and sub-global scale SAI could threaten the livelihood of some populations (e.g. those whose food and water supplies are threatened by droughts) while benefiting that of some others (e.g. those who live in coastal areas in the face of sea-level rise).

Svoboda et al. (2011) laid out five major theories of distributive justice and concluded that the inequities that would potentially arise from SAI violated all five theories. Distributive injustice is likely to be deepened because populations that are likely to be most vulnerable to any adverse effect of SAI are also the least responsible for global warming, the least resilient to dangerous climate change and the least engaged in international agendas for climate policymaking (Lenferna et al., 2017; Svoboda et al., 2011).

SAI field experiments and deployment could render as more distributively just if they were coupled with compensation. However, whether one could simply compensate for the loss of life, whether one could confidently attribute individual extreme events and their damages to SAI experiments or deployment, who should decide how much or in what way compensation would be justifiable, and who would be responsible for any compensation remain debatable obstacles to distributive justice of geoengineering research and deployment.

Because SAI could be more beneficial to some populations than the others, and field tests or deployment are likely to be inexpensive compared to mitigation and adaptation (Section 1.1), it is possible for a single nation, a corporation or even wealthy individuals to launch a field experiment or deploy geoengineering for their own interests without international agreement. The prospect of unilateral implementation is problematic because in one way or another,

literally every person living on Earth would be affected by the decision made by a small group of people non-representative of the world. This poses a challenge to procedural justice of SAI.

As mentioned in Section 1.1, continual replenishment of sulphate aerosols would be needed to maintain a desirable cooling effect from the unperturbed climate because of limited aerosol lifetimes in the stratosphere. The 'termination effect' (Section 1.1) is expected to occur in the event of sudden cessation of SAI due to any reasons such as unexpected technical failure, change in climate policy, or lack of funds.

This means any deployment of SRM technologies could put future generations at risk of the termination effect in the event of technical failure, or the policy dilemma between committing to the geoengineering efforts previous generations had signed up for and facing catastrophic termination consequences. Either case would be deemed intergenerationally unjust (Burns, 2011; Svoboda et al., 2011).

1.3.3   Governance

Adequate governance of geoengineering research and deployment may overcome some of the challenges presented above. Bevir (2012) defined governance as "all processes of governing, whether undertaken by a government, market or network, whether over a family, tribe, formal or informal organization or territory and whether through laws, norms, power or language". Under this definition, governance does not necessarily require laws enacted by a government or an international agreement, although it does not reject these possibilities.

Indeed, the most widely cited principles for geoengineering governance to date, which are commonly known as the Oxford Principles, were set out by an ad-hoc group of academics who wanted to highlight the importance of the issue of social control over research, development and deployment of geoengineering technologies (Rayner et al., 2013). The Oxford Principles require:

- Geoengineering to be regulated as a public good.

- Public participation in geoengineering decision-making.

- Disclosure of geoengineering research and open publication of results.

- Independent assessment of impacts.

- Governance before deployment.

These principles are not legally-binding, but are rather a voluntary code of conduct for researchers. Parker (2014) also emphasized that the way forward to governing SRM research would be to first develop a professional code of conduct among researchers. In particular, he suggested that researchers define an upper limit to the scale of field experiments such that low-risk research could be conducted without automatically escalating into large-scale experiments or deployment. Parker (2014) also proposed that funding agencies impose good practices on the research they fund, in a fashion similar to the responsible innovation process Research Councils UK imposed on the now cancelled SPICE project (Pidgeon et al., 2013).

For large-scale field experiments that would have transboundary impacts and full-scale deployment, however, both Rayner et al. (2013) and Parker (2014) called for international agreement. An international agreement could potentially justify geoengineering research and deployment through compensating those adversely affected by the decision, and prevent unilateral deployment as well as any associated conflicts. In their opinion piece, Frumhoff and Stephens (2017) specifically encouraged the engagement of stakeholders from both the Global North and South in a governance process that seeks to put together geoengineering research priorities and standards.

Nevertheless, it is never easy to define terms such as 'public participation' and 'international agreement'. How much participation from the general public and stakeholders in the Global South would be justifiable, or whether a majority of the world's nations could represent global interests, etc. remain open questions.

1.3.4 Moral corruption and moral hazard

One of the potential issues on which governance would have little effect is the impacts of geoengineering research and deployment on human psychology and behaviour. For example, it is possible for governments and companies to back geoengineering research or deployment just to evade their responsibilities for greenhouse gas mitigation, especially if mitigation is against their own interests. Researchers might advocate deployment in order to secure research funding from these agencies, even if research results suggested geoengineering would do more harm than good to the society. In other words, geoengineering could be a place for moral corruption (Hamilton, 2014).

Perhaps more innocently, the prospect of geoengineering, especially the potentially effective and affordable SAI technology, could lead people to believe that geoengineering is the solution to climate change and, therefore, become less committed to mitigation and adaptation. This is often known as the 'moral hazard' argument (Preston, 2013). Moral hazard is one of the main concerns of SRM research because while SRM techniques could reduce the magnitude or rate of global warming, they would not alleviate all of the pressing risks of increasing CO_2 concentrations, such as ocean acidification (Orr et al., 2005).

Transparent research ensured by governing policies could reduce misconception about the potential benefits and risks of SRM, but it would not eliminate any behavioural change caused by psychological biases or individuals' underlying values. For instance, Corner and Pidgeon (2014) surveyed 610 people in the UK and concluded that "people who were more self-oriented, more sceptical about climate change and who were of higher socio-economic status were more likely to agree that their own behaviour would be impacted by the prospect of geoengineering".

In contrast to the 'moral hazard' concern, there is the 'reverse moral hazard' argument which states that geoengineering research would increase the perceived risk of anthropogenic climate change and, consequently, the willingness to mitigate greenhouse gas emissions and

to develop adaptation strategies (Parker, 2014). It is indeed extremely difficult to evaluate what effects even the prospect of geoengineering has or may have on human psychology and behaviour. This is yet another contribution to the controversy which surrounds geoengineering.

1.3.5   The public's views

Sections 1.3.1 to 1.3.4 summarised the major ethical and governing concerns that climate and social scientists have about geoengineering. As the Oxford Principles require public participation in geoengineering decision-making (Section 1.3.3), various studies have investigated the public opinion on the prospect of geoengineering.

Mercer et al. (2011) surveyed 3105 individuals from the UK, the US and Canada about geoengineering and SRM online. 8% of the sampled population were able to correctly define 'geoengineering', whereas 45% of them could correctly define 'climate engineering'. Mercer et al. (2011)'s finding of low public awareness of the term geoengineering echos the conclusions of Pidgeon et al. (2012), which indicated that only 1% of their respondents (1822 individuals of the British population) felt they knew "a great amount" about geoengineering. However, after being briefly introduced to the geoengineering proposals (Section 1.1), Pidgeon et al. (2012)'s respondents generally preferred CDR to SRM. In Mercer et al. (2011)'s SRM-focused survey, respondents showed strong support for SRM research, but less support for deploying SRM immediately or in the event of climate emergency.

Indeed, general support for "keeping the door ajar for all options, including climate engineering" (akin to the 'arm the future' argument in Section 1.1) was also found in Wibeck et al. (2017)'s study, in which 136 members of the public from Japan, New Zealand, the US, and Sweden were interviewed in 23 qualitative focus groups. Nevertheless, Wibeck et al. (2017) also found that despite the participants' low prior familiarity with geoengineering, and their diverse geographical locations and cultural backgrounds, they raised common concerns about geoengineering that were remarkably similar to those mentioned in Sections 1.3.1 to

1.3.4. Specific terms such as 'moral hazard' (Section 1.3.4) were not used by the participants, but similar concerns were conveyed through the use of analogies and metaphorical descriptions, such as "a blood pressure pill but no change of lifestyles". Other common themes that emerged from the focus group discussions were the risk of unintended effects of geoengineering, the need for greenhouse gas mitigation, and the need for national and international geoengineering governance (akin to Section 1.3.3).

With the aim of examining how knowledge about SRM would affect public perception of SRM technologies, Sütterlin and Siegrist (2017) interviewed 250 members of the public from Switzerland in 3 groups. The first group was only told that technologies existed for combating climate change, whereas the second and the third group were both given specific information about SRM proposals, but only the third group was informed about the potential risks associated with SRM. Sütterlin and Siegrist (2017) came to the conclusions that the mere mention of SRM would lead to a negative perception of the technology already, and additional knowledge of the potential risks and uncertainties of SRM would result in an even more negative evaluation of SRM. These results suggest that public acceptance of SRM field experiments could be challenging to obtain.

1.4   Aims of this thesis

Sulphate aerosol geoengineering presents a risk-risk scenario: both developing it and not developing it in a world with elevated CO_2 concentrations are risky. The best climate policies can only be made by well-informed and rational policymakers. Scientific research, especially those done on computers and has no immediate impacts on the physical environment, provides a great opportunity to better understand climate change and geoengineering. The ultimate aim of this thesis is to find out *when*, *how* and *where* we could robustly detect the temperature responses to hypothetical, deliberately injected sulphate aerosols, so as to improve our understanding of the effectiveness of SAI for future climate policymaking.

SAI has been regarded as an efficient way of cooling the Earth's surface (Section 1.1). However, only Bürger and Cubasch (2015) have investigated the time scale between injecting sulphate aerosols into the stratosphere and detecting its effects on temperature. Being able to distinguish the temperature responses to geoengineering sulphate aerosols from other forcing factors and internal variability would be important in the event of:

- Field experiments that aim at evaluating the temperature effects of SAI, as we could only evaluate these effects after discerning them from other plausible sources.

- Unilateral experiments or deployment, as we would want to be able to tell if a nation or a small group of people were experimenting or deploying SAI in the real world.

- SAI deployment, as we would want to know how much of any temperature changes observed in the presence of SAI could be attributed to SAI, in order to work out the amount or location of aerosol injection for the years that follow, so that our climate objectives for the future could be met.

The earlier we could detect the temperature effects of SAI in any of the above scenarios, the shorter the field experiments could be, the sooner any large-scale unilateral SAI implementation would be realised, and the more effective the SAI monitoring and management system could be developed. Therefore, this thesis seeks to answer the following questions with the use of a GeoMIP future scenario, G4 (please refer to Section 2.2.1 for details):

1. When could we first detect the global-mean cooling response to 5 Tg yr^{-1} SO_2 injection?

2. How could we detect the global-mean cooling response to geoengineering early into implementation?

3. Where on the surface and in the atmosphere would be best for early geoengineering detection and monitoring?

1.5   Thesis outline

This section outlines the structure of the remainder of this thesis.

The GeoMIP experiments will be briefly described in Chapter 2. The GeoMIP G4 experiment, the climate models that participated in this experiment and their projections of near-surface air temperature and precipitation in the G4 scenario will then be explored and discussed in detail. The optimal fingerprint methodology for climate change detection and attribution will be explained in the second half of Chapter 2. In particular, the classical total least squares (TLS) detection and attribution algorithm and a recently-proposed, non-stationary variant of TLS will be delineated.

Chapter 3 is the first working chapter of this thesis. In this chapter, the questions of when we could first detect the global-mean cooling response to stratospheric sulphate aerosols, and how we could detect this response early into SAI deployment in the G4 scenario (Section 1.4) will be addressed. The latter will be investigated though the comparison of the global-mean detection results found with different optimal fingerprint detection techniques.

In Chapter 4, the question of where on the Earth's surface would be best for effective detection of the cooling response to stratospheric sulphate aerosol geoengineering will be answered. Various regions on the near-global, hemispheric, latitudinal, continental and sub-continental scales will be examined. Results of this chapter will provide the scientific basis for developing an optimal observational network on the surface for effective geoengineering monitoring.

Chapter 5 then explores the effects of increasing greenhouse gas concentrations and stratospheric sulphate aerosol geoengineering on the vertical temperature profile spanning the troposphere through to the upper stratosphere. Detection of the geoengineering effect on the vertical temperature structure over the whole globe, the Northern and Southern Hemispheres, and the Tropics as if observed by satellites will then be investigated.

Finally, the main research results from Chapter 3 to 5 will be summarised in Chapter 6. The implications of the results and limitations of the experiments presented in this thesis will be identified, and improvements for potential future work will be suggested.

Chapter 2

Methodology and data

2.1 Introduction

This thesis applies existing climate change detection and attribution techniques to a hypothetical, 5 Tg yr^{-1} SO$_2$ injection future scenario, in order to estimate the time scale between injecting the stratospheric sulphate aerosols and detecting their effects on temperature.

The first half of this chapter, i.e. Section 2.2, describes the Geoengineering Model Intercomparison Project (GeoMIP) and the GeoMIP G4 scenario, the scenario which is used throughout this thesis, in detail. In particular, the choice of climate models, as well as the model-simulated global-mean and grid-scale near-surface air temperature responses in G4 are discussed in Sections 2.2.1 and 2.2.1.1, respectively, in order to evaluate the magnitude and significance of some of the projected temperature responses that this thesis attempts to detect. The model-simulated precipitation changes brought about by SAI in G4 are then outlined in Section 2.2.1.2, mainly to illustrate why temperature, rather than precipitation, is studied in this thesis.

The second half of this chapter, i.e. Section 2.3, presents the underlying concept of climate change detection and attribution. In particular, the total least squares detection and attribution

algorithm and the non-stationary algorithm, both of which are used for detection proposes in this thesis, are delineated in Sections 2.3.1 and 2.3.2, respectively.

2.2   The GeoMIP

The Geoengineering Model Intercomparison Project (GeoMIP) (Kravitz et al., 2011) was designed to establish a coordinating framework for modelling groups to explore possible climate responses to various SRM methods. So far there have been 7 standardised GeoMIP experiments that involve solar irradiance reduction, planetary albedo enhancement through stratospheric sulphate aerosol injection, and marine cloud brightening through sea spray injection. These experiments are outlined below but can be found in greater detail in Kravitz et al. (2013a) and Kravitz et al. (2013b).

In the G1 experiment, instantaneous quadrupling of CO_2 concentration from pre-industrial levels is counteracted by reducing the solar constant. The G1 ocean-albedo experiment is also based on quadrupling of CO_2 concentration, but the increased CO_2 radiative forcing is counteracted by an increase in ocean albedo instead. In the G2 experiment, the solar constant is gradually reduced to balance the positive radiative forcing of a 1% increase in CO_2 concentration per year from pre-industrial levels. All of these experiments are conducted in climate models for 70 years, with SRM being applied in the first 50 years.

The G3 experiment is based on the Representative Concentration Pathway of greenhouse gases that leads to $4.5 \, \mathrm{Wm}^{-2}$ increase in radiative forcing in year 2100 relative to pre-industrial values, also known as RCP4.5 (Taylor et al., 2012). Starting from 2020, SO_2 is gradually injected into the tropical lower stratosphere to keep global average planetary temperature nearly constant. SAI stops in year 2070 in this experiment.

G4 is another GeoMIP experiment that involves SAI as a means of cooling the planet. Also based on RCP4.5, this experiment involves daily, constant injections of SO_2 at a rate of 5 Tg

yr^{-1} into the tropical lower stratosphere between 2020 and 2070. 5 Tg yr^{-1} of SO_2 injection is roughly equivalent to one Mount Pinatubo eruption every 4 years, and this injection rate was designed to bring global-mean temperature back to about the 1980 values (Kravitz et al., 2011).

This thesis investigates the detectability of the effects of sulphate aerosol geoengineering on climate, on which future decisions on SO_2 injection rate or method would likely depend. Hence it will be useful to assume constant SAI, as applied in G4, and to estimate the time needed for the geoengineering signal to be robustly detected, before making any changes to the injection rate or location. Therefore, this thesis focuses on the G4 scenario. This scenario is chosen to be illustrative only. It is not suggested that a real-world application would be likely to follow this pathway. Section 2.2.1 provides an overview of the projected climatic changes and effective radiative forcing in G4.

Although not studied in this thesis, G4 cdnc and G4 sea-salt are other 2 GeoMIP experiments that are based on RCP4.5. Starting from 2021, the cloud droplet number concentration in marine low clouds is increased by 50% in the G4 cdnc experiment, while sea salt aerosols are injected into the tropical marine boundary layer at a constant rate to achieve a global mean effective radiative forcing of -2 Wm^{-2} in the G4 sea-salt experiment. In both experiments geoengineering terminates abruptly in 2070, as in the G4 scenario.

2.2.1 The G4 scenario

This section describes the GeoMIP G4 experiment and the climate models that conducted this experiment, on which this thesis is based. In G4, SO_2 was designed to be injected daily into the stratosphere (16–25 km) at a rate equivalent to 5 Tg yr^{-1} during the period 2020–2070 on top of a base climate of RCP4.5. Greenhouse gas emissions in RCP4.5 peak in around 2040 and then decline. This was thought to be a plausible greenhouse gas concentration pathway with greenhouse gas mitigation implemented when the GeoMIP experiments were being designed.
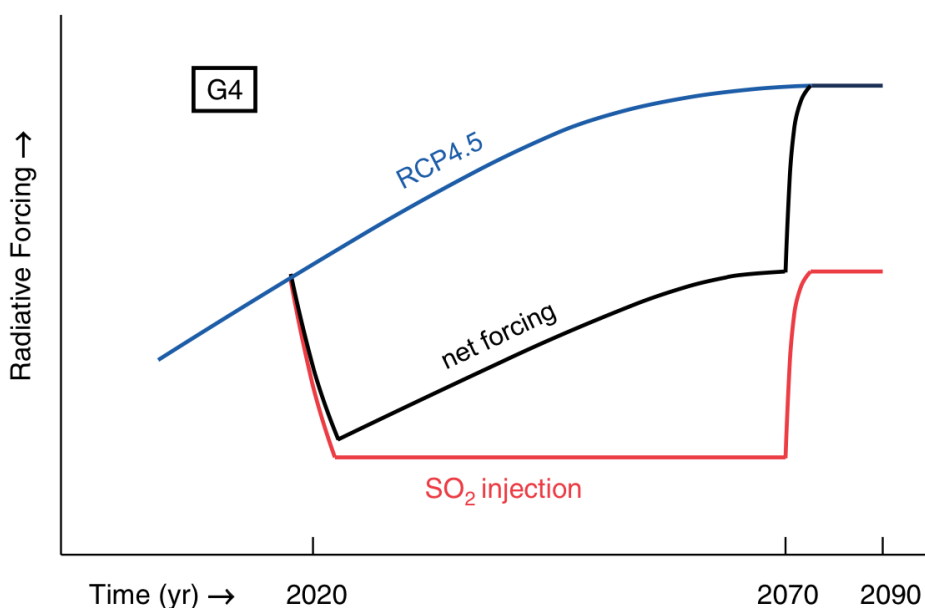
Figure 2.1 Schematic from Kravitz et al. (2011) showing increasing radiative forcing in RCP4.5 (blue line), constant negative radiative forcing between 2020 and 2070 introduced by SO_2 injections (red line), and the net radiative forcing in G4 (black line). Copyright ©2011 Royal Meteorological Society and Crown Copyright.

Figure 2.1 shows a schematic taken from Kravitz et al. (2011) that shows the expected time evolution of the background radiative forcing in RCP4.5 (blue line), the radiative forcing introduced by constant 5 Tg yr^{-1} SO_2 injection (red line), and the net forcing in the G4 scenario (black line). It is clear that the G4 experiment was designed to counteract some, but not all, of the positive radiative forcing in RCP4.5.

At the time this thesis started, 9 climate models had participated in the G4 experiment (Kravitz et al., 2013a). These included 7 fully coupled earth system models (ESMs) namely BNU-ESM (Ji et al., 2014), CanESM2 (Chylek et al., 2011), CSIRO-Mk3L-1-2 (Phipps et al., 2011), GISS-E2-R (Schmidt et al., 2014), HadGEM2-ES (Bellouin et al., 2011b), MIROC-ESM and MIROC-ESM-CHEM (Watanabe et al., 2011), and 2 chemistry-climate models, ULAQ (Pitari et al., 2002) and GEOSCCM (Oman and Douglass, 2014).

Using output from the 7 ESMs, Yu et al. (2015) estimated the difference between 2030–2069 and 2010–2029 global-mean near-surface air temperature (SAT) under the RCP4.5 scenario to

be $0.81 \pm 0.21°$C. This difference would reduce to $0.28 \pm 0.31°$C in the comparison between 2030–2069 G4 and 2010–2029 RCP4.5 global-mean SATs.

Output for the G4, RCP4.5 and pre-industrial control run from BNU-ESM, CanESM2, CSIRO-Mk3L-1-2, HadGEM2-ES and MIROC-ESM are most frequently used in this thesis. The G4 and RCP4.5 simulations from GISS-E2-R are not included because of incorrect initialisation between the two experiments (Bürger and Cubasch, 2015). Nonetheless, its pre-industrial control simulations are used to estimate internal climate variability in all of the following detection experiments (e.g. Section 3.2). All CMIP5 and GeoMIP modelling output were obtained from the Earth System Grid Federation (ESGF) (Earth System Grid Federation, 2014), or the individual modelling groups when ESGF was out of service. MIROC-ESM-CHEM is also not included in this thesis, as its pre-industrial run, which is essential for estimating climate variability, was unavailable at the time of the study. Finally, the 2 coupled chemistry-climate models are not used because they prescribed sea surface temperature, making their near-surface and tropospheric temperature simulations non-comparable to that of the other models.

Figure 2.2 shows the time series of the ensemble-mean annual-mean global-mean SAT anomalies with respect to the corresponding 2020 levels in RCP4.5 (dashed lines) and G4 (bold solid lines) from the 5 models that are included in almost all detection experiments in this thesis. Throughout this thesis, 'ensemble mean' refers to the average value taken across all available ensemble members of the same climate model. The BNU-ESM (blue) and MIROC-ESM (purple) trajectories are nosier than the others because each of these models has only one ensemble member. The rest of the included models have 3 ensemble members each.

Different temperature trajectories are projected for RCP4.5 in the climate models. In particular, CSIRO-Mk3L-1-2 (green dashed line, Figure 2.2) simulates the smallest increase in global-mean SAT by 2090, whereas HadGEM2-ES (red dashed line) simulates the largest positive SAT response to the standardised pathway of increasing greenhouse gas concentrations. Indeed, CSIRO-Mk3L-1-2 has the lowest transient climate response (TCR) among these models
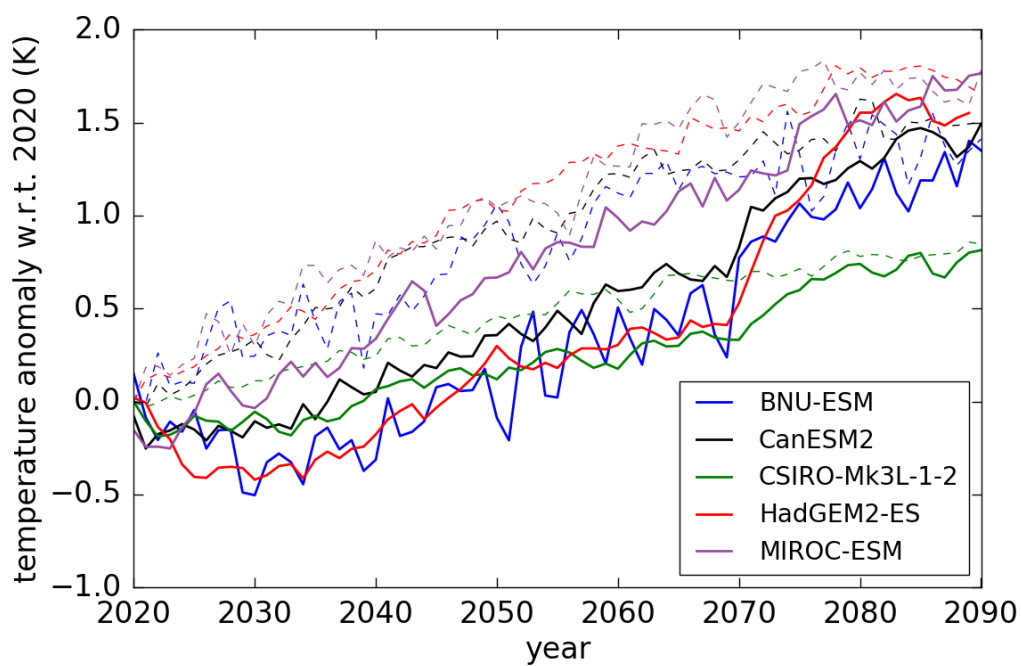
Figure 2.2 Ensemble-mean annual-mean global-mean near-surface air temperature anomalies relative to the corresponding 2020 levels in G4 (bold solid lines) and RCP4.5 (dashed lines), simulated by BNU-ESM, CanESM2, CSIRO-Mk3L-1-2, HadGEM2-ES and MIROC-ESM, respectively. BNU-ESM and MIROC-ESM have nosier time series as they have only 1 ensemble member each, while the rest of the models have 3.

(1.59 K, Phipps et al. (2012)), whereas HadGEM2-ES has the highest TCR (2.5 K, Senior et al. (2016)) to doubling of CO_2 in the scenario of 1% increase in CO_2 concentration per year (Cubasch et al., 2001).

Not only are model responses to increasing CO_2 concentrations different, but also their responses to stratospheric sulphate aerosols in G4 are diverse (Figure 2.2). The global-mean SAT difference between G4 and RCP4.5 averaged over the last two decades of SAI in G4 (i.e. 2051–2070), or ΔT_{SAI}, is calculated for each included climate model as a measure of the global-mean cooling response of a model to geoengineering aerosols. Consistent with the order of model sensitivities to CO_2, CSIRO-Mk3L-1-2 has the smallest cooling response of -0.31 K, whereas HadGEM2-ES has the largest response of -1 K.

Nevertheless, global-mean SAT drops swiftly by ~ 0.2 to 0.5 K during the first decade of sulphate aerosol geoengineering in G4, and then rises at a similar rate as RCP4.5 up until 2070 in all of the included models. Temperatures in G4 are consistently lower than that in RCP4.5 throughout the deployment period in all of the models, indicating that 5 Tg yr^{-1} SO_2 injections could cool the planet's surface from the background climate to a noticeable extent. When geoengineering terminates abruptly in 2070 in G4, global-mean SAT rises rapidly back to the RCP4.5 levels. As mentioned in Section 1.1, this phenomenon is often referred to as the 'termination effect', which could make adaption to the rapid increase in temperature more difficult compared to not implementing geoengineering at all.

With SAI implemented as hypothesised in G4, the climate models included in Figure 2.2 project a global-mean temperature rise that ranges between 1.30 K (CSIRO-Mk3L-1-2) and 2.22 K (MIROC-ESM) in 2061–2070, compared to the 1850–1900 pre-industrial levels. This warming range is calculated by adding the ensemble-mean temperature difference between 2061–2070 G4 and 2006–2015 RCP4.5 in each model, to the temperature difference between 2006–2015 and 1850–1900 in the HadCRUT4 dataset. Among the studied models, CSIRO-Mk3L-1-2 is the only model that projects a global-mean temperature rise that is below 1.5 K from the pre-industrial levels. The results, therefore, suggest that even if SAI were implemented

between 2020–2070 as it is in G4 to reduce the warming expected in RCP4.5, global-mean temperature rise would still likely exceed the 1.5 °C Paris target (Section 1.1) by 2070. On the other hand, only MIROC-ESM projects a temperature rise that exceeds the 2 °C Paris target by 2070, indicating that this target could potentially be achieved with 5 Tg yr^{-1} SO$_2$ injection on top of the RCP4.5 scenario. However, given that a rapid termination effect is expected at the end of SAI deployment, SO$_2$ injection would likely have to be sustained beyond 2070 in order to limit global-mean temperature rise to 2 °C throughout the 21st century.

Despite being a standardised hypothetical experiment, sulphate aerosol geoengineering in G4 is represented through different ways in the ESMs because of their different capabilities. Modelling groups were encouraged to conduct the G4 experiment in a similar way to how they previously simulated the 1991 Mount Pinatubo eruption (Kravitz et al., 2010).

For BNU-ESM, CanESM2 and MIROC-ESM, this meant prescribing stratospheric aerosol optical depth (AOD), as these models could not handle stratospheric aerosol layers directly. Since Mount Pinatubo injected approximately 20 Tg of SO$_2$ into the lower stratosphere, 5 Tg yr^{-1} of SO$_2$ injection in G4 is equivalent to one-fourth of a Mount Pinatubo eruption every year. As such, BNU-ESM and MIROC-ESM used an AOD distribution that was a 25% scaling of the Sato et al. (1993) dataset of stratospheric AOD following the 1991 Mount Pinatubo eruption (Kravitz, 2011; Sato, 2006). Figure 2.3d shows the annual cycle of the zonally averaged stratospheric AOD at 0.55 μm that was prescribed in BNU-ESM and MIROC-ESM repeatedly throughout 2020–2070 in G4.

CanESM2 also prescribed stratospheric AOD to represent the radiative effects of geoengineering in G4, but it was a constant field of $\sim$ 0.047 (Kashimura et al., 2017). CSIRO-Mk3L-1-2 was not able to handle stratospheric sulphate aerosols in any form, so solar irradiance was reduced as a means of representing solar radiation management in this model.

Finally, HadGEM2-ES injected 5 Tg yr^{-1}, or 0.0137 Tg day^{-1}, of SO$_2$ into the lower stratospheric (16–25 km) uniformly globally, and converted the aerosol precursors into sulphate aerosols internally (Jones et al., 2010; Kravitz et al., 2013a). It is the only model in this study
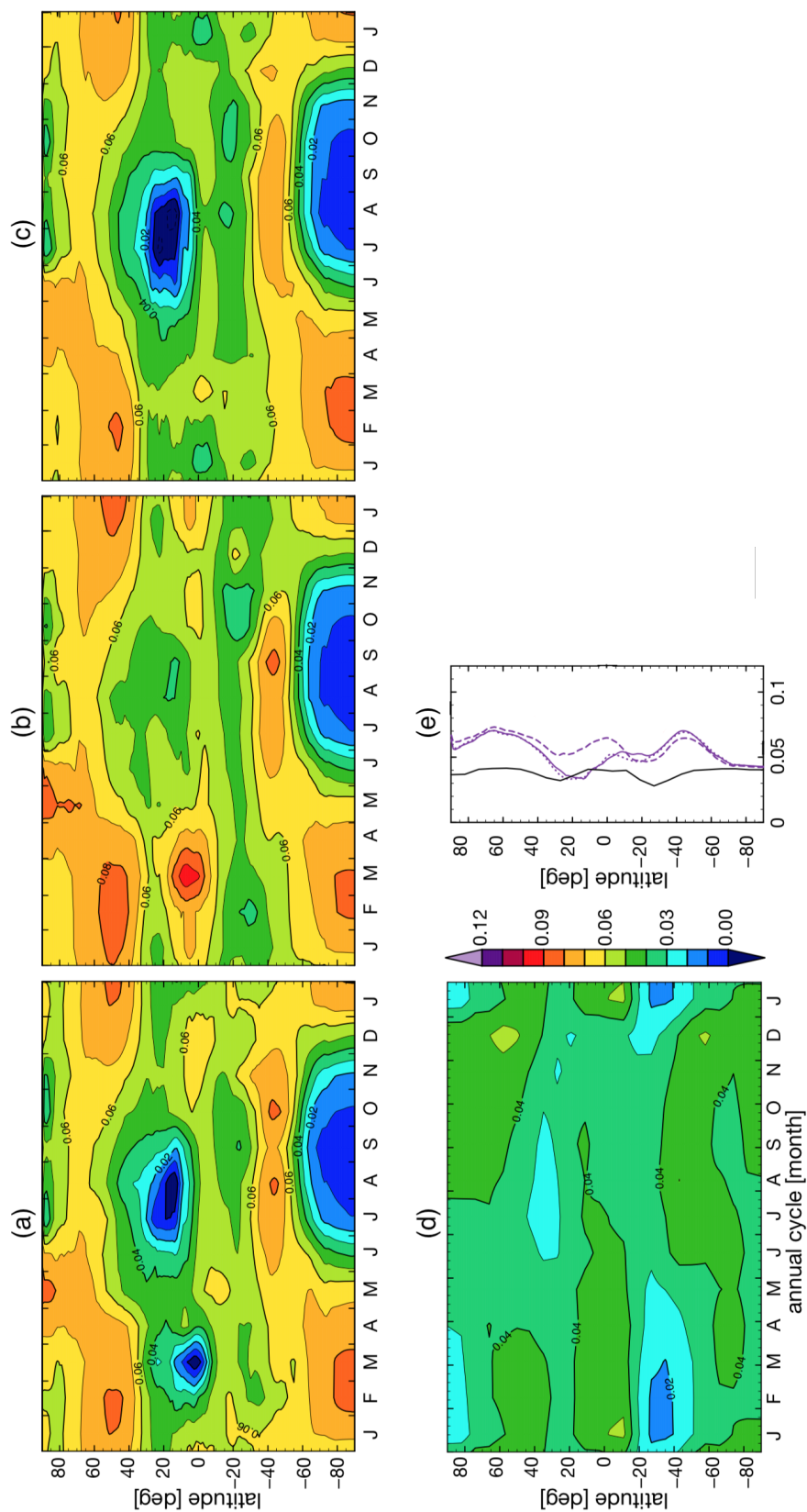
Figure 2.3 Figure adapted from the supplementary document to Kashimura et al. (2017), showing the annual cycle of zonally averaged (a–c) stratospheric and tropospheric sulphate AOD difference between G4 and RCP4.5 at 0.55 μm in the 3 realisations of HadGEM2-ES, and (d) stratospheric AOD at 0.55 μm in BNU-ESM and MIROC-ESM. The values shown are averages over the period 2040–2069. The AOD in HadGEM2-ES was internally calculated by the model, whereas that in BNU-ESM and MIROC-ESM was derived from the Sato et al. (1993) dataset and prescribed in the models. (e) shows the zonal and annual mean distribution of (a–d), with the purple solid, dashed and dotted lines showing the results from the first, second and third realisations of G4 from HadGEM2-ES, respectively, and the black line showing the prescribed stratospheric AOD in BNU-ESM and MIROC-ESM for G4. This figure is distributed and adapted under the Creative Commons Attribution 3.0 License.

33

that internally computed sulphate AOD when simulating SAI and the Mount Pinatubo eruption. Note, however, SO_2 was injected into the stratosphere globally rather than at one point on the Equator, which was originally specified in GeoMIP (Kravitz et al., 2011), as HadGEM2-ES's atmospheric component only extends up to 40 km. This means its stratospheric dynamics are not realistic and would not be able to distribute aerosols realistically in the stratosphere (c.f. Jones et al. (2010)).

Figures 2.3a to 2.3c show the mean annual cycle of the zonal-mean stratospheric sulphate AOD over 2040–2069 in the first, second and third reslisation of G4 in HadGEM2-ES. The median aerosol radius and geometric standard deviation of the log-normal size distributions (σ) of HadGEM2-ES's Aitken and accumulation sulphate modes are 0.0065 μm ($\sigma = 1.3$) and 0.095 μm ($\sigma = 1.4$) (Bellouin et al., 2011a), respectively, both the smallest among the models used (Kashimura et al., 2017).

Figure 2.3e shows the latitudinal distribution of the average stratospheric sulphate AOD over 2040–2069, as prescribed in BNU-ESM and MIROC-ESM (black line), and generated in the three G4 realisations in HadGEM2-ES (purple solid, dashed and dotted lines). The prescribed AOD is larger (~ 0.04) in 20 °N–20 °S and latitudes higher than 40 ° in both Hemispheres, compared to other latitudes (~ 0.03). On the other hand, the AOD calculated in the HadGEM2-ES G4 simulations is generally largest (~ 0.07) around 70 °N and 50 °S. In almost all latitudes the stratospheric sulphate AOD generated in HadGEM2-ES in the G4 experiment is larger than that prescribed in BNU-ESM and MIROC-ESM. The globally uniform stratospheric AOD of ~ 0.047 prescribed in CanESM2 for G4 lies between the global-mean AOD prescribed in BNU-ESM or MIROC-ESM and that simulated in HadGEM2-ES.

Table 2.1 summarises the resolution and vertical extent of the atmospheric component of the 5 climate models whose G4 simulations are used in this thesis, along with the corresponding geoengineering scheme applied, log-normal aerosol size distribution and G4 ensemble size.

In order to further understand the SAT changes brought about by 5 Tg yr^{-1} SO_2 injection (or equivalent) in the climate models included in this thesis, the effective radiative forcing

Model	Atmospheric horizontal & vertical resolution	Model top	Stratospheric aerosols	Particle size (μm) (σ)	Ensemble size
BNU-ESM	2.8 ° lat × 2.8 ° lon, 26 levels	2.917 hPa	Prescribed AOD*	0.426 (1.25)	1
CanESM2	2.8 ° lat × 2.8 ° lon, 35 levels	1 hPa	Prescribed AOD§	0.350 (2.0)	3
CSIRO-Mk3L-1-2	3.2 ° lat × 5.6 ° lon, 18 levels	4.5 hPa	None	N/A	3
HadGEM2-ES	1.25 ° lat × 1.875 ° lon, 38 levels	40 km	Global SO_2 injection	0.0065 (1.3), 0.095 (1.4)	3
MIROC-ESM	2.8 ° lat × 2.8 ° lon, 80 levels	0.003 hPa	Prescribed AOD*	0.243 (2.0)	1

Table 2.1 The atmospheric horizontal and vertical resolution, height of atmosphere model top, geoengineering scheme, sulphate aerosol size distribution and number of ensemble members of the ESMs whose G4 simulations are used in this thesis. Models with an * prescribed a 25% scaling of the Sato et al. (1993) AOD distribution dataset for the 1991 Pinatubo eruption, whereas models with a § prescribed AOD that was equivalent to 25% of their own Pinatubo simulations.

(ERF), which is defined as "the irradiance change at the top of atmosphere (TOA) following a perturbation to the climate system taking into account any rapid adjustments (Forster et al., 2016), is estimated for G4 in the included climate models. This is achieved by regressing the difference in the globally averaged TOA downward radiative flux between G4 and RCP4.5 against the global-mean SAT difference between G4 and RCP4.5 (Figure 2.4), following Gregory et al. (2004)'s method.

The data points in Figure 2.4 indicate the global annual mean changes in TOA downward radiative flux (y-axis) and SAT (x-axis) between G4 and RCP4.5 over the period 2020–2029, and the global decadal mean changes over the period 2030–2069. As such, the rapid adjustments during the first decade of SAI in G4 (Figure 2.2) are emphasised, whereas the subsequent slow feedbacks are given less weight in the calculation of the G4 ERFs (cf. Stjern et al. (2018)).

By definition (Gregory et al., 2004), the y-intercept of each best-fit straight line obtained through linear regression in Figure 2.4 gives an estimate of the ERF in G4 in the corresponding climate model. The estimated ERFs in BNU-ESM, CanESM2, HadGEM2-ES and MIROC-ESM are printed on the right of Figure 2.4 for comparison. CSIRO-Mk3L-1-2 is not included in this analysis because this model incorporated solar dimming as a representation of SAI in G4, making its ERF in G4 incomparable to that of the rest of the models.

Among the included models, MIROC-ESM has the highest ERF (0.22 W m^{-2}), which is also the only positive ERF estimated. This means a positive radiative forcing is brought about by the presence of additional stratospheric sulphate aerosols in MIROC-ESM. A positive ERF is not what one would expect from SAI nor SRM, but the small size of the sulphate aerosol forcing and the short time scale studied here might have led to this unexpected result. Moriyama et al. (2017) did a similar Gregory analysis with decadal averages, and they also found a particularly different result for MIROC-ESM from the rest of the models that participated in G4. Moreover, excluding CSIRO-Mk3L-1-2, MIROC-ESM does indeed simulate the smallest global-mean cooling response in G4 among the models included in this thesis (Figure 2.2), consistent with its highest (least negative) estimated ERF.
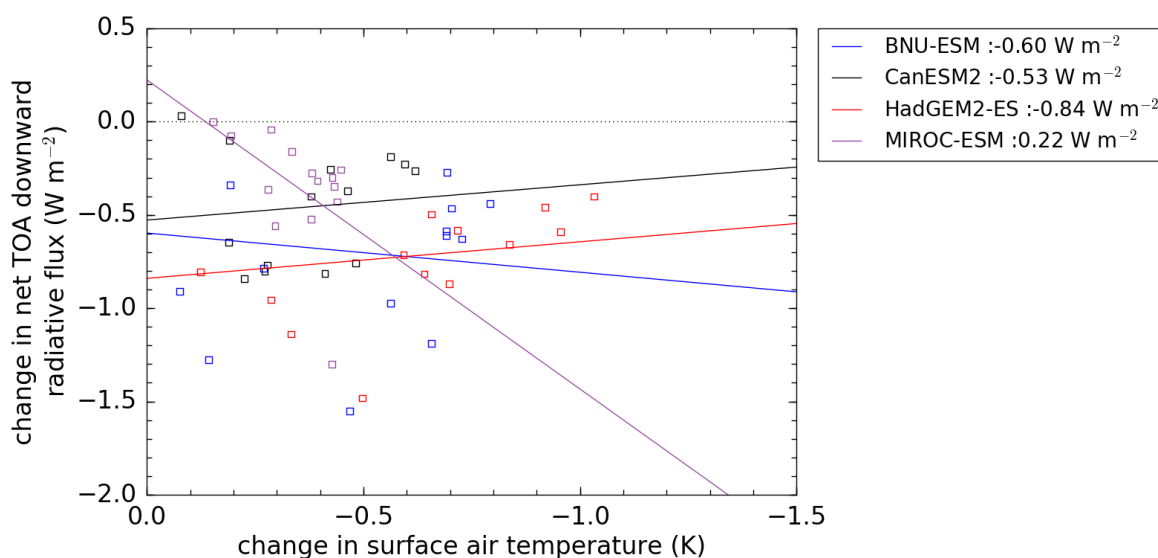
Figure 2.4 The evolution of global-mean TOA net radiative flux change with global-mean near-surface air temperature change in the G4 experiment in BNU-ESM, CanESM2, HadGEM2-ES and MIROC-ESM, respectively. The data points (squares) shown are the annual averages over the period 2020–2029 and the decadal averages over the period 2030–2069. The straight lines are the best-fit lines obtained through linear regression for each climate model. Values on the right represent the effective radiative forcings in G4 in the models.

BNU-ESM, CanESM2 and HadGEM2-ES all give a negative ERF in the G4 experiment, as expected. In particular, HadGEM2-ES has the most negative ERF (-0.84 W m^{-2}). This is consistent with its largest simulated global-mean cooling response to SAI in G4, as shown in Figure 2.2 and mentioned earlier in this section.

So far only the global-mean responses to SAI in G4 have been presented. The model-simulated changes that SAI would introduce to grid-scale SAT and precipitation in the hypothetical G4 scenario will be summarised in the next two sections.

2.2.1.1   Near-surface air temperature

Figure 2.5 shows the ensemble-mean SAT anomaly averaged over 2020–2029, i.e. the first decade of SAI in G4, relative to the mean over 2006–2019 in RCP4.5 (top panel) and G4 (middle panel) at model grid scale. The results shown are calculated from the simulations of the 5 climate models whose G4 simulations are used in this thesis. The bottom panel shows

the SAT changes introduced by SAI to the background climate over the same decade, i.e. 2020–2029 G4 - RCP4.5. Hatching on the graphs indicate changes insignificant from internal inter-annual variability at the 5% level found with the Welch's *t*-test (Welch, 1947).

In the RCP4.5 scenario, warming relative to the 2006–2019 mean is projected for 2020–2029 almost all over the world in all of the included models. Owing to positive ice-albedo feedback, largest warming is generally seen in high latitudes in the Northern Hemisphere and some parts of the Southern Ocean and Antarctica. The projected warming is statistically significant across the majority of the Earth's surface.

In the G4 scenario, statistically significant warming compared to 2006–2019 is still seen in some high-latitude areas such as Alaska and parts of the Southern Ocean in BNU-ESM (Figure 2.5c), and the Arctic and small areas in the southern high latitudes in CanESM2, CSIRO-Mk3L-1-2 and MIROC (Figures 2.5d, 2.5i and 2.5n). Nevertheless, when SAI is implemented, the significant warming that would have been caused by increasing greenhouse gas concentrations in RCP4.5 becomes statistically insignificant, or is even reversed, in large parts of the Tropics and mid-latitudes. In particular, various areas in BNU-ESM and HadGEM2-ES (Figure 2.5j for HadGEM2-ES) show lower SAT in 2020–2029 than in 2006–2019, suggesting that 5 Tg yr^{-1} SO_2 injection could reverse the warming in RCP4.5 as early as 10 years into deployment in some regions.

The net cooling effect of stratospheric sulphate aerosols is clearly shown in the bottom panel of Figure 2.5, where the difference between G4 and RCP4.5 SATs is plotted. Cooling is observed almost everywhere in all of the models, with strongest cooling seen in the northern high-latitudes except in CSIRO-Mk3L-1-2 (Figure 2.5k). Strongest cooling occurs in the northern high-latitudes in the models that internally generated sulphate aerosols or prescribed a spatial distribution of AOD (Table 2.1), because the temperature response to the close-to-spatially-uniform SRM radiative forcing (Kashimura et al., 2017) is amplified by Arctic sea ice in these models. CSIRO-Mk3L-1-2 does not simulate strongest cooling in the Arctic region
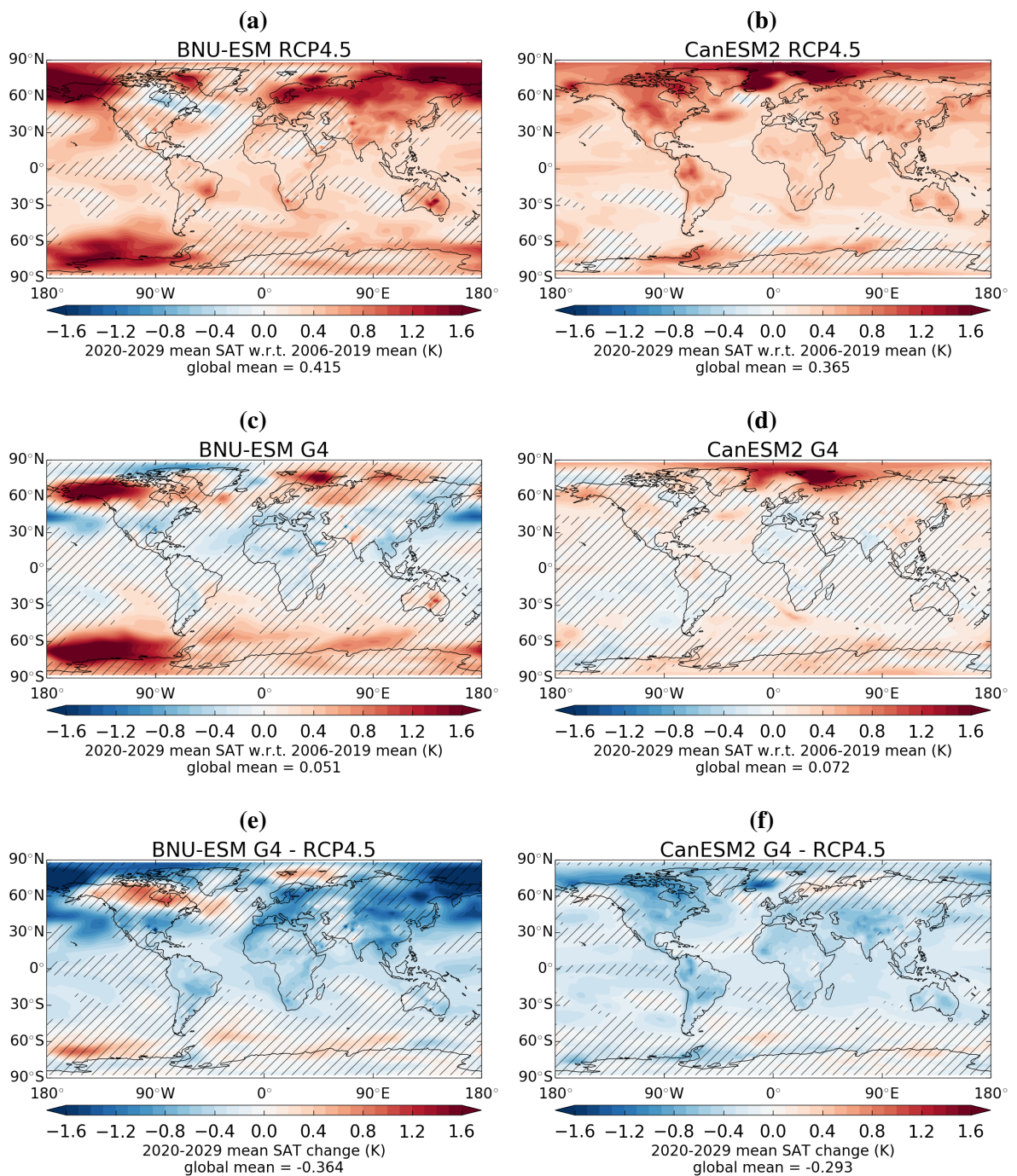
Figure 2.5 Maps of ensemble-mean, 2020–2029 mean SAT anomaly with respect to the corresponding 2006–2019 mean in (top panel) RCP4.5 and (middle panel) G4, and (bottom panel) the 2020–2029 mean SAT change between G4 and RCP4.5, in (left panel) BNU-ESM and (right panel) CanESM2. Hatch marks indicate changes that are insignificant from inter-annual variability at the 5% level. Figure continued overleaf.

39

Figure 2.5 continued from the previous page, but for (left panel) CSIRO-Mk3L-1-2 and (right panel) HadGEM2-ES. Figure continued overleaf.

(m)
MIROC-ESM RCP4.5

2020-2029 mean SAT w.r.t. 2006-2019 mean (K)
global mean = 0.517

(n)
MIROC-ESM G4

2020-2029 mean SAT w.r.t. 2006-2019 mean (K)
global mean = 0.184

(o)
MIROC-ESM G4 - RCP4.5

2020-2029 mean SAT change (K)
global mean = -0.333
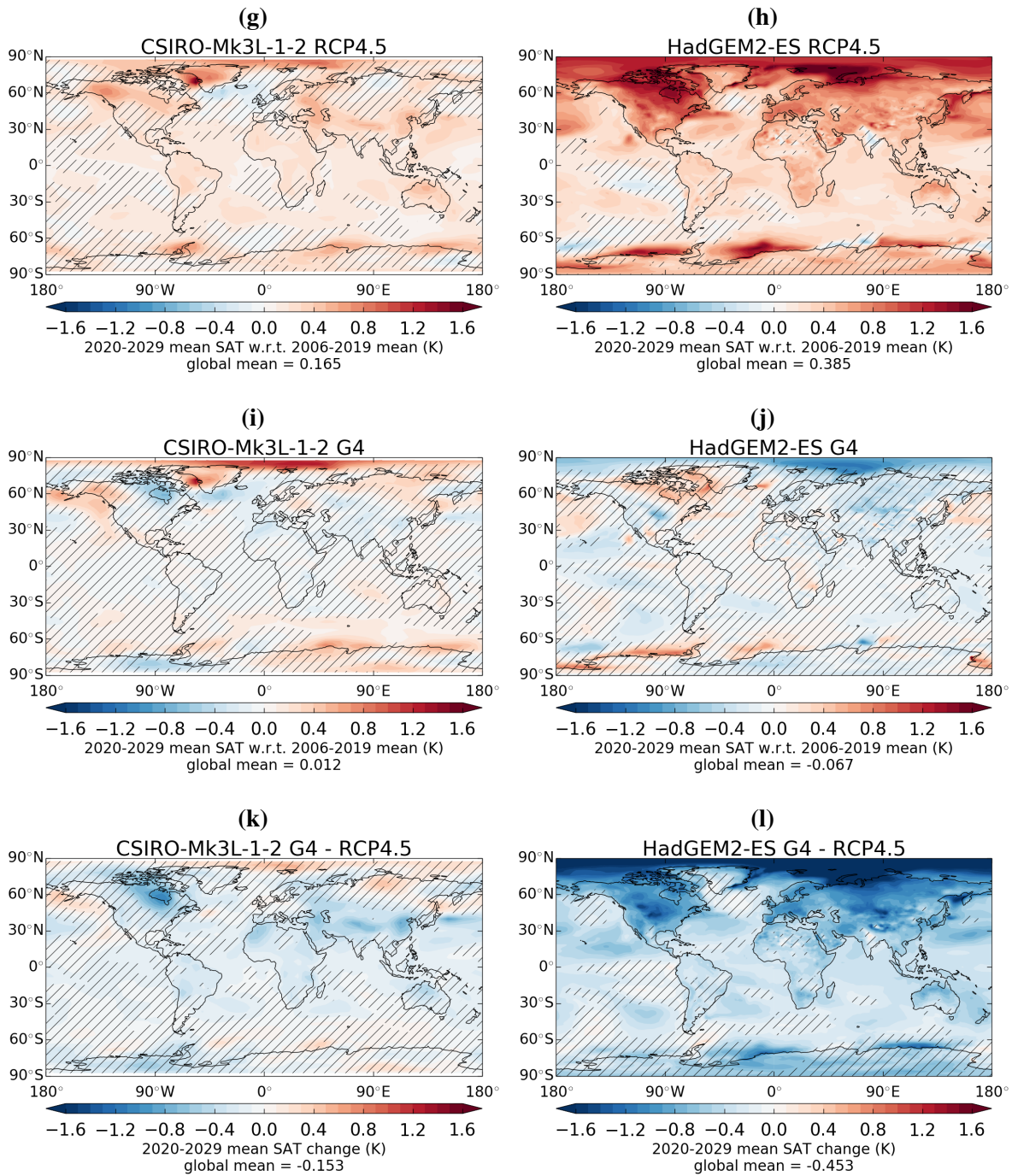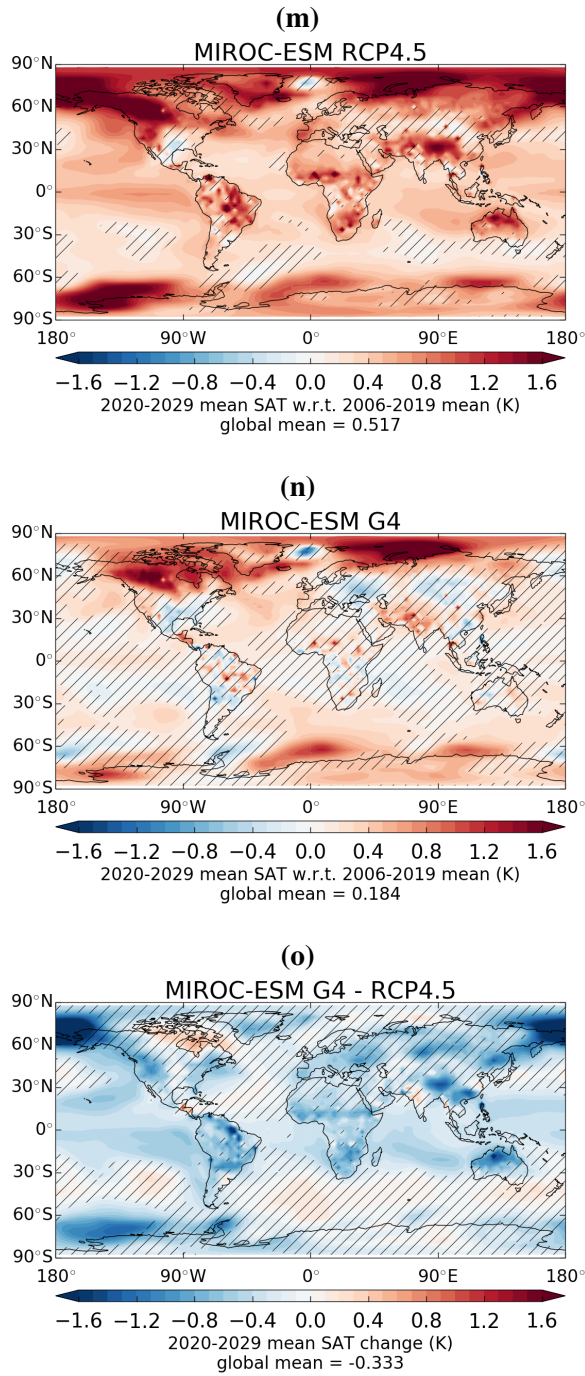
Figure 2.5 continued from the previous page, but for MIROC-ESM.

because it represented sulphate aerosol geoengineering by turning down the solar constant, which resulted in a SRM radiative forcing that is proportional to the cosine of latitude.

Apart from CSIRO-Mk3L-1-2, cooling over Greenland is relatively weak compared to other Arctic regions in all of the models. In other latitudes, cooling over land is generally stronger than over the ocean. All of these results are consistent with the geographical distribution of the SAI-induced SAT changes found by Kashimura et al. (2017), who compared 2040–2069 G4 and RCP4.5 temperatures. The net cooling effect of SAI is statistically significant in low to mid latitudes in all models including CSIRO-Mk3L-1-2. In CanESM2 and HadGEM2-ES (Figures 2.5f and 2.5l), significant cooling is extended to a majority of the high latitude regions in the Northern Hemisphere.

Results in this section have shown that the included climate models agree on the near-global cooling effect of SAI during the first 10 years of deployment in G4. Except CSIRO-Mk3L-1-2, the models are also in reasonable agreement on the spatial structure and statistical significance of such cooling. These suggest that the processes that affect SAT in the presence of stratospheric sulphate aerosols are reasonably well understood, and that these models could be used to monitor the effectiveness of SAI by means of optimal detection in SAT (please see Section 2.3 for details).

The discrepancy between the spatial distribution of SAT changes simulated by CSIRO-Mk3L-1-2 and the rest of the models also suggest that care should be taken when interpreting any detection results found with this model, as large uncertainties may arise from the fact that SAI was represented differently in CSIRO-Mk3L-1-2. Detection of the SAI cooling effect on the global and regional scales in the G4 scenario will be studied in Chapter 3 and Chapter 4, respectively.

2.2.1.2 Precipitation

With the SAT changes shown in Section 2.2.1.1, tropospheric specific humidity and, thus, precipitation is expected to change in both the RCP4.5 and G4 scenarios. Both greenhouse gases and stratospheric aerosols are also known to have negative temperature-independent effects on global-mean precipitation (Section 1.2) and tropical circulation (Section 1.1) through the reduction of tropospheric radiative cooling rate. As mentioned in Section 1.2, the effects of tropical SO_2 injection on precipitation could be regionally inhomogeneous. This section describes the model-simulated precipitation changes in the RCP4.5 and G4 futures.

Figure 2.6 shows the model-simulated ensemble-mean annual-mean global-mean precipitation time series between 2020 and 2090, relative to the 2020 levels. The dashed lines show precipitation changes in RCP4.5, whereas the solid lines indicate the corresponding changes in G4. Similar to the global-mean SAT changes shown in Figure 2.2, global-mean precipitation is projected to increase with time in elevated greenhouse gas concentrations in RCP4.5. 5 Tg yr^{-1} SO_2 injection between 2020 and 2070 in G4 would result in reduced global-mean precipitation from the RCP4.5 levels in all of the included models, but precipitation in G4 would still increase at a similar rate to that in RCP4.5 after an initial (1–10 years) drop. The termination effect (Section 2.2.1) is also apparent in precipitation.

Global-mean precipitation changes in RCP4.5 and G4 (Figure 2.6) are noticeably noisier than the corresponding global-mean SAT changes (Figure 2.2), even though the same ensemble members (Table 2.1) are used in both simulations. This suggests that discerning aerosol and greenhouse gas forced signals from internal variability would be more difficult in precipitation than in SAT. Discerning the forced signals from internal variability is expected to be even more challenging at smaller spatial scales. The following paragraphs describe the grid-scale precipitation changes projected for future periods in both RCP4.5 and G4 scenarios.

Figure 2.7 shows the precipitation change between 2020–2029 and 2006–2019 in the RCP4.5 (top panel) and G4 (middle panel) scenario, simulated by the 5 models included in this
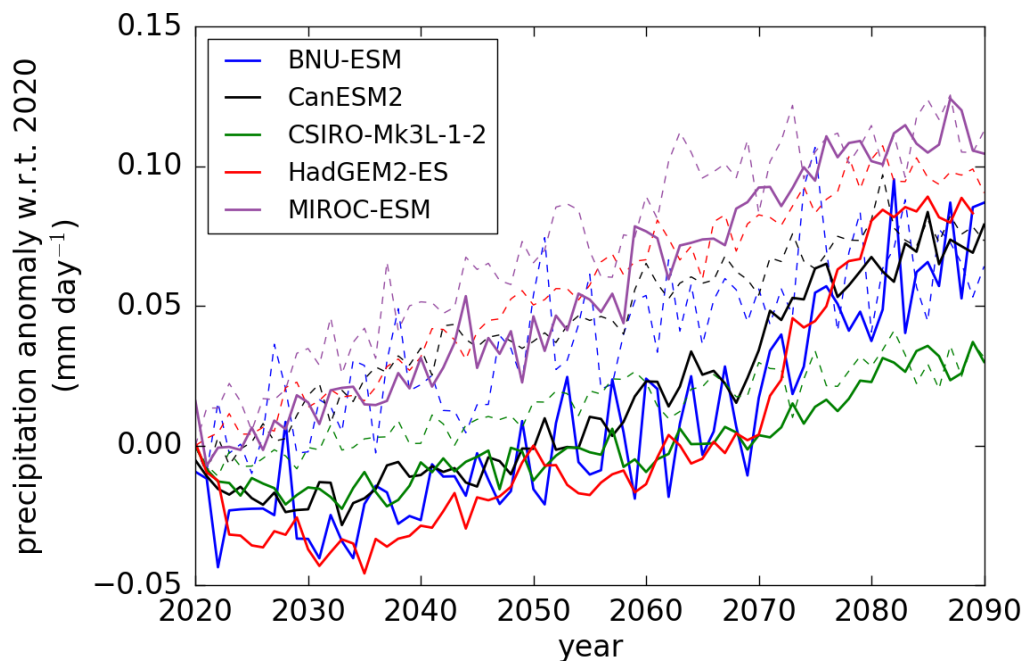
Figure 2.6 Ensemble-mean annual-mean global-mean precipitation anomalies relative to the corresponding 2020 levels in G4 (bold solid lines), and RCP4.5 (dashed lines), simulated by BNU-ESM, CanESM2, CSIRO-Mk3L-1-2, HadGEM2-ES and MIROC-ESM, respectively. BNU-ESM and MIROC-ESM have nosier time series as they have only 1 ensemble member each, while the rest of the models have 3.

thesis. The bottom panel shows the 2020–2029 mean precipitation difference between G4 and RCP4.5. Equivalent to the temperature graphs shown in the previous section, hatching here indicates insignificant precipitation changes at the 5% level.

Compared to the 2006–2019 average, global-mean increase in surface precipitation is simulated for 2020–2029 in the RCP4.5 scenario in all of the models. This is mainly due to the projected rise in global SAT for RCP4.5 (Section 2.2.1.1). The magnitude of precipitation increase ranges from 0.006 (CSIRO-Mk3L-1-2, Figure 2.7g) to 0.023 mm day^{-1} (MIROC-ESM, Figure 2.7m). However, the spatial distribution of the simulated precipitation change under RCP4.5 is diverse among the models.

When the effects of climate warming and geoengineering are combined in the G4 scenario, not all of the models agree on the sign of global-mean precipitation change. BNU-ESM, CanESM2, CSIRO-Mk3L-1-2 and HadGEM2-ES simulate a reduction in global-mean precipitation ranging from −0.002 to −0.017 mm day^{-1} (Figures 2.7c, 2.7d, 2.7i and 2.7j), whereas
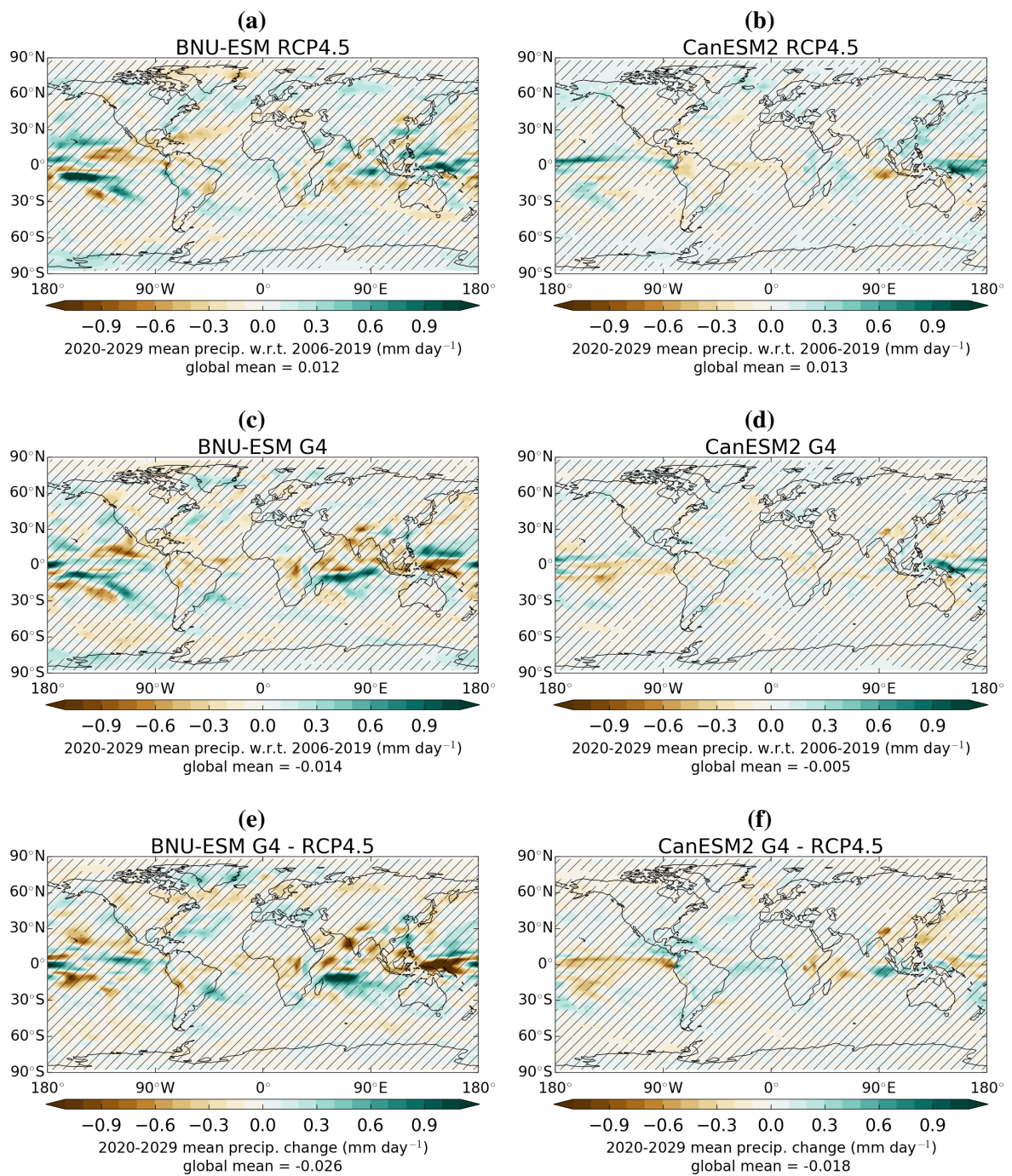
Figure 2.7 Maps of ensemble-mean, 2020–2029 mean precipitation anomaly with respect to the corresponding 2006–2019 mean in (top panel) RCP4.5 and (middle panel) G4, and (bottom panel) the 2020–2029 mean precipitation change between G4 and RCP4.5, in (left panel) BNU-ESM and (right panel) CanESM2. Hatch marks indicate changes that are insignificant from inter-annual variability at the 5% level. Figure continued overleaf.
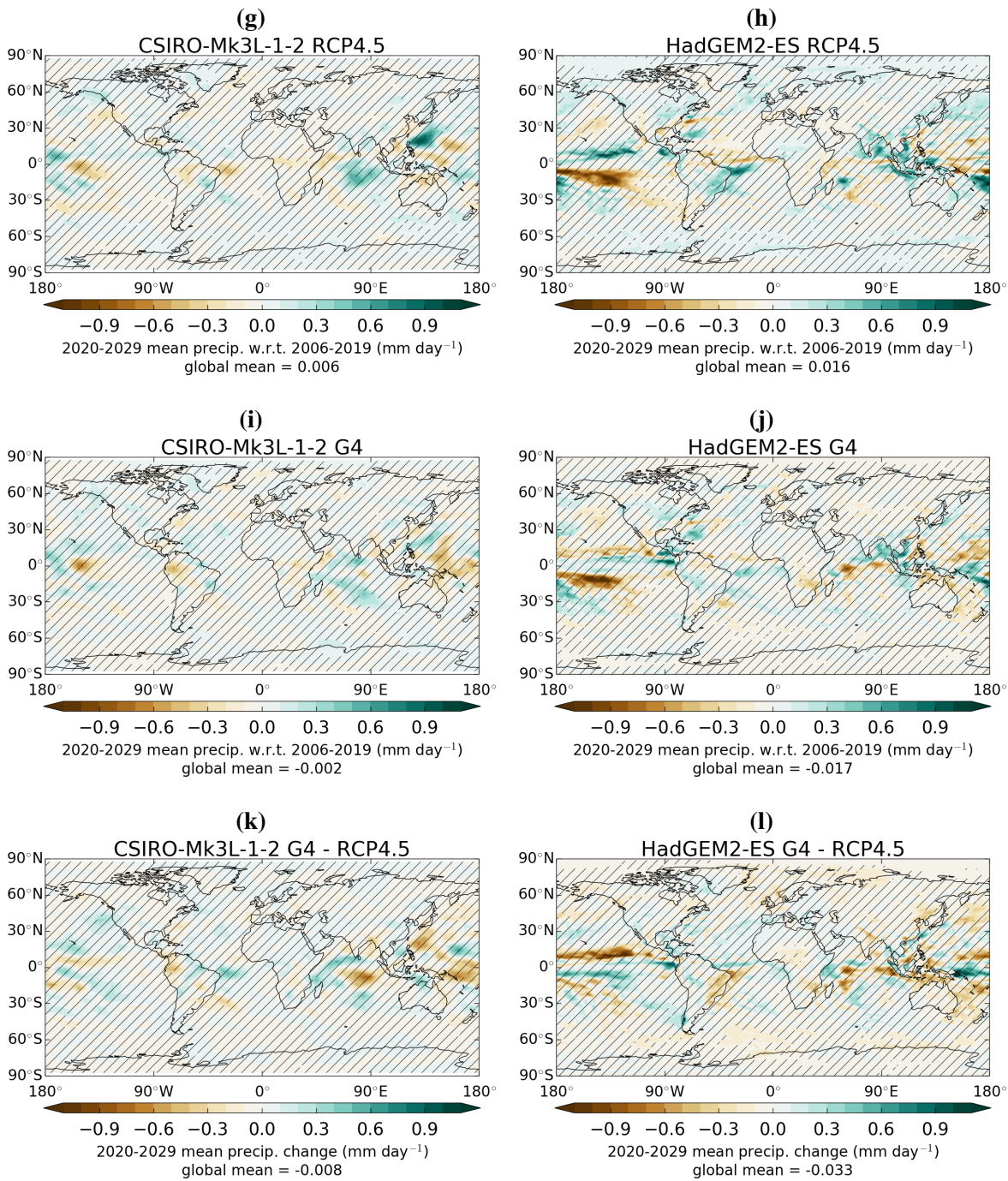
Figure 2.7 continued from the previous page, but for (left panel) CSIRO-Mk3L-1-2 and (right panel) HadGEM2-ES. Figure continued overleaf.
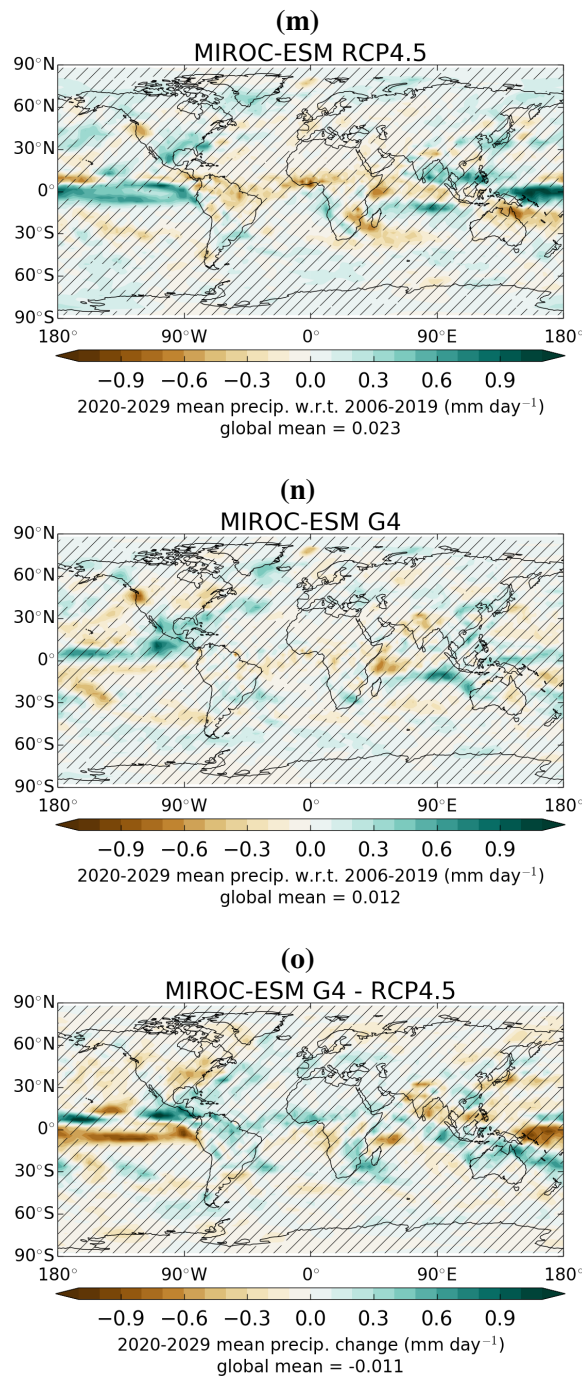
Figure 2.7 continued from the previous page, but for MIROC-ESM.

MIROC-ESM simulates an increase of 0.012 mm day^{-1} (Figure 2.7n) during the first decade of SAI in G4, with respect to the preceding 14 years.

The net effect of SAI on precipitation is explicitly shown in the bottom panel of Figure 2.7, where the precipitation changes SAI introduces to the background climate (RCP4.5) over the same period of 2020–2029 are plotted. All of the included models simulate a reduction in global-mean precipitation as a result of sulphate aerosol geoengineering. This is qualitatively consistent with the observed, globally averaged land precipitation reduction after the 1991 Mount Pinatubo eruption (Trenberth and Dai, 2007), as well as model simulations for the same (Ferraro and Griffiths, 2016; Yu et al., 2015) or similar SAI experiments in the literature (Jones et al., 2010, 2016). Stratospheric sulphate aerosols remove the temperature-dependent increase in precipitation projected for RCP4.5 by cooling the surface, but add to the temperature-independent decrease in precipitation by increasing downwelling longwave radiation from the warmed stratosphere into the troposphere (Ferraro and Griffiths, 2016).

However, the models are not in agreement on the spatial distribution of net precipitation change caused by SAI in G4. A variety of patterns is simulated across the models in the Tropics, where changes in precipitation are generally largest. Jones et al. (2010) found a southward shift in the tropical precipitation maxima in association with the inter-tropical convergence zone (ITCZ) in the Atlantic and Pacific oceans over the second decade of constant, 5 Tg yr^{-1} SO$_2$ injections using two different climate models. They linked this shift to the stronger geoengineering-induced cooling in the Northern Hemisphere, compared to the Southern Hemisphere. Although stronger SAI cooling effect is indeed simulated for the Northern Hemisphere over the first decade of SAI implementation in G4 (Section 2.2.1.1), no robust shift in annual-mean tropical precipitation is apparent in the models included here. Instead, complex yet statistically insignificant tropical precipitation changes are shown in the bottom panel of Figure 2.7.

All in all, results in this section have shown that apart from SAT, increasing greenhouse gas concentrations and SAI would have different effects on surface precipitation. Climate models

included in this thesis agree that increasing greenhouse gas concentrations in RCP4.5 would increase global-mean precipitation, whereas SAI in G4 would have the opposite effect. Bürger and Cubasch (2015) attempted to detect the effects of SAI (in both GeoMIP G3 and G4) on the spatial and spatio-temporal dimensions of SAT and precipitation, and found that the effect of SAI on global-mean precipitation would be detected and attributed soon after 2025 in the spatial dimension, and as soon as 2022 in the spatial-temporal dimension.

However, results here have also shown diverse spatial distributions of precipitation changes among our included models, and very few of them are statistically significant from internal variability. One of the aims of this thesis is to find out where would be best for SAI detection and monitoring (Section 1.4) through detection analyses at regional scales, i.e. scales at which climate models disagree on the sign of precipitation change and any change is likely overwhelmed by internal variability. For these reasons, this thesis does not attempt to detect the geoengineering effect in precipitation.

2.3   Optimal fingerprint detection and attribution

Detection and attribution of climate change involve quantifying the level of agreement between patterns of externally forced changes simulated by a climate model and the observed changes in the real world (Bindoff et al., 2013). 'Detection' is to establish that an observed change in climate cannot be ascribed to natural internal (unforced) variability alone at a certain confidence level, whereas 'attribution' is to demonstrate that the detected climate change signal is consistent with the model-simulated change from a single or a group of external forcing(s) but inconsistent with that of alternative forcing scenarios that do not include the external forcing(s) in question (Allen and Tett, 1999; Bindoff et al., 2013; Hasselmann, 1997). As such, attributing an observed change to a certain cause is often only done if the change is already detected, and if we confine our attention *a priori* to a finite set of plausible forcing scenarios (Allen and Tett, 1999).

Methodology and data

 Three components are generally required in a detection (and attribution) study:

1. An observational dataset of the climate variable of interest.

2. Model-simulated response patterns of the same climate variable to plausible external forcings or groups of forcings.

3. An estimate of natural variability of the same variable that is internal to the climate system.

The observations are compared to the model-simulated, externally forced response patterns in order to statistically evaluate the level of agreement between them. This evaluation takes into account uncertainty associated with natural climate variability that arises from interactions within the climate system, but excludes any natural, external forcings such as volcanic and solar activities (Hasselmann, 1997).

 The observations and the model-simulated response patterns are usually compared through a form of multi-variate linear regression. In this thesis, total least squares regression (TLS) (Allen and Stott, 2003) is used to estimate the amplitudes of the model-simulated response patterns in the observations. In addition to natural variability internal to the climate system, the TLS algorithm takes into account sampling uncertainty in the model-simulated response patterns, i.e. variability that exists between realisations within a finite ensemble. Before Allen and Stott (2003), ordinary least squares regression (OLS) (Allen and Tett, 1999) that assumes zero sampling uncertainty in the model-simulated responses was commonplace in detection and attribution studies. Zero sampling uncertainty is impossible to achieve as it requires response patterns to be generated from an infinite ensemble. In a perfect model study, Stott et al. (2003a) showed that at least 8 ensemble members were needed to eliminate the low bias OLS introduced to the estimated amplitude of the 'greenhouse gas plus sulphate aerosol' signal in near-surface temperature over the second half of the 20th century. The models included in this thesis have at most 3 ensemble members in the G4 experiment (Table 2.1); therefore TLS is employed throughout this thesis. Section 2.3.1 describes the TLS algorithm in detail.

Without long observations of the pre-industrial period or spatially complete proxies for paleoclimate reconstruction, internal variability is usually simulated by a climate model under a control run that has no change in anthropogenic and natural forcings. In CMIP5 this is known as the pre-industrial control experiment. This thesis estimates internal variability from a six-model ensemble of pre-industrial control simulations (please see Section 3.2 for details). Another common technique is to derive intra-ensemble variability from an ensemble of realisations. More details about the latter technique can be found in Tett et al. (2002) and Lott et al. (2013).

Estimates of internal variability are not expected to be the same as that in the real world, especially at small spatio-temporal scales where variability is likely underestimated in climate models (Allen and Tett, 1999). Therefore, the observations and model-simulated response patterns are often projected onto κ leading modes of variability, i.e. statistical modes that account for the largest percentage of noise variance, in a detection and attribution study (Stott et al., 2001). These modes, also known as empirical orthogonal functions (EOFs), can be computed by decomposing the covariance matrix calculated from the estimated internal variability into eigenvectors and eigenvalues (Hannachi et al., 2007). This will be further explained in Section 2.3.1. Only modes in which variability is adequately sampled are included in a detection study (Stott et al., 2001). They are chosen via a residual consistency test (Allen and Stott, 2003; Allen and Tett, 1999), which will be outlined below.

The 'optimal' methodology in detection and attribution refers to the rotation of the observations and model-simulated response patterns in such a way that the signal-to-noise ratio (SNR) is maximised. Figure 2.8 is a schematic taken from Mitchell et al. (2001), illustrating the principle of optimal detection in an example where 2 modes of internal variability (represented by the shaded ellipse) are included. The signal **OB** is rotated away from the direction of the main mode of variability (along OX) onto **OC**, such that the SNR is enhanced. In practice, optimisation is achieved by giving more weight to the included modes of variability that explain less variance, and vice versa (Thorne, 2001). Optimisation in the TLS algorithm will be explicitly shown in Section 2.3.1.
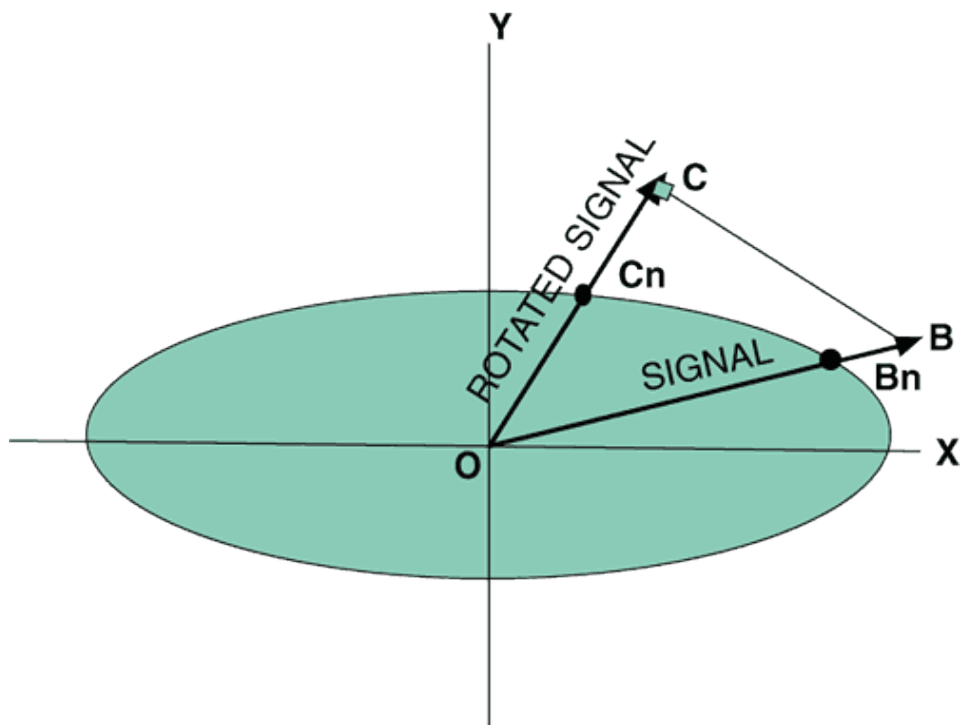
Figure 2.8 Figure from Box 12.1 from Mitchell et al. (2001) to illustrate 'optimal' detection in a simplified example of optimal detection that includes only 2 modes of internal variability (shaded ellipse): signal **OB** is rotated onto **OC** so that its signal-to-noise ratio is maximised.

Because both optimisation and hypothesis testing (whether a climate response pattern is detected against the null hypothesis) require knowledge of the characteristics of internal climate variability, it is very important that internal variability is realistically represented, at least in the chosen detection diagnostic (e.g. global mean temperature). As mentioned above, only κ leading modes of variability, or EOFs, are included in a detection analysis because subsequent modes are likely inadequately sampled. In this thesis, the maximum reliable EOF is chosen via a residual consistency test, in which the weighted sum of squared residuals of regression is compared to the model-simulated noise variance via an F-test (Allen and Stott, 2003).

The above paragraphs introduced the general principle of optimal detection and attribution in the classical framework, within which variants exist (OLS (Allen and Tett, 1999) and TLS (Allen and Stott, 2003)). In addition to these classical methods that project climate data onto leading EOFs for maximising SNR, Ribes et al. (2013) proposed an optimal fingerprinting algorithm that avoids such projection by estimating a regularised noise covariance matrix.

Nevertheless, all of these algorithms employ a null hypothesis of internal (unforced) climate variability.

Such conventional optimal fingerprint detection and attribution techniques have been used extensively to demonstrate human influence on the climate system. Observed increase in global-mean surface temperature since the 1950s, decrease in lower stratospheric temperatures since 1979, increase in upper ocean (above 700 m) temperature and global-mean sea level rise since the 1970s, changes in surface and subsurface oceanic salinity since the 1960s and loss of Arctic sea ice since 1979 (Bindoff et al., 2013), among other observed changes such as global-mean land precipitation changes in the 20th century (Lambert et al., 2004), warming in continental and sub-continental scale regions over the 20th century (Stott, 2003), etc. have been robustly (with 90% confidence) attributed to the combination of natural and anthropogenic forcings. A majority of this thesis explores whether and how effectively the conventional TLS detection algorithm could be used in a new way for detecting temperature responses to geoengineering aerosols in the G4 scenario.

Alternative to conventional optimal detection, Bürger and Cubasch (2015) detected the geoengineering signal against a gradual warming background caused by RCP4.5 forcings and natural interactions internal to the climate system. The following sections describe the methodology of each approach—conventional TLS in Section 2.3.1 and Bürger and Cubasch (2015)'s approach in Section 2.3.2. Chapter 3 then explores the application of these two detection approaches to geoengineering detection in global-mean SAT in the G4 scenario.

2.3.1   The total least squares (TLS) algorithm

This section describes the conventional TLS detection algorithm (Allen and Stott, 2003) in detail. TLS is sometimes referred to as the 'stationary multi-variate approach' or the 'conventional multi-variate approach' in this thesis in order to explicitly distinguish it from the non-stationary alternative proposed by Bürger and Cubasch (2015).

As mentioned in Section 2.3, conventional detection and attribution estimates the amplitudes, or scaling factors, of model-simulated response patterns to different, or different groups of, external forcings in the observations, with the null hypothesis of unforced, internal climate variability. In TLS, this is done by regressing the observations against the model-simulated response patterns, also known as 'fingerprints', simultaneously, taking into account unforced variability in the observations and sampling uncertainty in the simulated responses.

Assuming fingerprints of different external forcings, $\mathbf{x}_i$, are linearly additive, that they can be scaled up or down without affecting the other fingerprints, and that they are independent of unforced, internal variability, v_0, the TLS detection model can be written as follows:

$$\mathbf{y} = \sum_{i=1}^{m} (\mathbf{x}_i - v_i)\beta_i + v_0 \tag{2.1}$$

where $\mathbf{y}$ is the observations, v_i is the sampling uncertainty in $\mathbf{x}_i$, m is the total number of fingerprints and β_i is the scaling factor of the the ith fingerprint that is to be estimated. This assumption of linear additivity was found to be valid for large-scale temperature changes, but it might not be valid at regional scales or for climate variables such as precipitation (Bindoff et al., 2013).

The first step to solving Equation 2.1 is to compute the noise covariance matrix from v_0:

$$\mathbf{C}_N = \mathbb{E}(v_0 v_0^T) \tag{2.2}$$

where $\mathbb{E}$ is the expectation operator. As climate noise is not uncorrelated and uniformly distributed, or 'white', in either space or time, $\mathbf{C}_N \neq \sigma^2 \mathbf{I}$ (Allen and Tett, 1999), where σ^2 is the variance and $\mathbf{I}$ is an identity matrix. Therefore, a pre-whitening operator, $\mathbf{P}$, is introduced such that:

$$\mathbb{E}(\mathbf{P} v_0 v_0^T \mathbf{P}^T) = \mathbf{P}\mathbf{C}_N \mathbf{P}^T = \mathbf{I} \tag{2.3}$$

and

$$\mathbf{P}^T \mathbf{P} = \mathbf{C}_N^{-1} \tag{2.4}$$

In practice, $\mathbf{C}_N$ is unknown because the estimation of internal variability from climate model simulations does not capture all significant modes and scales of natural internal variability (Allen and Tett, 1999; Thorne, 2001). Fortunately, the noise covariance spanning the subspace that includes κ leading modes of variability can be reliably estimated as:

$$\hat{\mathbf{C}}_N = \frac{1}{n}\mathbf{Y}_N\mathbf{Y}_N^T \tag{2.5}$$

where a total of n successive vectors extracted from model simulations, in this thesis the pre-industrial control simulations, form the columns of $\mathbf{Y}_N$.

$\hat{\mathbf{C}}_N$ is non-invertible, but by using the Moore-Penrose pseudo-inverse (Allen and Tett, 1999),

$$\mathbf{P}^{(\kappa)T}\mathbf{P}^{(\kappa)} = \mathbf{C}_N^{-1} \tag{2.6}$$

where the rows of $\mathbf{P}^{(\kappa)}$ are the κ EOFs (eigenvectors of $\hat{\mathbf{C}}_N$) that explain the highest variance in an unforced climate system, weighted by their corresponding inverse singular values (reciprocal of the square root of the corresponding eigenvalues). The EOF that explains the largest noise variance has the largest eigenvalue. Therefore, dividing the EOFs by their inverse singular values is equivalent to giving less weight to the higher-variance EOFs, i.e. optimisation as mentioned in Section 2.3.

In addition to noise in the observations, sampling uncertainty in the model-simulated fingerprints generated from a finite ensemble, v_i, is taken care of in TLS. Under the assumption that every v_i has the same autocorrelation structure as v_0 (Allen and Stott, 2003), the same pre-whitening operator, $\mathbf{P}^{(\kappa)}$, can be applied to every variable such that:

$$\mathbb{E}(\mathbf{P}^{(\kappa)}v_i v_i^T \mathbf{P}^{(\kappa)T}) = \mathbf{I}_\kappa \tag{2.7}$$

This assumption only holds if internal climate variability, but not other non-negligible errors, is the dominating source of noise (Thorne, 2001).

Following the notation in Allen and Stott (2003) and for simplicity, $\mathbf{P}^{(\kappa)}$ is simply written as $\mathbf{P}$ hereafter. The projection of the observations and model-simulated response patterns onto κ leading modes of variability (Section 2.3) is done by defining an $m' \times \kappa$ matrix:

$$\mathbf{Z} \equiv [\mathbf{PX}, \mathbf{Py}] \tag{2.8}$$

where $m' \equiv m + 1$ and the columns of $\mathbf{X}$ are $\mathbf{x}_i$ from Equation 2.1.

To solve Equation 2.1, we must minimise the sum of squared perpendicular distances from the best-fit m-dimensional plane to the κ noise-contaminated observation and simulated points (defined by the rows in $\mathbf{Z}$). The solution to this is the eigenvector of $\mathbf{Z}^T\mathbf{Z}$ that has the smallest eigenvalue (Allen and Stott, 2003; Thorne, 2001). In other words, the solution vector is the m'^{th} right singular vector of $\mathbf{Z}$ that can be found through singular value decomposition:

$$\mathbf{Z} = \mathbf{Q}\mathbf{\Lambda}\mathbf{V}^T \tag{2.9}$$

and

$$\tilde{\mathbf{v}} = \mathbf{v}_{m'} \tag{2.10}$$

where elements on the diagonal of $\mathbf{\Lambda}$ are the non-zero singular values sorted in descending order, columns of $\mathbf{Q}$ are the corresponding left singular vectors of $\mathbf{Z}$ (orthonormal eigenvectors of $\mathbf{Z}\mathbf{Z}^T$), columns of $\mathbf{V}$ are the corresponding right singular vectors of $\mathbf{Z}$ (orthonormal eigenvectors of $\mathbf{Z}^T\mathbf{Z}$) (Hannachi et al., 2007), and the solution vector $\tilde{\mathbf{v}}$ is the m'^{th} column of $\mathbf{V}$, i.e. $\mathbf{v}_{m'}$.

The best-estimate scaling factor of the ith fingerprint, $\tilde{\beta}_i$, is then the ratio of the ith element of the solution vector to the m'^{th} element of the solution vector, i.e.:

$$\tilde{\beta}_i = \frac{[\tilde{\mathbf{v}}]_i}{[\tilde{\mathbf{v}}]_{m'}} \tag{2.11}$$

Uncertainty analysis is done with the use of a set of noise realisations that are statistically independent of those used to estimate $\mathbf{P}$, or, equivalently, $\mathbf{P}^{(\kappa)}$ in Equation 2.6. In practice, this

is usually achieved by separating the control simulations into two halves—the first half for optimisation and the second for uncertainty analysis.

The uncertainty associated with $\tilde{\beta}_i$ is found by first choosing a confidence level, in this thesis this is 90%, and then by defining a set of points on an m-dimensional sphere whose radius equals the critical value corresponding to the 90$^{\text{th}}$ percentile of an F-distribution. For each of these points, the corresponding eigenvector in $\mathbf{V}$ is weighted by the inverse of the square root of the difference between its eigenvalue and the smallest eigenvalue (Allen and Stott, 2003). Similar to the best-estimate above, estimates of the scaling factor of the ith fingerprint are then found by taking the ratio of the ith element to the m'^{th} element of the weighted eigenvectors $\mathbf{v}$, i.e. $\beta_i = [\mathbf{v}]_i / [\mathbf{v}]_{m'}$. The upper and lower limits of the confidence interval of the scaling factor of the ith fingerprint are then the maximum and minimum values of β_i, respectively.

If the solution, $\tilde{\beta}_i$, and its two-tailed confidence interval, that is its 5 to 95 percentile in this thesis, include zero, then the null hypothesis that the ith fingerprint is absent from the observations cannot be ruled out at $P_{<0.1}$. Rejection of this null hypothesis, i.e. β_i and its uncertainty range differ from zero, implies detection of the ith fingerprint at the 10% significance level (an example of hypothesis testing can be found in Figure 3.3). Attribution requires a detected signal to be consistent with the observations. Therefore, if the 5 to 95 percentile uncertainty range of $\tilde{\beta}_i$ is away from zero and includes 1, then the observed changes are attributed to the ith cause (Stott, 2003).

2.3.1.1 Linear transformation of scaling factors

There are two known components in the G4 scenario—the background RCP4.5 forcings and the forcing from the hypothetically injected stratospheric sulphate aerosols. As such, Equation 2.1 can be written as the following in this thesis:

$$\mathbf{y} = (\mathbf{x}_{\text{RCP}} - \nu_{\text{RCP}})\beta_{\text{RCP}} + (\mathbf{x}_{\text{SAI}} - \nu_{\text{SAI}})\beta_{\text{SAI}} + \nu_0 \qquad (2.12)$$

where $\mathbf{x}_{\text{RCP}}$ and $\mathbf{x}_{\text{SAI}}$ are the model-simulated fingerprints of the RCP4.5 and geoengineering aerosol forcings, respectively, and β_{RCP} and β_{SAI} are the corresponding scaling factors.

Regressing the observations against the fingerprints will give us the scaling factors of the fingerprints, and the magnitude and uncertainty range of β_{SAI} will indicate whether the geoengineering signal would be detected in an observable variable in the G4 scenario over a future time period of interest.

However, $\mathbf{x}_{\text{SAI}}$ is not directly obtainable due to a lack of SAI-only simulations. If OLS were employed for detection purposes in this thesis, $\mathbf{x}_{\text{SAI}}$ could be extracted by performing $\mathbf{x}_{\text{G4}} - \mathbf{x}_{\text{RCP}}$, under the assumption of linear additivity of climate signals (Section 2.3.1). Indeed, Allen and Tett (1999) subtracted the greenhouse-gas-only fingerprint from the 'greenhouse gas, sulphate and ozone' fingerprint to isolate the response pattern to the 'sulphate and ozone' forcing for input into the OLS algorithm.

While subtraction of climate signals is acceptable in OLS, it becomes problematic when the fingerprints are contaminated with sampling noise in TLS. This is because upon subtraction, the noise term in the resulting fingerprint is no longer independent from that of the other fingerprints (Allen and Tett, 1999). Linear transformation of scaling factors (Tett et al., 2002) after TLS regression is, therefore, needed to extract the scaling factors for the RCP4.5 and SAI signals from that of G4. Assuming $\mathbf{x}_{\text{G4}} = \mathbf{x}_{\text{RCP}} + \mathbf{x}_{\text{SAI}}$:

$$
\begin{aligned}
\tilde{\mathbf{y}} &= \tilde{\beta}_{\text{RCP}}\mathbf{x}_{\text{RCP}} + \tilde{\beta}_{\text{G4}}\mathbf{x}_{\text{G4}} \\
&= \tilde{\beta}_{\text{RCP}}\mathbf{x}_{\text{RCP}} + \tilde{\beta}_{\text{G4}}(\mathbf{x}_{\text{RCP}} + \mathbf{x}_{\text{SAI}}) \\
&= (\tilde{\beta}_{\text{RCP}} + \tilde{\beta}_{\text{G4}})\mathbf{x}_{\text{RCP}} + \tilde{\beta}_{\text{G4}}\mathbf{x}_{\text{SAI}} \\
&= \tilde{\beta}_{\text{RCPT}}\mathbf{x}_{\text{RCP}} + \tilde{\beta}_{\text{G4}}\mathbf{x}_{\text{SAI}}
\end{aligned}
\tag{2.13}
$$

where $\tilde{\beta}$'s are best-estimate scaling factors and $\tilde{\beta}_{\text{RCPT}} = \tilde{\beta}_{\text{RCP}} + \tilde{\beta}_{\text{G4}}$ denotes the scaling factor of the *total* climate response to the RCP4.5 forcing required to match the best-fit observations, $\tilde{\mathbf{y}}$. This makes sense because both the RCP4.5 and G4 scenarios contribute to the RCP4.5 forcing, while only the G4 scenario contributes to the SAI forcing.

Linear transformation in matrix form is thus:

$$
\begin{pmatrix} \tilde{\beta}_{\text{RCPT}} \\ \tilde{\beta}_{\text{SAI}} \end{pmatrix} = \begin{pmatrix} 1 & 1 \\ 0 & 1 \end{pmatrix} \begin{pmatrix} \tilde{\beta}_{\text{RCP}} \\ \tilde{\beta}_{\text{G4}} \end{pmatrix}
\tag{2.14}
$$

Equation 2.14 will be used in conjunction with the conventional TLS algorithm in order to estimate $\tilde{\beta}_{\text{RCPT}}$ and $\tilde{\beta}_{\text{SAI}}$ for hypothesis testing in the following chapters.

2.3.2 The non-stationary algorithm

This section describes the non-stationary approach to detecting the geoengineering effect in hypothetical future scenarios, as proposed and used by Bürger and Cubasch (2015). This approach is largely based on the TLS detection algorithm (Section 2.3.1), with the exception that its null hypothesis is non-stationary.

As mentioned in Section 2.3, conventional detection is to demonstrate that an observed change in climate is not due to internal (unforced) variability alone. Bürger and Cubasch (2015) argued that if SAI were deployed as a means of geoengineering the climate, the unperturbed base climate would then be continued warming. Applied to the G4 deployment scenario, this means the conventional, multi-variate approach attempts to detect the RCP4.5 and SAI signals simultaneously against the climate system's internal variability (Section 2.3.1), whereas the non-stationary approach attempts to detect the net SAI signal against a gradual warming background caused by RCP4.5 forcings, plus variability internal to the climate system.

Bürger and Cubasch (2015) stated that they used 395 RCP4.5 simulations to serve as control runs. They suggested that imperfect knowledge of climate sensitivity had led to a larger spread among these RCP4.5 simulations further into the 21$^{\text{st}}$ century, or 'long-term stationarity'. For this reason, they emphasized that uncertainty in climate sensitivity should be included in a geoengineering detection algorithm, and subsequently questioned the use of pre-industrial

simulations as the control, a common practice of estimating internal variability in conventional detection and attribution.

In fact, conventional detection and attribution accounts for uncertainty in the magnitude of climate sensitivity, by allowing for uncertainty in the magnitude of a climate response and/or the radiative forcing of a particular factor. Any difference in climate sensitivity between the real world and the climate model that simulates the fingerprints is reflected in the resulting scaling factors. For instance, if the climate model has a lower climate sensitivity to a certain forcing scenario than the real world, then a higher-than-unity scaling factor that pulls up the model response to match the observations should be resulted, and vice versa. An example of this is apparent in Figure 3.2a, which shows a model-simulated G4 fingerprint (green line) that has approximately half the cooling effect of the observations (black line) during 2020–2049. The resulting best-estimate scaling factors for the SAI signal (black dots in Figure 3.3) during this time period are therefore around 2 (please refer to Section 3.2 for details about Figures 3.2a and 3.3). Indeed, a lot of research has used conventional detection and attribution results to constrain future climate change (e.g. Allen et al. (2000); Stott et al. (2003b, 2006)).

As such, the conventional, multi-variate detection approach and the non-stationary approach are simply two different perspectives of detection and attribution. Both approaches will be used for detecting the global-mean surface cooling effect of SAI in G4 in Chapter 3. Unlike Bürger and Cubasch (2015), only 114 unique CMIP5 RCP4.5 runs are found on the JASMIN super-data-cluster (Lawrence et al., 2013) for representing the non-stationary control climate in this thesis (Section 3.3 and Appendix A). In order to comply with the assumption of detection and attribution that the control climate has a mean of zero, the mean over the RCP4.5 control ensemble has to be subtracted from each control run (Bürger and Cubasch, 2015). More details on data pre-processing in association with the non-stationary detection approach can be found in Section 3.3.

To deal with 'short-term non-stationarity', i.e. the climate in 2020 (the first year of geoengineering implementation in G4) would be warmer than that of 2006–2019 (the base

period defined by Bürger and Cubasch (2015) and assumed to be perfectly known) under a warming trend, Bürger and Cubasch (2015) introduced a mean-based $C0$ and a trend-based $C1$ moving filter to represent 'climate at time t'.

$C0$ is a moving filter that estimates the climate at year t from the mean climate of its previous N years. N is equal to 14 throughout this thesis, following Bürger and Cubasch (2015)'s choice. For example, global-mean SAT in year 2020 is estimated from the mean global-mean SAT over the period 2006–2019, that in 2021 is estimated from the mean over the period 2007–2020, and so on and so forth. The estimation is based on past years because future information that is not available would be needed otherwise. Because the filter window is not centred at any year of interest but 7 years before it, a time series that is filtered by the 14-year-wide $C0$ filter has a lag of approximately 7 years from the true mean climate (the resulting climate from using a symmetric mean filter). Figure 2.9, as taken from Bürger and Cubasch (2015)), shows this is the case, with the black dashed line being the $C0$ filtered HadGEM2-ES global-mean temperature time series, and the thick grey line representing the corresponding true mean climate. Note the incorrect line labels for $C0$ and $C1$ on this original figure. The root-mean-square error introduced by the $C0$ filter from the true mean climate is 16.5 in this particular example.

The $C1$ filter, on the other hand, estimates the climate in any given year t from the trend of its previous N years. N is also equal to 14 in this thesis, as it was in the original paper. The trend is estimated by using ordinary least squares regression (Bürger and Cubasch, 2015). A 14-year-wide $C1$ filter does not result in an obvious phase shift from the true mean climate. This is illustrated in Figure 2.9, where the black solid line represents the $C1$ filtered HadGEM2-ES global-mean temperature series. The root-mean-square error introduced by the $C1$ filter is 9.7, which is smaller than that introduced by the $C0$ filter mentioned above. Nonetheless, $C1$ produces a slightly noisier time series than $C0$.

$N = 14$ is the optimal width for both filters, for both capturing the short-term climate response to the SAI shock in G4 and retaining the temporal shape of the data without a large
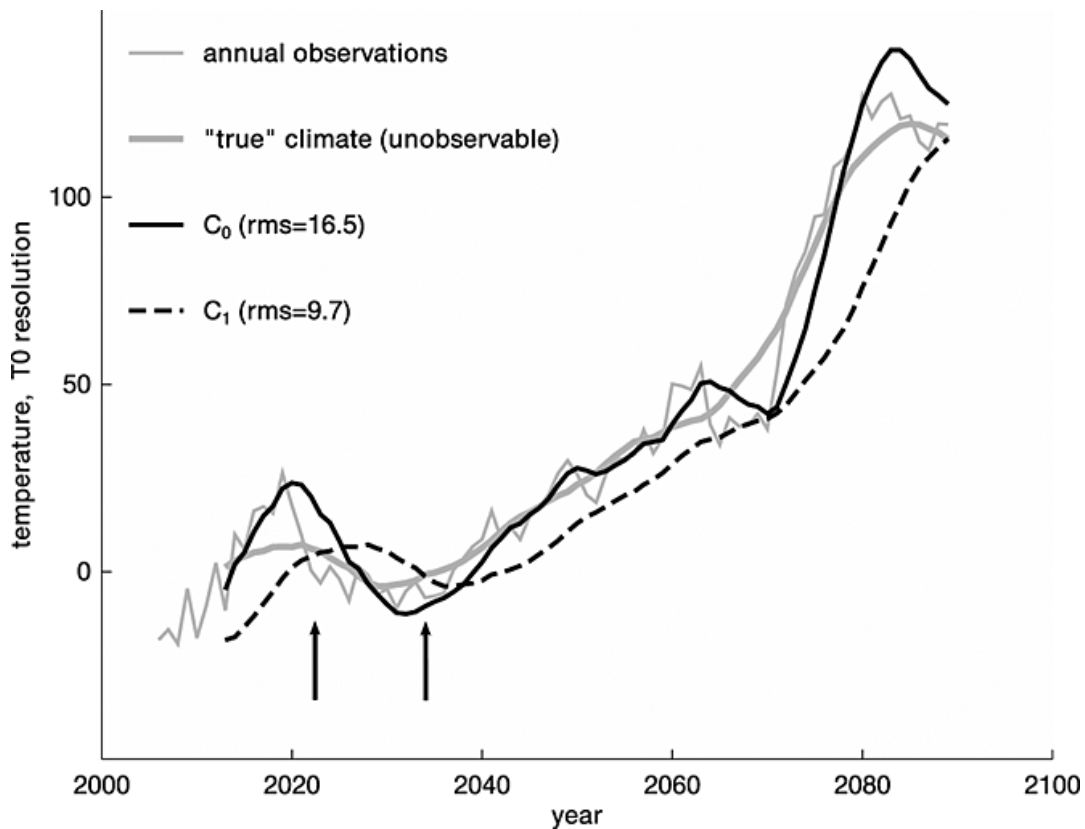
Figure 2.9 Figure from Bürger and Cubasch (2015), showing the annual-mean global-mean temperature simulated for G4 by HadGEM2-ES (thin grey line), the true mean climate calculated from a symmetrical 14-year moving mean filter (thick grey line), the 14-year $C0$ filtered series (black dashed line), and the 14-year $C1$ filtered series (black solid line). Note the incorrect line labels for $C0$ and $C1$. This figure is used under the terms of the Creative Commons Attribution-NonCommercial-NoDerivs License.

time delay (Bürger and Cubasch, 2015). This length is also representative of required geo-political timescales surrounding climate. Therefore, a filter width of 14 years will be used when a filter is applied in this thesis. A wider filter, e.g. 30 years, results in a much smoother time series but also a time lag of around 15 years from the true mean climate even with the $C1$ filter (please see Section 3.2.1 for more details). In addition to the 14-year-wide filters, a 30-year-wide $C1$ filter will be used for detecting the global-mean cooling effect of SAI on the surface in Chapter 3 as a sensitivity test.

Apart from the above data pre-processing procedure necessary for dealing with long-term and short-term non-stationarities, the non-stationary detection algorithm largely follows the TLS optimal fingerprint algorithm (Section 2.3.1). Bürger and Cubasch (2015) used Ribes et al. (2013)'s regularisation scheme to invert the noise covariance matrix, $\mathbf{C}_N$, whereas in this thesis the Moore-Penrose pseudo-inverse (Equations 2.5 and 2.6) is used throughout. Both the conventional TLS and non-stationary detection algorithms are solved using Environment Canada's Optimal Fingerprint (ECOF) package, which will be described in the following section.

2.3.3 Environment Canada's Optimal Fingerprint (ECOF) package

The Environment Canada's Optimal Fingerprint (ECOF) package (Feng, 2014) contains R functions that implement the ordinary least squares (OLS) (Allen and Tett, 1999), total least squares (TLS) (Allen and Stott, 2003) and regularised optimal fingerprint (ROF) (Ribes et al., 2013) algorithms.

Only the TLS function (algorithm detailed in Section 2.3.1) is used in this thesis. Although this function has a regularisation option for evaluating a regularised estimate of $\hat{\mathbf{C}}_N$ (Ribes et al., 2013), this flag is turned off in the experiments in this thesis, so that all data are projected onto κ leading modes of variability, following the classical optimal fingerprinting approach (Sections 2.3 and 2.3.1).

The function is also modified to allow post-regression linear transformation of scaling factors, particularly for extracting $\tilde{\beta}_{RCPT}$ and $\tilde{\beta}_{SAI}$ from $\tilde{\beta}_{RCP}$ and $\tilde{\beta}_{G4}$ (Section 2.3.1.1) in this thesis.

Chapter 3

Method comparison for geoengineering detection in global-mean temperature

Work in this chapter has been published in:

3.1 Introduction

Effective monitoring of sulphate aerosol geoengineering would require a series of robust techniques that can separate the climate signal forced by geoengineering aerosols from other externally forced changes and the climate system's internal variability. Various variants of optimal fingerprint detection and attribution exist (Section 2.3), and there are many possible choices to make: the climate variable and time period of study, the data pre-processing procedure to employ etc., as long as the observations, model-simulated fingerprints and control segments receive the same treatment.

It is, therefore, important to weigh the pros and cons of different combinations of these choices in order to identify the optimal approach to detecting the climate impacts of SAI early into implementation. This chapter assesses the methods one might use for detection of geoengineering signals in global-mean near-surface air temperature.

This chapter addresses the following research questions:

1. Would the cooling signal of SAI be detected in global-mean near-surface air temperature and when would this happen?

2. How would filtering climate noise in the temperature time series affect the global-mean detection results?

3. What is the optimal method for detecting the SAI cooling effect in global-mean near-surface air temperature?

4. How would the inclusion of pre-deployment observations affect the global-mean detection results?

In this chapter, 7 variations of the total least squares optimal fingerprint technique are applied to detect the SAI cooling effect in future annual-mean global-mean SAT in the GeoMIP G4 scenario. Global-mean temperature is chosen because it is a relatively straightforward and physically meaningful variable that the media and the public are most interested in in the context of geoengineering. The global-mean diagnostic can serve as a good starting point for comparing detection methods and several filters for geoengineering. The regional impacts of geoengineering are likely to be different from the global mean (Section 2.2.1), and they are of great relevance to climate policymaking. The detectability of the geoengineering signal in regional SAT at a range of spatial scales will be studied in Chapter 4.

The 7 experiments included in this chapter are summarised in Table 3.1. Each of them is a unique combination of a detection algorithm (the multi-variate approach or the non-stationary approach), a noise reduction technique (no data smoothing, the $C0$ filter, the $C1$ filter or a wide $C1$ filter) and a detection diagnostic (beginning in 2020 or 2000). Please refer to Chapter 2 for

the explanation of the multi-variate and non-stationary detection approaches, and the $C0$ and $C1$ filters. Detailed description of the experimental setup and data pre-processing procedure for each experiment listed in Table 3.1 is included in the corresponding section in this chapter.

Name	Fingerprint(s)	Filter (width)	Background climate	Start year
TfNo	RCP4.5, SAI	None	Six-model pre-industrial simulations	2020
TfC0	RCP4.5, SAI	$C0$ (14)	Six-model pre-industrial simulations	2020
TfC1	RCP4.5, SAI	$C1$ (14)	Six-model pre-industrial simulations	2020
TfC1(30)	RCP4.5, SAI	$C1$ (30)	Six-model pre-industrial simulations	2020
TfC1-2K	RCP4.5, SAI	$C1$ (14)	Six-model pre-industrial simulations	2000
BgC0	SAI	$C0$ (14)	Multi-model RCP4.5 simulations	2020
BgC1	SAI	$C1$ (14)	Multi-model RCP4.5 simulations	2020

Table 3.1 Detection methods that are used to detect the cooling effect of SAI in global-mean SAT in this chapter. The 'Tf' experiments use the multi-variate approach for detecting two fingerprints (RCP4.5 and SAI) simultaneously. The 'Bg' experiments use the non-stationary approach for detecting the SAI fingerprint. 'No' represents no data smoothing in addition to global and annual averaging, 'C0' and 'C1' represent the use of $C0$ and $C1$ filters, and 'C1(30)' represents the use of a wide $C1$ filter in the experiment. TfC1-2K uses a diagnostic that starts in 2000.

3.2 Global detection using the multi-variate approach

The conventional, multi-variate detection approach described in Section 2.3.1 is used in this section to find out whether and when the cooling signal of SAI would be detected in future annual-mean global-mean SAT under the G4 sulphate injection scenario. The scaling factors of the model-simulated RCP4.5 and SAI fingerprints, $\mathbf{x}_{\text{RCP}}$ and $\mathbf{x}_{\text{SAI}}$, are estimated simultaneously in the 'observations' using total least squares regression followed by linear transformation of scaling factors (Section 2.3.1.1). The fingerprints are detected at the 10% level if their scaling factors and their 5 to 95 percentile ranges do not cross zero.

Since there are no real-world observations of the future or geoengineering, the 'observations', $\mathbf{y}$ in Equation 2.1, are represented by single realisations of climate model simulations in G4. They are referred to as pseudo-observations hereafter. With pseudo-observations from HadGEM2-ES, CSIRO-Mk3L-1-2, CanESM2, BNU-ESM and MIROC-ESM in turn being

compared to fingerprints from the other models, 44 pseudo-observations model comparisons are made in total (please refer to Table 3.2).

Comparisons between pseudo-observations and fingerprints that are simulated by the same climate model are not included in the 44 comparisons made. This is to avoid positive biases in the detection results: the SAI scaling factors estimated in these comparisons are very close to 1 because the pseudo-observations and one of the realisations included in the G4 fingerprint are exactly the same, which is very unlikely to happen in any real-world application. Nonetheless, these close-to-unity scaling factors prove the credibility of the optimal detection algorithm employed.

The first experiment in this chapter involves the use of the conventional, multi-variate detection approach but no climate noise reduction technique except global and annual averaging. This experiment is referred to as TfNo in Table 3.1 and hereafter. For each of the pseudo-observation model comparisons, the data pre-processing procedure for TfNo is as follows. Monthly area-weighted global average SAT is taken over all grid cells of the model in use, regardless of the spatial resolution of the model. Annual means are then calculated from the monthly SAT data. $\mathbf{y}$ comes from a single G4 realisation. It is a time series of annual-mean global-mean SAT anomalies with respect to the ensemble member's 2006–2019 mean. This base period is the same as the one used in Bürger and Cubasch (2015), such that a fair comparison between the results in this chapter and their results can be made.

The input model-simulated fingerprints, $\mathbf{x}_{\mathrm{RCP}}$ and $\mathbf{x}_{\mathrm{G4}}$, are ensemble-mean time series of annual-mean global-mean RCP4.5 and G4 SAT anomalies relative to the corresponding 2006–2019 means, respectively. All time series of pseudo-observations and fingerprints begin in 2020 in this experiment, as this is the year when SAI starts in G4.

Internal climate noise, v_0 in Equation 2.1, is estimated from the pre-industrial control simulations of a six-model ensemble, which includes HadGEM2-ES, CSIRO-Mk3L-1-2, GISS-E2-R, CanESM2, BNU-ESM and MIROC-ESM. These models are used because the power spectra of their unforced annual-mean global-mean pre-industrial SAT time series are found

to be comparable to those of the detrended Hadley Centre-Climatic Research Unit Version 4 (HadCRUT4) (Morice et al., 2012) and GISS Surface Temperature Analysis (GISTEMP) (Hansen et al., 2006) 1981–2015 global-mean observations individually (cf. Gillett et al. (2000)). Figure 3.1 shows that the power spectral densities of the observed variability are within the range of that of the modelled variability on the timescales of 5 to 30 years, the timescales of interest in this thesis. Note the peaks in the observed power spectral densities between 3 and 4 years may be linked to El Niño/Southern Oscillation (ENSO) (cf. Gillett et al. (2000)) and the two major volcanic eruptions, El Chichón and Mount Pinatubo, that took place in 1982 and 1991, respectively.

A linear trend is removed from BNU-ESM's and MIROC-ESM's annual-mean global-mean pre-industrial control time series because they show a linear drift, whereas a mean is removed from the remaining pre-industrial simulations that show no obvious drift. This includes HadGEM2-ES, CSIRO-Mk3L-1-2, GISS-E2-R and CanESM2. The standardised control simulations are then split into segments of the length of **y**. The same diagnostic that was applied to **y** above is applied to every control segment. Half of these segments are used for optimisation, while the other half is used for hypothesis testing (Section 2.3). The number of segments in the second half is the number of degrees of freedom for internal variability estimation.

The same six-model internal variability estimates are used in all comparisons irrespective of the choice of models for representing the pseudo-observations and the fingerprints. This is to facilitate direct comparison across the results for the various pseudo-observation model comparisons, and to increase the number of degrees of freedom in the null distribution for hypothesis testing, which is further explained in the following paragraph.

Individual climate models can also be used to estimate internal climate variability instead of a multi-model ensemble. In fact, it is quite common to use a single climate model to simulate both the externally-forced fingerprints and unforced variability in a detection and attribution study (e.g. Lambert et al. (2004), Stott (2003) and Stott et al. (2010)). However, long control
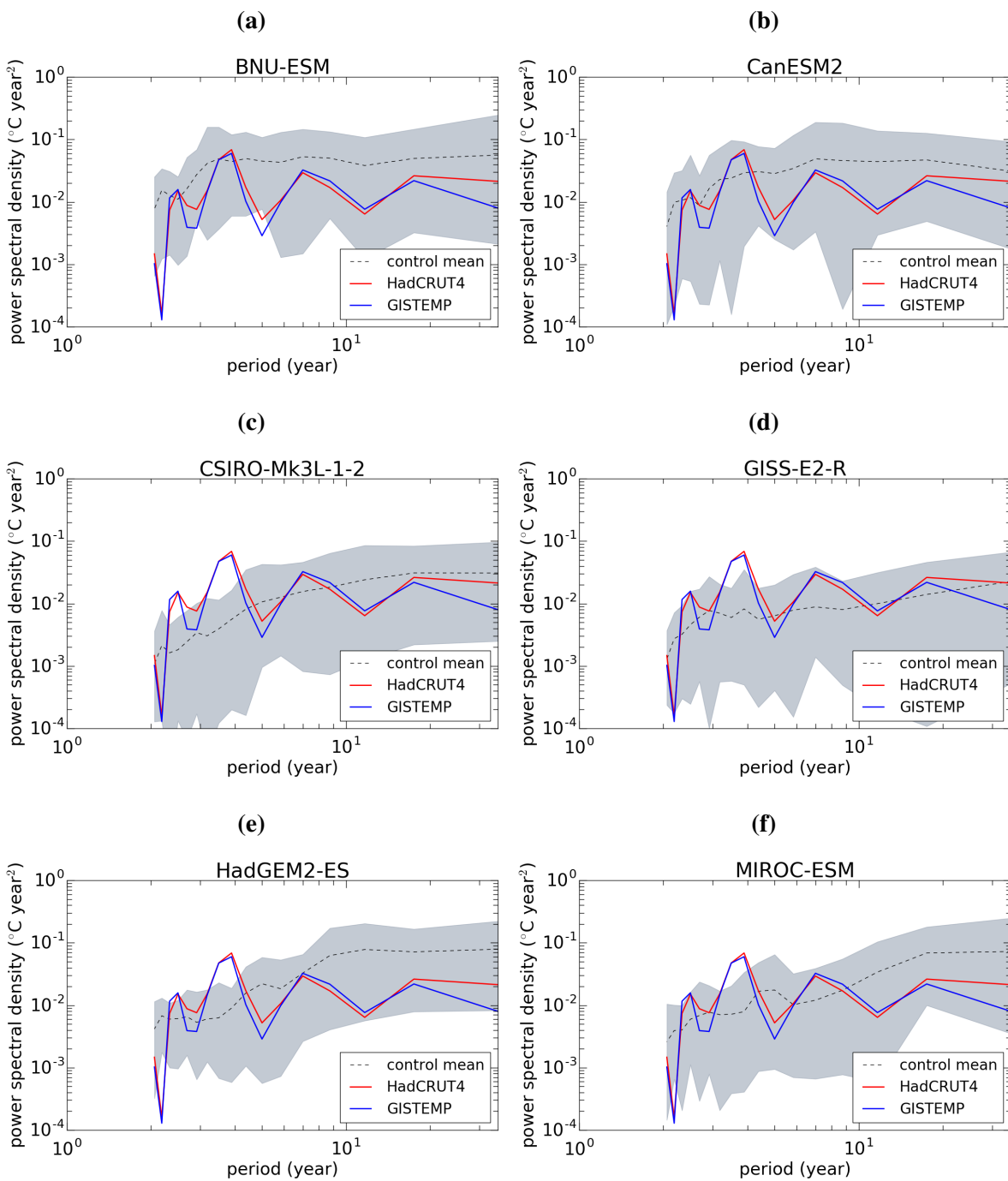
Figure 3.1 Power spectral densities of the detrended 1981–2015 HadCRUT4 (red line) and GISTEMP (blue line) annual-mean global-mean temperatures, compared to the mean spectral density of 35 year-long segments from the climate model's pre-industrial control simulations (dashed line). The grey region represents the range of spectral densities found in the control for each model. The 3–4 year observational peak may be an ENSO or volcanic signal.

simulations are not available in most of the models that are included in this study. For instance, BNU-ESM has only 559 years of SAT simulation under no change in radiative forcing, of which only half of them (280 years) are used in hypothesis testing. This gives fewer than ten non-overlapping 30-year long control segments when the period 2020–2049 is studied, and does not provide enough number of degrees of freedom for hypothesis testing at the 10% significance level (Allen and Tett, 1999). Overlapping the control segments from a single model can increase the number of degrees of freedom, but not to the extent that is obtained in a multi-model ensemble. Given that the individual models do simulate realistic internal inter-annual temperature variability (Figure 3.1), and that any detection results are subjected to the residual consistency test (Section 2.3), the six-model ensemble is chosen to estimate climate noise.

Figure 3.2a shows the pre-processed pseudo-observations, $\mathbf{y}$, (black line); model-simulated fingerprints, $\mathbf{x}_{RCP}$ and $\mathbf{x}_{G4}$, (blue and green lines) and six-model control segments (grey lines) in the example where the first G4 realisation of HadGEM2-ES, i.e. HadGEM2-ES r1, is used as the pseudo-observations and the ensemble-mean G4 and RCP4.5 simulations from CanESM2 are used as the fingerprints in the TfNo experiment.

In order to estimate the time needed for the SAI cooling effect to be detected in global-mean SAT, the length of the input time series to the detection algorithm is varied from 5 to 30 years at 5-year intervals until the SAI fingerprint is detected at the 10% level. For example, the best-estimate scaling factors of the SAI fingerprint, $\tilde{\beta}_{SAI}$, (black dots) and their two-tailed confidence intervals (error bars) estimated for time periods 2020–2024, 2020–2029, etc., up until 2020–2049 in the HadGEM2-ES versus CanESM2 example are shown in Figure 3.3. Since 2020–2029 is the first time period (since 2020) in which the SAI scaling factor moves away from zero, the 'SAI detection horizon' is estimated to be 10 years in this particular example. The SAI detection horizon is estimated at 5-year resolution, in every pseudo-observation model comparison and detection experiment in this thesis.
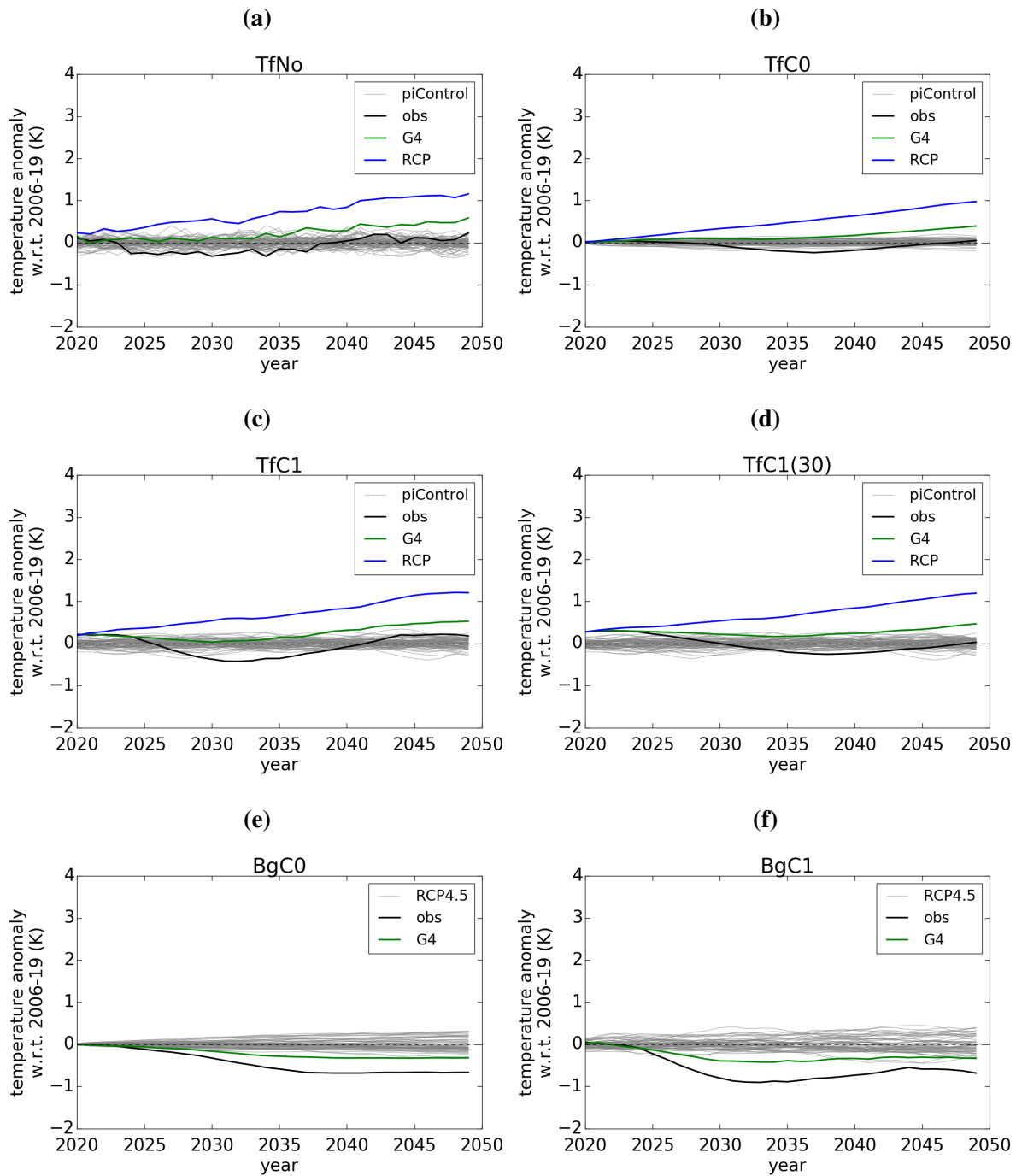
Figure 3.2 Time series of the HadGEM2-ES r1 pseudo-observations (black line), the ensemble-mean RCP4.5 and G4 fingerprints simulated by CanESM2 (blue and green lines, respectively), and the six-model control (grey lines) in the (a) TfNo, (b) TfC0, (c) TfC1 and (d) TfC1(30) experiment, respectively. For (e) BgC0 and (f) BgC1, the grey lines are the background RCP4.5 climates and the green line is the SAI fingerprint, both with the mean RCP4.5 background climate removed.
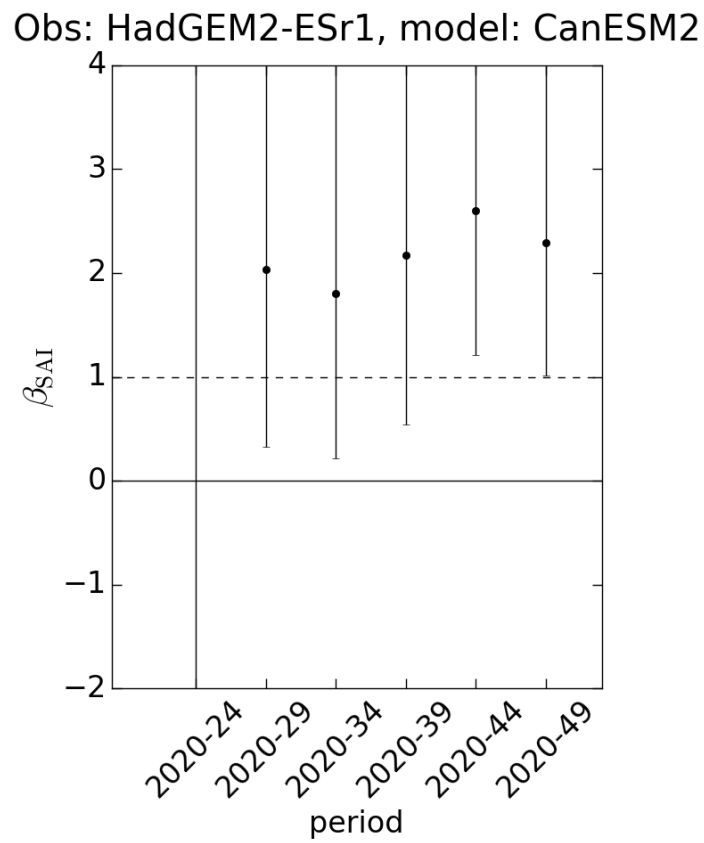
Figure 3.3 The best-estimate scaling factor for the SAI signal (black dots) and its two-tailed confidence interval (5 to 95 percentile, error bars) during each studied time period in the HadGEM2-ES r1 verse CanESM2 comparison. The SAI detection horizon is 10 years in this example.

pseudo-observations	model-simulations				
	HadGEM2-ES (3)	CSIRO-Mk3L-1-2 (3)	CanESM2 (3)	BNU-ESM (1)	MIROC-ESM (1)
HadGEM2-ES r1		25	10	15	25
HadGEM2-ES r2		5	10	5	25
HadGEM2-ES r3		25	30	5	30+
CSIRO-Mk3L-1-2 r1	25		15	30+	25
CSIRO-Mk3L-1-2 r2	25		25	30+	25
CSIRO-Mk3L-1-2 r3	30+		30	30	30
CanESM2 r1	5	30+		30	20
CanESM2 r2	25	30+		20	25
CanESM2 r3	20	10		10	25
BNU-ESM r1	5	5	10		25
MIROC-ESM r1	30+	30+	30+	30+	

Table 3.2 Number of years of pseudo-observations since deployment in 2020 that would be needed for the SAI influence to become detectable in annual-mean global-mean near-surface air temperature estimated at 5-year resolution, using the TfNo method at the 10% significance level.

Table 3.2 shows the estimated SAI detection horizon at 5-year resolution for each of the 44 comparisons made. Each row represents a different realisation observable in the same 5 Tg yr^{-1} SO$_2$ injection scenario, while each column is a different climate model used for generating the fingerprints. The number in bracket in each of the columns indicates the number of ensemble members over which the mean is taken to reduce noise in the fingerprints. BNU-ESM and MIROC-ESM have only 1 ensemble member each, and that is likely to be insufficient for separating the forced signals from natural climate variability. The use of 1 realisation as a fingerprint is not recommended, but its sensitivity to different detection or data smoothing methods is still useful to study.

More than half of the studied comparisons would need at least 25 years of observations for the cooling effect of SAI to be detected in global-mean SAT. This is clearly shown in Figure 3.4a, where the distribution of the estimated horizons shown in Table 3.2 is plotted. This means that even though swift global cooling is expected from SAI, and is indeed observed in the model simulations for G4 (Figure 2.2), robust detection of the cooling effect would likely take much longer to achieve on the global scale with the TfNo method.

This thesis does not look at timescales longer than 30 years, as it would seem too long a period in the political context of sulphate aerosol geoengineering. With large volcanic eruptions being its natural analogue and climate model simulations suggesting global surface cooling from geoengineering a few years into deployment (Figure 2.2), geoengineering by sulphate aerosol injections has been perceived as a highly effective potential way of lessening climate warming caused by greenhouse gases (Shepherd, 2009). A scenario in which the geoengineering cooling effect is still undetectable after 30 years of continual aerosol injection and no alteration to the amount of aerosols to be injected is made would be highly unlikely. As such, this thesis does not look beyond 30 years of constant SO$_2$ injection where the surface cooling effect of geoengineering is not robustly detected.

Nonetheless, all the comparisons that use MIROC-ESM as the pseudo-observations result in a detection horizon that is longer than 30 years. This is in part due to the weak global

cooling response of the model to stratospheric sulphate aerosols (Figure 2.2), and in part due to insufficient separation of the weak SAI signal from climate noise with the use of only 1 ensemble member, especially when no noise reduction technique is employed except global and annual averaging in TfNo. The results suggest that in the event of 5 Tg yr^{-1} SO$_2$ injection, detection of the SAI cooling signal in global-mean SAT would be particularly challenging using TfNo, should future observations follow the MIROC-ESM trajectory.

3.2.1 The effects of noise reduction

The mean-based $C0$ and trend-based $C1$ moving filters (Section 2.3.2) are used in conjunction with the multi-variate detection method respectively in this section, in order to test the sensitivity of the SAI detectability in global-mean temperature to different filtering techniques. These 2 experiments are referred to as TfC0 and TfC1 in Table 3.1, respectively. The filters are not necessary for the multi-variate optimal fingerprint algorithm to work, but they could reduce noise in the pseudo-observations and fingerprints and potentially lead to earlier detection of the SAI cooling effect in the G4 scenario.

Both filters have a 14 year-wide moving window in this section, as it was found to be optimal for capturing the short-term SAT response to the abrupt deployment of SAI in G4 and retaining the temporal shape of the time series without much delay (Section 2.3.2). The same window width was also used in Bürger and Cubasch (2015), so direct comparisons between the results can be made.

The same pseudo-observation model comparisons that were shown in the previous section are studied here. Data pre-processing for the TfC0 and TfC1 experiments are very similar to that described for TfNo above, except that in this section all the input time series are also $C0$ or $C1$ filtered, in addition to global and annual averaging. The base period for filtering is 2006–2019, so the resulting SAT time series also start in 2020.

Figures 3.4b and 3.4c show the distributions of the detection horizons estimated for the SAI cooling signal using TfC0 and TfC1, respectively. Compared to TfNo in which the pseudo-observations, fingerprints and control simulations are not smoothed by any filters, the cooling signal of SAI becomes detectable 15 years into geoengineering implementation in more comparisons when the $C0$ filter is applied.

However, the estimated detection horizons are still spread out between 5 and more than 30 years, with a peak at more than 30 years. The peak is mainly the result of comparisons that involve CSIRO-Mk3L-1-2, the model that employed solar irradiance reduction instead of aerosol injection. Even though the SAT responses to SAI are globally averaged in this chapter, the difference between CSIRO-Mk3L-1-2 and the rest of the models are still revealed in the detection results.

The residual consistency test (Section 2.3) fails in more comparisons when the $C0$ filter is used than when no filtering is done. In other words, the weighted sum of squared residuals from the regression becomes inconsistent with the model-simulated noise variance in a number of comparisons when the detection method is switched from TfNo to TfC0. Detection cannot be claimed in these comparisons because the control simulation of climate variability and, as a result, the uncertainty range of the estimated scaling factor is distrusted. The failed residual consistency tests have affected some of the detection results, and they are likely to be due to larger inconsistencies in model responses on longer timescales.

Figures 3.4a and 3.4c show that switching from TfNo to TfC1 results in a shift in a majority of the estimated detection horizons, from 25 years or more to less than a decade since geoengineering deployment, even though the same null hypothesis is made in both methods. The SAI cooling effect would be detected during the first decade of SAI implementation at the 10% significance level in 29 of the 44 comparisons using TfC1, while only 10 of the 44 comparisons would result in successful detection within 10 years using TfNo. Among the 29 within-a-decade detections in the TfC1 experiment, 17 would require as few as 5 years for the cooling signal of SAI to be detected. This suggests that the detectability of the SAI cooling
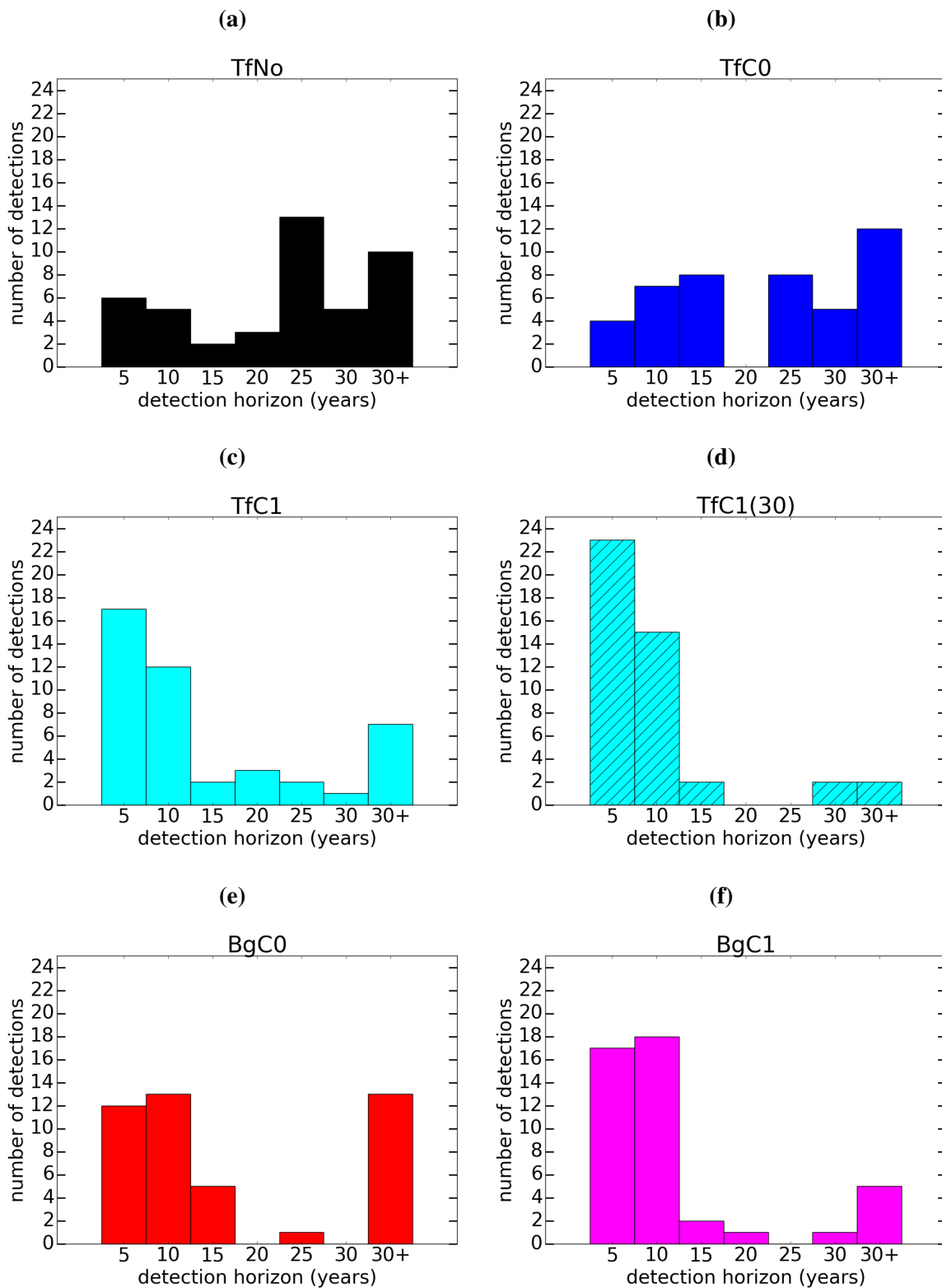
Figure 3.4 The distribution of SAI detection horizons estimated with (a) TfNo, (b) TfC0, (c) TfC1, (d) TfC1(30), (e) BgC0 and (f) BgC1. The same pseudo-observation model comparisons, 44 in total, are examined using each method.

signal early into geoengineering deployment is highly sensitive to the choice of filter, and that $C1$ works best for noise reduction in the temporal SAT data.

The $C1$ filter works best with the conventional, multi-variate method for detecting the global surface cooling effect of sulphate aerosol geoengineering early into deployment because it effectively removes unforced climate noise, while retaining the temporal shape of the raw data without producing a significant time lag. Figures 3.2a, 3.2b and 3.2c show the time series of the pseudo-observations (first G4 realisation of HadGEM2-ES, HadGEM2-ES r1), fingerprints (CanESM2 3-member ensemble mean) and the control (six-model pre-industrial control simulations) in TfNo, TfC0 and TfC1, respectively, for comparison.

As can be seen in the HadGEM2-ES r1 versus CanESM2 example, the annual-mean global-mean pseudo-observational SAT anomaly starts to drop below zero slightly before 2025, and remains at its lowest values until around 2035 (black line in Figure 3.2a). When the $C0$ filter is applied to the same time series, nearly all of the climate noise is removed while the trend of initial cooling and subsequent warming is preserved, but maximum cooling is shifted to after 2035 in the $C0$ filtered pseudo-observations (Figure 3.2b). However, when the $C1$ filter is used, not only is a majority of the climate noise removed, but also the trend in the non-filtered pseudo-observations is retained without an obvious time lag: negative anomaly starts in 2025 and maximum cooling is reached before 2035 in the $C1$ filtered pseudo-observations (Figure 3.2c).

Given that $C1$ is found to be the optimal filter for noise reduction in the multi-variate optimal fingerprinting algorithm, a sensitivity test on the SAI detectability to the width of the moving filter is carried out. A 30 year-wide $C1$ filter is applied to the same pseudo-observation model comparisons for SAI detection horizon estimation (TfC1(30) in Table 3.1). Figures 3.2a and 3.2d show that a 30-year filter period produces much smoother time series but also a time lag of around 15 years from the non-filtered SAT responses.

This wider filter, in conjunction with the multi-variate approach, results in 23, 5-year and 15, 10-year detections, numbers that are significantly larger than those found in the 14

year-wide TfC1 experiment. The distribution of all the estimated detection horizons found in the TfC1(30) experiment is shown in Figure 3.4d. The cooling effect of SAI would be detected in the first 10 years of geoengineering in a majority of the studied comparisons. However, some of these results may be false positives, as $C1(30)$ filtered temperatures in the first decade of geoengineering in G4 are mainly estimated from pre-deployment temperature trends that are not influenced by geoengineering aerosols at all.

Similar to decadal or multi-decadal averaging, techniques that are commonly used for data smoothing in conventional detection and attribution of climate warming, the $C1$ filter makes the forced climate signals more distinguishable from climate noise in temporal data series. However, unlike conventional time averaging, it does not require multi-decadal geoengineering observations that would not be available at the beginning of geoengineering implementation. For this reason, and in order to avoid false positives that may result from a wider filter, the 14-year $C1$ filter will be used in the following chapters to look at the detectability of the SAI cooling signal on different spatial scales and in other detection diagnostics.

3.3   Global detection using the non-stationary approach

This section investigates how the use of Bürger and Cubasch (2015)'s non-stationary detection approach (Section 2.3.2) would affect the detectability of the SAI cooling effect in global-mean SAT. The $C0$ and $C1$ filters are used in combination with the non-stationary detection method separately, to estimate the detection horizon of the SAI fingerprint at 5-year resolution in the same 44 pseudo-observation model comparisons as above. Experiments in this section are referred to as BgC0 and BgC1 as shown in Table 3.1, respectively.

Contrary to the multi-variate detection approach, the application of the mean-based $C0$ and the trend-based $C1$ filter are necessary for the non-stationary method to work (Section 2.3.2). In addition to noise reduction in the data, the filters extract climate signals and deal with the short-term non-stationarity arising from abrupt geoengineering deployment in G4. The window

width is chosen to be 14 years for both filters throughout this section in order to reduce the risk of false positive results.

Pseudo-observations in this section, $\mathbf{y}_{Bg}$, is also a time series of annual-mean global-mean G4 SAT that begins in 2020. It is anomalised as described in the previous section and filtered according to the experiment, but with a mean RCP4.5 background climate removed in order to separate the climate signal from the non-stationary background noise. This is achieved by subtracting the corresponding mean SAT over 114 RCP4.5 simulations from each value in the G4 time series. A list of the climate models used to estimate this RCP4.5 background climate can be found in Table A.1 in Appendix A.

The only searched-for fingerprint is $\mathbf{x}_{SAI}$ in the BgC0 and BgC1 experiments. It is an ensemble-mean model-simulated response in G4 that is processed in exactly the same way as $\mathbf{y}_{Bg}$. No linear transformation of scaling factors is required in this section because the RCP4.5 component is already removed from the G4 simulations through subtraction.

Each of the 114 RCP4.5 simulations obtained from the climate models listed in Table A.1 is processed in exactly the same manner as $\mathbf{y}_{Bg}$, in order to estimate the warming background climate that is assumed to be the null hypothesis in the non-stationary detection approach. Similar to the treatment to the pre-industrial control simulations in the Tf experiments, the background RCP4.5 simulations are divided into two groups: one for optimisation and the other one for hypothesis testing. This background climate estimation is fixed across the pseudo-observation model combinations. Figures 3.2e and 3.2f show $\mathbf{y}_{Bg}$, $\mathbf{x}_{SAI}$ and the processed RCP4.5 background climates for the HadGEM2-ES r1 versus CanESM2 comparison in the BgC0 and BgC1 experiments, respectively.

The distribution of the SAI detection horizons estimated in the BgC0 experiment is shown in Figure 3.4e. Compared to TfC0 (Figure 3.4b), BgC0 results in a shift in the detection horizons from longer timescales to within 10 years. This suggests that the non-stationary detection approach is slightly more capable of detecting the cooling effect of SAI in global-mean SAT early into geoengineering deployment than the multi-variate approach, although the

shift in detection horizons is not obvious. However, the residuals mismatch problem reported with TfC0 persists in the BgC0 experiment.

Switching from TfC1 to BgC1 also results in a shift in the estimated detection horizons to shorter timescales, as can be seen by comparing Figure 3.4f with Figure 3.4c. This is consistent with the early geoengineering detectability found by Bürger and Cubasch (2015), even though spatial information is not included in our BgC1 experiment but is in theirs. Nevertheless, the main results concluded from TfC1 have not changed due to the use of the non-stationary detection approach: both methods result in peaks in the detection horizons at the first 5 and 10 years of SAI deployment in G4.

The results of the Tf and Bg experiments in this thesis have two implications. First, the shifts of the estimated detection horizons to shorter timescales due to the change from TfC0 to BgC0 and from TfC1 to BgC1 are not as significant as those resulted from the change from TfNo to TfC1 in the previous section. This means that the detectability of the SAI cooling signal in global-mean SAT is less sensitive to the choice between the two studied detection approaches than to the choice of filtering technique.

Secondly, the TfC1 and BgC1 results confirm that the cooling effect of geoengineering aerosols could be robustly detected in global-mean SAT within the first decade of deployment, regardless of whether the multi-variate or the non-stationary detection approach is used, as long as the pseudo-observations, fingerprints and estimated climate variability are adequately $C1$ filtered. This means that within 5 to 10 years of initial SAI deployment, we would be able to identify the attributable effects of initial SAI on global-mean SAT, and make subsequent changes to the injection scheme, should that be needed to meet the global climate target then.

3.4   Inclusion of pre-deployment observations

Only data from 2020 onward were included in the experiments shown in the previous sections, as SAI only starts in 2020 in the G4 scenario, and this is the year in which the G4 simulations diverge from RCP4.5. In the real-world application, however, any detection of the cooling effect of the stratospheric geoengineering aerosols in global-mean temperature may also make use of observations and model simulations prior to geoengineering implementation. This section investigates how the use of prior observations may affect the global mean SAI detection results as a sensitivity test.

The temporal diagnostic used in the above experiments is extended backwards to 2000 in this experiment (TfC1-2K in Table 3.1). This is achieved by adding historical and RCP4.5 simulations to the pseudo-observations and fingerprint time series, respectively. Using pre-deployment data will potentially lead to noise contamination with the non-stationary detection approach, as this approach uses RCP4.5 simulations to estimate the background warming climate and noise. For this reason, and because the $C1$ filter was found to work best with the multi-variate detection approach in Section 3.2.1, a global-mean diagnostic that begins in 2000 is used in conjunction with TfC1 in this sensitivity test.

Figure 3.5 shows the distribution of the detection horizons estimated for the SAI cooling signal in the same 44 comparisons as before, but with the TfC1-2K method. Using data since 2000, 10 comparisons would have the SAI cooling signal detected at the 10% level by 2025, i.e. 5 years into geoengineering deployment; while 14 other comparisons would have the signal detected by 2030, i.e. 10 years into geoengineering deployment in G4.

There is a noticeable drop in the number of 5-year detections in the TfC1-2K results compared to that of TfC1 (Figure 3.4c). This is likely to be due to signal degeneracy in the detection algorithm (Allen et al., 2006; Bindoff et al., 2013): the extended 2000–2024 RCP4.5 and G4 fingerprints are so similar that amplifying one of them while diminishing the other may explain the pseudo-observations just as well as the other way round. This means
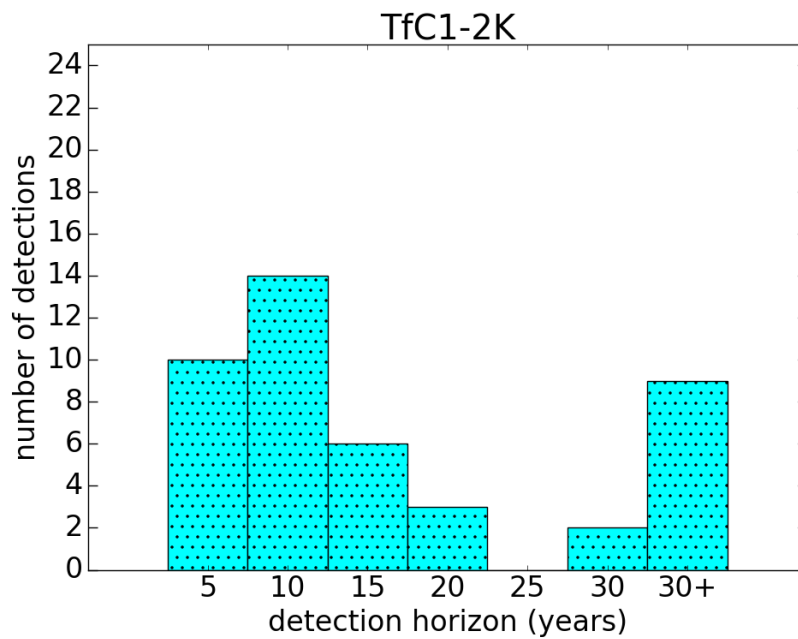
Figure 3.5 Distribution of the SAI detection horizons estimated with TfC1-2K.

a large range of scaling factors is possible for both fingerprints to account for the observed changes in SAT from 2000 to 2024. This results in large uncertainties associated with the fingerprints' corresponding best estimates of scaling factor, prohibiting detection at the chosen 10% significance level.

Figure 3.6 shows the pseudo-observations, fingerprints and noise estimates in the HadGEM2-ES r1 versus CanESM2 comparison in the TfC1-2K experiment. Indeed, the RCP4.5 and G4 fingerprint time series (blue and green lines) are nearly indistinguishable, with only values toward the end of the time series differing very slightly.

Given that close monitoring of sulphate aerosol geoengineering would require early detection of its cooling effect, it is not recommended to use SAT data since 2000 for detecting the global cooling signal of SAI in a 5 Tg yr^{-1} SO$_2$ injection scenario that begins in 2020. This does not mean geoengineering detection would not benefit from using pre-deployment observations at all, as only one sensitivity test is done here. Earlier SAI detection may result from the use of less pre-deployment data or more spatial information. The next chapter will investigate the latter, as detection of the regional and spatial impacts of sulphate aerosol geoengineering is
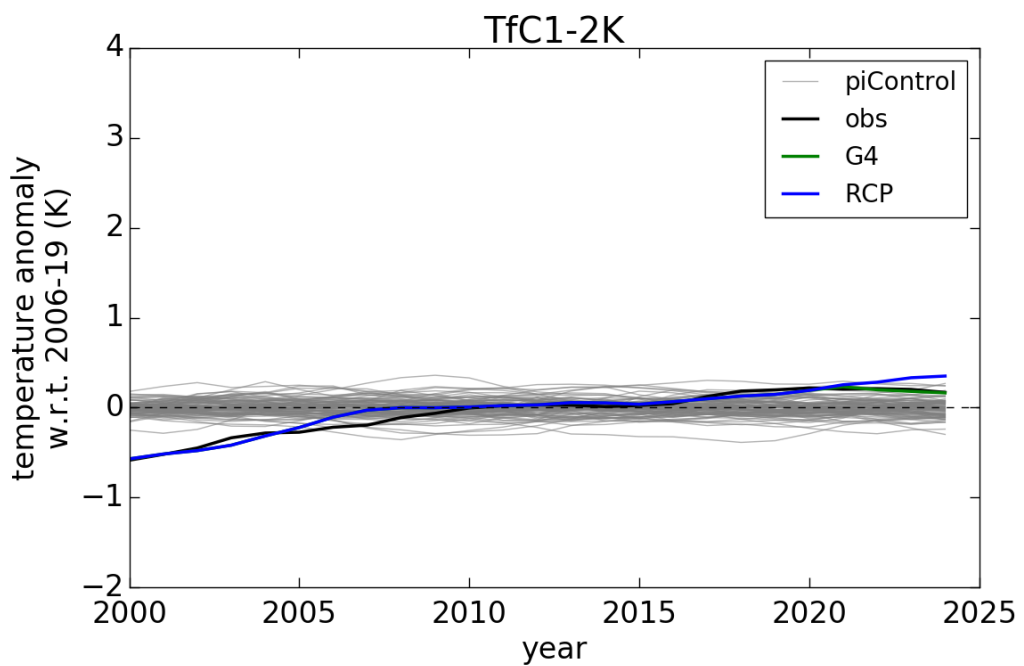
Figure 3.6 The pseudo-observations (HadGEM2-ES r1, black line), fingerprints (ensemble mean RCP4.5 and G4 anomalies from CanESM2, blue and green lines, respectively) and the six-model control (grey lines) in the TfC1-2K experiment. The two fingerprints are exactly the same in the period 2000–2019, and only differ from one another slightly in the period 2020–2024. Signal degeneracy makes them hard to be detected simultaneously.

of high political and social importance. Nevertheless, future work could investigate how much pre-deployment data would be optimal for SAI detection using the multi-variate detection algorithm.

3.5   Applications of the methods

With the use of the $C1$ filter, the multi-variate detection approach (TfC1) and the non-stationary approach (BgC1) give very similar SAI detection results in global-mean SAT, even though the two approaches have very different null hypotheses. This on the one hand shows the robustness of the early global-mean SAI detectability found, but on the other hand the result makes it hard for us to decide which approach would be more suitable for geoengineering detection in a plausible future. Whilst there is unlikely a single detection approach that would result in the earliest geoengineering detection in every climate variable, detection diagnostic and period of study, there are certain advantages of using TfC1 over BgC1 in general.

First of all, the multi-variate approach has been very widely used for detecting and attributing anthropogenic climate change in climate variables such as surface and air temperatures (e.g. Allen et al. (2006); Lott et al. (2013); Stott et al. (2001); Tett et al. (2002)), precipitation (e.g. Lambert et al. (2004)), stratospheric ozone (e.g. Gillett et al. (2011)), sea level (e.g. Slangen et al. (2014)), ocean waves (e.g. Dobrynin et al. (2015)) and snow cover extent (e.g. Rupp et al. (2013)). On the other hand, there is no proven credibility of the non-stationary approach except for its application to surface temperature and precipitation in hypothetical geoengineered worlds. One may argue that this is because the non-stationary approach was specifically designed for geoengineering detection, but given that the two approaches give similar geoengineering detection results and neither of their null hypotheses is incorrect, there seems to be a lack of strong reasons for the detection and attribution community to turn to the non-stationary approach, even if SAI is deployed in the future.

Secondly, the multi-variate detection approach allows simultaneous detection of climate responses to different forcings or groups of forcings. This means the detection of anthropogenic warming before geoengineering could serve as a check of the detection algorithm, as climate warming should have been robustly detected before stratospheric aerosol geoengineering is considered, not to mention implemented. Indeed, in the TfC1 experiment, the RCP4.5 fingerprint is detected before or in the same year as the SAI fingerprint in almost all of the studied comparisons. This is a useful check that the non-stationary approach does not provide.

Thirdly, a step forward from detecting the effect of SAI would be to understand how much of the observed changes in climate is due to the intentionally injected sulphate aerosols relative to other external forcings such as greenhouse gases, solar activity and volcanic aerosols. Attributing climatic changes observable with SAI would be crucial in the event of deployment, as we would likely want to adjust the rate or location of SO_2 injection based on the estimated effectiveness of prior injections and our future climate targets via explicit feedback (Kravitz et al., 2014; MacMartin et al., 2014). An attribution approach could also help us to understand by what extent the climate models that we use to calculate the amount of SO_2 needed to achieve certain climate goals are underestimating or overestimating the real world's responses to stratospheric sulphate aerosols. These will all be possible only with the use of the multi-variate approach.

Finally, the multi-variate approach allows the inclusion of pre-deployment observations in the diagnostic while the non-stationary approach does not. It is not clear whether including observations prior to geoengineering deployment would increase the detectability of SAI in the first decade yet, but this can only be found out with the use of the multi-variate method in future work. Higher flexibility in the detection diagnostic or use of data allowed in the multi-variate approach will encourage more research to be done in this area. The scientific community, policymakers and, thus, the general public will only benefit from this.

3.6   Summary

This chapter has investigated the detectability of the cooling effect of 5 Tg yr^{-1} SAI on global-mean SAT by cross-comparing climate model simulations. Two variants of total least squares optimal fingerprinting were used in conjunction with 4 different noise reduction techniques and global-mean detection diagnostics, in order to determine the time horizon over which the global-mean SAI cooling signal would first be detected since hypothetical geoengineering implementation in 2020 in the GeoMIP G4 scenario at the 10% significance level.

The first research question raised in this chapter was whether the global-mean SAI cooling signal would be detected and when this would become possible. It was found in all the experiments (Table 3.1) that we would be able to detect the global-mean cooling signal of SAI in a majority of the pseudo-observation model comparisons examined. Using the multi-variate approach with no additional noise reduction procedure (TfNo), the detection horizon could span from 5 to more than 30 years, showing that the global-mean SAI detectability would highly depend on the temperature changes observed with geoengineering and the choice of climate model for detecting purposes. In particular, robust detection of the SAI cooling signal would require more than 30 years if future SAT observations followed the MIROC-ESM trajectory (Section 3.2).

The application of a 14 year-wide $C0$ or $C1$ moving filter (TfC0 and TfC1), however, would shift the estimated detection horizons to shorter timescales. The shift was particularly evident with TfC1, where the SAI cooling signal would become detectable in a majority of the comparisons within the first 5 or 10 years of geoengineering deployment (Section 3.2.1). This means within-a-decade SAI detection would be likely in global-mean SAT, provided that the temporal data are $C1$ filtered.

A sensitivity test was performed with the use of a 30-year $C1$ filter (TfC1(30)). Compared to the 14 year-wide $C1$ filter, this longer filter window resulted in more within-a-decade SAI detections, but it also poses the risk of false positive results. Therefore, in answer to question

2 in Section 3.1, filtering the temperature time series would generally improve the detection results, and the 14 year-wide C1 filter would be best for early detection.

The non-stationary detection approach was also taken in order to answer question 3. Using non-stationary warming simulated in RCP4.5 as the null climate and the C0 and C1 filters (BgC0 and BgC1), the SAI cooling signal would become detectable in 14 and 6 more comparisons during the first decade of geoengineering implementation in G4 than TfC0 and TfC1, respectively (Section 3.3). BgC1 resulted in early detectability in the highest number of studied comparisons, but this new method does not allow simultaneous detection and attribution of forcing factors that would be essential for geoengineering monitoring, and has limitations on the use of pre-deployment data (Section 3.5). Therefore, the optimal method for global-mean SAI detection would be TfC1, the method that gave the second highest number of within-a-decade detections.

The final research question in this chapter was how the use of data prior to 2020 would affect the above results. TfC1 was repeated with a detection diagnostic that starts in 2000 (TfC1-2K). Fewer 5-year and, thus, total within-a-decade SAI detections were found as a result, compared to TfC1 (Section 3.4). This can be explained by signal degeneracy in the fingerprints. A temporal diagnostic that starts in 2000 is, therefore, not recommended for SAI monitoring. Nonetheless, future work could determine the optimal detection diagnostic by using other starting years.

Detection of geoengineering is not limited to the global-mean diagnostic. Knowledge of the detectability of the regional impacts of sulphate aerosol geoengineering could be of great importance for practical political purposes. The next chapter will look at where on the surface would be best for detecting the cooling effect of 5 Tg yr^{-1} SO$_2$ injection.

Chapter 4

Hemispheric, regional and spatio-temporal detection of geoengineering

4.1 Introduction

While detecting and monitoring the global mean effects of sulphate aerosol geoengineering is important, improved understanding of the regional impacts of SAI on SAT would be more relevant to climate policymaking, especially if we aim to control geoengineering through detecting and attributing the observed temperature changes to the injected sulphate aerosols in a geoengineered world. How SAT in different parts of the world might respond differently to geoengineering aerosols, and how quickly into implementation these responses would be detected in the observations are open questions that are of high interest to the public, scientists and policymakers.

In addition, knowing where the cooling signal from geoengineering aerosols could be best detected can help us design an optimal observational network for effective SAI monitoring.

Regional detection and attribution of anthropogenic climate change has become more common in recent years (e.g. Bindoff et al. (2013); Stott et al. (2010)), and similar approaches can be taken towards detecting the regional effects and spatial patterns of SAT changes due to SAI on sub-global scales.

This chapter addresses the following research questions:

1. How would the limited spatial resolution and coverage in an observational dataset like HadCRUT4 affect the global mean detection results?

2. Where would be best for detecting geoengineering in surface temperature and why?

3. What would be the optimal spatial scale and amount of information for geoengineering detection in SAT?

The multi-variate detection method is used in conjunction with the $C1$ filter (TfC1 in Chapter 3) to determine the detectability of geoengineering in SAT in different regions and on different spatial or spatio-temporal scales in this chapter. TfC1 is chosen because it was found to work as well as Bürger and Cubasch (2015)'s method for detecting the geoengineering cooling signal in the previous chapter, allow more flexibility in data usage in the detection algorithm, and its multi-variate nature allows us to compare the relative contribution of different forcing factors to the observed changes in climate, making geoengineering management via an explicit feedback mechanism easier compared to Bürger and Cubasch (2015)'s approach (Section 3.5).

In this chapter, all detection diagnostics start in 2020, i.e. the year in which SAI is turned on in the G4 scenario, in order to avoid signal degeneracy (Section 3.4). The same 44 pseudo-observation model comparisons that were examined in the previous chapter are studied here in every optimal detection experiment.

4.2   Detection in the HadCRUT4 network

Detecting the cooling signal of the injected sulphate aerosols in global-mean SAT is an important first step because global cooling is likely to be the primary aim of sulphate aerosol geoengineering. However, true global SAT averages are impossible to obtain from *in situ* measurements in the real-world application because of their incomplete global coverage. Non-uniformly distributed missing data could lead to biases in the estimated temperature and affect geoengineering detection in the real world.

The Hadley Centre-Climatic Research Unit Version 4 (HadCRUT4) is currently the most widely cited combined land and sea-surface temperature data set (Morice et al., 2012). It provides monthly average surface temperature observations that are binned onto 5° by 5° latitude/longitude resolution without spatial infilling; therefore it only covers about 84% of Earth's surface area.

The missing data in HadCRUT4 are mainly located in Africa, South America, over the Arctic and the Antarctic region. Figure 4.1 shows the unsampled regions as of January 2016 in white colour. These non-uniformly distributed unsampled regions have led to an underestimation in recent global temperature trends (Cowtan and Way, 2014). The first part of this chapter investigates how the lack of full global coverage in the observations may affect the detectability of geoengineering in global mean SAT.

In order to resemble real-world detection of the SAI cooling signal in annual-mean global-mean SAT time series, and ensure fair comparison between pseudo-observations and model simulations, all model SAT output (including the pre-industrial control) are first interpolated onto HadCRUT4's 5° by 5° grid in this section through area-weighted regridding. The unsampled grid cells in HadCRUT4 in January 2016 are then identified and given zero weight when area-weighted global average SAT is calculated. Annual means are then calculated from the monthly data before detection is attempted with the TfC1 technique, as was done in the previous chapter.
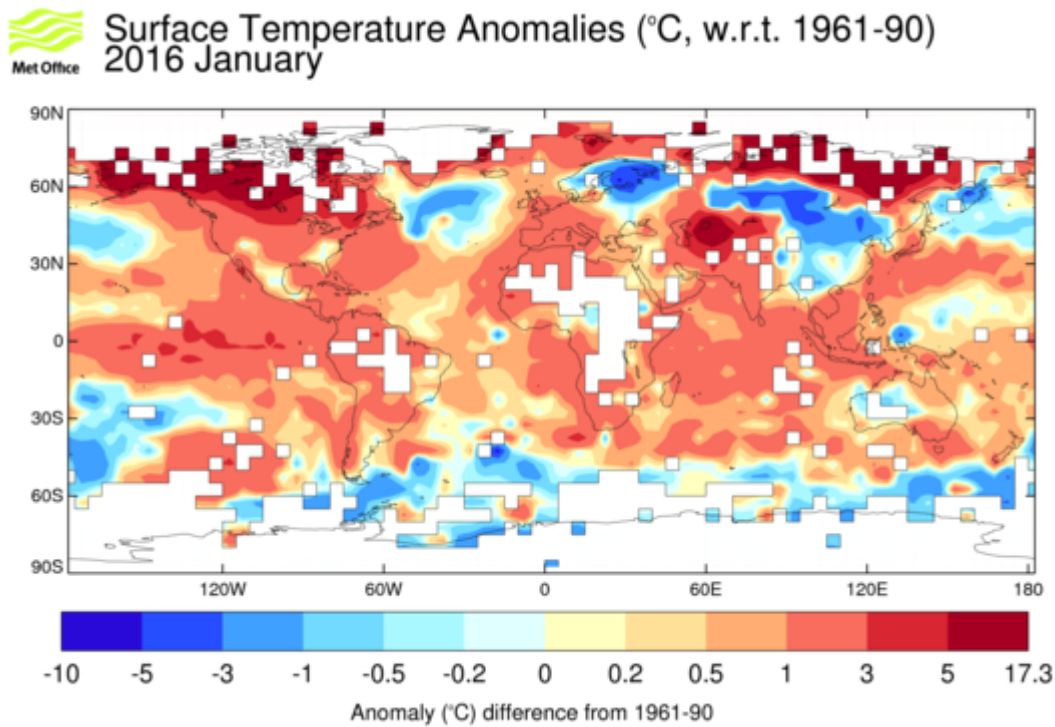
Figure 4.1 HadCRUT4's January 2016 gridded surface temperature anomalies with respect to 1961–1990 (Morice et al., 2012). Grid cells with missing data are in white colour. Contains public sector information licensed under the Open Government Licence v1.0.

Table 4.1 shows the detection horizons of the SAI cooling signal in all studied pseudo-observation model comparisons, estimated only with the near-global average of modelled SAT that are within HadCRUT4's January 2016 coverage at 5-year resolution. The signal would be detected within 10 years of SAI deployment, i.e. by 2029, at the 10% level in 30 of the 44 comparisons. This number is very similar to the 29 out of 44 within-a-decade SAI detectability found in the TfC1 experiment in the previous chapter, in which simple global means were taken across grid cells without regridding or masking.

Among the 30 comparisons that would require 10 years or fewer for successful SAI detection, 23 would require only 5 years for the cooling signal to be detected. This is higher than the number found for the idealised global experiment at the same confidence level, i.e. 17 of 29 within-a-decade comparisons requiring only 5 years for SAI detection. These results can be easily compared in Figure 4.2.

		model-simulations				
		HadGEM2-ES (3)	CSIRO-Mk3L-1-2 (3)	CanESM2 (3)	BNU-ESM (1)	MIROC-ESM (1)
pseudo-observations	HadGEM2-ES r1		10	10	10	25
	HadGEM2-ES r2		10	5	5	5
	HadGEM2-ES r3		10	10	5	30+
	CSIRO-Mk3L-1-2 r1	5		5	5	5
	CSIRO-Mk3L-1-2 r2	5		30+	30+	30
	CSIRO-Mk3L-1-2 r3	30		25	5	5
	CanESM2 r1	10	15		5	25
	CanESM2 r2	20	25		25	25
	CanESM2 r3	5	5		5	5
	BNU-ESM r1	5	5	5		25
	MIROC-ESM r1	5	5	5	5	

Table 4.1 Estimated detection horizons for the SAI signal in future HadCRUT4-masked global-mean SAT. Each row represents a plausible geo-engineering future observed with January 2016's HadCRUT4 network, and each column represents a different climate model used for fingerprint simulations. Numbers in brackets are the number of ensemble members included when generating the fingerprints. These comparisons are exactly the same as those presented in the previous study but the diagnostic is slightly different.

The improvement of geoengineering detectability in the masked experiment may have arisen from the exclusion of the polar regions, where internal variability and the inter-model spread in the simulated sea ice extent for the RCP4.5 base climate are large, especially in the Arctic summer (Massonnet et al., 2012). Also, although CSIRO-Mk3L-1-2 incorporated a solar dimming scheme while the rest of the climate models used prescribed or injected aerosols, the Arctic region where the degree of cooling is significantly different between CSIRO-Mk3L-1-2 and other models due to this discrepancy is effectively masked in the HadCRUT4 network. This leads to earlier detection even in comparisons involving CSIRO-Mk3L-1-2.

Sulphate aerosol geoengineering starts in 2020 in G4, which is only a few years from now. Much as the implementation of geoengineering itself, vast improvements in the coverage of the HadCRUT4 data set is unlikely within the next few years. Nonetheless, if sulphate aerosol geoengineering were to be implemented as it is imagined in G4, results in this section show that the limited resolution and coverage in our current observational network based on surface measurements not only would not decrease our ability to detect the SAI signal in SAT within the first 10 years of geoengineering deployment on the global level, but it would increase the likelihood of SAI detection after just 5 years of implementation.

However, although we are likely to be able to detect the cooling effect of SAI in near-global surface temperature with the use of ground-based temperature measurements, we would not know the impacts of the injected sulphate aerosols on the Arctic and Antarctic regions due to a lack of polar temperature data. This highlights a drawback of using ground-based observations only for geoengineering monitoring, as the polar regions have the largest feedbacks to the positive radiative forcing of carbon dioxide, and reducing polar ice cap melt would likely be a major objective of sulphate aerosol geoengineering.

In reality, other global temperature products based on extrapolation, optimal interpolation or satellite temperature measurements exist, and their geographically complete coverage has been shown to remove HadCRUT4's coverage bias in recent global temperature reconstructions (Cowtan and Way, 2014). These products could be used to monitor sulphate aerosol

geoengineering in the future. In such cases, the detectability of SAI in global-mean SAT may be more similar to that of the idealised experiment, in which the Arctic and Antarctic were not excluded due to a lack of weather stations. Nevertheless, results in the previous chapter and this section show that the cooling signal due to SAI could be robustly detected within the first decade of 5 Tg yr^{-1} sulphate aerosol geoengineering in global- or near-global mean SAT.

4.3 Hemispheric and latitudinal detection

With the aim of answering questions 2 and 3 as stated in Section 4.1, and understanding why the exclusion of parts of South America, Africa, the Arctic and the Antarctic would lead to more SAI detections in SAT in the first 5 years of geoengineering implementation on the near-global level, the Northern Hemisphere, Southern Hemisphere and 5 different latitudinal bands are studied separately in this section.

The two Hemispheres and bands between 90°N and 60°N (Arctic), 60°N and 25°N (Northern mid-latitudes), 25°N and 25°S (Tropics), 25°S and 60°S (Southern mid-latitudes) and 60°S and 90°S (Antarctic) are extracted from the global data that are regridded to 5° by 5° resolution without masking, and the same detection procedure is applied to the time series of annual-mean, area-weighted SAT averages in the same 44 pseudo-observation model comparisons in these bands alone, respectively.

Figure 4.2 shows the number of within-a-decade SAI detections, i.e. the total number of comparisons in which the cooling signal of SAI is detected in the 5 year-long and 10 year-long pseudo-observations at the 10% level, in the studied Hemispheres and latitudinal bands. 17 comparisons would need 5 years to robustly detect the aerosol-induced cooling signal, whilst 10 other comparisons would need 10 years to do so in the Northern Hemisphere. The within-a-decade detectability of SAI in the Northern Hemisphere is only slightly lower than the global-mean results.
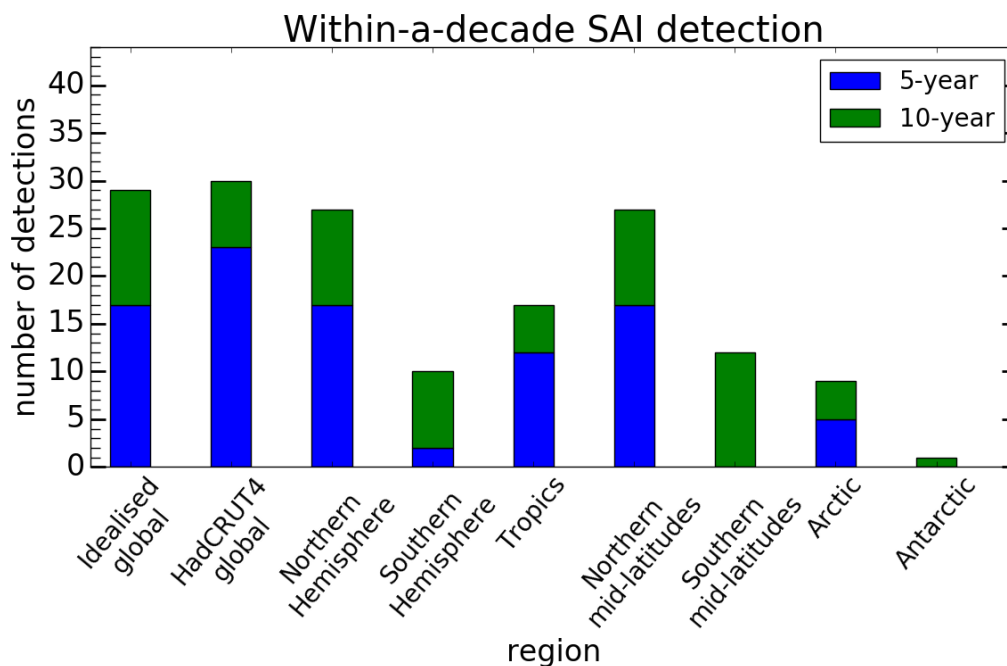
Figure 4.2 The number of successful within-a-decade SAI detections in SAT time series beginning in 2020 in each experiment. The same 44 pseudo-observations model comparisons are done in each experiment. Blue colour represents the number of 5-year detections (detections by 2024) while green colour represents the number of 10-year detections (detections that happen between 2025 and 2029).

However, using the averaged SAT in the Southern Hemisphere as the detection diagnostic would only result in 2 successful detections in the first 5 years of geoengineering deployment and 8 detections in the first 10 years of deployment. This shows a large North-South hemispheric contrast in the detectability of SAI in SAT. This is likely because the Northern Hemisphere has more land and less ocean than the Southern Hemisphere, and land responds to the aerosols faster than the ocean in all of the climate model simulations (Section 2.2.1 and Jones et al. (2010)) due to its lower heat capacity. The stronger cooling signal outweighs the larger climate noise over land in the Northern Hemisphere.

In the Tropics, 12 comparisons would require 5 years while 5 other comparisons would require 10 years to first detect the SAI signal. This makes a total of 17 within-a-decade detections out of 44, which is significantly lower than that in the global and Northern Hemisphere experiments. This may be explained by the slightly larger internal variability over the Tropics compared to the whole globe and the Northern Hemisphere due to averaging over a smaller area. Grid-scale tropical internal variability is generally smaller than the grid-scale variability

at higher latitudes because of the tropical oceans (this will be further investigated in Section 4.5). The slightly larger internal variability found for the tropical band here is, thus, mainly the effect of area averaging. Large climate noise masks the cooling effect of the injected sulphate aerosols, making it harder to detect.

To quantify and compare internal variability in different regions, the mean standard deviation of internal variability is estimated from 10 year-long non-overlapping samples of $C1$ filtered annual-mean area-mean SAT time series from the pre-industrial control simulations of a six-model ensemble (BNU-ESM, CanESM2, CSIRO-Mk3L-1-2, GISS-E2-R, HadGEM2-ES and MIROC-ESM) for different regions. Its uncertainty range is estimated from the differences between this mean and the 90% confidence intervals of the Student's t distribution for the standard deviations (c.f. Braganza et al. (2003)). The tropical standard deviation of internal variability is 0.065 ± 0.055 K, while that of the globe and the Northern Hemisphere are 0.044 ± 0.038 K and 0.062 ± 0.056 K, respectively.

This shows that the internal variability averaged over the Tropics is very slightly larger than that averaged over the Northern Hemisphere. However, the difference between tropical and Northern hemispheric variabilities is not significant enough to explain the significantly lower within-a-decade SAI detectability in tropical SAT. The slower cooling response of the tropical oceans to geoengineering aerosols is likely to be another contributor to the lower tropical detectability as compared to the Northern Hemisphere. This will be further explored in Section 4.5.

In contrast, detection of the cooling effect of SAI is easier over the first decade of implementation in the Tropics than in the Southern Hemisphere, even though the former has larger climate noise than the latter (0.054 ± 0.043 K). This is likely due to the slow cooling response in the oceans, which cover most of the Southern Hemisphere. The size of the cooling signal and climate noise will be further quantified and discussed in Section 4.5.

The Northern mid-latitudes has a high within-a-decade SAI detectability that is comparable to global and Northern hemispheric results. The latitudinal band gives 17, 5-year and 10,

10-year detections, while Southern mid-latitudes only give 12, 10-year detections. This again exhibits a North-South hemispheric contrast in the detectability of the cooling signal over the first decade of SAI implementation.

The Northern mid-latitudes has the highest within-a-decade SAI detectability amongst the studied latitudinal bands. This is likely to be because the average SAT change due to the injected sulphate aerosols in this band is large relative to the region's unforced climate variability, with its mean standard deviation being 0.063 ± 0.058 K. Figure 4.3 shows the $C1$ filtered time series of the pseudo-observations, the RCP4.5 and SAI fingerprints, and the estimated internal variability from the six-model ensemble in the HadGEM2-ES r1 versus CanESM2 comparison, averaged within the HadCRUT4 network, the Tropics, Northern and Southern mid-latitudes, the Arctic and the Antarctic, respectively. As can be seen in the comparison between Figures 4.3b and 4.3c, the SAI cooling effect is noticeably stronger over the Northern mid-latitudes than in the Tropics, while their internal climate variabilities are comparable in size.

In the Arctic, 5 comparisons would require 5 years and 4 other comparisons would need 10 years to first detect the cooling signal of SAI. The within-a-decade SAI detectability in the Arctic is lower than that on the global mean level, in either Hemisphere, the Tropics and the mid-latitudes. This can be explained by the very high Arctic internal variability, which has a standard deviation of 0.172 ± 0.142 K. Even though both the cooling signal from the injected aerosols and the warming signal from greenhouse gases are large in the Arctic due to poleward transport of sulphate aerosols through large-scale circulation (Jones et al., 2010) and positive ice-albedo feedback, the high internal variability masks the large signals (Figure 4.3e), making SAI detection challenging.

Over the Antarctic region, the cooling from the aerosols would become detectable 10 years into deployment in only 1 of the 44 comparisons. Nearly 90% of the rest of the studied comparisons would need more than 30 years for successful detection (not shown). This is due to high climate noise in the region, which has a standard deviation of 0.147 ± 0.136 K, but
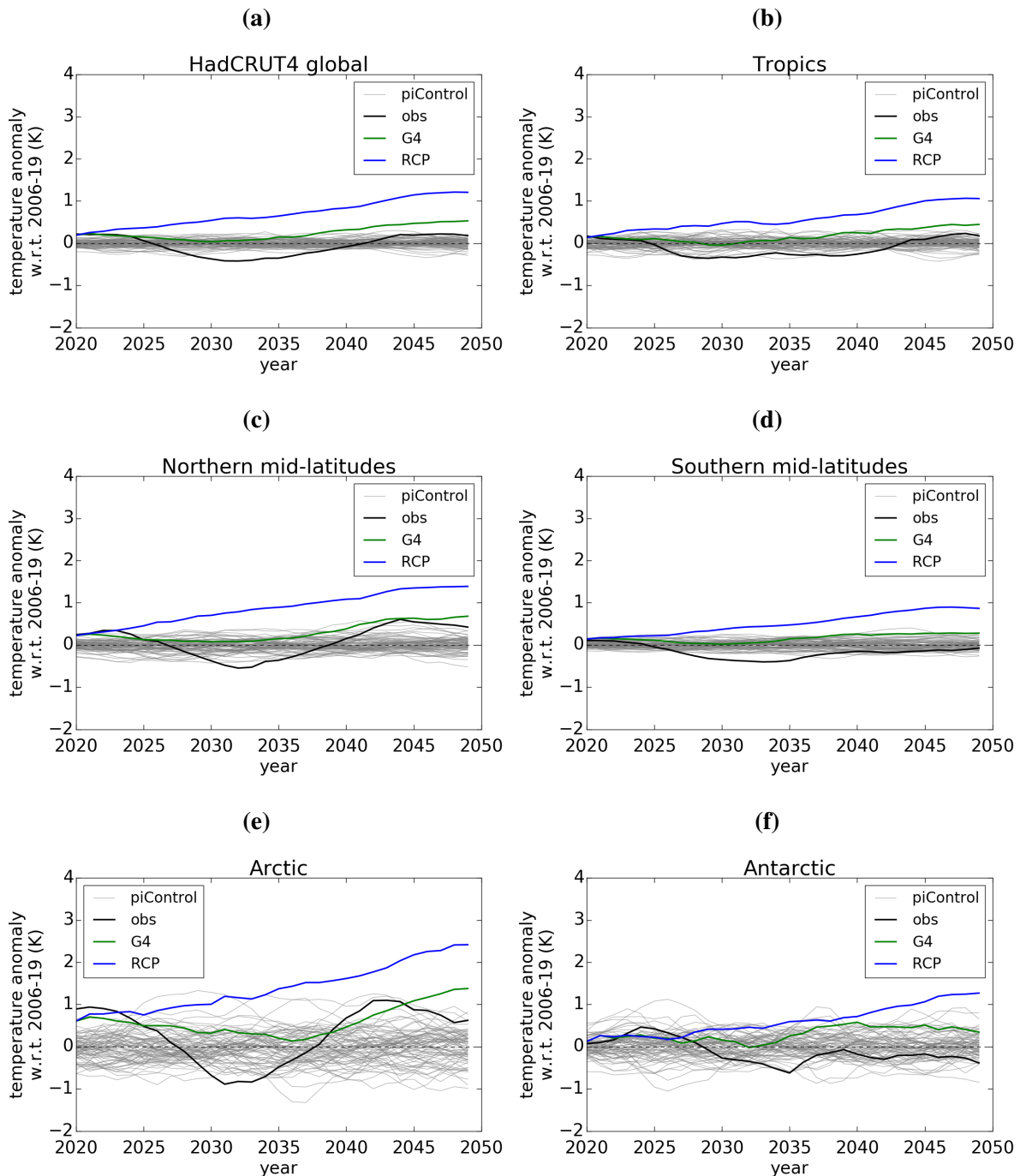
Figure 4.3 Annual mean time series of the pseudo-observations (first G4 realisation of HadGEM2-ES, black line), the ensemble-mean RCP4.5 and G4 fingerprints simulated by CanESM2 (blue and green lines, respectively) and segments of the six-model pre-industrial control simulations (grey lines) averaged over (a) HadCRUT4 data points globally, (b) the Tropics (25°N to 25°S), (c) Northern mid-latitudes (60°N to 25°N), (d) Southern mid-latitudes (25°S to 60°S), (e) the Arctic (90°N to 60°N) and (f) the Antarctic (60°S to 90°S). All time series are C1 filtered.

101

small cooling signal relative to the North Pole (Figures 4.3e and 4.3f), where aerosol burden (in HadGEM2-ES) is significantly higher as a result of stronger wave-driven stratospheric meridional circulation in the Northern Hemisphere (Jones et al., 2010), and more sea ice is present.

The low detectability of the cooling signal in Arctic and Antarctic SATs explains why the missing data in these regions would make detection easier within the HadCRUT4 network than in true global datasets. Detection of the SAI cooling effect is particularly difficult in comparisons involving CSIRO-Mk3L-1-2 in the Arctic and the Antarctic. In none of these comparisons the SAI signal could be detected within the first 30 years of SAI deployment. This is again due to the fact that CSIRO-Mk3L-1-2 employed solar dimming as a representation of solar radiation management, and that its resulting cooling effect is very different from that of the other models in the polar regions (Figure 2.2.1.1).

CSIRO-Mk3L-1-2 is kept in the studies because the sampling pool would be a lot smaller without its 3 ensemble members. Nonetheless, the numbers of within-a-decade SAI detections in the 24 comparisons without CSIRO-Mk3L-1-2 are as follows: 18 in the idealised global experiment, 17 in the HadCRUT4 experiment, 15 in the Northern Hemisphere, 7 in the Southern Hemisphere, 9 in the Tropics, 15 in the Northern mid-latitudes, 12 in the Southern mid-latitudes, 9 in the Arctic and 1 in the Antarctic. These results agree well with the results above. The detectability of SAI induced cooling is highest and comparable over the first decade of implementation on the global and near-global levels, in the Northern Hemisphere and Northern mid-latitudes. North-South hemispheric contrasts exist and detection in the Tropics is easier than in the polar regions.

4.4 Sensitivity of the SAI detection horizon to climate noise

It is evident from the previous section that having a large enough cooling signal of SAI relative to the background internal variability is one of the key factors for successful geoengineering

detection in SAT within the first decade of implementation. In this section, an idealised approach is used to investigate how variation in the the size of background climate noise might affect the detection horizon of geoengineering in G4.

Idealised pseudo-observations and fingerprints are constructed so that the effect of background noise on the geoengineering detection horizon can be isolated. Equations 4.1 to 4.3 show the analytical expressions for the temporal, idealised fingerprints and pseudo-observations as a function of time.

$$x_{\text{RCP}}(t) = \tanh(0.06t) + 0.01t + 0.1 \tag{4.1}$$

$$x_{\text{G4}}(t) = 0.7\sin(0.2t + 0.7\pi) + 0.01t - 0.5 \tag{4.2}$$

$$y(t) = x_{\text{RCP}}(t) + x_{\text{G4}}(t) \tag{4.3}$$

where t is the number of years since deployment in 2020 in G4, $x_{\text{RCP}}(t)$ and $x_{\text{G4}}(t)$ are the idealised and RCP4.5 and G4 fingerprints, and $y(t)$ is the idealised pseudo-observations that equals the sum of the two fingerprints.

Figure 4.4 shows the 30 year-long idealised pseudo-observations (black line), and RCP4.5 and G4 fingerprints (blue and green lines) as an example. $x_{\text{RCP}}(t)$ increases from 0 with a decreasing rate between 2020 and 2049, whereas $x_{\text{G4}}(t)$ decreases from 0, reaches its minimum at around -1K soon after 2030 and increases subsequently . These fingerprints are designed in such a way that they resemble the general shape of the model-simulated RCP4.5 and G4 temporal fingerprints of SAT anomalies such as those shown in Figures 3.2c and 4.3; hence the convention of labelling the y-axis as 'temperature anomaly w.r.t. 2006–19 (K)' is kept on Figure 4.4. The idealised fingerprints are free of sampling uncertainty, which are impossible to obtain with a finite ensemble of model simulations in reality.

The pseudo-observations (black line in Figure 4.4) are the sum of the RCP4.5 and G4 fingerprints by set up. The grey lines in Figure 4.4 are 30-year segments of idealised internal
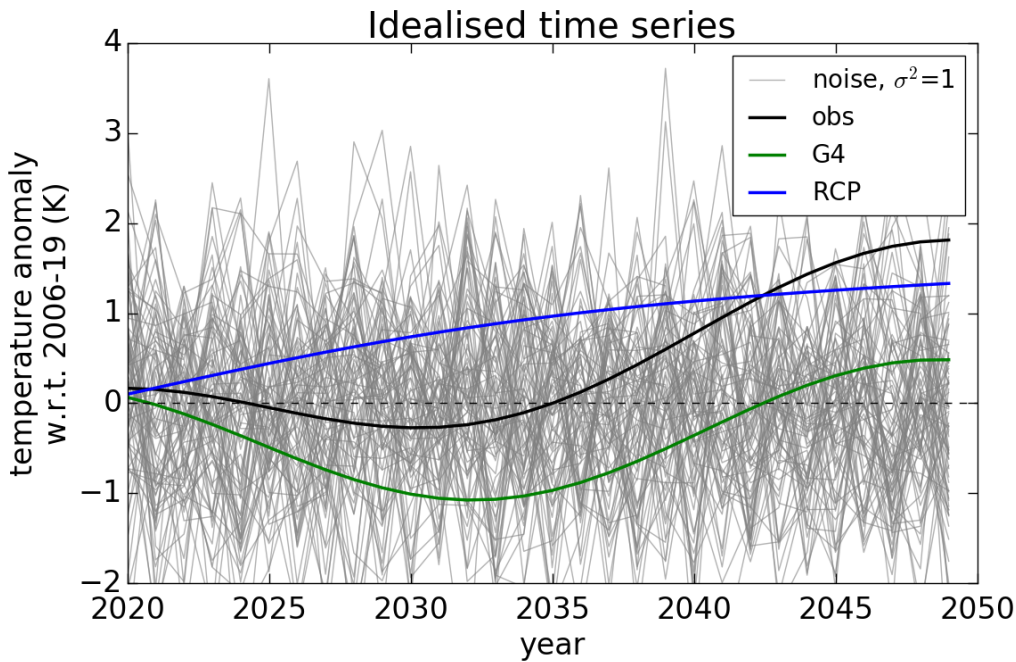
Figure 4.4 Temporal pseudo-observations (black line), fingerprints (RCP4.5 in blue and G4 in green) and background white noise (grey lines) used in the idealised detection study. The mean and variance of the background white noise are 0 and 1 K^2, respectively, in this example.

inter-annual SAT variability constructed with random samples from a standard Gaussian distribution of mean 0 and variance σ^2, which is equal to 1 K^2 in this example.

TLS regression is done on the fixed, idealised time series of pseudo-observations and fingerprints (Equations 4.1 to 4.3) but with varying background noise. The variance of background white noise is varied from 0.01 K^2 by 0.01 at a time while its mean is kept at 0 K^2. For each level of noise variance, the length of the idealised pseudo-observations and fingerprints is increased year by year until the SAI cooling signal is detected at the 10% significance level with the conventional, multi-variate detection method (TfNo in Section 3.2). As in the previous detection experiments, the minimum number of years needed for the SAI signal to be detected is referred to as the 'detection horizon', only that in this experiment this metric is estimated at 1-year resolution. The study terminates at the noise variance level that the resulting detection horizon is longer than 30 years, as a detection horizon this long is not of interest in this thesis.

No filtering is needed as the idealised time series are free of noise (please refer to the TfNo detection method in Section 3.2 for more technical details). Linear transformation (Section 2.3.1.1) is used to extract the scaling factors for the RCP4.5 and SAI signals from the input fingerprints as before. By set up, the best estimate scaling factors of the RCP4.5 and SAI signals would be 2 and 1 respectively, as both the RCP4.5 and G4 fingerprints contribute toward the RCP4.5 signal, and the G4 fingerprint has the SAI component. This is proven to be true in all of the estimated scaling factors, so the only factor that determines whether the idealised SAI cooling effect is detected or not is the uncertainty range around the scaling factor, which is influenced by the size of background noise.

Figure 4.5 shows the relationship between SAI detection horizon and background noise variance. The higher the background noise variance, the longer time is needed for successful geoengineering detection, as expected. However, the relationship between the two variables is non-linear but rather logarithmic. The black line on Figure 4.5 shows the best-fit natural logarithmic line to the idealised detection results. At low noise variance, a small increase in the variance results in a dramatic increase in the SAI detection horizon. An increase in noise variance from 0.02 to 0.04 K^2 results in a jump in the SAI detection horizon from 9 to 17 years. On the other hand, at high noise variance, the detection horizon is a lot less sensitive to the same change in background noise. For example, increasing the noise variance from 1.42 to 1.44 K^2 lengthens the SAI detection horizon from 26 to 27 years only.

Given the idealised nature of this experiment, the above results may not be quantitatively comparable to those of any detection studies involving the use of climate model simulations or real-world SAT measurements. However, they do suggest that in places where climate variability is large, for example at high latitudes, the resulting SAI detection horizons may be long, but they may not vary from one location to another as much as those in places where internal variability is low, such as in the Tropics. This will be further looked at in the next two sections.
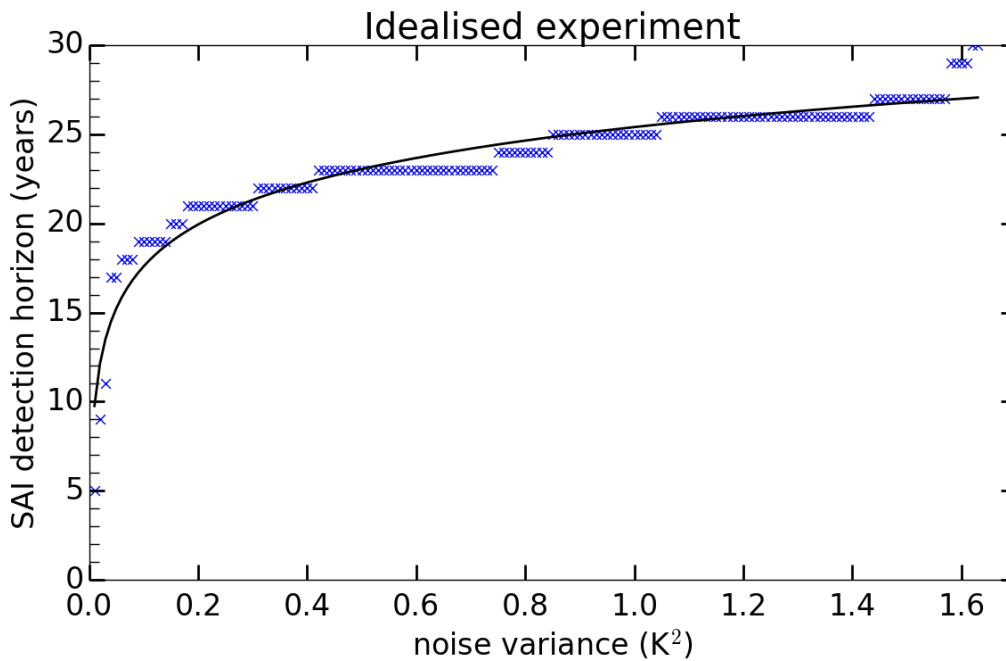
Figure 4.5 SAI detection horizon at different white noise variance levels (blue crosses) and the best-fit natural logarithm function to the results (black line).

4.5   Signal-to-noise ratio and time of emergence

Estimating the relative magnitudes of the cooling signal and background climate noise at grid scale can help us understand the potential local effectiveness of aerosol geoengineering on the surface and predict where might be best for SAI detection from a slightly different perspective than optimal detection. In this section, the SAI cooling signal, $S_{\text{SAI}}(t)$, and climate noise, N, are estimated at each grid cell for 5 climate models (BNU-ESM, CanESM2, CSIRO-Mk3L-1-2, HadGEM2-ES and MIROC-ESM) at CSIRO-Mk3L-1-2's resolution.

Assuming that local SAT changes scale with global temperatures, the local SAT at each grid cell, T_{local}, is regressed against a smoothed global-mean SAT projection, $\widetilde{T}_{\text{global}}$, for each model. This is done with both RCP4.5 and G4 simulations from each model, so that $S_{\text{SAI}}(t)$ can be extracted from the RCP4.5 and G4 signals, $S_{\text{RCP4.5}}(t)$ and $S_{\text{G4}}(t)$. Both T_{local} and T_{global} are time series of 2020–2089 ensemble-mean annual-mean SAT anomalies with respect to the 2006–2019 mean. This base period is the same as that in the detection study to facilitate comparison between SAI detectability and its signal-to-noise ratio (SNR).

106

T_{global} in RCP4.5 is smoothed by a 4th order polynomial, following Hawkins and Sutton (2012)'s approach. T_{global} in G4 is smoothed by Locally Weighted Scatterplot Smoothing (LOWESS) (Cleveland, 1981). The fraction of data points used to estimate each dependent variable is 0.25. The regression between T_{local} and $\widetilde{T}_{\text{global}}$ for RCP4.5 and G4 give us 2 separate sets of regression coefficients, $\alpha_{\text{RCP4.5}}$ and $\beta_{\text{RCP4.5}}$, and α_{G4} and β_{G4}, which are then used to estimate the individual forced temperature signals:

$$S_{\text{RCP4.5}}(t) = \alpha_{\text{RCP4.5}}\widetilde{T}_{\text{RCP4.5,global}}(t) + \beta_{\text{RCP4.5}} \tag{4.4}$$

$$S_{\text{G4}}(t) = \alpha_{\text{G4}}\widetilde{T}_{\text{G4,global}}(t) + \beta_{\text{G4}} \tag{4.5}$$

$$S_{\text{SAI}}(t) = S_{\text{RCP4.5}}(t) - S_{\text{G4}}(t) \tag{4.6}$$

With the same assumption as in the optimal detection algorithm that the climate system's internal variability is the dominant source of climate noise, and that the unforced variability does not change over time, noise (N) is estimated from the pre-industrial control simulations from each model. N is defined as the standard deviation of the time series of annual means for each grid cell. Both $S_{\text{SAI}}(t)$ and N are computed for each model separately, so that SNR(t), i.e. $S_{\text{SAI}}(t)/N$, can be estimated for each model before the simple multi-model mean is calculated.

Figure 4.6 shows the maps of S_{SAI} in 2029, N, and the SNR of SAI in 2029 calculated from HadGEM2-ES (left panel) and CanESM2 (right panel), respectively. These two climate models are selected as examples because they show the strongest (HadGEM2-ES) and weakest (CanESM2) cooling signals amongst the models in the study. Nevertheless, there are a few features in the patterns of the cooling signal and climate noise common to the 5 studied models. For example, all models show the strongest cooling signal in Northern high latitudes, lowest climate noise near the Equator and in particular in Southeast Asia, and a larger cooling signal and climate noise over land than over ocean.

By comparing Figures 4.6a with 4.6b, and 4.6c with 4.6d, it is clear that inter-model differences are larger in the SAI cooling signal than in the noise. This indicates that the
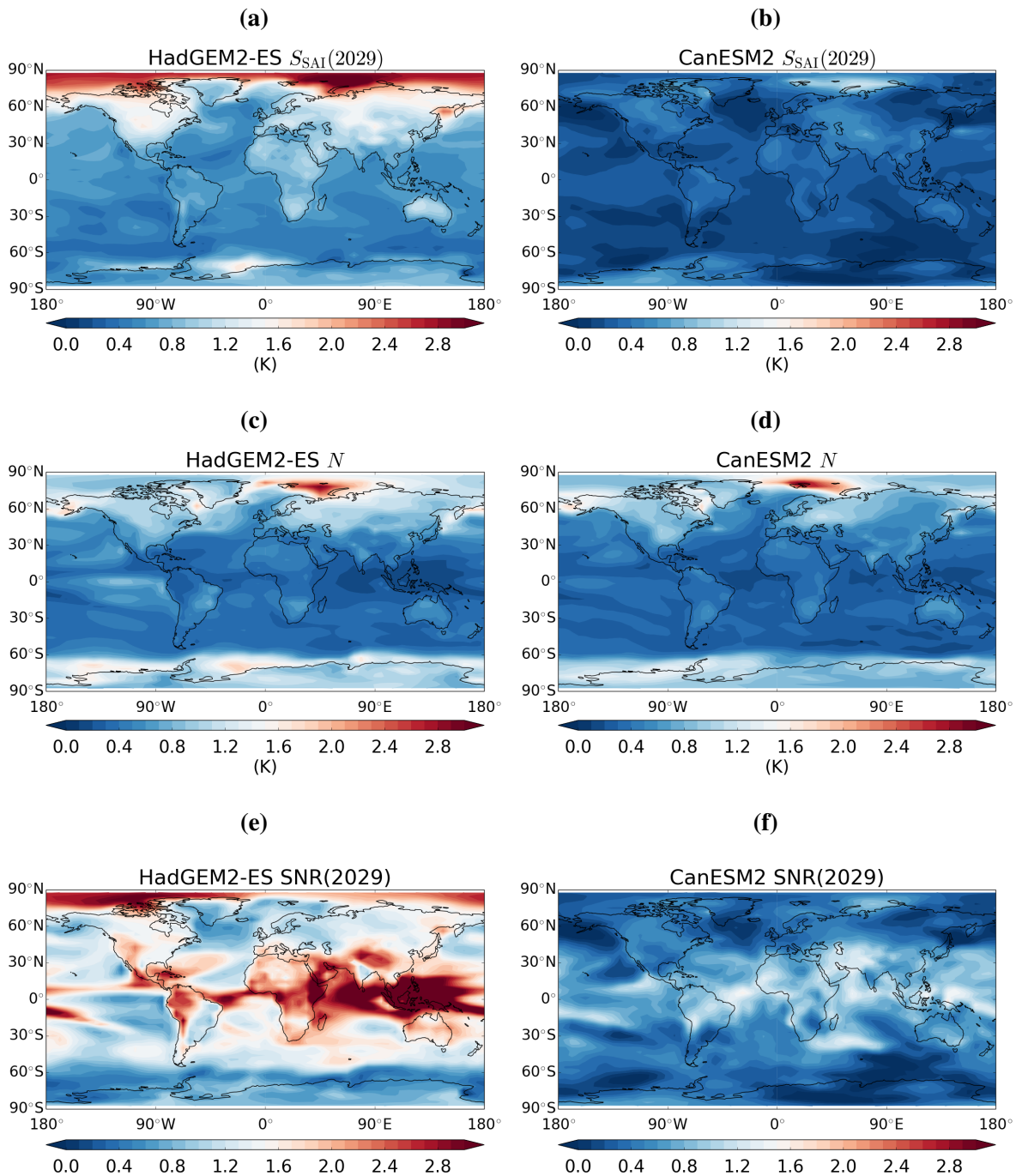
Figure 4.6 The cooling signal of SAI in 2029, standard deviation of model interannual variability and the signal-to-noise ratio of SAI in 2029, calculated using annual means from (left panel) HadGEM2-ES and (right panel) CanESM2, respectively. All values are estimated on 3.2° latitude by 5.6° longitude grids.
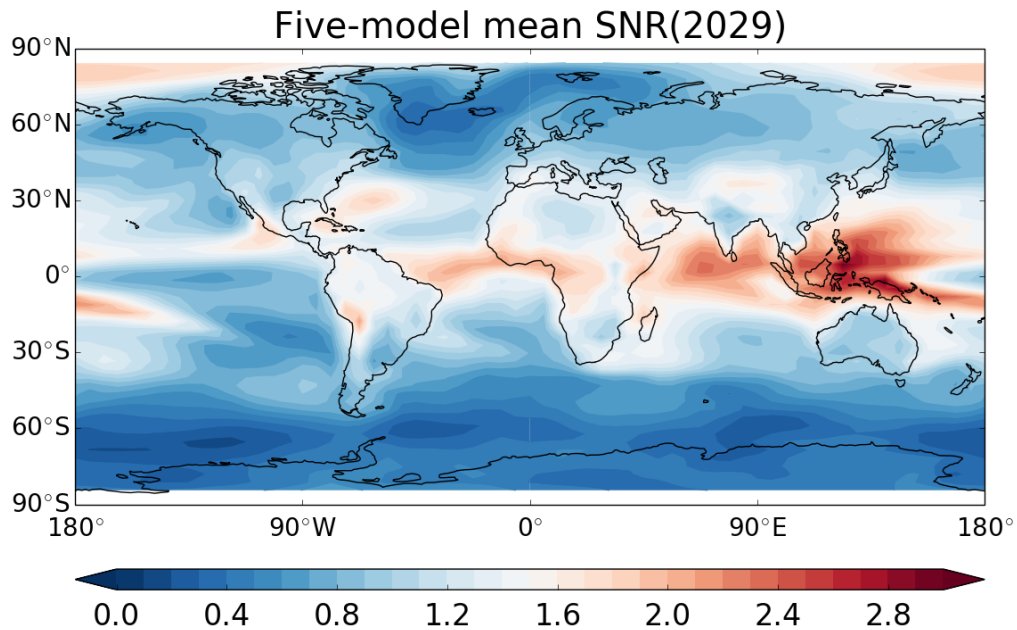
Figure 4.7 Five-model mean signal-to-noise ratio of SAI in year 2029.

different transient climate sensitivities of the models do not have a significant impact on the simulated internal variability. Thus, any difference in the estimated SNR in 2029 across the models (e.g. Figures 4.6e and 4.6f) is mainly the result of the different magnitudes of the simulated cooling signal of geoengineering.

Figure 4.7 shows the five-model mean SNR of SAI in 2029. In the 10th year of constant SAI deployment in G4, the Tropics has the highest sulphate SNR in general, followed by the Arctic, then by the mid-latitudes in both Hemispheres. The Antarctic region has the smallest SNR of SAI in 2029. These are all common features across the climate models examined, and are consistent with the results found for the Tropics, the Arctic and the Antarctic in Section 4.3.

However, contrary to the results shown for the Tropics and Northern mid-latitudes in Section 4.3, the SAI SNR is found to be generally higher in the Tropics than at mid-latitudes in the Northern Hemisphere in 2029 in all of the models in this section. This may be due to the following reasons. First, the simple analysis in this section does not involve any filtering, but the data are pre-processed and $C1$ filtered for optimal detection in the previous section. This may have led to some discrepancy in the estimation of the standard deviation of internal variability.

Second, S_{SAI} and N are estimated for individual climate models in this section, whereas a six-model ensemble is used to estimate internal variability for inter-model comparison in the last section. In other words, this section compares the ratio of the cooling signal and climate noise between individual climate models, whereas the detection study in the previous section compares the SAI forced cooling signal between models on the basis of a fixed estimate of internal climate variability.

On smaller scales, the spatial patterns of the SAI SNR are very similar across the models. All models show the highest SNR in Southeast Asia, but with different magnitudes due to their different climate sensitivities. The reason that this region has the highest SNR is its climate noise being particularly low, which may be explained by the proximity of the West Pacific warm pool acting as a buffer (de Garidel-Thoron et al., 2005). Other land regions that have a relatively high SNR in 2029 are Central Africa and Northern South America. In contrast to Southeast Asia where climate noise is particularly small, these regions have a relatively high SNR because they have a stronger cooling signal from SAI than the surrounding oceans in 2029.

SNR(t) tells us if the magnitude of the SAT changes due to SAI in year t lies outside the unforced range of SAT fluctuations at a certain place. This means in 2029, people living in Southeast Asia, Central Africa and Northern South America are likely to experience the most noticeable temperature changes from the injected sulphate aerosols compared to the natural temperature fluctuations that they are used to. Whether or not they would also experience sulphate-induced temperature changes outside the unforced range earlier than others depends on when the SAI signal first emerges from the climate noise in these places.

Time of emergence (ToE) (Hawkins and Sutton, 2012) is defined in this study as the first year in which the sulphate SNR crosses and remains above the threshold of 1 throughout the course of SAI implementation in G4. It is estimated for each 3.2° latitude by 5.6° longitude grid cell for each studied model, before the median is taken across the models.
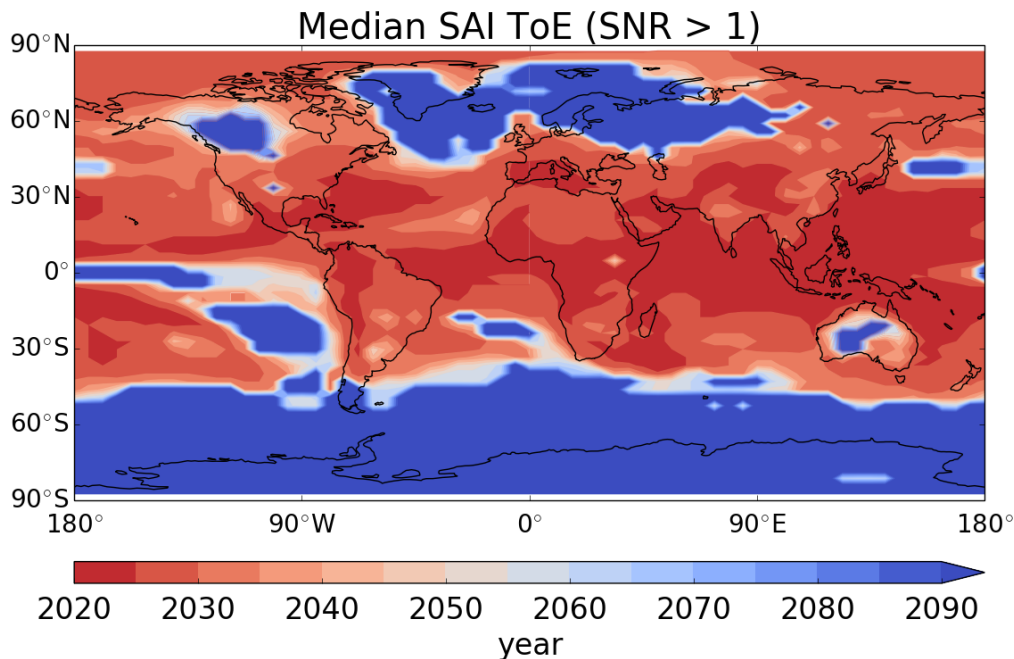
Figure 4.8 Median time of emergence, i.e. first year in which the SAI signal-to-noise ratio crosses the threshold of 1, of the SAI signal at $3.2°$ latitude by $5.6°$ longitude resolution.

Figure 4.8 shows the median ToE of the SAI signal in each grid cell. In the Tropics and Northern mid-latitudes, the SAI cooling signal would emerge from the unforced range of variability over the first 5 to 15 years of geoengineering implementation in G4. In particular, earliest emergence (by 2025) is observed in the equatorial regions in the Eastern Hemisphere in all models.

The median ToE is within the first 15 to 20 years of SAI deployment in some regions in the Northern high latitudes. These regions include Alaska, Northwestern Canada and Siberia. However, the median SAI cooling signal would not emerge from the noise throughout the course of SAI implementation in a large part of Greenland. This means the cooling effect expected from SAI would likely be masked by the climate system's unforced variability which could still lead to melting or thickening of Greenland ice sheets.

The extra-tropical ToE pattern is similar across the models except in CanESM2, in which emergence before 2070 is mainly confined to the Tropics. There is also a noticeable contrast

between Northern Hemispheric and Southern Hemispheric ToE. The cooling signal does not emerge from the noise in the Southern Ocean and Antarctica in this century in the models.

In summary, should 5 Tg yr^{-1} of SO$_2$ be injected to reduce some of the warming in the RCP4.5 pathway from 2020 to 2070, people living in equatorial regions would likely experience a drop in near-surface temperature that goes beyond the unforced range of variability as soon as 2025, while those in the mid-latitudes and certain high-latitudinal regions in the Northern Hemisphere could experience a noticeable change 10 to 20 years into deployment, depending on where they live. On the other hand, the cooling signal from the sulphate aerosols would likely be masked by the climate system's internal variability in Greenland, the Southern Ocean and Antarctica throughout the whole implementation period.

Results shown in this section are robust to the smoothing method used for obtaining $\widetilde{T}_{\text{global}}$ in the RCP4.5 scenario. Smoothing T_{global} in RCP4.5 with LOWESS (as is done with T_{global} in G4) instead of a 4$^{\text{th}}$ order polynomial gives very similar SNR and median SAI ToE results quantitatively to those shown in Figures 4.7 and 4.8.

4.6   Detection in SREX regions

Sections 4.3 and 4.5 showed that the SAT response to geoengineering aerosols could be very different in different parts of the world. In addition, internal climate variability becomes important at regional scales and could mask the cooling effect of SAI. There may also be a non-linear relationship between internal climate variability and the resulting SAI detection horizon, as found in Section 4.4.

Increased understanding of the regional differences in the SAI detectability in SAT is essential to future climate and geoengineering policymaking because these are the scales where people live, countries sit and political decisions are made. Knowing where would be best for detecting the SAI cooling signal geographically could also help us develop an observational
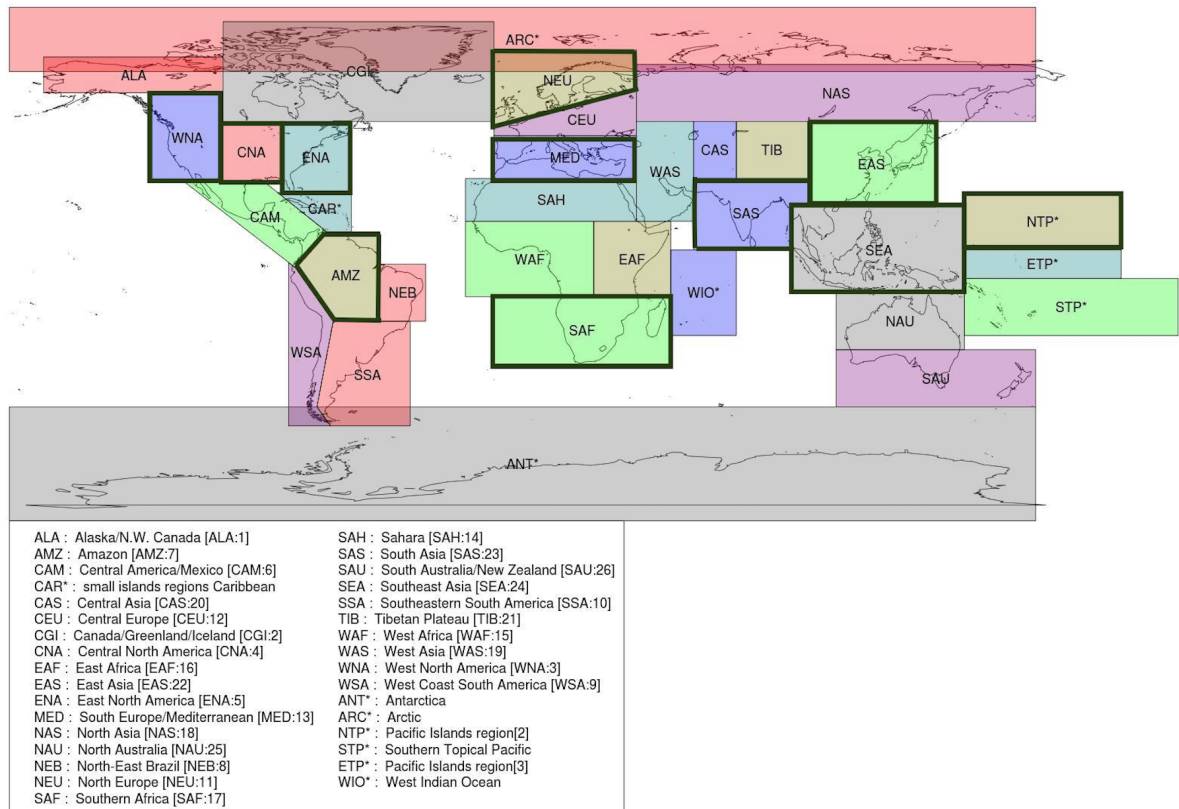
Figure 4.9 The 33 SREX regions. This figure is adapted from Figure 21-4 of Hewitson et al. (2014). Regions with bold borders are studied in this chapter.

network that could most effectively monitor the effectiveness of SAI in the future, should that be needed.

This section provides a regional focus on the detectability of the cooling signal from sulphate aerosol geoengineering from the formal optimal detection perspective. The globe is divided into various SREX regions (Figure 4.9) that were defined in the Contribution of Working Group II to the Fifth Assessment Report of the Intergovernmental Panel on Climate Change (IPCC AR5) (Hewitson et al., 2014), and the RCP4.5 and SAI fingerprints are looked for in the annual-mean regional-mean SAT pseudo-observations in each of these regions.

Figure 4.10 shows the number of within-a-decade SAI detections in 11 SREX regions: West North America (WNA), Central North America (CNA), East North America (ENA), Amazon (AMZ), North Europe (NEU), Mediterranean (MED), Southern Africa (SAF), South Asia (SAS), East Asia (EAS), Southeast Asia (SEA) and Pacific Islands region (NTP*).

Figure 4.10 Number of within-a-decade SAI detections (out of 44 comparisons) in different SREX regions. Spatial variation of SAI detectability by 2029 is obvious yet cannot solely be explained by the differences in SNR between different regions in 2029.

These regions are chosen because they are relatively populated, vulnerable to climate change or politically important in climate policymaking. The same 44 pseudo-observation model comparisons are done throughout this section.

In general, regions in the Tropics and up to ~ 45 °N in the Northern Hemisphere give more within-a-decade detections of the SAI cooling signal than regions in higher latitudes. This agrees with the findings and discussion in Sections 4.3 and 4.5. Regions around East Asia have the highest number of successful detections within the first 5 or 10 years of SAI deployment, with EAS having 19 and NTP* having 16 within-a-decade detections in the 44 comparisons made. The regions that have the lowest SAI detectability by 2029 are WNA, NEU and MED, each of which having 3 within-a-decade SAI detections only. The rest of the studied regions have 7 to 10 within-a-decade SAI detections, as shown in Figure 4.10.

Based on these results, more observations should be made, or more weights should be given to observations made around East Asia and the surrounding Pacific area in order to most

effectively monitor sulphate aerosol geoengineering in the event of deployment. However, none of the studied regions has a majority of within-a-decade SAI detection, which is defined as having more than or equal to 22 within-a-decade SAI detections in the 44 comparisons made. This suggests that on this spatial scale detection of the SAI cooling signal from the 5 Tg yr^{-1} scenario would be difficult.

Interestingly, large differences in the number of within-a-decade SAI detections are seen between SAS and EAS, EAS and SEA, and SEA and NTP*, despite them being neighbouring regions in or close to the Tropics (Figure 4.10). Other connected regions such as WNA, CNA and ENA that are at higher latitudes do not show as large a contrast in the number of within-a-decade SAI detection across them. This is likely to be because there is relatively low but more variable internal variability across SAS, EAS, SEA and NTP* than across WNA, CNA, ENA, where internal variability is relatively high but less variable from one location to another (e.g. Figures 4.6c and 4.6d). These results echo the findings of the idealised experiment in Section 4.4, in which the prediction of having more variable SAI detection horizons in the Tropics than in higher latitudes was made.

Even though the median ToE is as early as 2025 in many Eastern equatorial regions, the SAI fingerprint can only be detected in fewer than half of the studied comparisons within the first 10 years of SAI implementation in SAS, SEA and NTP*. This means even if noticeable cooling is observed outside the expected range of internal variability a few years into geoengineering deployment in these areas, robust detection of the SAI signal in the temporal SAT observations would take longer time to be achieved.

Also, although SEA has clearly the highest SAI SNR in year 2029 (Figure 4.7), it has only 10 within-a-decade detections, far fewer than the 19 found for its neighbouring region EAS (Figure 4.10). The same is true for AMZ where the SAI signal is about twice as large as the climate noise in 2029 but gives only 8 within-a-decade detections out of the 44 comparisons made.

115

This is because detection using TLS regression does not only require the climate signal to be sufficiently large and, thus, easily distinguishable from the noise, but also the shape of the observations and fingerprint to be similar enough to give a non-zero scaling factor. In other words, although necessary, having a large enough SNR is only a partial requirement for formal detection of a climate signal. As ToE does not take into account the temporal nor spatial pattern of climate signals or climate variability, it is likely to overestimate the effectiveness of SAI. This could lead to serious consequences, for example not injecting enough SO_2 to meet certain climate goals, regionally or globally.

On the other hand, results in this section suggest that formal detection techniques could take longer to detect the effects of SAI in regional surface temperature, even though these effects might exceed the unforced range of temperature fluctuations. Indeed, it would be difficult to know the true time horizon over which the SAI cooling effect would become detectable, as it would highly depend on how we define detection.

However, the ultimate aim of monitoring the effectiveness of sulphate aerosol geoengineering would likely be controlling the SO_2 injection rate based on the detection results and our climate goal. This would require knowing to what extent the observed changes in climate is due to the injected sulphate aerosols in relation to other external forcings (attribution). For this reason, formal detection and attribution would be necessary for advising regional governments on geoengineering, even though SNR and ToE are extremely useful and convenient metrics that provide a slightly different perspective.

Detection of the geoengineering signal at SREX regional scales is a lot more challenging than on the global and latitudinal scales. This is expected as the pseudo-observation and fingerprint SAT time series are noisier when averaged over a small region. This means it is a lot harder to separate the forced signal of geoengineering from the unforced variability when considering a region on the SREX scale. Variations and biases in model simulations are also more profound at smaller spatial scales where climate processes are not represented as well by climate models as at larger scales. Since detection essentially involves inter-model comparisons

in this thesis, it is not surprising that regional detection of the SAI cooling signal is not as easy as global or latitudinal detection in the first decade of SAI implementation at the 10% level.

In fact, because of the noisier climate signals and larger model differences on small spatial scales, even the RCP4.5 fingerprint is not as detectable in any of the SREX regions as it is in the global or latitudinal experiments. In particular, the RCP4.5 fingerprint would not be detected at the 10% level before or in the same year as the SAI fingerprint in as many as 25% of the studied comparisons in regions such as CNA, NTP*, SAF and SEA. This was not observed in the global and latitudinal detection experiments, in which detection of the RCP4.5 signal was claimed at the 10% level within the corresponding detection horizon of SAI in nearly all of the studied comparisons.

SREX regions (Hewitson et al., 2014) are chosen for regional detection in this chapter because they are simple polygons that represent different climatic regimes. Except NTP* (a sea-only region), the studied regions cover mainly land areas of interest and of relevance to climate policymaking. Regional detection results may improve if only the land data are included in these regions, as land responses to climate forcings faster than the ocean. Nonetheless, results in this section show that SAI detection in the first decade of geoengineering implementation at such small spatial scales could be challenging in the 5 Tg yr^{-1} injection scenario. The use of longer temporal datasets could potentially give more positive geoengineering detection results, but effective monitoring of geoengineering would require swift detection of its impacts on the climate. More spatial information may thus be needed for early geoengineering detection on sub-global scales.

4.7 Detection on continental scales

Since detection and attribution is challenging on the scale of individual SREX regions, but hemispheric scales may be too large for countries to be interested in, detection of the cooling signal from the geoengineering sulphate aerosols is attempted in continental-scale regions

that consist of a few SREX regions in the same 44 pseudo-observation model comparisons in this section. This will also help us find out which would be the optimal spatial scale for geoengineering detection in a 5 Tg yr^{-1} injection scenario.

Continental-scale detection is achieved in two ways, first by detecting the average temporal SAT change due to the injected sulphate aerosols in each of the chosen continental-scale regions, and second by detecting the spatio-temporal SAT pattern across the few SREX regions in each of the continental-scale regions. The latter means constructing a vector of the time series of annual-mean SAT in WNA, followed by that in CNA, and then by that in ENA in the example of detection in the Contiguous United States. This spatio-temporal diagnostic adds information about large-scale spatial contrast between neighbouring SREX regions to the original temporal data, and is aimed at improving the detectability of SAI during the first decade of deployment.

Similar to the SREX regional study presented in the previous section, SREX regions are combined to form bigger, continental-scale regions here as they are. This means the ocean component of an SREX region that constitutes a continental-scale region, if present, is also included in the continental-scale region. Future work could look at SAI detection on the continental scale without ocean data.

Table 4.2 shows the number of successful detections when 5 years and 10 years of pseudo-observations since geoengineering deployment in G4 are used under the 'average' and 'vector' construction in the Contiguous United States, South & East Asia, South America and Africa, respectively.

The contiguous United States consists of WNA, CNA and ENA. Alaska (ALA in Figure 4.9) is not included because both the greenhouse gas and sulphate aerosol driven climate signals are overwhelmed by its large multi-model climate noise due to its high-latitude location. Detection was originally attempted in the United States consisting WNA, CNA, ENA and ALA, but no within-a-decade detection of the SAI cooling signal was found. This contradicts the early SAI ToE found for Alaska (Figure 4.8). However, as discussed in Section 4.6, formal detection also

Continent/ sub-continent	Average		Vector	
	5-year	10-year	5-year	10-year
Contiguous United States (WNA, CNA, ENA)	7	7	6	3
South & East Asia (SAS, EAS, SEA)	14	6	14	8
South America (AMZ, NEB, SSA, WSA)	2	9	3	11
Africa (SAH, WAF, EAF, SAF)	2	3	6	7

Table 4.2 The number of successful 5-year and 10-year detections at the 10% level in the continental-scale study. The SREX regions in brackets are the regions included in each continental-scale region.

requires the shapes of the pseudo-observations and the fingerprints to be comparable, and a multi-model approach is used to estimate climate noise in the detection algorithm, whereas individual models are used to estimate noise in the ToE study.

Averaging the SAT changes across WNA, CNA and ENA give us 7, 5-year and 7, 10-year successful detections. The within-a-decade SAI detectability in the Contiguous United States is higher than that in any of its consisting SREX regions. Under the vector construction in which the SAT response contrast across the consisting SREX regions is taken into account in regression, however, the total number of within-a-decade detections drops to 9. This is likely due to the fact that WNA, CNA and ENA all have relatively large internal variability, and only averaging can reduce this noise to enable detection in the first decade of geoengineering deployment.

South & East Asia consists of SAS, EAS and SEA. Averaging the SAT responses in these regions give 14, 5-year and 6, 10-year successful detections, which in total is again more than the number of within-a-decade detections in any of the individual regions. Constructing a vector that captures the SAT response contrast across the consisting regions does increase the within-a-decade SAI detectability slightly on the continental scale. This suggests that the additional spatial information in the spatio-temporal diagnostic does improve SAI detectability in the first decade, if the spatial contrast across regional SAT responses to stratospheric sulphate aerosols is not overwhelmed by large climate noise. South & East Asia gives the highest number of within-a-decade SAI detections among the studied continental-scale regions under both the average and vector constructions.

South America consists of 4 SREX regions, namely AMZ, NEB, SSA and WSA (Figure 4.9). Under the average construction, there are 2 successful detections when 5 years of pseudo-observations are used and 9 other detections when 10 years of pseudo-observations are used. This makes a total of 11 within-a-decade detections, a number higher than that when considering AMZ alone, even though AMZ has a higher SNR for SAI than the rest of South America in 2029 (Figure 4.7). The spatio-temporal vector construction gives 3, 5-year and 11, 10-year detections across South America. This again shows an increased SAI within-a-decade detectability when the regional contrast of SAT response to the injected sulphate aerosols is taken into account.

SAH, WAF, EAF and SAF form Africa (Figure 4.9). Averaging the SAT responses in these regions give 2, 5-year and 3, 10-year SAI detections. The within-a-decade SAI detectability in Africa as a whole is lower than that in SAF alone. This may be due to the fact that SAF has an exceptionally low level of multi-model climate noise among African regions. This is not shown in Figures 4.6c and 4.6d, but is evident in the six-model pre-industrial simulations that go into the detection algorithm. The vector construction results in 6, 5-year and 7, 10-year successful detections of the SAI signal in Africa. This again shows that the additional spatial information increases the within-a-decade SAI detectability in a continental-scale region.

All in all, detection of the SAI cooling signal in annual-mean area-average SAT time series in the first decade of SAI implementation in G4 is easier on the continental scale than on the SREX regional scale in a majority of the studied cases. An exception is SAF, which gives more within-a-decade SAI detections than Africa as a whole. This implies that if one sub-region has smaller climate noise than the continental-scale region, averaging the SAT response on the continental scale would not increase the geoengineering detectability. Likewise, additional information of the spatial contrast of the SAT response to the geoengineering aerosols across different SREX regions increases the within-a-decade SAI detectability in most of the studied cases. An exception occurs when all the consisting sub-regions have a high level of unforced climate noise that masks both the SAI signal and the contrast of SAI signals across the sub-regions. An example of this is the contiguous United States.

4.8   Optimal scale for geoengineering detection in SAT

Results from Section 4.3 to 4.7 are put together in this section to investigate whether there is a correlation between the detectability of the SAI cooling signal and the spatial scale on which optimal detection is attempted. If a correlation is present, it could potentially be used to determine the optimal spatial scale for SAI detection in SAT.

Figures 4.11a, 4.11c and 4.11e show the number of successful 5-year, 10-year and within-a-decade (the sum of 5-year and 10-year) detections of the SAI fingerprint versus the surface area of the region. Figures 4.11b, 4.11d and 4.11f are the equivalent scatter plots for the RCP4.5 fingerprint for comparison.

The rightmost point in each figure (surface area $\sim 5.1 \times 10^8$ km^2) corresponds to the idealised global scale (Section 3.2.1), whereas the second point from the right (surface area $\sim 4.3 \times 10^8$ km^2) corresponds to the masked HadCRUT4 global scale (Section 4.2). The two points located third from the right (surface area $\sim 2.6 \times 10^8$ km^2) represent the hemispheric scale (Northern and Southern Hemispheres, Section 4.3), and the smaller areas (counting from the right) are those of the studied latitudinal bands (Section 4.3), continental-scale regions (Section 4.7) and SREX regions (Section 4.6). The surface area of all of these regions is estimated by assuming a spherical Earth.

The Spearman's rank correlation coefficient (r_s) (Spearman, 1904) is calculated to measure the rank correlation between the number of detections and the size of studied region for each of the figures mentioned above. r_s is used because it does not require any assumption about the frequency distributions of the variables (Hauke and Kossowski, 2011), and is therefore appropriate for discrete variables such as integer numbers of detections as well. For each calculated r_s the associated p-value is estimated to test its significance. $p < 0.05$ is considered statistically significant in this section.

r_s between the number of 5-year SAI detections and the surface area of region is 0.476. The positive correlation coefficient indicates that the number of detections tend to increase
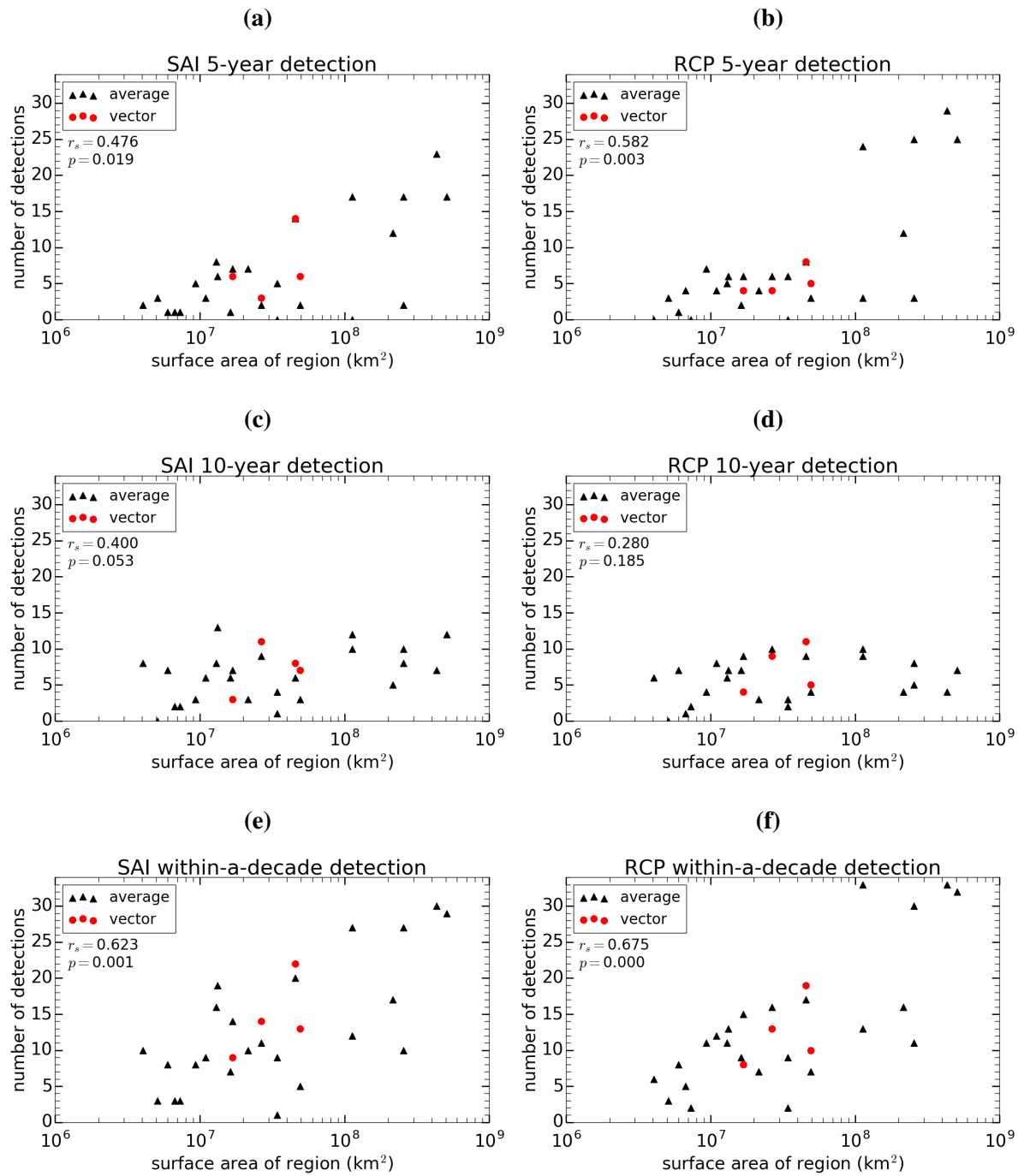
Figure 4.11 The number of (a) and (b) 5-year detections, (c) and (d) 10-year detections, and (e) and (f) within-a-decade detections of the SAI cooling signal and the RCP4.5 warming signal versus the surface area of studied regions, respectively. The spatial scale included in this figure ranges from the SREX regional scale (the leftmost points) to the idealised global scale (the rightmost point). Black triangles represent the results under the average (temporal) construction, whereas red circles represent the results under the vector (spatio-temproal) construction. The r_s and p values shown on each graph are the Spearman's rank correlation coefficient and its associated p-value of the plotted variables.

when the size of the considered region increases, when 5 years of pseudo-observations from the start of geoengineering are used for detection purposes. The correlation is significant as its associated p-value is 0.019. However, this does not mean the monotonic relationship between the two variables is linear (note the logarithmic scale on the x-axis in Figure 4.11a). The monotonic relationship between the two variables is also imperfect, i.e. it is not equal to 1, because the detectability of the cooling signal from SAI is also dependent on the geographic location of the region.

On the other hand, a significant monotonic relationship is not observed between the number of successful SAI detections in the second half of the first decade of geoengineering deployment and the size of studied region (Figure 4.11c). r_s is 0.400 and its p-value is 0.053, which is slightly higher than the 5% significance level.

The monotonic relationship between the detectability of the SAI cooling signal and the size of region is the most positive and highly significant when the total number of 5-year and 10-year SAI detections is considered (Figure 4.11e), with its r_s being 0.623 and p-value being 0.001.

Similar results are found for the RCP4.5 fingerprint. The Spearman's correlation coefficients between the number of 5-year, 10-year and within-a-decade RCP detections and the size of the region are 0.582, 0.280 and 0.675, respectively. Their corresponding p-values are 0.003, 0.185 and 0.000, respectively. These show a stronger positive correlation that is more significant between the detectability of the RCP4.5 fingerprint and the spatial scale of the studied region than the SAI fingerprint except for when 10 years of pseudo-observations are used, in which case both correlations are weak and insignificant.

To answer question 3, geographical differences aside, the optimal spatial scale for SAI detection in SAT under this scenario would be the near-global and global scales. This is because averaging over a large area significantly reduces climate noise, and this makes rejection of the null hypothesis, i.e. the observed SAT changes are due to internal variability alone, easier. Adding spatial information to the time series (vector construction discussed in Section 4.7, red

circles in Figure 4.11) does increase the detectability of both fingerprints in a number of cases, but not to an extent as great as by increasing the spatial scale on which detection is done.

4.9 Summary

This chapter has investigated the detectability of the cooling signal from 5 Tg yr^{-1} sulphate aerosol geoengineering in the average SAT response in different sub-global regions of different spatial scales at the 10% level, and how additional information of the spatial contrast of these responses would affect the detection results. An idealised experiment was also conducted with analytical pseudo-observations, fingerprints and white background climate noise with increasing variance in order to test the sensitivity of the SAI detection horizon to the size of internal variability. TfC1 was used for optimal fingerprinting unless otherwise stated, and the same 44 pseudo-observation model comparisons were made throughout this chapter where applicable.

In answer to question 1 raised at the start of this chapter, the limited spatial resolution and coverage in HadCRUT4 would increase the overall within-a-decade detectability of the SAI cooling signal in global-mean SAT (Section 4.2). This improvement mainly comes from the significant increase in the number of successful detections in the first 5 years of geoengineering implementation in G4 due to the missing data in the polar regions where internal variability is high and climate model simulations differ most.

A lot of different types of analysis were done to answer question 2. On the hemispheric level, it would be easier to detect the SAI cooling signal in the Northern Hemisphere than the Southern Hemisphere over the first decade of SAI deployment because there is more land in the Northern Hemisphere, and land responds quicker to the geoengineering aerosols than the ocean (Section 4.3).

For different regions of the Earth, the Northern Hemisphere mid-latitudes gave the highest number of within-a-decade SAI detections, likely because the average cooling signal of SAI in this band was the largest relative to its average multi-model internal climate variability. The detectability of the cooling signal in Northern Hemisphere mid-latitudes was followed by the Tropics, Southern mid-latitudes, the Arctic and, at last, the Antarctic (Figure 4.2). The North-South hemispheric contrast in the within-a-decade detectability of the cooling signal was also present in the mid-latitudes and in the polar regions.

On regional scales, East Asia and the Pacific Islands region would be the best places for monitoring the regional effects of SAI, as these two regions gave the highest number of within-a-decade SAI detections among all studied SREX regions (Figure 4.10). However, none of the studied regions gave more than 22 (half of the number of comparisons made) within-a-decade SAI detections, suggesting that regional scales are too small for robust detection of the SAI cooling signal in a 5 Tg yr^{-1} scenario.

Both the idealised (Section 4.4) and the regional detection experiment (Section 4.6) suggest that the time needed for the SAI cooling signal to be robustly detected may vary from one location to another in the Tropics more than in higher latitudes, as the SAI detection horizon was noticeably more sensitive to changes in internal variability where it was low than where it was already high.

The SNR of SAI was determined at grid scales to understand the spatial variation of the SAI cooling response and climate noise in climate models. The SAI cooling signal would emerge from the unforced SAT variability in the first 5 to 15 years of geoengineering implementation in G4 in the Tropics and Northern mid-latitudes, and in the first 15 to 20 years in regions such as Alaska, Northwestern Canada and Siberia. However, ToE tended to be an underestimate of the SAI detection horizon estimated by formal detection and attribution techniques. ToE is, therefore, not recommended to be used to advise regional governments, but to be viewed as a different perspective (Section 4.5).

In answer to question 3, detection of the average cooling signal on continental scales would be easier than on the regional level except for Africa over the first 10 years of SAI implementation (Section 4.7). In fact, a positive monotonic relationship between the total number of within-a-decade SAI detections and the size of region was found (Figure 4.11e). The optimal scale for geoengineering detection in temporal SAT time series would, thus, be the near-global and global scales.

Finally, additional information about the spatial contrast of the SAT responses across different sub-regions in a continental-scale region increased the within-a-decade SAI detectability in the studied continental-scale regions, except in the contiguous United States. However, the extent to which the within-a-decade SAI detectability increased due to the additional spatial dimension was not as great as that due to the increase in the spatial scale on which detection was attempted.

So far geoengineering detection has been attempted in temporal and spatio-temporal surface temperature changes in this thesis. The following chapter will use techniques similar to those employed in Chapters 3 and 4 to explore the potential of detecting the geoengineering response in the vertical temperature profile, on which stratospheric sulphate aerosols are expected to have noticeable radiative effects.

Chapter 5

Geoengineering detection in the vertical temperature profile

5.1 Introduction

Sulphate aerosols in the stratosphere not only influence surface temperature, but they also alter the vertical temperature profile radiatively. Observations after major volcanic eruptions such as the Mount Pinatubo eruption in 1991 show global tropospheric cooling as a result of aerosol reflection of solar radiation, and tropical lower stratospheric warming as a consequence of solar near-infrared and terrestrial longwave radiation absorption by volcanic aerosols in the stratosphere (Parker et al., 1996; Stenchikov et al., 1998).

The radiative effects of stratospheric sulphate aerosols on the atmosphere, together with ozone depletion in high latitudes, can cause observable dynamical responses such as a strengthened Northern Hemisphere polar vortex and a pronounced positive phase of the Arctic Oscillation (AO) for one or two Northern Hemisphere winters after a major volcanic eruption (Stenchikov et al., 2002). While state-of-the-art climate models may be imperfect in reproducing these observed post-volcanic dynamical changes, they are, on broad scales, capable

of reproducing the radiative effects of volcanic aerosols on tropospheric and stratospheric temperatures (Driscoll et al., 2012).

Tilmes et al. (2009) used large volcanic eruptions as the natural analogue of future sulphate aerosol geoengineering and showed, with the use of the chemistry climate model WACCM, that volcanic-like geoengineering aerosols (of dry mode radius $0.37 \pm 1.25 \ \mu m$) equivalent to a 2 Tg yr^{-1} sulphur injection rate would produce a vertical temperature pattern consisting of tropospheric cooling and tropical lower stratospheric warming, which is clearly different from the significant decrease in stratospheric temperature and increase in tropospheric temperature projected for increasing greenhouse gas concentrations in the IPCC A1B scenario (Nakicenovic et al., 2000). Carbon dioxide in the atmosphere absorb more longwave radiation than they emit upward into space, radiatively warming the troposphere and cooling the stratosphere (Rind et al., 1990).

As a result of radiative, chemical and dynamical changes, stratospheric ozone is expected to change in future climates with or without geoengineering. Tilmes et al. (2009) estimated up to 25% increase in column ozone between 2010–2020 and 2040–2050 in middle and high latitudes due to decreased upper stratospheric temperatures and halogen content in the A1B scenario, and up to 10% increase mainly due to enhanced chlorine activation in a 2 Tg yr^{-1} geoengineering scenario. A downward trend of global-mean column ozone was also observed after the Mount Pinatubo eruption (Schoeberl et al., 1993).

Changes in stratospheric ozone in turn alter atmospheric temperatures through the absorption of ultraviolet (UV) and visible radiation, although the impacts of sulphate aerosols on stratospheric ozone depend strongly on altitude, latitude, the season, aerosol area and background chlorine abundances (Prather, 1992). Unlike WACCM, the CMIP5 models that are included in this study do not have interactive stratospheric ozone chemistry (Eyring et al., 2013). As such, this chapter focuses on the first-order radiative effects of geoengineering aerosols on the vertical temperature profile, but future work could investigate geoengineering-induced ozone changes and the subsequent changes in atmospheric temperature.

Various studies, including Karoly (1987), Allen and Tett (1999), Lott et al. (2013) and Santer et al. (2013), have detected and attributed historical changes in the vertical temperature structure to human influences. Since the expected radiative effects of stratospheric sulphate aerosols would produce a very different vertical temperature profile to that due to increasing greenhouse gas concentrations, the vertical temperature profile has the potential to prove useful in early geoengineering detection and monitoring.

In this chapter, the detectability of the influence of stratospheric geoengineering sulphate aerosols on the vertical temperature profile as if observed by the satellite-based Advanced Microwave Sounding Units Version A (AMSU-A) (Wang and Zou, 2014) is investigated. AMSU-A is chosen because its data, together with the observational records from its predecessor Microwave Sounding Units (MSU), have been widely used for atmospheric temperature monitoring thanks to their near-global coverage under nearly all atmospheric weather conditions (Mears and Wentz, 2009; Wang and Zou, 2014). It is likely to continue to be the dominant method of Earth monitoring in the future when geoengineering might be deployed. Radiosondes and satellite-borne infrared sounders are also often used for atmospheric temperature monitoring, but the former suffer from limited spatial sampling while the latter are sensitive to cloud and aerosol contamination.

This chapter seeks to answer the following research questions:

1. What vertical temperature responses do geoengineering aerosols and greenhouse gases produce in CMIP5 models?

2. Would the inclusion of the vertical structure of equivalent AMSU-A temperatures lead to earlier global, hemispheric or tropical detection of the SAI signal than is possible at the surface?

3. How could we best make use of AMSU-A channels for geoengineering detection?

5.2   Vertical temperature patterns of SAI and RCP4.5

As with near-surface air temperature that was studied in the previous chapters, tropospheric and stratospheric temperatures under the influence of hypothetical sulphate aerosol geoengineering can only be simulated by climate models. This section looks at the responses of the vertical temperature structure in the 5 climate models that have been included in the detection studies in this thesis, in the RCP4.5 and G4 scenario, respectively.

Figure 5.1 shows the vertical profiles of ensemble-mean zonal-mean atmospheric temperature averaged over 2020–2029 (the first decade of SAI in G4) relative to the corresponding average in 2006–2019 (the 14 years preceding geoengineering deployment in G4) in RCP4.5 (top panel) and G4 (middle panel). The reference period upon which temperature anomalies are calculated, i.e. 2006–2019, is the same throughout this thesis for direct comparison of results. The bottom panel of Figure 5.1 shows the atmospheric temperature changes introduced by SAI to the background climate, i.e. G4 - RCP4.5, over the first decade of geoengineering implementation in G4.

The solid line on each figure in the top and middle panels indicates the ensemble-mean zonal-mean thermal tropopause height during 2020–2029 in the corresponding climate model and scenario. The ensemble-mean zonal-mean thermal tropopause height in G4 during 2020–2029 in the corresponding climate model is plotted on the graphs in the bottom panel. The tropopause height is determined from gridded model atmospheric temperature output using Reichler et al. (2003)'s algorithm, in which interpolation is performed to compensate for the coarse vertical resolution of the data, before zonal means are calculated. The algorithm uses the World Meteorological Organization (1957)'s lapse rate definition, i.e. "the lowest level at which the lapse rate decreases to $2\,^{\circ}\mathrm{C}\ \mathrm{km}^{-1}$ or less, provided that the average lapse rate between this level and all higher levels within 2 km does not exceed $2\,^{\circ}\mathrm{C}\ \mathrm{km}^{-1}$", to identify the pressure at which the tropopause sits.
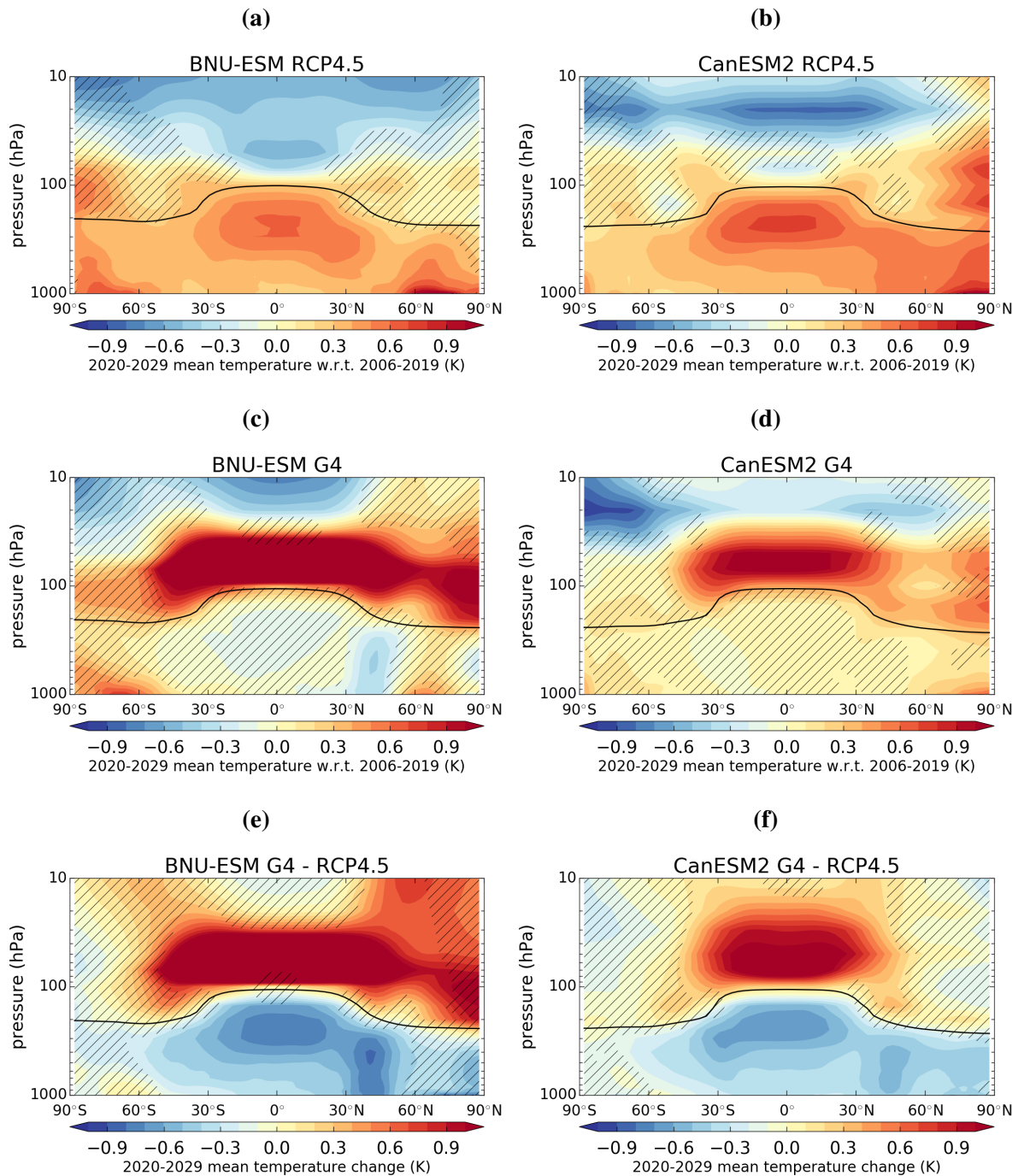
Figure 5.1 Zonal mean air temperature averaged over 2020–2029 relative to the 2006–2019 mean in the (top panel) RCP4.5 and (middle panel) G4 scenarios. The bottom panel shows the 2020–2029 mean atmospheric temperature change between G4 and RCP4.5. Data shown on the graphs are generated from (left panel) BNU-ESM and (right panel) CanESM2. The solid lines in the top and middle panels indicate the corresponding 2020–2029 climatological thermal tropopause in each of the climate model and future scenario. The 2020–2029 climatological thermal tropopause in G4 is shown in the corresponding graphs in the bottom panel. Hatching indicates insignificant temperature change ($p \geq 0.05$) from inter-annual internal temperature variability. Figure continued overleaf.
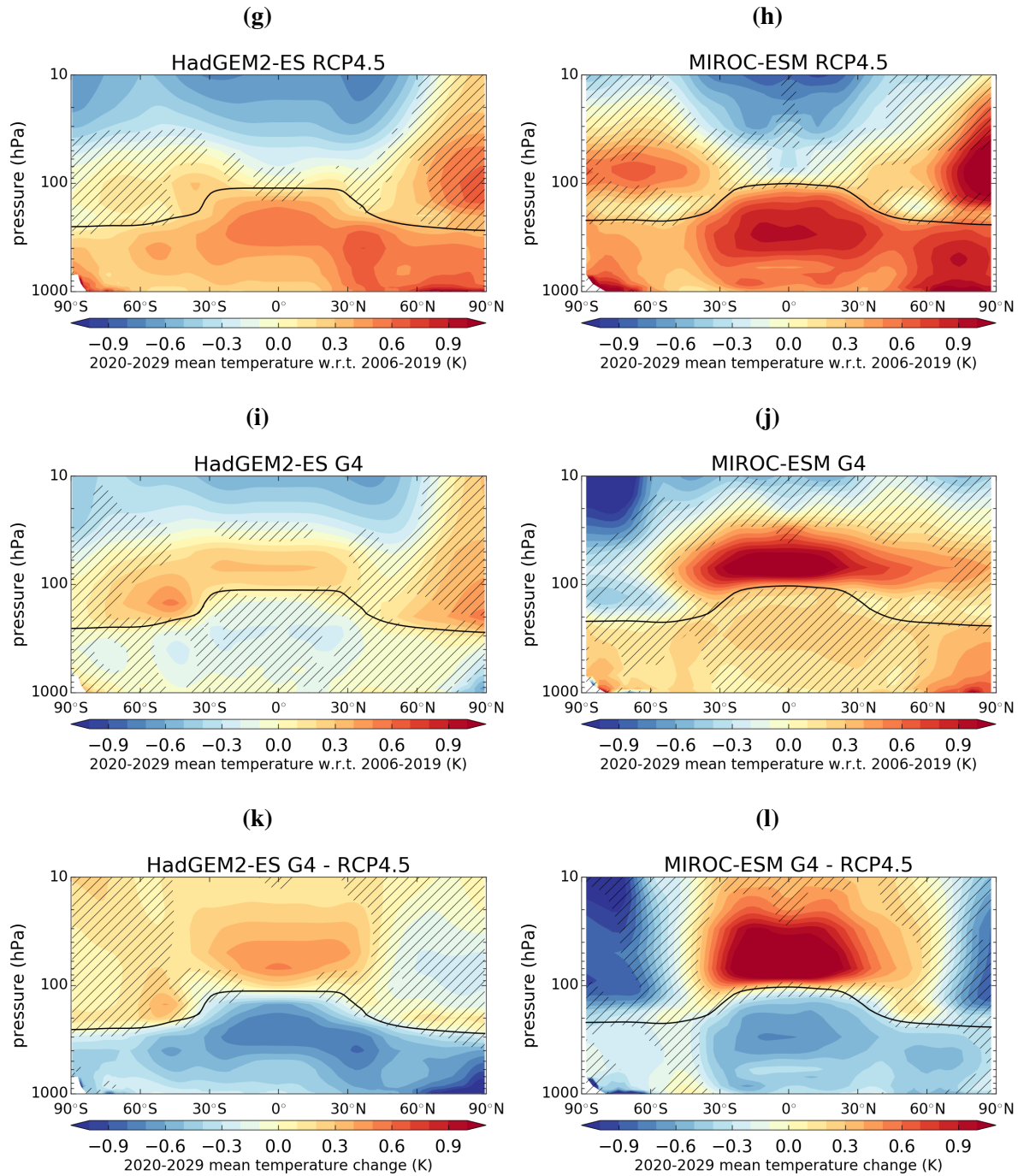
Figure 5.1 continued from the previous page, but for (left panel) HadGEM2-ES and (right panel) MIROC-ESM. Figure continued overleaf.

(m)

(n)

(o)
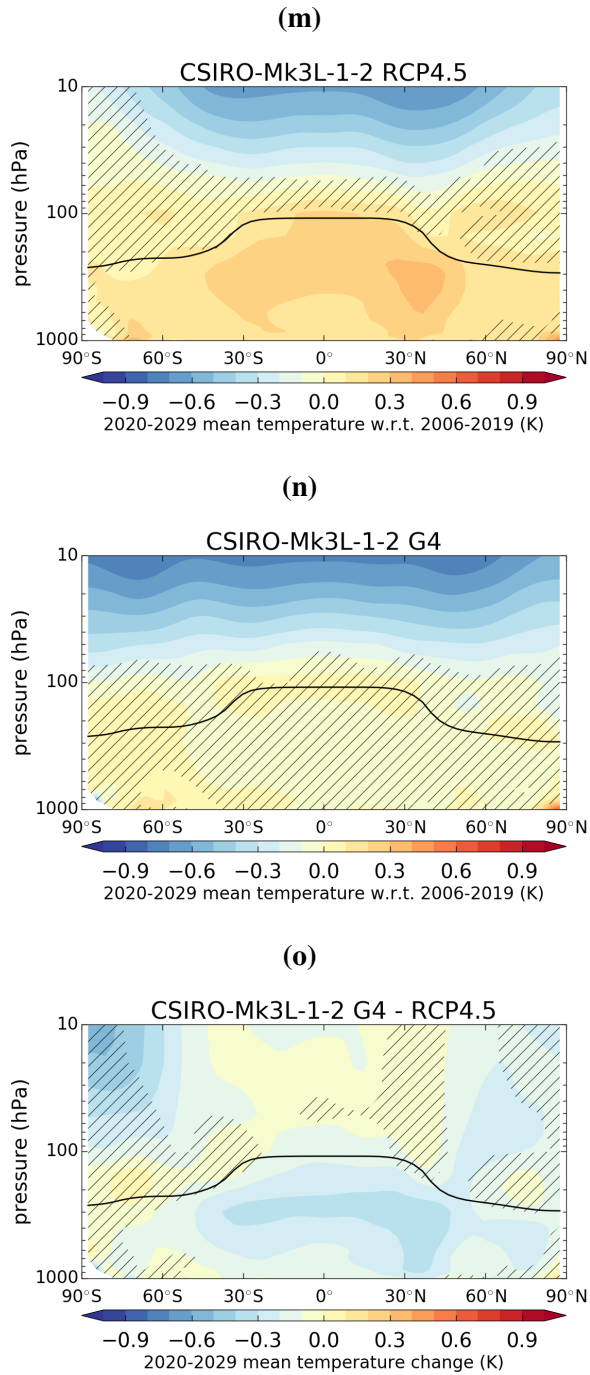
Figure 5.1 continued from the previous page, but for CSIRO-Mk3L-1-2.

The tropopause height is determined here because differing positions of the tropopause between the models, if present, may produce different vertical temperature structures even under the same forcing scenarios. This, or potential changes of the tropopause height in the RCP4.5 and G4 experiments, may lead to suboptimal estimation of tropospheric and stratospheric temperatures with the selected AMSU-A channels, adding uncertainty to the geoengineering detection analysis.

As can be seen from Figure 5.1, the climatological height of the tropopause is very similar in both scenarios and among the climate models. Tropopause height changes that are unresolved at the coarse model vertical resolution might occur because of temperature changes induced by greenhouse gases and geoengineering aerosols, but this is out of the scope of this project. At the broad vertical scale that this chapter focuses on, it is assumed that the uncertainty in detecting the SAI pattern in the vertical temperature profile due to tropopause height changes is negligible.

Hatching on the graphs shown in Figure 5.1 indicates latitudes and pressure levels at which the displayed mean atmospheric temperature anomaly in RCP4.5 or G4, or atmospheric temperature change between G4 and RCP45, is not significantly different from the respective mean inter-annual internal temperature variability simulated in the pre-industrial control run by the same model. The statistical hypothesis test used is the Welch's t-test (Welch, 1947), and the temperature anomaly is deemed significant where the two-tailed p-value is smaller than 0.05.

In the RCP4.5 scenario, all of the studied models show warming in the troposphere and cooling in the upper and tropical lower stratosphere in 2020–2029 relative to 2006–2019, as one would expect from increasing anthropogenic greenhouse gas concentrations. In particular, warming in the troposphere is statistically significant from internal variability in all latitudes and models, whereas significant cooling is simulated in the upper stratosphere in the models in almost all latitudes except near the poles.

Due to inter-model differences in climate processes and feedbacks, the magnitude and spatial pattern of the change in atmospheric temperature in RCP4.5 are quite diverse among

the models. This suggests that model differences that are independent of geoengineering are non-negligible and would contribute to uncertainties in future climate change detection in any real-world implementation.

In the G4 scenario, tropospheric cooling is observed relative to RCP4.5 in the first decade of SAI at nearly all latitudes and altitudes in all models, as one would expect. The SAI cooling effect outpaces RCP4.5 warming in the low-latitude troposphere in BNU-ESM and HadGEM2-ES and (Figures 5.1c and 5.1i), leading to a net cooling effect in 2020–2029 with respect to 2006–2019. This is not seen in CanESM2, MIROC-ESM and CSIRO-Mk3L-1-2 (Figures 5.1d, 5.1j and 5.1n), however, which show a slightly warmer troposphere in 2020–2029 than in 2006–2019. This means the tropospheric cooling effect of constant injections of geoengineering aerosols is overwhelmed by the warming effect of increasing greenhouse gas concentration earlier into SAI implementation in these models.

Nevertheless, with geoengineering implemented to reduce global warming, the significantly warmed troposphere that would happen in RCP4.5 during 2020–2029 relative to 2006–2019 becomes statistically insignificant from internal variability in a large part of the troposphere in all models in G4, even though RCP4.5 warming outpaces SAI cooling in some of these models.

On the other hand, there are regions of cooling in the mid-latitudes in BNU-ESM and HadGEM2-ES, and warming in high latitudes in one or both Hemispheres in CanESM2 and MIROC-ESM in the troposphere in G4 that are statistically significant from internal variability. This suggests that although sulphate aerosol geoengineering was proposed to reduce the overall amount of global warming, it might not return climate to the natural state, but might rather introduce complex changes to atmospheric circulation. For instance, Ferraro et al. (2015) and Ferraro et al. (2014) found that SAI would add to the poleward shift of tropospheric midlatitude jets in winter and the weakening of tropical circulation caused by increasing greenhouse gas concentrations.

The tropical lower stratosphere is expected to warm from the absorption of incoming solar near-infrared radiation and outgoing terrestrial longwave radiation by geoengineering

aerosols. BNU-ESM, CanESM2, HadGEM2-ES and MIROC-ESM all exhibit stratospheric warming at low and middle latitudes in G4 during 2020–2029, as compared to the 14 years before geoengineering is deployed in G4. This means heating of the stratosphere due to geoengineering aerosols outweighs the countering cooling caused by increasing greenhouse gas concentrations during the first decade of SAI implementation in G4. However, the magnitude of tropical lower stratospheric warming ranges from ~ 0.3 K in HadGEM2-ES to ~ 1 K in the rest of the models. This could be due to different aerosol microphysics or radiative and dynamical treatments in the climate models.

As mentioned in Section 2.2.1, the climate models included in this thesis used different methods for implementing sulphate aerosol geoengineering, and have differing aerosol sizes due to different aerosol schemes within the models. In particular, sulphate aerosols generated in HadGEM2-ES are the smallest, and are about 2 to 5 times smaller than the aerosols in the other models.

To investigate the effect of sulphate aerosol sizes on radiative transfer in the atmosphere, Mie calculations are done for different sulphate aerosol size distributions using the Suite Of Community RAdiative Transfer codes based on Edwards and Slingo (SOCRATES) (Edwards and Slingo, 1996; Randles et al., 2013). By assuming spherical aerosols, the scattering and absorption efficiencies of the geoengineering aerosols in HadGEM2-ES and BNU-ESM are calculated with known complex refractive indices of 75% sulphuric acid (H_2SO_4) droplets from the World Meteorological Organization Radiation Commission (1986) and aerosol log-normal size distributions from Table 2.1. HadGEM2-ES and BNU-ESM are chosen here because they have the smallest (0.0065 μm (1.3), 0.095 μm (1.4)) and largest (0.426 μm (1.25)) sulphate aerosol sizes among the 5 models, respectively.

Figure 5.2 shows the scattering and absorption efficiencies of geoengineering sulphate aerosols in HadGEM2-ES (in red) and BNU-ESM (in blue), respectively. At wavelengths shorter than 0.5 μm, i.e. in the UV region and the blue end of the visible spectrum, a kilogram of HadGEM2-ES aerosols has a larger scattering cross-section than a kilogram of BNU-ESM

(a)   (b)
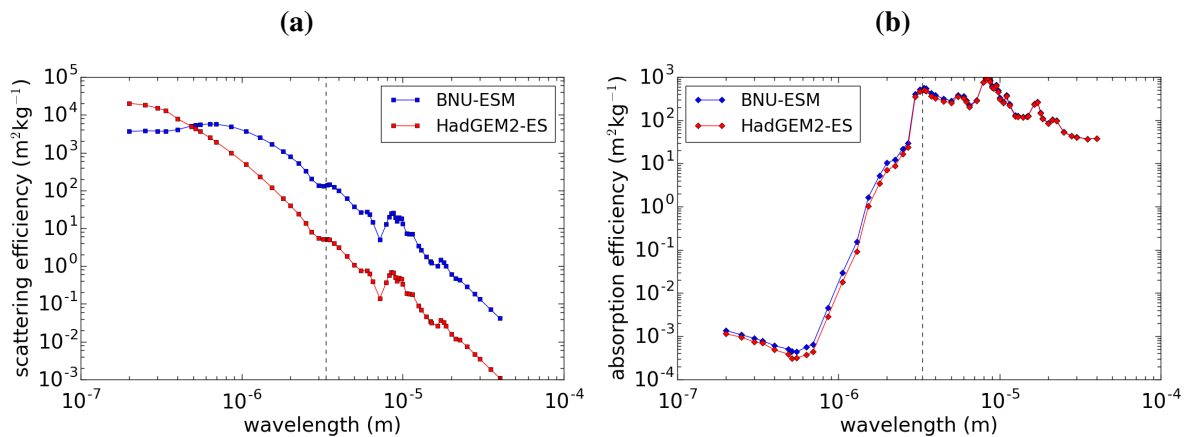
Figure 5.2 (a) Scattering and (b) absorption efficiencies of stratospheric sulphate aerosols in HadGEM2-ES (red colour) and BNU-ESM (blue colour), respectively. The dashed line at 3.33 μm marks the ending wavelength of the shortwave regime in the Edward and Slingo radiative transfer model.

aerosols. The reverse is true for longer wavelengths. Since the top-of-atmosphere solar irradiance peaks around 0.5 μm, but $\sim 50\%$ of the integrated solar irradiance is at wavelengths longer than 0.7 μm (Liou, 2002; Thuillier et al., 2003), the results suggest that the amount of solar radiation scattered by a unit mass of geoengineering aerosols is higher in BNU-ESM than in HadGEM2-ES.

The absorption efficiencies of the HadGEM2-ES and BNU-ESM aerosols are similar, with the larger aerosols in BNU-ESM being slightly more absorbing at wavelengths up to around 7 μm. This may explain the larger lower tropical stratospheric warming effect observed in Figure 5.1c than in Figure 5.1i.

Nevertheless, radiation attenuation by stratospheric aerosols is influenced not only by the size distribution, but also the mass burden of the aerosols, which is dependent on the lifetime of aerosols in the stratosphere. The lifetime of stratospheric aerosols is a balance between the rates of aerosol injection and aerosol loss through dry and wet deposition. The rate of dry deposition depends on the size, altitude and latitudinal extent of the aerosols. Larger aerosols, and aerosols that are injected to lower altitudes or higher latitudes settle out of the stratosphere more quickly.

As already shown in Figure 2.3, the stratospheric AOD (at 0.55 μm) prescribed in BNU-ESM is generally smaller than that generated in the HadGEM2-ES G4 simulations over 2040–2069. Since it is found here that, on average, a unit mass of stratospheric sulphate aerosols in BNU-ESM attenuate more radiation at 0.55 μm than those in HadGEM2-ES (Figure 5.2), the results imply a smaller sulphate aerosol burden in BNU-ESM than in HadGEM2-ES, over the period 2040–2069. This could be due to a shorter lifetime of the larger BNU-ESM aerosols.

Contrary to the other models, CSIRO-Mk3L-1-2 produces stratospheric cooling relative to RCP4.5 after geoengineering is turned on in G4. This is because geoengineering was simulated as reductions in solar irradiance in CSIRO-Mk3L-1-2. This had caused challenging detection of sulphate geoengineering's cooling effect in surface air temperatures with this model in previous chapters, and is likely to result in even larger uncertainties in the detection of the vertical temperature pattern caused by geoengineering aerosols. Niemeier et al. (2013) estimated that the atmospheric heating imbalance, defined as the difference between the changes in global-mean TOA and surface net radiative fluxes, in a scenario where total solar irradiance was reduced to balance the radiative forcing of RCP4.5, would be 0.37 W m^{-2} smaller than that of the equivalent SAI scenario. This was due to the lack of stratospheric heating response to solar dimming. Ferraro et al. (2011) also reported that modelling stratospheric aerosol geoengineering by turning the total solar irradiance down would be insufficient to capture the stratospheric heating effect of the aerosols. For this reason, this model will be excluded from the detection studies in this chapter.

The effects of 5 Tg yr^{-1} SO$_2$ injection on atmospheric temperature can be most clearly seen in the bottom panels of Figure 5.1. Statistically significant tropospheric cooling in low to 60 $^\circ$ latitude in both Hemispheres, as well as tropical warming in the lower stratosphere up to $\sim$ 30 hPa, are projected for 2020–2029 due to SAI in all models but CSIRO-Mk3L-1-2 (Figure 5.1o). The tropospheric cooling effect is the strongest in the Tropics mainly because insolation is high at low latitudes throughout the year, and the subsequent annual-mean radiative cooling through scattering of shortwave radiation by geoengineering aerosols is strongest in this region.

In BNU-ESM and MIROC-ESM, the strong tropical tropospheric cooling response may be in part due to the relative equatorial peak in their prescribed stratospheric AOD (Figure 2.3e). Note, however, that the prescribe AOD also features similar peaks at high latitudes, and that CanESM2 prescribed a constant field of AOD, HadGEM2-ES's internally generated AOD peaks around 70 °N and 50 °S (Figure 2.3e), whereas CSIRO-Mk3L-1-2 turned down the solar irradiance (Section 2.2.1); hence the maximum tropical tropospheric cooling due to SAI is mainly due to a larger annual amount of solar radiation being scattered in the Tropics than the rest of the world, but not the latitudinal distribution of the aerosols or AOD.

Results in this section have shown that simulations from the CMIP5 models included in this study are in agreement with post-volcanic observations and Tilmes et al. (2009)'s results on the broad vertical temperature structure under the influence of stratospheric sulphate aerosols and increasing greenhouse gas concentrations. The large-scale vertical temperature patterns in G4 and RCP4.5 are indeed distinctive and, therefore, likely to be easily distinguished from one another. The t-tests also suggest that the tropospheric warming and upper stratospheric cooling responses in RCP4.5, and the aerosol-induced tropospheric cooling and tropical lower stratospheric warming in G4 during 2020–2029 are statistically significant from internal variability. 5 Tg yr^{-1} SAI from 2020 would reduce tropospheric warming caused by increasing greenhouse gas concentrations to warming that is statistically insignificant from internal variability, or even return the troposphere to a cooler temperature than the 2006–2019 mean.

However, there are clear inter-model differences that are independent of geoengineering, in addition to geoengineering related differences arising from different SO_2 injection or SAI representation strategies resulting in effectively different distributions of aerosol mass, and different aerosol optical and microphysical properties within the models. This could delay the detection of the vertical temperature pattern of geoengineering. The following sections will investigate the detectability of the effects of sulphate geoengineering in vertical temperature profiles observed by satellites, as satellite observations have been, and will likely continue to be, the dominant way of atmospheric temperature monitoring.

5.3 AMSU-A for atmospheric monitoring

5.3.1 AMSU-A

The Advanced Microwave Sounding Units Version A (AMSU-A) is a series of microwave sounding instruments flown on polar-orbiting weather satellites that began operation in 1998 (Wang and Zou, 2014). They are cross-track scanning total power microwave sounders that make measurements of microwave radiance in 15 channels of frequencies ranging from 23.8 to 89 GHz (NASA Goddard Earth Science Data and Information Services Center, 2002). Figure 5.3 shows the representative weighting functions of these 15 channels at nadir view, which are provided by the UK Met Office based on the 1976 U.S. standard atmosphere.

In particular, AMSU-A channels 3 to 14 measure thermal emission from oxygen molecules between 50 and 60 GHz, and are primarily used for atmospheric temperature retrieval. Since atmospheric absorption by oxygen molecules generally increases with electromagnetic radiation frequency in the 50–60 GHz band (Mears and Wentz, 2009; Meeks and Lilley, 1963), channels that measure frequencies toward the 50 GHz end are sensitive to atmospheric layers that are closer to the Earth's surface, whereas channels that measure frequencies toward the 60 GHz end are sensitive to the upper layers of the atmosphere. As such, AMSU-A channels 3 (centred at 50.3 GHz) to 14 (centred at 57.29 GHz) (Wang and Zou, 2014) span the surface through the top of stratosphere (Figure 5.3).

AMSU is the successor of the Microwave Sounding Units (MSU), which operated between 1978 and 2006 for atmospheric temperature observation (Wang and Zou, 2014). Although the AMSU-A instruments make temperature measurements in a larger number of channels that sample the atmosphere at a higher vertical resolution than the MSU, channels 5, 7 and 9 of AMSU-A (bold lines in Figure 5.3) are equivalent to channels 2, 3 and 4 of MSU, making long-term satellite-based tropospheric and stratospheric temperature records available for climate research (Mears and Wentz, 2009).
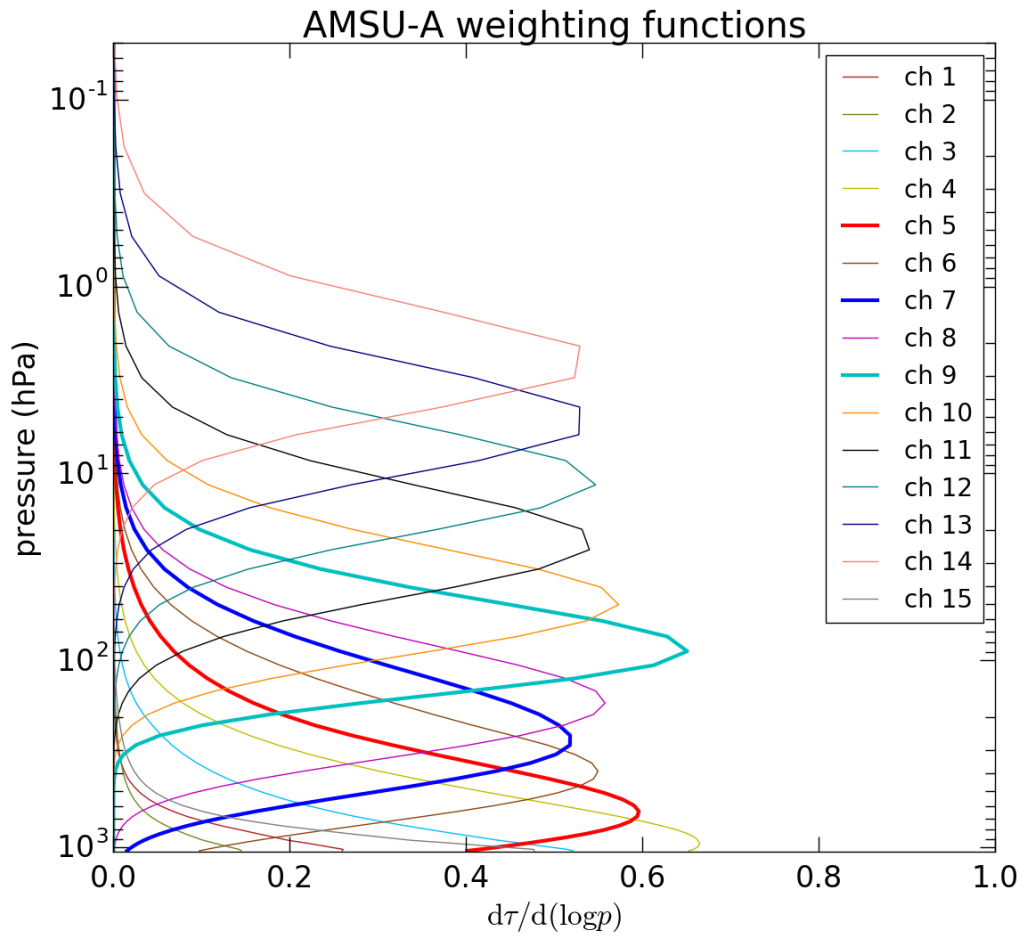
Figure 5.3 Weighting functions for AMSU-A channels 1 to 15, simulated on 54 pressure levels under the US76 standard atmosphere at nadir view. The bold red, blue and cyan lines indicate the weighting functions of channels 5, 7 and 9, which are the channels included in the vertical detection study in this chapter. The weighting functions were simulated and provided by the UK Met Office.

The rest of this chapter focuses on detecting the influence of G4 geoengineering aerosols on the vertical temperature profile comprising AMSU-A measurements from channels 5, 7 and 9, which correspond to the middle troposphere, the upper troposphere and the lower stratosphere, respectively. These channels are chosen because they span the altitudes where geoengineering aerosols have the largest temperature impacts (Figure 5.1), and they have longer observational records from MSU than the other channels.

5.3.2   Equivalent AMSU-A temperatures

In order to compare AMSU-A pseudo-observations with climate model simulations for detection purposes, model atmospheric temperature output is converted into mean deep-layer temperatures equivalent to those estimated by AMSU-A using a static, global-mean weighting function for each of the channels 5, 7 and 9 (Figure 5.3). The approach described in Santer et al. (1999) is used to compute equivalent satellite temperatures.

AMSU-A weighting functions are described by normalised weights at 54 discrete pressure levels, whereas the models have atmospheric temperature data at $n_z =17$ (HadGEM2-ES and BNU-ESM), 22 (CanESM2) and 35 (MIROC-ESM) pressure levels. For each climate model and AMSU-A channel, c, pressure boundaries are defined so that a mean weight, $\bar{W}(c,z)$, can be computed for each model pressure level, z, from one to a few weights whose pressure levels are within the boundaries. The equivalent AMSU-A temperature at longitude x, latitude y, year t and channel c is then:

$$\hat{T}(x,y,t,c) = \frac{\sum\limits_{z=1}^{n_z} T(x,y,z,t)\bar{W}(c,z)}{\sum\limits_{z=1}^{n_z} \bar{W}(c,z)} \tag{5.1}$$

Depending on the detection diagnostic, ensemble-mean area-weighted global, hemispheric or tropical mean AMSU-A equivalent temperature is then calculated from $\hat{T}(x,y,t,c)$ for each included channel. The temperature anomalies with respect to the corresponding 2006–2019 mean are calculated, and the resulting time series of each of the channels is smoothed by

a 14-year wide moving $C1$ filter, as was done in previous chapters, before they are spliced into vertical-temporal pseudo-observations and fingerprints as inputs to the multi-variate TLS detection algorithm.

Figure 5.4 shows the time evolution of the $C1$-filtered, ensemble-mean global-mean equivalent AMSU-A temperature anomalies in channels 5, 7 and 9 in the RCP4.5 and G4 scenarios. The time series shown are computed from HadGEM2-ES and BNU-ESM because these two models show the weakest and strongest stratospheric heating responses during the first decade of SAI among the models used (Section 5.2). The other models show similar trends but with different magnitudes.

Despite model differences, Figures 5.4a and 5.4c show a clear warming trend in the middle (channel 5) and upper troposphere (channel 7) in the RCP4.5 scenario. The BNU-ESM time series are noisier than those of HadGEM2-ES in general because BNU-ESM has only one ensemble member for both scenarios.

No noticeable trend is observed in the global-mean lower stratosphere (channel 9) in HadGEM2-ES or BNU-ESM. This is likely to be the result of averaging greenhouse gas forced lower stratospheric cooling and high internal variability in the mid to high latitudes (e.g. Figures 5.1g and 5.1a). These results suggest that the vertical temperature structure of RCP4.5 seen in Figure 5.1 is broadly captured in AMSU-A channels 5, 7 and 9, and that this vertical structure persists throughout the period 2020–2049.

For the G4 scenario, initial cooling and subsequent warming is seen in channel 5 in both models (Figures 5.4b and 5.4d). This temporal evolution is similar to the ones observed in global-mean SAT in various models (Figure 2.2). The temperature time series in channel 7 are very similar to their respective channel 5 series in both models, as channel 7 peaks at 236 hPa (Figure 5.3), which is below the tropopause. A small, initial warming is captured in the BNU-ESM series because some weight is given to the lowermost stratosphere in channel 7, and that pronounced stratospheric heating response to geoengineering aerosols is simulated in BNU-ESM.
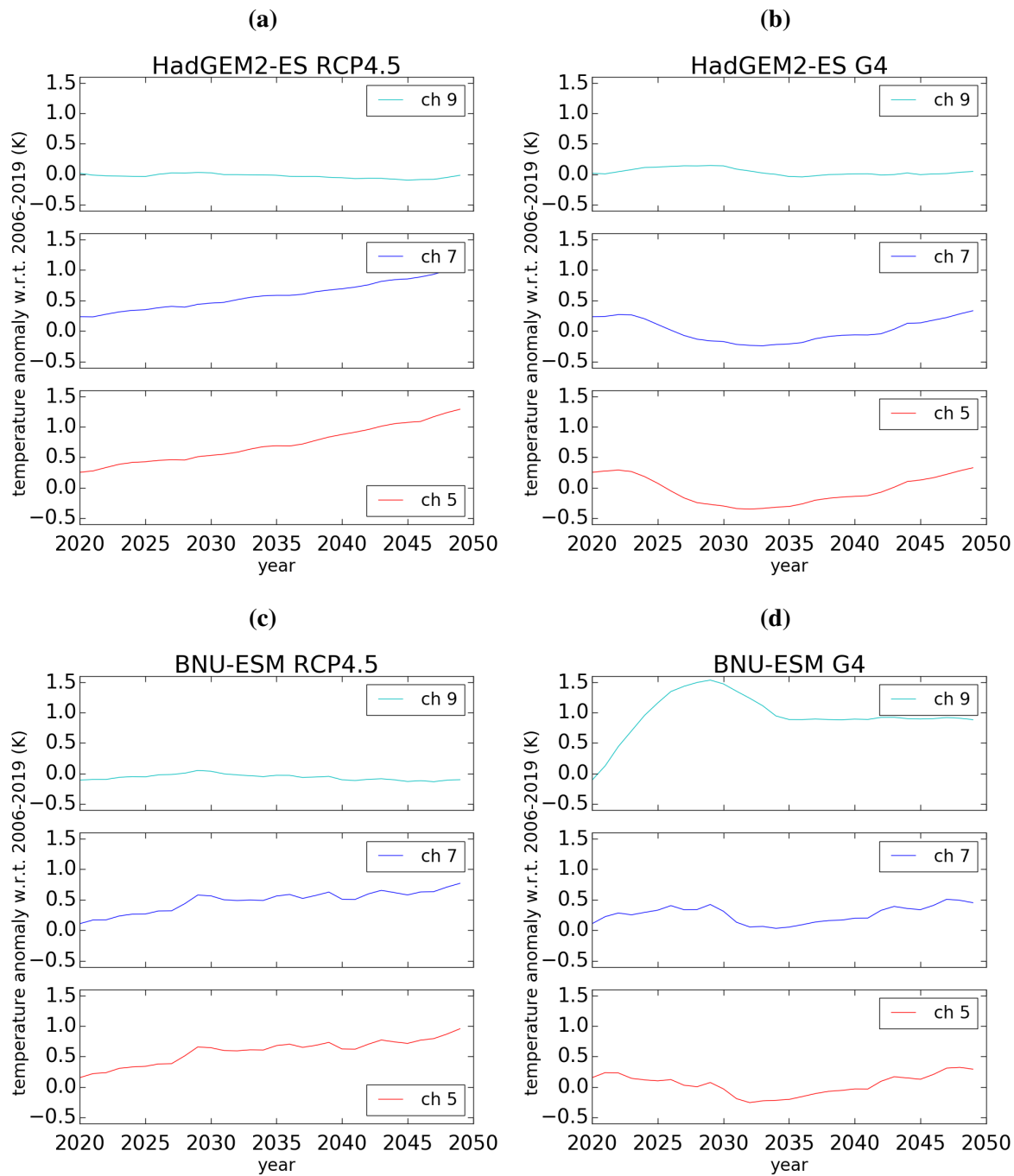
Figure 5.4 Ensemble-mean global-mean equivalent AMSU-A temperature anomalies during 2020–2049 in channels 5, 7 and 9, computed from HadGEM2-ES and BNU-ESM simulations using global static weighting functions. The left panel shows the temperature time series in the RCP4.5 scenario, whereas the right panel shows the temperature time series in G4. The BNU-ESM time series are noisier because this model has only one realisation in each scenario. All time series are $C1$ filtered.

Lower stratospheric temperature captured in channel 9 increases very slightly in the first decade of geoengineering in HadGEM2-ES, bringing the temperature to slightly above the 2006–2019 level. Since channel 9 of AMSU-A has a tail that extends up to ~ 3 hPa (Figure 5.3), upper stratospheric cooling caused by greenhouse gases is also captured in this channel. This may have further weakened the warming signal one might expect to see in channel 9, especially when lower stratospheric warming is already weak in HadGEM2-ES (Figure 5.4b). After slight initial warming, slight cooling occurs between 2030 and 2035, followed by temperatures that remain around the 2006–2019 average until 2049.

BNU-ESM, on the other hand, shows a different temperature trajectory in channel 9. Lower stratospheric temperature increases drastically in BNU-ESM after SAI deployment, peaking at ~ 1.5 K above the 2006–2019 mean just before 2030. This heating response is much stronger than that captured in channel 9 for HadGEM2-ES, consistent with the model differences shown in Section 5.2. The degree of stratospheric warming then decreases rapidly in the 5 years that follow, and remains relatively constant after 2035. At the end of the first 30 years of SAI, global-mean temperature in the lower stratosphere stays at about 1 K above the 2006–2019 mean in BNU-ESM.

CMIP5 models were required to interpolate air temperatures to 17 standard pressure levels ranging from 1000 to 10 hPa (Taylor and Doutriaux, 2010). Atmospheric temperatures on portions of pressure surfaces that are underground are marked as missing in HadGEM2-ES and MIROC-ESM, whereas underground data are available in BNU-ESM and CanESM2 via interpolation. All relevant data, including those underground where available, are taken into account when computing global, hemispheric and tropical mean temperatures in this chapter. This is because for both BNU-ESM and CanESM2, there is only $\sim 1\%$ difference in the resulting mean temperature when grid points that have a surface pressure below 1000 hPa are masked, and $\sim 0.2\%$ difference when grid points whose surface pressure is below 925 hPa (second standard pressure level in CMIP5) are masked. Given the relatively low weighting of the surface layers in the chosen AMSU-A channels, the effect of underground data on the detection results is assumed to be negligible.

5.4 Geoengineering detection in AMSU-A vertical temperature profiles

5.4.1 Global detection

As with previous chapters, the period of study is progressively lengthened from the first 5 to 30 years of geoengineering in G4 at 5-year intervals until the climate pattern, in this case the vertical atmospheric temperature pattern, of geoengineering is detected in the pseudo-observations at the 10% significance level.

Table 5.1 shows the time horizons estimated for the SAI fingerprint to be robustly detected in plausible pseudo-observations that comprise the time evolution of global-mean equivalent AMSU-A temperature in channels 5, 7 and 9. Without CSIRO-Mk3L-1-2, the sampling size of pseudo-observation model comparison is reduced to 24. The effect of SAI on the vertical temperature structure would be detected within a decade in *all* of these comparisons: 22 comparisons would result in robust detection of the SAI signal 5 years into geoengineering deployment in G4, whereas the remaining 2 comparisons would result in SAI detection 10 years into deployment.

Without the vertical temperature information, the global-mean surface cooling effect of geoengineering sulphate aerosols would be detected in only 11 and 7 of the 24 comparisons that exclude CSIRO-Mk3L-1-2 in the first 5 and 10 years of implementation, respectively (Section 3.2.1). The near-global or global-mean surface diagnostic was found to give the highest number of 5-year, as well as within-a-decade, SAI detections among all spatial scales (Section 4.8). By adding the vertical dimension of deep-layer atmospheric temperature that spans the troposphere through the stratosphere to the global-mean detection diagnostic, not only does the number of 5-year SAI detections double, but also the total number of within-a-decade detections increases from 18 to 24. This indicates that the tropospheric cooling and stratospheric warming effects

model-simulations				
	HadGEM2-ES (3)	CanESM2 (3)	BNU-ESM (1)	MIROC-ESM (1)
HadGEM2-ES r1		5	5	10
HadGEM2-ES r2		5	5	5
HadGEM2-ES r3		5	5	10
CanESM2 r1	5		5	5
CanESM2 r2	5		5	5
CanESM2 r3	5		5	5
BNU-ESM r1	5	5		5
MIROC-ESM r1	5	5	5	

(The leftmost vertical label reads "pseudo-observations".)

Table 5.1 Estimated time horizons for the SAI fingerprint to be detected at the 10% level in global-mean vertical-temporal equivalent AMSU-A temperature that comprises channels 5, 7 and 9. Each row represents a plausible vertical temperature profile observable with AMSU-A under the G4 scenario, and each column represents a different climate model for fingerprints simulation. Numbers in brackets are the number of ensemble members included when generating the fingerprints.

147
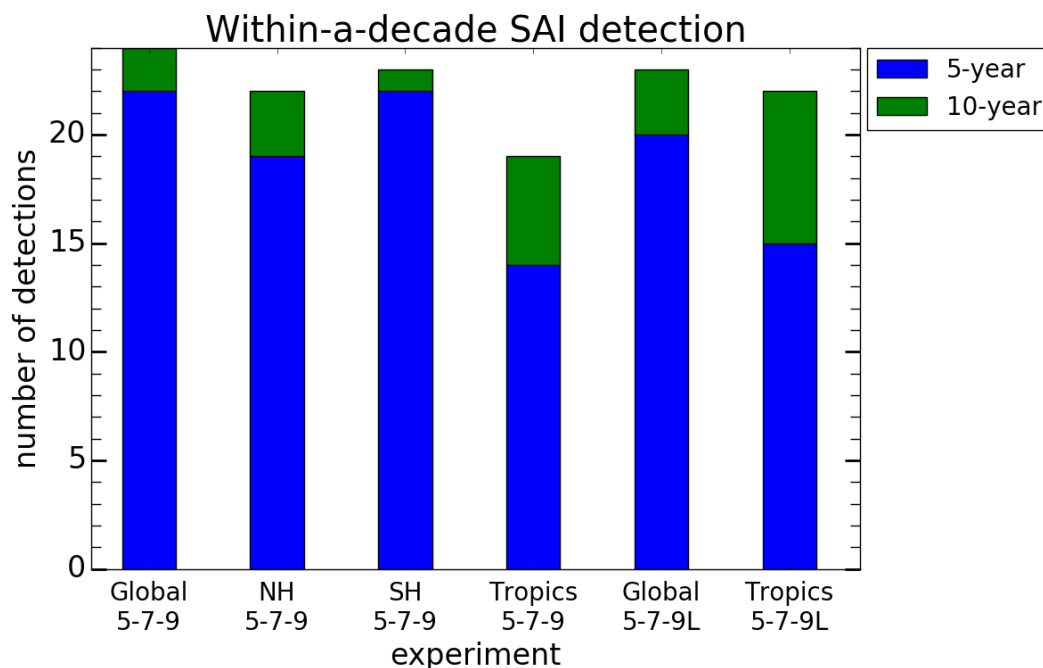
Figure 5.5 The number of successful within-a-decade SAI detections in the vertical temperature profile consisting of AMSU-A channels 5, 7 and 9 (first 4 bars from the left) or 5, 7 and effective channel 9L (the 2 bars from the right, please refer to Section 5.5 for these 2 experiments) in this chapter. The same 24 pseudo-observations model comparisons are done in each experiment. Blue colour represents the number of 5-year detections (detections by 2025) while green colour represents the number of 10-year detections (detections that happen between 2025 and 2029).

of geoengineering aerosols do provide vital information for early geoengineering detection on the global scale.

5.4.2 Hemispheric and tropical detection

In addition to the global scale, geoengineering detection in the vertical temperature structure consisting of AMSU-A channels 5, 7 and 9 is done in the Northern Hemisphere, Southern Hemisphere and the Tropics (25 °N to 25 °S), akin to the surface detection experiments presented in Section 4.3. Figure 5.5 shows the number of 5- and 10-year SAI detections among the same 24 comparisons as shown in Table 5.1 on these scales. As before, the detection horizons are estimated at 5-year resolution and at the 10% significance level.

In the Northern Hemisphere, the effect of geoengineering on the vertical temperature structure would be detected in 19 and 3 pseudo-observation model comparisons 5 and 10 years into SAI implementation in G4, respectively. In the Southern Hemisphere, the corresponding SAI signal would be detected in 22 comparisons during the first 5 years of geoengineering implementation, and 1 comparison in the 5 years that follow. The within-a-decade SAI detectability is all similarly high at the global scale and in both Hemispheres. This was not seen in the surface detection results (Section 4.3), in which the within-a-decade SAI detectability varied hugely between the Northern and Southern Hemispheres.

Moreover, there is a significant increase in the number of within-a-decade SAI detections in both Hemispheres as the detection diagnostic changes from SAT to the vertical temperature structure. There were only 10, 5-year and 5, 10-year SAI detections among the comparisons that exclude CSIRO-Mk3L-1-2 in Northern Hemisphere SAT, and 0, 5-year and 7, 10-year SAI detections in Southern Hemisphere SAT. These results not only suggest that the vertical information of atmospheric temperature would be useful for early geoengineering monitoring in both Hemispheres as well as over the whole globe, but also that the additional information in the vertical dimension may compensate for some of the increased climate noise as the horizontal scale of detection is reduced by half.

In the Tropics, 14 of the 24 comparisons would take 5 years, whereas 5 other comparisons would need 10 years from the start of geoengineering in G4 for the SAI influence on the vertical temperature structure to be detected. This is, again, an improvement from the corresponding detection results on the surface, in which 6, 5-year and 3, 10-year SAI detections were found in the same comparisons. Nevertheless, there is a noticeable drop in the within-a-decade SAI detectability as detection is moved from the global or hemispheric vertical temperature structure to the Tropics. This may be in part due to increased noise in the pseudo-observations as the horizontal scale of study reduces to the tropical band, and in part due to pronounced inter-model differences in the degree and meridional extent of stratospheric warming in low latitudes (Figure 5.1).

7 of the 8 detection horizons that are estimated to be longer than 10 years in the global, hemispheric and tropical vertical-temporal detection experiments come from comparisons that use a G4 realisation of HadGEM2-ES as the pseudo-observations (not shown). This is likely to be because HadGEM2-ES simulates the weakest stratospheric warming response, and that this small warming signal is overwhelmed by the large cooling response of the upper stratosphere (above 30 hPa) to greenhouse gases when the deep-layer temperature for channel 9 is computed (Figure 5.1i and Section 5.3.2). Vertical-temporal geoengineering fingerprints that consist of tropospheric cooling of a similar magnitude but significantly stronger stratospheric warming have to be scaled down to match the HadGEM2-ES pseudo-observations, leading to a near-zero scaling factor whose noise uncertainty range includes zero in some cases. As such, the null hypothesis has to be accepted until the geoengineering pattern can be detected at longer timescales.

This means if the real-world stratospheric temperature response to geoengineering aerosols were more similar to the HadGEM2-ES simulations than to the other models, periods longer than a decade might be needed for the SAI influence to be detected in the vertical temperature structure. As discussed in Section 5.2, the real-world stratospheric response to geoengineering aerosols would depend strongly on the size distribution and lifetime of the aerosols. It is likely to be the case that smaller sulphate aerosols (such as the ones internally generated in HadGEM2-ES) would be favoured in the event of sulphate aerosol geoengineering because of the following reasons.

Sulphate aerosols that are smaller than volcanic aerosols are more effective in cooling the planet because they scatter more incoming shortwave radiation per unit mass (in particular in the UV and blue end of the visible regime, Figure 5.2a), and they have longer lifetimes in the stratosphere due to a slower particle settling speed than larger, volcanic-like particles (Rasch et al., 2008a). Smaller particles also absorb less in the infrared regime, producing a smaller adverse radiative heating effect in the lower stratosphere.

Deliberate injections of sulphate particles that are smaller than volcanic aerosols could potentially be achieved by direct emissions of sulphuric acid vapour from aircrafts (Pierce et al., 2010). This might result in real-world atmospheric temperature observations that resemble the HadGEM2-ES simulations, but are noticeably different from the climate model simulations that relied on the AOD data from the Pinatubo eruption. Similar to the results here, time periods longer than 10 years might be needed for the geoengineering fingerprint to be detected in the vertical temperature profile if the models used for fingerprint estimation generated or were prescribed with unrealistically large aerosols.

In other words, although large volcanic eruptions are the closest natural analogue to sulphate aerosol geoengineering and, thus, provide a starting point to constrain physical processes in relation to stratospheric sulphate aerosols in climate models and to test model simulations against the real world (e.g. Driscoll et al. (2012)), they are an imperfect analogue not only because volcanic eruptions are transient whereas geoengineering could be continual, but also because optimal solar radiation management may use sulphate aerosols that are appreciably smaller than volcanic aerosols, or even other aerosols that have a stronger impact on shortwave radiation (Ferraro et al., 2011).

Therefore, in order to be able to detect the geoengineering effect in the vertical temperature structure early into deployment, it would be critical for us to be able to measure the real-world evolution of the optical and microphysical properties of the aerosols, and to develop climate models that inject, generate and transport or prescribe geoengineering aerosols of realistic properties in a manner that is close to the real world, whatever it might be.

5.5 Can we improve the detection?

5.5.1 Effective AMSU-A channel 9L

It was mentioned in Section 5.3.2 and 5.4 that the tropical lower stratospheric warming caused by geoengineering aerosols in G4 could be diluted by the upper stratospheric cooling caused by increasing greenhouse gas concentrations in AMSU-A channel 9. If the real geo-engineered world turned out to produce a weak tropical lower stratospheric warming response to sulphate aerosols, one that is similar to the response in the HadGEM2-ES pseudo-observations, then we would need to see if there is a way to improve the detectability of such a response. This section investigates how minimising the upper stratospheric contribution to AMSU-A channel 9 by linearly combining the weighting functions of different channels would affect the global- and tropical-mean vertical-temporal detection results.

Fu and Johanson (2005) developed a technique to derive tropical tropospheric temperatures by linearly combining the weighting functions of different MSU channels. In their study, an effective weighting function was defined as $W_{ij} = a_{ij}W_i + (1 - a_{ij})W_j$, where W_i and W_j were physical weighting functions of MSU channels i and j, and a_{ij} was found by minimising $\int_{p_1}^{p_2} W_{ij}^2 dp$ between pressure levels p_1 and p_2 in hPa. By minimising $\int_0^{100} W_{24}^2 dp$ as well as $\int_0^{250} W_{23}^2 dp$, Fu and Johanson (2005) found $a_{24} = 1.1$ and $a_{23} = 1.69$ for deriving tropical temperatures in the entire troposphere and lower troposphere, respectively. The a_{24} they computed was consistent with the equivalent coefficient they derived with radiosonde data in an earlier study (Fu et al., 2004).

Here, the same technique is applied to AMSU-A weighting functions for the derivation of an effective weighting function, W_{9L}, where the contribution from 30 hPa or above to AMSU-A channel 9 is minimised. 30 hPa is chosen because it is the upper extent of geoengineering-induced stratospheric warming in the models (Figures 5.1i to 5.1j). Since AMSU-A channel 11 peaks just above 30 hPa, W_{9L} is derived from the physical weighting functions of AMSU-A

(a)

AMSU-A weighting functions

(b)

Effective weighting functions
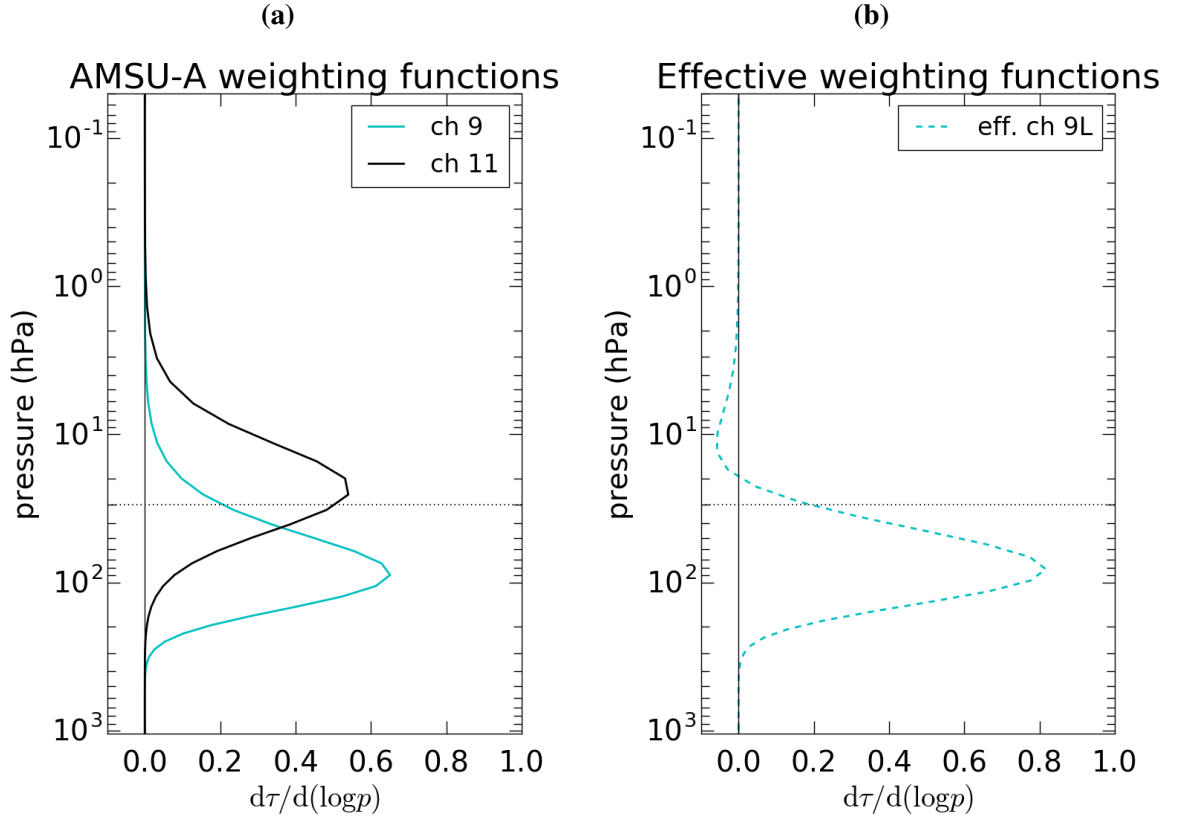
Figure 5.6 (a) Physical weighting functions of channels 9 and 11 of AMSU-A. They are the same as those shown for the same channels in Figure 5.3. (b) Effective weighting function of channel 9L derived in this thesis. This channel peaks at the same altitude as channel 9 but with more weight, and has minimal contribution from atmospheric layers above 30 hPa.

channels 9 and 11, W_9 and W_{11}. Figure 5.6a shows W_9 and W_{11}, with the dotted line indicating the 30 hPa level.

Minimisation of $F_{ij}(a) = \int_{p_1}^{p_2} W_{ij}^2 dp$ is done by equating $\frac{dF_{ij}(a)}{da}$ to 0 in this thesis:

$$
\begin{aligned}
F_{ij}(a) &= \int_{p_1}^{p_2} W_{ij}^2 dp \\
&= \int_{p_1}^{p_2} \left(a_{ij} W_i + (1 - a_{ij}) W_j \right)^2 dp \\
&= a_{ij}^2 \int_{p_1}^{p_2} W_i^2 dp + 2 a_{ij}(1 - a_{ij}) \int_{p_1}^{p_2} W_i W_j dp + (1 - a_{ij})^2 \int_{p_1}^{p_2} W_j^2 dp \\
&= a_{ij}^2 I_i + 2 a_{ij}(1 - a_{ij}) I_{ij} + (1 - a_{ij})^2 I_j
\end{aligned}
\tag{5.2}
$$

153

Coefficient a_{ij} is then:

$$\frac{dF_{ij}(a_{ij})}{da_{ij}} = 2a_{ij}I_i + 2(1 - 2a_{ij})I_{ij} - 2(1 - a_{ij})I_j \tag{5.3}$$

$$= 0$$

$$a_{ij} = \frac{-I_{ij} + I_j}{I_i - 2I_{ij} + I_j} \tag{5.4}$$

where $I_i = \int_{p_1}^{p_2} W_i^2 dp$, $I_{ij} = \int_{p_1}^{p_2} W_i W_j dp$ and $I_j = \int_{p_1}^{p_2} W_j^2 dp$. Using Equation 5.4 and the physical weighting functions of MSU channels 2, 3 and 4 provided by the UK Met Office, $a_{24} = 1.1$ and $a_{23} = 1.69$ found in Fu and Johanson (2005) are exactly reproduced.

By substituting $W_i = $ AMSU-A W_9, $W_j = $ AMSU-A W_{11}, $p_1 = 0$ and $p_2 = 30$ into Equation 5.4, $a_{9,11}$, or a_{9L}, is found to be 1.29. Hence, the weighting function of the effective channel 9L is defined as:

$$W_{9L} = 1.29W_9 - 0.29W_{11} \tag{5.5}$$

Figure 5.6b shows W_{9L} at the same pressure levels as the original AMSU-A data. This linear combination of W_9 and W_{11} (Figure 5.6a) peaks at the same pressure level as channel 9 but has a heavier weight at the peak. The integrated influence of the upper stratosphere is effectively removed in channel 9L, which now has a negative contribution from above 20 hPa and positive contribution from the layer between 20 and 30 hPa. Negative atmospheric contribution to upwelling radiances is not physical, but it is common in effective weighting functions (e.g. Fu et al. (2004)) given the way they are derived.

The effective channel 9L, together with the original AMSU-A channels 5 and 7, will be used for detecting the geoengineering signal in the global- and tropical-mean vertical-temporal equivalent AMSU-A temperatures in the following sections.

5.5.2 Global detection

It is useful to visualise the changes effective channel 9L introduce to the RCP4.5 and G4 temperature time series in channel 9, and to check whether the upper stratospheric cooling contribution from elevated CO_2 concentrations is reduced in the newly-derived channel 9L. Figure 5.7a shows the $C1$ filtered, ensemble-mean global-mean equivalent AMSU-A temperature anomalies during 2020–2049 with respect to the 2006–2019 mean in the physical channel 9 (solid line) and the effective channel 9L (dashed line), respectively. As in Figure 5.4, time series computed from HadGEM2-ES (top panel) and BNU-ESM (bottom panel) are shown.

With minimal contribution from above 30 hPa, the temperature anomaly is higher over the whole period of 2020–2049 in both scenarios and in both climate models. This indicates that the upper stratospheric cooling contribution from increasing greenhouse gas concentrations is indeed reduced in effective channel 9L. HadGEM2-ES RCP4.5 temperature anomaly sees a maximum increase of ~ 0.2 K in 2049, whereas the G4 temperature anomaly in HadGEM2-ES, as well as both RCP4.5 and G4 anomalies in BNU-ESM, are increased by ~ 0.1 K at the end of the investigated period (note the different y-scales between the top and bottom panels). Nevertheless, despite the observed increase in magnitude of the temperature anomalies, there is trivial change in the temporal structure of the time series shown in Figure 5.7a.

Using the vertical-temporal temperature structure that includes global-mean equivalent AMSU-A deep-layer temperatures in channels 5, 7 and effective channel 9L as a diagnostic, the SAI signal would be detected in 20 (of the same 24) comparisons during the first 5 years of geoengineering implementation in G4. 3 other comparisons would take 10 years for the SAI influence to be detected. Compared to the global 5-7-9 experiment, the number of within-a-decade SAI detections is reduced by 1 (Figure 5.5). Nevertheless, the global-mean within-a-decade detectability of SAI remains very high in the vertical temperature structure regardless of the lower stratospheric channel used.
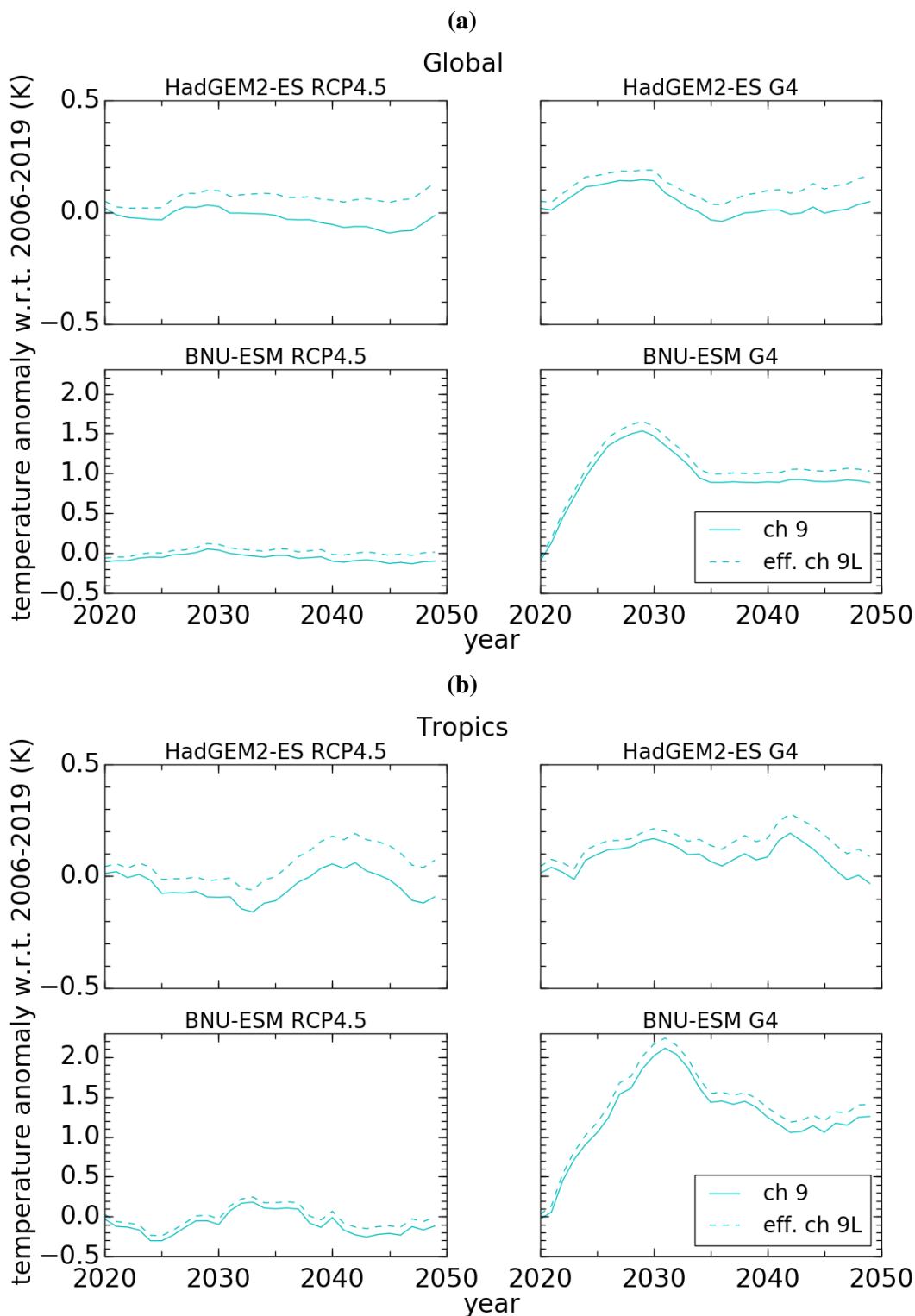
Figure 5.7 Ensemble-mean (a) global-mean and (b) tropical-mean equivalent AMSU-A temperature anomalies during 2020–2049 in physical channel 9 (solid line) and effective channel 9L (dashed line), computed from HadGEM2-ES and BNU-ESM simulations using the respective global static weighting functions. The left panel shows the temperature time series in the RCP4.5 scenario, whereas the right panel shows the temperature time series in G4. All time series are $C1$ filtered.

5.5.3 Tropical detection

Since the lower stratospheric warming response to geoengineering aerosols is mainly confined to low to mid latitudes (middle panel in Figure 5.1), the effect of minimal contribution from 30 hPa or above on the tropical (25 °N to 25 °S) temporal temperature anomalies in the effective channel 9L and, thus, the tropical vertical-temporal detection results are also investigated.

Figure 5.7b shows the ensemble-mean tropical-mean RCP4.5 and G4 atmospheric temperature anomalies in 2020–2049 relative to 2006–2019 in the AMSU-A physical channel 9 (solid line) and effective channel 9L (dashed line) from HadGEM2-ES and BNU-ESM. It is clear that in both scenarios and models, the channel 9 tropical-mean temperature time series are nosier than the corresponding global-mean time series (Figure 5.7a), even though all of them are C1 filtered. This explains why the tropical within-a-decade SAI detectability is lower than the global within-a-decade SAI detectability in the vertical temperature structure in the first place (Sections 5.4.1 and 5.4.2).

As with the global-mean effect, the channel 9L temperature anomalies are higher than those of channel 9 in all years between 2020 and 2049, in both RCP4.5 and G4 scenarios, and in both climate models. The use of channel 9L does not alter the temporal structure of the time series, but shifts its values up by ~ 0.1 to 0.2 K, with the largest shift occurring in 2049.

Detection of the SAI signal is claimed in 15 and 7 different pseudo-observation model comparisons in the first 5 and 10 years of geoengineering deployment in G4, respectively, in the vertical structure that includes tropical-mean equivalent AMSU-A temperatures of channels 5, 7 and 9L. This means the number of tropical within-a-decade SAI detections is increased from 19 to 22 as the newly-derived, effective weighting function 9L is introduced. The detection horizons are shortened from 30+, 15 and 20 years to 10 years in 3 comparisons whose pseudo-observations are represented by HadGEM2-ES simulations, respectively (not shown). The improved tropical SAI detectability is most likely to be the result of enhanced stratospheric warming response to geoengineering aerosols in G4 in the effective channel 9L. As such, the

SAI signal-to-noise ratio is also enhanced, enabling earlier SAI detection, particularly in the Tropics where climate noise is bigger than that at larger spatial scales.

Many other latitudinal bands and regions such as those studied in Chapter 4 could have been studied in this chapter, with additional vertical information of atmospheric temperature included in the detection diagnostic. The intention of this chapter was mainly to compare the detectability of the geoengineering effect on near-surface temperature and the broad vertical temperature structure. Given that the results above have already shown significant improvement in the within-a-decade SAI detectability at some of the large spatial scales which geoengineering has the highest detectability in near-surface temperature (please see Section 4.8), this chapter does not look beyond the global, hemispheric and tropical scales. Future work is recommended for investigating the detectability of SAI in regional vertical temperature profiles, and to explore detection possibilities using other AMSU-A channels, Earth monitoring instruments and climate variables.

5.6   Summary

This chapter has investigated the vertical temperature responses of CMIP5 climate models to increasing greenhouse gas concentrations in RCP4.5 and sulphate aerosol geoengineering in G4. The number of years needed (since SAI deployment in 2020 in G4) for the geoengineering vertical temperature pattern as if observed by AMSU-A to be detected at the 10% level was estimated at 5-year resolution. Detection experiments were done at the global, hemispheric and tropical scales, using the TfC1 detection method and different combinations of AMSU-A channels in 24 pseudo-observation model comparisons.

In answer to question 1 raised at the beginning of this chapter, all studied models, BNU-ESM, CanESM2, HadGEM2-ES, MIROC-ESM and CSIRO-Mk3L-1-2, simulated global tropospheric warming and upper stratospheric cooling in the RCP4.5 scenario during 2020–2029, with respect to 2006–2019. These results are consistent with the literature.

During the same time period, BNU-ESM, CanESM2, HadGEM2-ES and MIROC-ESM simulated a net, global tropospheric cooling response, and a stratospheric warming response slightly above the tropopause at low to mid latitudes, to geoengineering aerosols during the first decade of SAI in G4, as compared to the RCP4.5 base climate. These results are consistent with both observations of large volcanic eruptions and the simulations of Tilmes et al. (2009).

Nevertheless, inter-model differences were apparent among the zonal-mean vertical temperature profiles simulated by these 4 models in both scenarios. In particular, HadGEM2-ES simulated the weakest tropical lower stratospheric heating response in G4. CSIRO-Mk3L-1-2 was the only model that represented SAI by solar irradiance reduction in this thesis. It insufficiently simulated the stratospheric warming response to sulphate aerosols and, therefore, was not included in any vertical-temporal detection experiment in this chapter (Section 5.2).

With regard to question 2, the effect of stratospheric geoengineering aerosols would be detected in the global-mean vertical profile of equivalent AMSU-A temperatures from channels 5, 7 and 9 by 2029 in *all* of the 24 studied comparisons. The within-a-decade SAI detectability was similarly high in the Northern and Southern hemispheric vertical temperature structures. In the Tropics, 19 SAI detections would be claimed within the first decade of geoengineering in G4 (Section 5.4).

On all of these scales, there was an increase in the number of within-a-decade SAI detections from the corresponding detection results found with surface temperature. Hence, to answer question 2, the inclusion of the vertical structure of equivalent AMSU-A temperatures would indeed lead to earlier global, hemispheric and tropical detection of the SAI signal than on the surface. This suggests the importance of vertical temperature information in a detection diagnostic for geoengineering monitoring.

In answer to question 3, AMSU-A channels can be combined linearly to emphasise the temperature effect of SAI on certain atmospheric layers for earlier geoengineering detection. Effective channel 9L was derived from physical channels 9 and 11, in order to minimise greenhouse gas forced cooling from above 30 hPa (Section 5.5.1). Using the vertical tem-

perature structure consisting of channels 5, 7 and 9L, instead of 5, 7 and 9, as the detection diagnostic decreased the global-mean within-a-decade SAI detectability by 1, but increased the tropical-mean detectability by 3 (out of 24). All of the 3 improvements were found in comparisons that assumed HadGEM2-ES pseudo-observations. This indicates that such use of AMSU-A channels would be effective in improving the detectability of SAI in the Tropics, especially if the real-world stratosphere responded to geoengineering aerosols to a similar degree as the HadGEM2-ES simulations.

All in all, AMSU-A has been useful for atmospheric temperature monitoring since 1998, and it is likely to be able to provide important information for detecting and monitoring the effects of deliberately injected sulphate aerosols in the stratosphere on the vertical temperature structure, should that happen in the near future to counteract some of the anthropogenic warming in surface climate. Nonetheless, there are many other possibilities of effective geoengineering monitoring that have not been investigated in this thesis, including detection using other AMSU-A channels or other Earth monitoring instruments, and detecting the geoengineering effects in regional vertical temperature profiles and in other climate variables, leaving a lot of potential for related future work. Suggestions on future work can be found in Section 6.5.

Chapter 6

Conclusions and future work

6.1   Overview

Active research on stratospheric sulphate aerosol geoengineering has taken place over the last decade, as keeping global warming under control by rigorous greenhouse gas mitigation has seemed to be 'a pious wish' (Crutzen, 2006). Despite the effort that has gone into exploring the possibility and potential impacts of sulphate aerosol geoengineering, there are many outstanding questions about the effectiveness, technical feasibility, ethics and governance of this kind of geoengineering. Answers to these questions will be essential for future climate policymaking.

The aim of this thesis was to estimate the time horizon over which the temperature effects of 5 Tg yr^{-1} SO_2 injection would be detected amid the RCP4.5 background climate and internal climate variability in the GeoMIP G4 scenario. Through answering the questions of *when* we could detect the global-mean cooing effect of sulphate aerosol geoengineering, and *how* and *where* we could robustly detect temperature responses to sulphate aerosol geoengineering within a decade into implementation, this thesis provides insights into the prospect of developing an effective network for geoengineering monitoring and control.

Total least squares (TLS) detection and attribution algorithms were employed to search for model-simulated fingerprints of sulphate aerosol injection (SAI) and RCP4.5 in pseudo-observations projected by other climate models. The SAI detection horizon was estimated at 5-year resolution, by increasing the temporal length of the pseudo-observational and model data by 5 years at a time until the SAI fingerprint was detected at the 10% significance level.

This experimental procedure was applied to the mean near-surface air temperature on the global, hemispheric, and various latitudinal, continental and regional scales, as well as the spatio-temporal near-surface air temperature pattern across several regions constituting different continental areas, and the vertical temperature structure as if observed by the satellite-borne Advanced Microwave Sounding Units A (AMSU-A). These geoengineering detection experiments were designed with reference to the global (e.g. Allen et al. (2006)), regional (e.g. Stott et al. (2010)) and vertical (e.g. Santer et al. (2013)) perspectives of historical detection of anthropogenic climate change. Major results from these experiments are summarised in the following section.

6.2 Summary of results

6.2.1 Methods for geoengineering detection in global-mean temperature

The time horizon over which the global-mean surface cooling response to 5 Tg yr^{-1} SO$_2$ injection would be detected since implementation in 2020 in G4 was estimated in Chapter 3. The classical TLS algorithm (Tf) and a non-stationary variant of TLS (Bg) were used in conjunction with 4 different noise reduction techniques, i.e. no filter (No), a 14-year mean-based $C0$ moving filter (C0), a 14-year trend-based $C1$ moving filter (C1) or a 30-year trend-based $C1$ moving filter (C1(30)); and 2 global-mean detection diagnostics, i.e. since 2020 or 2000 (-2K), for detection purposes. The SAI detection horizon was estimated in 44

pseudo-observation model comparisons using each of these 7 unique detection methods. Key results are as follows:

- Detection of the global-mean cooling response to SAI would be possible within 30 years of deployment using all of the studied detection methods. The SAI detection horizon would depend strongly on the detection method used.

- The total number of 5- and 10-year (collectively known as 'within-a-decade') SAI detections out of 44 comparisons in descending order are: TfC1(30): 38, BgC1: 35, TfC1: 29, BgC0: 25, TfC1-2K: 24, and TfNo and TfC0: 11 each.

- Application of the $C1$ filter generally resulted in a higher number of within-a-decade SAI detections than using the $C0$ filter or no filter at all, regardless of the detection algorithm used. The only exception was when the detection diagnostic started in year 2000 (TfC1-2K), where the RCP4.5 and SAI fingerprints were indistinguishable due to signal degeneracy before geoengineering deployment in 2020.

- Filtering technique aside, the non-stationary detection algorithm was generally more capable of detecting the global-mean cooling response to SAI a decade into deployment than the classical TLS algorithm. The only exception was when a 30-year $C1$ filter was used to remove some of the climate noise (TfC1(30)). This filter, however, is prone to false positive detection results and is not recommended for geoengineering monitoring.

- The nature of the non-stationary detection algorithm does not allow simultaneous detection and attribution of climatic changes to forcing factors, and it has limitations on the use of pre-deployment data. Therefore, it is also not recommended for geoengineering monitoring despite BgC1's high capability of detecting the SAI signal 10 years into deployment.

- The optimal method for detecting a temperature response to SAI in G4 would be the classical TLS algorithm along with the 14-year $C1$ filter, i.e. TfC1.

6.2.2   Geoengineering detection in regional surface temperatures

Based on the conclusions from Chapter 3, the detectability of SAI in near-surface air temperatures averaged over the near-global HadCRUT4 observational network, the Northern and Southern Hemispheres, the Arctic (90–60 °N), Northern mid-latitudes (60–25 °N), Tropics (25 °N–25 °S), Southern mid-latitudes (25–60 °S) and Antarctica (60–90 °S), as well as 4 continental regions and 11 SREX regions were investigated with the use of TfC1 in Chapter 4. Additionally, detection was attempted in the spatio-temporal near-surface air temperature pattern across several sub-regions in the 4 continental-scale regions.

At each spatial scale, the same 44 pseudo-observation model comparisons as those in Chapter 3 were made. The estimated SAI detection horizons were qualitatively compared to the results from an idealised experiment consisting of analytical pseudo-observations, fingerprints and white noise; and quantitatively compared to the time of emergence (ToE) of the SAI signal at grid-scale. Key results are as follows:

- Using the global-mean temperature calculated from the HadCRUT4 dataset that covers about 84% of the Earth's surface as the detection diagnostic increased the number of within-a-decade SAI detections from 29 (TfC1 in Section 6.2.1) to 30. This suggests that geoengineering monitoring might benefit from our existing, incomplete observational network, in which observations near the Poles and in areas particularly vulnerable to climate risks such as Africa are unavailable.

- The number of within-a-decade SAI detections at hemispheric and latitudinal scales in descending order are: Northern Hemisphere (NH) and Northern mid-latitudes: 27 each, Tropics: 17, Southern mid-latitudes : 12, Southern Hemisphere (SH): 10, Arctic: 9 and Antarctic: 1. The surface cooling effect of SAI was generally more detectable in the NH, where the land to sea ratio is higher, than in the SH, where the land to sea ratio is lower.

- On the continental scale, South & East Asia gave 20 within-a-decade SAI detections, followed by the Contiguous United States: 14, South America: 11 and Africa: 5.

Using the spatio-temporal temperature pattern across several sub-regions within these continents as the detection diagnostics, instead of the original continental-mean temporal temperature series, increased the number of within-a-decade SAI detections in South & East Asia to 22, that in South America to 14 and that in Africa dramatically to 13, but decreased that in the Contiguous United States to 9.

• Among the studied SREX regions, East Asia and the neighbouring Pacific Islands area, giving 19 and 16 within-a-decade SAI detections, respectively, would be the best places for effective monitoring of the regional impacts of SAI.

• If a threshold of 22 within-a-decade SAI detections in the 44 comparisons defines the efficacy of a certain region or detection diagnostic for effective geoengineering monitoring, then only (in descending order) the near-global HadCRUT4 scale, the NH, the Northern mid-latitudes, and South & East Asia under the spatio-temporal diagnostic would qualify. This suggests considerable challenge in monitoring SAI in sub-global near-surface air temperatures in a scenario like G4.

• The idealised experiment showed that the SAI detection horizon would be noticeably more sensitive to changes in climate noise when it is small than when it is already large. This was demonstrated in the SREX regional detection results, where the number of within-a-decade SAI detections varied from one region to another more at low latitudes than at high latitudes. This suggests that the SAI cooling signal might be detected in one region but not another in the Tropics if a smaller amount of SO_2 were injected into the stratosphere for geoengineering.

• The ToE of the SAI cooling signal was estimated to range from 5 to 15 years since geoengineering deployment in G4 in the Tropics and the Northern mid-latitudes, and between 15 and 20 years in Alaska, Northwestern Canada and Siberia. ToE is, therefore, an underestimate of the SAI detection horizon derived from the classical optimal fingerprint TLS technique.

6.2.3 Geoengineering detection in the vertical temperature profile

SAI detection was attempted in the vertical-temporal atmospheric temperature structure as if observed in AMSU-A channels 5 (middle troposphere), 7 (troposphere/stratosphere) and 9 (lower stratosphere) in the global-mean, the NH and SH, and the Tropics. In addition, global and tropical SAI detection was explored in the vertical-temporal temperature structure spanning AMSU-A channels 5 and 7, and an effective channel 9L that had minimal radiance contribution from 30 hPa or above.

All vertical detection experiments were done in 24 pseudo-observation model comparisons that excluded CSIRO-MkL-1-2. This was because CSIRO-Mk3L-1-2 represented SAI with a reduction in solar irradiance and failed to simulate the lower stratospheric warming expected from stratospheric sulphate aerosols. Key results are as follows:

- All models included in the 24 comparisons projected significant tropospheric warming and upper stratospheric cooling in RCP4.5, and a global tropospheric cooling response and lower stratospheric warming response in low to mid latitudes to SAI. However, inter-model differences were apparent, with HadGEM2-ES simulating the weakest tropical lower stratospheric heating response in G4.

- Using AMSU-A channels 5, 7 and 9, the number of within-a-decade SAI detections out of the 24 comparisons in descending order are: global-mean: 24, SH: 23, NH: 22 and Tropics: 19. These are all higher than the corresponding results found in the same comparisons with near-surface air temperature, highlighting the importance of vertical temperature information in geoengineering monitoring.

- In both RCP4.5 and G4, some of the greenhouse gas forced upper stratospheric cooling was removed in effective channel 9L, whose weighting function is a linear combination of those of channels 9 and 11.

- Using AMSU-A channels 5, 7 and 9L, the number of within-a-decade SAI detections in the global-mean dropped to 23, but that in the Tropics increased to 22 (out of 24). Hence,

channel 9L would be important for tropical geoengineering monitoring, especially if the real-world stratospheric response to SAI was similarly weak as the HadGEM2-ES simulations.

6.3 Conclusions of this thesis

This section addresses the research questions posed in Section 1.4 based on the results obtained in this thesis.

1. **When could we first detect the global-mean cooling response to 5 Tg yr^{-1} SO$_2$ injection?**

   The time needed between implementation of 5 Tg yr^{-1} SO$_2$ injection in 2020 in G4 and detection of its global-mean cooling effect could range from 5 to more than 30 years, depending on the level of agreement between the pseudo-observations and the model simulations, the technique for climate noise removal, and the algorithm used for detection. This thesis did not consider timescales longer than 30 years for political reasons, given that sulphate aerosol geoengineering is implemented constantly for 50 years in the G4 scenario only.

2. **How could we detect the global-mean cooling response to geoengineering early into implementation?**

   Various combinations of an optimal fingerprint detection and attribution algorithm, noise removal technique and detection diagnostic could result in early SAI detection in global-mean surface temperature. 'Early' was defined as within 10 years of geoengineering implementation in this thesis. Using the time evolution of global-mean near-surface air temperature since deployment in 2020 as the detection diagnostic, the classical TLS detection algorithm with a 30-year $C1$ filter, the non-stationary detection algorithm with a 14-year $C1$ filter, and the classical TLS detection algorithm with a 14-year $C1$ filter gave the highest numbers of with-a-decade SAI detections, respectively. However, the

30-year $C1$ filter is prone to false positive results, and the non-stationary algorithm has limited functionality. Therefore, the optimal method for detecting the global-mean surface cooling response to SAI within 10 years of deployment would the classical TLS detection algorithm with a 14-year $C1$ filter.

3. **Where on the surface and in the atmosphere would be best for early geoengineering detection and monitoring?**

   On the surface, the mean temperature over the near-global HadCRUT4 network, followed by the Northern Hemisphere and the Northern mid-latitudes (60–25 °N) would be the best places for detecting the cooling effect of SAI within 10 years of implementation. Using the spatio-temporal temperature pattern across several sub-regions in South & East Asia would also likely result in robust SAI detection within 10 years of implementation. Regionally, East Asia and the Pacific Islands region would see the highest chance of detecting the SAI cooling effect 10 years into deployment. However, regional detection of SAI is expected to be noticeably more challenging than detection at larger spatial scales.

   Including the vertical structure of tropospheric and stratospheric temperatures would be vital for increasing the detectability of SAI during the first 10 years of implementation on the global and hemispheric scales, and in the Tropics (25 °N–25 °S). In particular, minimising the upper stratospheric (above 30 hPa) cooling response to greenhouse gases could significantly improve the SAI detectability in the Tropics. The best detection diagnostic for SAI monitoring within 10 years of deployment would be the global-mean vertical temperature structure spanning the middle troposphere to the lower stratosphere, although vertical temperature structures averaged over the NH, the SH and the Tropics would likely give similarly high within-a-decade SAI detectabilities.

6.4   Discussion

6.4.1   Implications of this work

As mentioned in Section 3.5, a step forward from detecting the effects of SAI would be to attribute observable changes in climate to the deliberately injected stratospheric sulphate aerosols in the event of large-scale field experiments or deployment. Attributing observed climate responses to stratospheric geoengineering aerosols would be useful for evaluating the intended and unintended effects of SAI, managing climate goals by an explicit feedback mechanism (Kravitz et al., 2014), and constraining future projections in climate models (Section 3.5). Detection is a prerequisite for attribution (Section 2.3). The positive SAI detection results obtained in this thesis suggest that attributing temperature changes to 5 Tg yr^{-1} SO$_2$ injection in a geoengineered world like G4 would be possible at various time and space scales.

A majority of this thesis was devoted to finding the best way (in terms of detection method, diagnostic and space) to detect the temperature effects of 5 Tg yr^{-1} SO$_2$ injection a decade into hypothetical deployment. Nevertheless, the 'best way' for SAI detection would very likely be context- and scenario-dependent. For example, three plausible cases in which SAI detection in temperature could be important were listed in Section 1.4. Different detection diagnostics and spatial scales would be most relevant in these cases, even though the vertical temperature profile and the global-mean surface temperature diagnostic were found to be the best detection diagnostics for early detection of 5 Tg yr^{-1} SO$_2$ geoengineering in temperature in this thesis:

- Field experiments that aim at evaluating the temperature effects of SAI. In this case a regional detection approach similar to that employed in Chapter 4 might be most relevant. Note this does not mean the effects of small-scale field experiments would be most detectable in East Asia (result from Section 4.6), as the magnitude and spatial distribution of the impacts of smaller scale SAI could be very different from what was projected in G4.

- Unilateral experiments or deployment. In this case the global-mean vertical temperature structure would be most useful for efficiently detecting the SAI effects on temperature, if tropical SO_2 injection similar to what was implemented in G4 were deployed. However, the most direct and potentially fastest way of realising any unilateral SAI implementation would likely be by monitoring aerosol loading in the stratosphere (Section 6.5).

- SAI deployment. If the goal of deployment were to control the global thermostat such that a desired temperature or rate of warming could be maintained, then the global-mean near-surface air temperature should be considered, even though the vertical temperature profile is more likely to result in early SAI detection.

More importantly, this thesis only studied geoengineering detection in temperature. There are many other climate variables and metrics one could study for geoengineering monitoring. Therefore, the conclusions of this thesis should be understood with their underlying assumptions and limitations in mind. The limitations of this work will be discussed in the next section, and potential future work will be outlined in Section 6.5.

6.4.2   Limitations of this work

Since stratospheric sulphate aerosol geoengineering has not happened in real life, assumptions have to be made in order to study it. A lot of assumptions had been made in the GeoMIP G4 scenario (Section 2.2.1), the geoengineering scenario that this thesis was based on. The background climate in G4 is RCP4.5, which was thought to be a plausible greenhouse gas concentration trajectory when the GeoMIP experiments were designed. However, global CO_2 emissions data showed that we have been tracking the highest greenhouse gas concentration pathway adopted in IPCC AR5, i.e. the RCP8.5 (Sanford et al., 2014). Under such warming, the tropospheric cooling effects of 5 Tg yr^{-1} SO_2 would likely be harder to detect than in the G4 scenario studied in this thesis.

Nevertheless, they are many plausible scenarios of SAI deployment, including not deploying SAI, other than that assumed in G4. Constant, 5 Tg yr^{-1} SO$_2$ injection that starts and ends abruptly in 2020 and 2070 in G4 have provided climate scientists a great opportunity to study the initial geoengineering shock and the termination effect, and to understand the physical processes that govern climate responses to large amounts of sulphate aerosols in the stratosphere. However, if SAI were deployed, it might be gradually phased in and out to avoid rapid meteorological changes associated with abrupt implementation and termination. The aerosol-forced climate signals would likely take more time to emerge from climate noise than it would in G4 if SAI were introduced gradually.

As the amount of CO$_2$ we have emitted into the atmosphere has likely committed us to a warmer future than that anticipated in RCP4.5 (Friedlingstein et al., 2014), a higher SO$_2$ injection rate than 5 Tg yr^{-1} might be needed to cool the climate back to pre-industrial levels. In this case, a larger tropospheric cooling signal might emerge from climate noise, although a larger burden of aerosols also means less efficient solar radiation management (SRM) due to faster coagulation and shorter aerosol lifetimes. Moderate SAI that aims at reducing the rate of surface temperature rise is also a plausible geoengineering scenario. In any case, a significantly different injection rate or strategy would likely lead to different geoengineering detection outcomes.

All in all, uncertainties on the estimated SAI detection horizons are inevitable due to uncertainties about future climate objectives, future climate policies including those about geoengineering, and the time, amount, location and radiative properties of SAI if deployed. Therefore, the detection horizons estimated in this thesis should not be taken at face value. Rather, they should be understood as estimates under the aforementioned assumptions. Nonetheless, the optimal method, regions and diagnostics for efficient SAI detection and monitoring identified in this thesis (Section 6.3) are expected to be more scenario-independent. They may prove useful for developing an effective system for geoengineering monitoring and informative to future climate decision-making.

6.5   Potential for future work

This thesis has presented the first comprehensive work that explores the potential of a robust and effective SAI monitoring system. The optimal detection method, regions and diagnostics for different plausible SAI monitoring purposes found in this thesis are novel results to both the fields of climate change detection and attribution, and geoengineering. Nevertheless, this work can be extended in multiple ways to consolidate our understanding of the detectability of the intended and unintended effects of SAI, the potential impacts of geoengineering stratospheric sulphate aerosols on Earth observations, the possibility of attributing extreme weather events to SAI, and the possibility of detecting the climate impacts of other reflective materials or solar radiation management (SRM) methods. Potential future work is outlined below.

- **SAI detection with interactive ozone chemistry.**

  As mentioned in Sections 1.2 and 5.1, stratospheric ozone is expected to change as a result of the radiative, chemical and dynamical changes introduced by stratospheric sulphate aerosols. The atmospheric temperature response to chemistry-related ozone changes were not considered in Chapter 5 due to the lack of interactive stratospheric ozone chemistry in the climate models used. Pitari et al. (2014) showed that an atmosphere-ocean general circulation model (AOGCM) that lacked heterogeneous chemistry on aerosol particles simulated a larger reduction of column ozone in the Tropics than chemistry climate models, primarily because the suppression of the NO_x cycle was not represented in the AOGCM. The vertical detection results presented in Chapter 5 could be tested with the use of chemistry climate models.

- **Seasonal SAI detection and detection in other climate variables.**

  This thesis has focused on detecting the annual-mean temperature responses to SAI over a range of horizontal and vertical scales, but the seasonal temperature pattern of SAI could be studied too. Figure A.1 in Appendix A shows the model-simulated differences in near-surface air temperature averaged over December–February (DJF, left panel) and June–September (JJAS, right panel) between G4 and RCP4.5 during the first

decade of SAI implementation in G4. Although the majority of the simulated changes are statistically insignificant from internal climate variability (hatching on Figure A.1) during this decade, all models but CanESM2 project a greater degree of global-mean cooling in DJF than in JJAS. The spatial distribution of the temperature changes is also noticeably different between DJF and JJAS in all of the models. These suggest that a seasonal detection diagnostic could be used for detecting the SAI effects on temperature. In addition, the work in this thesis could be extended to changes in other climate variables such as precipitation, ozone, Arctic sea ice extent, and the other Earth system aspects discussed in Section 1.2. This will expand our knowledge on the detectable side effects of sulphate aerosol geoengineering and, potentially, the control of these side effects.

- **Observing the stratospheric aerosol cloud.**

  By design, implementation of SAI would increase sulphate aerosol loading in the stratosphere. Observing the stratospheric aerosol layer itself would be essential for understanding the formation, transport and cooling efficiency of the geoengineering sulphate aerosols. As mentioned in Section 6.4, monitoring stratospheric aerosol loading could also be one of the fastest and most direct ways of realising any unilateral SAI implementation. Solar or stellar occultation techniques such as the Stratospheric Aerosol and Gas Experiment III (SAGE III) (Thomason and Taha, 2003), the Atmospheric Chemistry Experiment Fourier Transform Spectrometer (ACE-FTS) (Bernath et al., 2005), Measurement of Aerosol Extinction in the Stratosphere and Troposphere Retrieved by Occultation (MAESTRO) (McElroy et al., 2007), Global Ozone Monitoring by Occultation of Stars (GOMOS) (Vanhellemont et al., 2010), and the Optical Spectrograph and InfraRed Imaging System (OSIRIS) (Llewellyn et al., 2004), as well as active sounders such as the Cloud-Aerosol Lidar and Infrared Pathfinder Satellite Observation (CALIPSO) (Winker et al., 2010), have provided valuable observations of the development, dispersion and dissipation of stratospheric aerosol clouds after small volcanic eruptions in recent years (e.g. Vernier et al. (2011), Sioris et al. (2010)). Instruments like these would be needed for close monitoring of stratospheric aerosol loading in the event of SAI.

- **A more realistic geoengineering scenario.**

  The main limitation of this work lies in the potentially unrealistic assumptions made in the GeoMIP G4 scenario (Section 6.4.2). Recognising both the usefulness and shortcomings of the original GeoMIP experiments, Kravitz et al. (2015) proposed a new set of GeoMIP6 experiments, including one that involves SAI. The G6sulfur experiment involves the injection of time-varying amounts of sulphate aerosols or their precursors into the equatorial stratosphere (10 °N to 10 °S) in order to reduce the net anthropogenic radiative forcing from the Tier 1 high forcing scenario to the Tier 1 medium forcing scenario of the Scenario Model Intercomparison Project (ScenarioMIP) (O'Neill et al., 2016). This seems to be a more realistic scenario than G4 given the high CO_2 emission rates in recent years (Section 6.4.2). The time-varying nature of SAI in G6sulphur may also be closer to what might happen in real-world deployment. The work presented in this thesis could be extended with the G6sulphur scenario.

- **Radiative impacts of stratospheric sulphate aerosols and their implications on Earth observations.**

  Stratospheric sulphate aerosols scatter shortwave radiation, and absorb solar near-infrared and terrestrial longwave radiation. As such, they can substantially affect radiation bands where remote sensing instruments operate for Earth monitoring. For example, the Mount Pinatubo aerosols absorbed infrared radiation from the surface and re-emitted it at lower temperatures, causing negative biases in the tropical sea surface temperature retrieved by the Advanced Very High Resolution Radiometer (AVHRR) between 1991 and 1992 (Reynolds, 1993). The aerosols also caused low biases in the retrievals of the Normalized Difference Vegetation Index (NDVI), which is the ratio of the difference between the near-infrared and visible spectral reflectances to the sum of the two (Vermote et al., 1997).

  As both Earth and geoengineering monitoring would likely heavily rely on satellite measurements, it would be essential to study the effects of geoengineering stratospheric aerosols on the radiation field and their implications on Earth observations. Radiative

transfer code could be used to calculate the top of atmosphere (TOA) net radiances over a large spectral range, under both aerosol-free and aerosol-contaminated conditions, and at different solar and viewing angles. The Santa Barbara DISORT Atmospheric Radiative Transfer code (SBDART) (Ricchiazzi et al., 1998) is used here as an example because it is a relatively simple tool for calculating radiances, but other code such as SOCRATES (Edwards and Slingo, 1996) could also be used. Figure 6.1 shows the TOA radiances calculated by SBDART for a clear sky (black line) and when a layer of fresh volcanic aerosols whose optical depth is 0.3 at 0.55 μm (World Meteorological Organization Radiation Commission, 1986) is present between 16–25 km (blue line) as an example. In both skies the solar zenith angle is assumed to be 60 $^\circ$, the viewer zenith and azimuth angles are both set as 0 $^\circ$, a standard tropical atmosphere profile is assumed, and the surface albedo of a combination of snow, seawater, sand and vegetation is assumed.
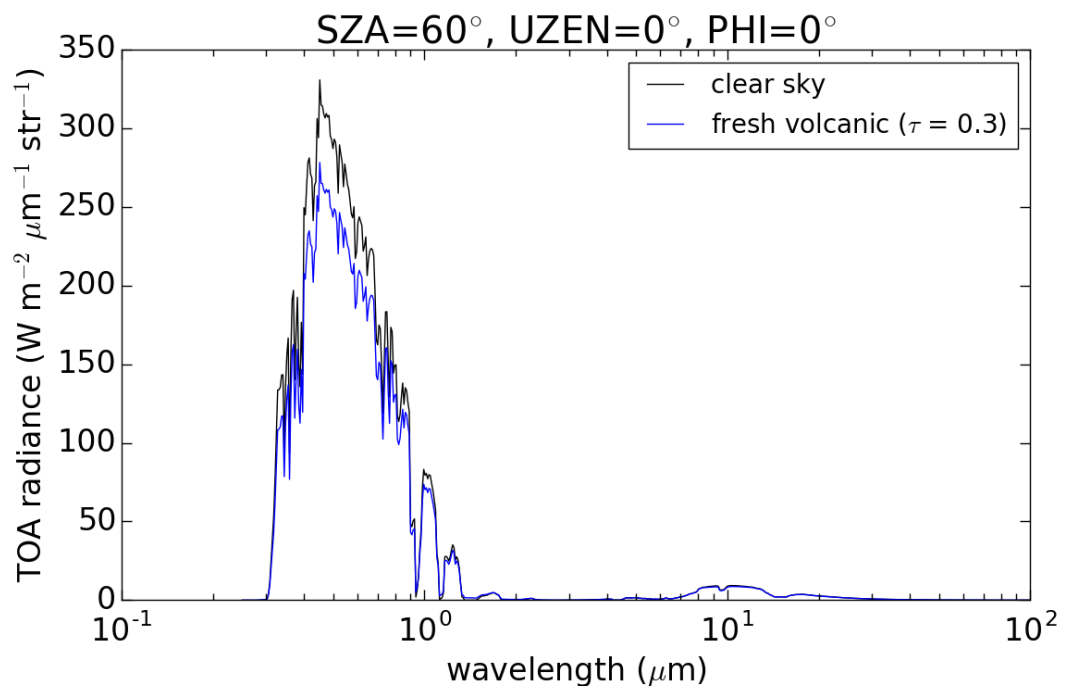
Figure 6.1 TOA radiances under clear sky (black line) and the influence of fresh volcanic aerosols between 16–25 km (blue line). The optical depth of the aerosol layer at 0.55 μm is 0.3. The radiances are generated by SBDART, by assuming a standard tropical atmospheric profile, a solar zenith angle of 60 $^\circ$, and viewer zenith and azimuth angles both of 0 $^\circ$.

- **Extreme event attribution and its use for compensation in a geoengineered world.**

  If SAI were tested or deployed in the real world, the question of 'whether an extreme weather event was linked to SAI' would definitely be raised at some point. Probabilistic

attribution techniques have been used to estimate how anthropogenic climate change has changed the likelihood and/or magnitude of certain types of extreme events, including heatwaves, floods and droughts (Stott et al., 2017). The same techniques could be applied to a geoengineered world to determine whether SAI had made an extreme event more or less likely. It was mentioned in Section 1.3.2 that compensation for loss and damages related to SAI could address some of the distributive injustice that deliberate sulphate aerosol injections would potentially bring. Any compensation systems would require extreme event attribution. Therefore, it would be prudent to explore the possibility of attributing extreme events to geoengineering with large ensembles of climate model simulations, and developing a compensation framework based on the obtained information. Geoengineering has been proposed to alleviate some of the adverse effects of climate warming. It could be that some extreme events would become less likely or less intense if geoengineering were implemented. In either case, extreme event attribution in a geoengineering scenario would benefit future climate policymaking.

- **Effects of SAI on plant growth and its implications on climate change and geoengineering.**

  In addition to climatic changes, geoengineering stratospheric sulphate aerosols are expected to affect terrestrial ecosystems and plant growth. While SO_2 injection could damage the most poorly buffered ecosystems through sulphuric acid deposition (Kravitz et al., 2009), it could promote plant growth by increasing the ratio between diffuse radiation and direct sunlight (Section 1.2). The potential effects of SAI on plant growth under elevated CO_2 concentrations do not only have implications on the net primary productivity, but also the effectiveness of another SRM technique—crop albedo enhancement. Although Crook et al. (2015) found that albedo enhancement in all grasslands between 2020 and 2070 on an RCP4.5 base climate would not return surface air temperature to the 1986–2005 mean, it would be interesting to study the combined effects of SAI and crop albedo enhancement, and to explore the possibility of disentangling their effects.

- **Detectability of the climate impacts of other solar-reflective materials.**

  Finally, SRM by injections of solar-reflective materials is not limited to the use of sulphate aerosols. Ferraro et al. (2011) examined the radiative effects of titania, limestone and soot on stratospheric temperature, and demonstrated that although all types of aerosols (including sulphate) would warm the tropical lower stratosphere, they could either warm (titania, limestone and soot) or cool (sulphate) the summer pole, and have no effect (sulphate and soot) or cool (titania and limestone) the winter pole. In particular, Keith et al. (2016) suggested that injecting limestone into the stratosphere could simultaneously reduce net radiative forcing and restore ozone concentrations, thus reversing one of the drawbacks of SAI. Since different temperature and other climatic responses to these potential SRM materials are expected, future work could extend the detection analyses presented in this thesis to these materials.

References

Alexander, L. V., S. K. Allen, N. L. Bindoff, F. Breon, U. Church, J. A.and Cubasch, S. Emori, P. Forster, P. Friedlingstein, N. Gillett, and Coauthors, 2013: Summary for policymakers. *Intergovernmental Panel on Climate Change, Working Group I Contribution to the IPCC Fifth Assessment Report (AR5).*

Allen, M. R., and P. A. Stott, 2003: Estimating signal amplitudes in optimal fingerprinting, Part I: Theory. *Climate Dynamics*, **21 (5-6)**, 477–491.

Allen, M. R., P. A. Stott, J. F. B. Mitchell, R. Schnur, and T. L. Delworth, 2000: Quantifying the uncertainty in forecasts of anthropogenic climate change. *Nature*, **407 (6804)**, 617.

Allen, M. R., and S. F. B. Tett, 1999: Checking for model consistency in optimal fingerprinting. *Climate Dynamics*, **15 (6)**, 419–434.

Allen, M. R., N. P. Gillett, J. A. Kettleborough, G. Hegerl, R. Schnur, P. A. Stott, G. Boer, C. Covey, T. L. Delworth, G. S. Jones, J. F. B. Mitchell, and T. P. Barnett, 2006: Quantifying anthropogenic influence on recent near-surface temperature change. *Surveys in Geophysics*, **27 (5)**, 491–544.

Aquila, V., C. I. Garfinkel, P. A. Newman, L. D. Oman, and D. W. Waugh, 2014: Modifications of the quasi-biennial oscillation by a geoengineering perturbation of the stratospheric aerosol layer. *Geophysical Research Letters*, **41 (5)**, 1738–1744.

Aswathy, V. N., O. Boucher, M. Quaas, U. Niemeier, H. Muri, J. Mülmenstädt, and J. Quaas, 2015: Climate extremes in multi-model simulations of stratospheric aerosol and marine cloud brightening climate engineering. *Atmospheric Chemistry and Physics*, **15 (16)**, 9593–9610.

Baldwin, M. P., L. J. Gray, T. J. Dunkerton, K. Hamilton, P. H. Haynes, W. J. Randel, J. R. Holton, M. J. Alexander, I. Hirota, T. Horinouchi, and Coauthors, 2001: The quasi-biennial oscillation. *Reviews of Geophysics*, **39 (2)**, 179–229.

Bellouin, N., J. Rae, A. Jones, C. Johnson, J. Haywood, and O. Boucher, 2011a: Aerosol forcing in the Climate Model Intercomparison Project (CMIP5) simulations by HadGEM2-ES and the role of ammonium nitrate. *Journal of Geophysical Research: Atmospheres*, **116 (D20)**, d20206.

Bellouin, N., W. J. Collins, I. D. Culverwell, P. R. Halloran, S. C. Hardiman, T. J. Hinton, C. D. Jones, R. E. McDonald, A. J. McLaren, F. M. O'Connor, and Coauthors, 2011b: The HadGEM2 family of met office unified model climate configurations. *Geoscientific Model Development*, **4 (3)**, 723–757.

References

Berdahl, M., A. Robock, D. Ji, J. C. Moore, A. Jones, B. Kravitz, and S. Watanabe, 2014: Arctic cryosphere response in the Geoengineering Model Intercomparison Project G3 and G4 scenarios. *Journal of Geophysical Research: Atmospheres*, **119 (3)**, 1308–1321.

Bernath, P. F., C. T. McElroy, M. C. Abrams, C. D. Boone, M. Butler, C. Camy-Peyret, M. Carleer, C. Clerbaux, P.-F. Coheur, R. Colin, and Coauthors, 2005: Atmospheric Chemistry Experiment (ACE): Mission overview. *Geophysical Research Letters*, **32 (15)**, l15S01.

Betz, G., 2012: The case for climate engineering research: an analysis of the 'arm the future' argument. *Climatic change*, **111 (2)**, 473–485.

Bevir, M., 2012: *Governance: A very short introduction*. Oxford University Press.

Bindoff, N. L., P. A. Stott, K. M. AchutaRao, M. R. Allen, N. Gillett, D. Gutzler, K. Hansingo, G. Hegerl, Y. Hu, S. Jain, I. I. Mokhov, J. Overland, J. Perlwitz, R. Sebbari, and Z. Zhang, 2013: Detection and attribution of climate change: from global to regional. *Climate Change 2013: The Physical Science Basis. Contribution of Working Group I to the Fifth Assessment Report of the Intergovernmental Panel on Climate Change*, T. F. Stocker, D. Qin, G. K. Plattner, M. Tignor, S. K. Allen, J. Boschung, A. Nauels, Y. Xia, V. Bex, and P. M. Midgley, Eds., Cambridge University Press, Cambridge, United Kingdom and New York, NY, USA.

Bluth, G. J. S., S. D. Doiron, C. C. Schnetzler, A. J. Krueger, and L. S. Walter, 1992: Global tracking of the SO_2 clouds from the june, 1991 mount pinatubo eruptions. *Geophysical Research Letters*, **19 (2)**, 151–154.

Braganza, K., D. Karoly, A. Hirst, M. Mann, P. Stott, R. Stouffer, and S. Tett, 2003: Simple indices of global climate variability and change: Part I–variability and correlation structure. *Climate Dynamics*, **20 (5)**, 491–502.

Budyko, M. I., 1977: *Climatic changes (transl. Izmeniia Klimata Leningrad: Gidrometeoizdat, 1974)*. American Geophysical Union, Washington, DC.

Bürger, G., and U. Cubasch, 2015: The detectability of climate engineering. *Journal of Geophysical Research: Atmospheres*, **120 (22)**, 11,404–11,418, 2015JD023954.

Burke, C., P. Stott, A. Ciavarella, and Y. Sun, 2016: Attribution of extreme rainfall in Southeast China during May 2015. *Bulletin of the American Meteorological Society*, **97 (12)**, S92–S96.

Burns, W. C. G., 2011: Climate geoengineering: solar radiation management and its implications for intergenerational equity. *Stanford Journal of Law, Science and Policy*, **4**, 39–55.

Butchart, N., 2014: The Brewer-Dobson circulation. *Reviews of geophysics*, **52 (2)**, 157–184.

Butchart, N., A. A. Scaife, M. Bourqui, J. De Grandpré, S. H. E. Hare, J. Kettleborough, U. Langematz, E. Manzini, F. Sassi, K. Shibata, and Coauthors, 2006: Simulations of anthropogenic change in the strength of the Brewer-Dobson circulation. *Climate Dynamics*, **27 (7-8)**, 727–741.

Chylek, P., J. Li, M. K. Dubey, M. Wang, and G. Lesins, 2011: Observed and model simulated 20th century Arctic temperature variability: Canadian earth system model CanESM2. *Atmospheric Chemistry and Physics Discussions*, **11 (8)**, 22 893–22 907.

Cleveland, W. S., 1981: Lowess: A program for smoothing scatterplots by robust locally weighted regression. *The American Statistician*, **35 (1)**, 54.

Cook, B. I., J. E. Smerdon, R. Seager, and S. Coats, 2014: Global warming and 21st century drying. *Climate Dynamics*, **43 (9-10)**, 2607–2627.

Corner, A., and N. Pidgeon, 2014: Geoengineering, climate change scepticism and the 'moral hazard' argument: an experimental study of UK public perceptions. *Philosophical Transactions of the Royal Society of London A: Mathematical, Physical and Engineering Sciences*, **372 (2031)**.

Cowtan, K., and R. G. Way, 2014: Coverage bias in the HadCRUT4 temperature series and its impact on recent temperature trends. *Quarterly Journal of the Royal Meteorological Society*, **140 (683)**, 1935–1944.

Crook, J. A., L. S. Jackson, S. M. Osprey, and P. M. Forster, 2015: A comparison of temperature and precipitation responses to different earth radiation management geoengineering schemes. *Journal of Geophysical Research: Atmospheres*, **120 (18)**, 9352–9373.

Crutzen, P. J., 2006: Albedo enhancement by stratospheric sulfur injections: a contribution to resolve a policy dilemma? *Climatic change*, **77 (3)**, 211–220.

Cubasch, U., G. A. Meehl, G. J. Boer, R. J. Stouffer, M. Dix, A. Noda, C. A. Senior, S. Raper, and K. S. Yap, 2001: Projections of future climate change. *Climate Change 2001: The Scientific Basis: Contribution of Working Group I to the Third Assessment Report of the Intergovernmental Panel*, J. T. Houghton, Y. Ding, D. J. Griggs, M. Noguer, P. J. Van der Linden, X. Dai, K. Maskell, and C. A. Johnson, Eds., 526–582.

de Garidel-Thoron, Y., T.and Rosenthal, F. Bassinot, and L. Beaufort, 2005: Stable sea surface temperatures in the western pacific warm pool over the past 1.75 million years. *Nature*, **433 (7023)**, 294.

Dobrynin, M., J. Murawski, J. Baehr, and T. Ilyina, 2015: Detection and attribution of climate change signal in ocean wind waves. *Journal of Climate*, **28 (4)**, 1578–1591.

Driscoll, S., A. Bozzo, L. J. Gray, A. Robock, and G. Stenchikov, 2012: Coupled Model Intercomparison Project 5 (CMIP5) simulations of climate following volcanic eruptions. *Journal of Geophysical Research: Atmospheres*, **117 (D17)**, d17105.

du Pont, Y. R., M. L. Jeffery, J. Gütschow, J. Rogelj, P. Christoff, and M. Meinshausen, 2017: Equitable mitigation to achieve the Paris Agreement goals. *Nature Climate Change*, **7 (1)**, 38–43.

Earth System Grid Federation, 2014: Earth system grid federation. URL https://esgf.llnl.gov, [Online; accessed 23-August-2017].

Eastham, S. D., 2015: Human health impacts of high altitude emissions. Ph.D. thesis, Massachusetts Institute of Technology.

Edenhofer, O., R. Pichs-Madruga, Y. Sokona, C. Field, V. Barros, T. F. Stocker, Q. Dahe, J. Minx, K. Mach, G.-K. Plattner, S. Schlömer, G. Hansen, and M. Mastrandrea, Eds., 2012: *Meeting Report of the Intergovernmental Panel on Climate Change Expert Meeting on*

References

Geoengineering, IPCC Working Group III Technical Support Unit, Postdam Institute for Climate Impact Research, Postdam, Germmany.

Edwards, J. M., and A. Slingo, 1996: Studies with a flexible new radiation code. i: Choosing a configuration for a large-scale model. *Quarterly Journal of the Royal Meteorological Society*, **122 (531)**, 689–719.

Effiong, U., and R. L. Neitzel, 2016: Assessing the direct occupational and public health impacts of solar radiation management with stratospheric aerosols. *Environmental Health*, **15 (1)**, 7.

Eyring, V., J. M. Arblaster, I. Cionni, J. Sedláček, J. Perlwitz, P. J. Young, S. Bekki, D. Bergmann, P. Cameron-Smith, W. J. Collins, and Coauthors, 2013: Long-term ozone changes and associated climate impacts in cmip5 simulations. *Journal of Geophysical Research: Atmospheres*, **118 (10)**, 5029–5060.

Feng, Y., 2014: Environment canada's optimal fingerprint. URL https://www.wcrp-climate. org/ictp-2014-tutorials, [Online; accessed 23-February-2015], World Climate Research Programme.

Ferraro, A. J., 2013: Atmospheric responses to geoengneering in the stratosphere. Ph.D. thesis, University of Reading.

Ferraro, A. J., A. J. Charlton-Perez, and E. J. Highwood, 2015: Stratospheric dynamics and midlatitude jets under geoengineering with space mirrors and sulfate and titania aerosols. *Journal of Geophysical Research: Atmospheres*, **120 (2)**, 414–429.

Ferraro, A. J., and H. G. Griffiths, 2016: Quantifying the temperature-independent effect of stratospheric aerosol geoengineering on global-mean precipitation in a multi-model ensemble. *Environmental Research Letters*, **11 (3)**, 034 012.

Ferraro, A. J., E. J. Highwood, and A. J. Charlton-Perez, 2011: Stratospheric heating by potential geoengineering aerosols. *Geophysical Research Letters*, **38 (24)**, l24706.

Ferraro, A. J., E. J. Highwood, and A. J. Charlton-Perez, 2014: Weakened tropical circulation and reduced precipitation in response to geoengineering. *Environmental Research Letters*, **9 (1)**, 014 001.

Forster, P. M., T. Richardson, A. C. Maycock, C. J. Smith, B. H. Samset, G. Myhre, T. Andrews, R. Pincus, and M. Schulz, 2016: Recommendations for diagnosing effective radiative forcing from climate models for CMIP6. *Journal of Geophysical Research: Atmospheres*, **121 (20)**, 12,460–12,475, 2016JD025320.

Friedlingstein, P., R. M. Andrew, J. Rogelj, G. P. Peters, J. G. Canadell, R. Knutti, G. Luderer, M. R. Raupach, M. Schaeffer, D. P. Van Vuuren, and C. Le Quéré, 2014: Persistent growth of CO_2 emissions and implications for reaching climate targets. *Nature geoscience*, **7 (10)**, 709–715.

Frumhoff, P., and J. C. Stephens, 2017: The 1.5 C target and the conundrum of solar geoengineering research. *Philosophical Transactions of the Royal Society of London A: Mathematical, Physical and Engineering Sciences*, (submitted).

Fu, Q., and C. M. Johanson, 2005: Satellite-derived vertical dependence of tropical tropospheric temperature trends. *Geophysical Research Letters*, **32 (10)**, 110703.

Fu, Q., C. M. Johanson, S. G. Warren, and D. J. Seidel, 2004: Contribution of stratospheric cooling to satellite-inferred tropospheric temperature trends. *Nature*, **429 (6987)**, 55–58.

Garcia, R. R., and W. J. Randel, 2008: Acceleration of the Brewer-Dobson circulation due to increases in greenhouse gases. *Journal of the Atmospheric Sciences*, **65 (8)**, 2731–2739.

Gillett, N. P., M. R. Allen, and S. F. B. Tett, 2000: Modelled and observed variability in atmospheric vertical temperature structure. *Climate dynamics*, **16 (1)**, 49–61.

Gillett, N. P., H. Akiyoshi, S. Bekki, P. Braesicke, V. Eyring, R. Garcia, A. Y. Karpechko, C. A. McLinden, O. Morgenstern, D. A. Plummer, J. A. Pyle, E. Rozanov, J. Scinocca, and K. Shibata, 2011: Attribution of observed changes in stratospheric ozone and temperature. *Atmospheric Chemistry and Physics*, **11 (2)**, 599–609.

Gregory, J. M., W. J. Ingram, M. A. Palmer, G. S. Jones, P. A. Stott, R. B. Thorpe, J. A. Lowe, T. C. Johns, and K. D. Williams, 2004: A new method for diagnosing radiative forcing and climate sensitivity. *Geophysical Research Letters*, **31 (3)**, l03205.

Hamilton, C., 2014: *Ethical Anxieties about Geoengineering*, 439–455. Palgrave Macmillan UK, London.

Hannachi, A., I. T. Jolliffe, and D. B. Stephenson, 2007: Empirical orthogonal functions and related techniques in atmospheric science: A review. *International journal of climatology*, **27 (9)**, 1119–1152.

Hansen, J. E., R. Ruedy, M. Sato, and K. Lo, 2006: NASA GISS surface temperature (GISTEMP) analysis. *Trends: A Compendium of Data on Global Change*.

Hardiman, S. C., N. Butchart, and N. Calvo, 2014: The morphology of the Brewer–Dobson circulation and its response to climate change in CMIP5 simulations. *Quarterly Journal of the Royal Meteorological Society*, **140 (683)**, 1958–1965.

Harvard University Center for the Environment, 2017: Harvard's solar geoengineering research program. URL https://geoengineering.environment.harvard.edu, [Online; accessed 7-September-2017].

Hasselmann, K., 1997: Multi-pattern fingerprint method for detection and attribution of climate change. *Climate Dynamics*, **13**, 601–611.

Hauke, J., and T. Kossowski, 2011: Comparison of values of pearson's and spearman's correlation coefficients on the same sets of data. *Quaestiones geographicae*, **30 (2)**, 87–93.

Hawkins, E., and R. Sutton, 2012: Time of emergence of climate signals. *Geophysical Research Letters*, **39 (1)**, l01702.

Haywood, J. M., A. Jones, N. Bellouin, and D. Stephenson, 2013: Asymmetric forcing from stratospheric aerosols impacts Sahelian rainfall. *Nature Climate Change*, **3 (7)**, 660–665.

References

Heckendorn, P., D. Weisenstein, S. Fueglistaler, B. P. Luo, E. Rozanov, M. Schraner, L. W. Thomason, and T. Peter, 2009: The impact of geoengineering aerosols on stratospheric temperature and ozone. *Environmental Research Letters*, **4 (4)**, 045 108.

Hewitson, B. C., J. A. C., T. R. Carter, F. Giorgi, R. G. Jones, W. T. Kwon, L. O. Mearns, E. L. F. Schipper, and M. van Aalst, 2014: Regional context. *Climate Change 2014: Impacts, Adaptation, and Vulnerability. Part B: Regional Aspects. Contribution of Working Group II to the Fifth Assessment Report of the Intergovernmental Panel on Climate Change*, V. R. Barros, C. B. Field, D. J. Dokken, M. D. Mastrandrea, K. J. Mach, T. E. Bilir, M. Chatterjee, K. L. Ebi, Y. O. Estrada, R. C. Genova, B. Girma, E. S. Kissel, A. N. Levy, S. MacCracken, P. R. Mastrandrea, and L. L. White, Eds., Cambridge University Press, Cambridge, United Kingdom and New York, NY, USA.

Hulme, M., 2012: Climate change: Climate engineering through stratospheric aerosol injection. *Progress in Physical Geography*, 694–703.

Irvine, P. J., B. Kravitz, M. G. Lawrence, and H. Muri, 2016: An overview of the earth system science of solar geoengineering. *Wiley Interdisciplinary Reviews: Climate Change*, **7 (6)**, 815–833.

Ito, A., 2017: Solar radiation management and ecosystem functional responses. *Climatic Change*, **142 (1-2)**, 53–66.

Ji, D., L. Wang, J. Feng, Q. Wu, H. Cheng, Q. Zhang, J. Yang, W. Dong, Y. Dai, D. Gong, and Coauthors, 2014: Description and basic evaluation of Beijing Normal University Earth system model (BNU-ESM) version 1. *Geoscientific Model Development*, **7 (5)**, 2039–2064.

Jones, A., J. Haywood, O. Boucher, B. Kravitz, and A. Robock, 2010: Geoengineering by stratospheric SO2 injection: results from the Met Office HadGEM2 climate model and comparison with the Goddard Institute for Space Studies ModelE. *Atmospheric Chemistry and Physics*, **10 (13)**, 5999–6006.

Jones, A., J. M. Haywood, K. Alterskjær, O. Boucher, J. N. S. Cole, C. L. Curry, P. J. Irvine, D. Ji, B. Kravitz, J. Egill Kristjánsson, and Coauthors, 2013: The impact of abrupt suspension of solar radiation management (termination effect) in experiment G2 of the Geoengineering Model Intercomparison Project (GeoMIP). *Journal of Geophysical Research: Atmospheres*, **118 (17)**, 9743–9752.

Jones, A. C., J. M. Haywood, and A. Jones, 2016: Climatic impacts of stratospheric geo-engineering with sulfate, black carbon and titania injection. *Atmos. Chem. Phys*, **16 (5)**, 2843–2862.

Karoly, D. J., 1987: Southern hemishere temperature trends: A possible greenhouse gas effect? *Geophysical research letters*, **14 (11)**, 1139–1141.

Kashimura, H., M. Abe, S. Watanabe, T. Sekiya, D. Ji, J. C. Moore, J. N. S. Cole, and B. Kravitz, 2017: Shortwave radiative forcing, rapid adjustment, and feedback to the surface by sulfate geoengineering: analysis of the Geoengineering Model Intercomparison Project G4 scenario. *Atmospheric Chemistry and Physics*, **17 (5)**, 3339–3356.

Keith, D. W., R. Duren, and D. G. MacMartin, 2014: Field experiments on solar geoengineering: report of a workshop exploring a representative research portfolio. *Philosophical Transactions of the Royal Society of London A: Mathematical, Physical and Engineering Sciences*, **372 (2031)**, 20140 175.

Keith, D. W., D. K. Weisenstein, J. A. Dykema, and F. N. Keutsch, 2016: Stratospheric solar geoengineering without ozone loss. *Proceedings of the National Academy of Sciences*, **113 (52)**, 14 910–14 914.

Kravitz, B., 2011: Stratospheric aerosol optical depth prescription for GeoMIP. URL http://climate.envsci.rutgers.edu/GeoMIP/geomipaod.html, [Online; accessed 01-August-2017].

Kravitz, B., D. G. MacMartin, and K. Caldeira, 2012: Geoengineering: Whiter skies? *Geophysical Research Letters*, **39 (11)**, l11801.

Kravitz, B., D. G. MacMartin, D. T. Leedal, P. J. Rasch, and A. J. Jarvis, 2014: Explicit feedback and the management of uncertainty in meeting climate objectives with solar geoengineering. *Environmental Research Letters*, **9 (4)**, 044 006.

Kravitz, B., D. G. MacMartin, M. J. Mills, J. H. Richter, S. Tilmes, J.-F. Lamarque, J. J. Tribbia, and F. Vitt, 2017: First simulations of designing stratospheric sulfate aerosol geoengineering to meet multiple simultaneous climate objectives. *Journal of Geophysical Research: Atmospheres*, **122 (23)**, 12,616–12,634, 2017JD026874.

Kravitz, B., A. Robock, O. Boucher, H. Schmidt, K. Taylor, G. Stenchikov, and M. Schulz, 2010: Specifications for GeoMIP experiments G1 through G4.

Kravitz, B., A. Robock, O. Boucher, H. Schmidt, K. E. Taylor, G. Stenchikov, and M. Schulz, 2011: The Geoengineering Model Intercomparison Project (GeoMIP). *Atmospheric Science Letters*, **12 (2)**, 162–167, Wiley Online Library.

Kravitz, B., A. Robock, P. M. Forster, J. M. Haywood, M. G. Lawrence, and H. Schmidt, 2013a: An overview of the Geoengineering Model Intercomparison Project (GeoMIP). *Journal of Geophysical Research: Atmospheres*, **118 (23)**, 13,103–13,107.

Kravitz, B., A. Robock, L. Oman, G. Stenchikov, and A. B. Marquardt, 2009: Sulfuric acid deposition from stratospheric geoengineering with sulfate aerosols. *Journal of Geophysical Research: Atmospheres*, **114 (D14)**, d14109.

Kravitz, B., P. M. Forster, A. Jones, A. Robock, K. Alterskjær, O. Boucher, A. K. L. Jenkins, H. Korhonen, J. E. Kristjánsson, H. Muri, and Coauthors, 2013b: Sea spray geoengineering experiments in the Geoengineering Model Intercomparison Project (GeoMIP): Experimental design and preliminary results. *Journal of Geophysical Research: Atmospheres*, **118 (19)**, 11 175–11 186, 2013JD020351.

Kravitz, B., A. Robock, S. Tilmes, O. Boucher, J. M. English, P. J. Irvine, A. Jones, M. G. Lawrence, M. MacCracken, H. Muri, M. J. C., U. Niemeier, S. J. Phipps, J. Sillmann, T. Storelvmo, H. Wang, and S. Watanabe, 2015: The Geoengineering Model Intercomparison Project Phase 6 (GeoMIP6): simulation design and preliminary results. *Geoscientific Model Development*, **8**, 3379–3392.

References

Lambert, F. H., P. A. Stott, M. R. Allen, and M. A. Palmer, 2004: Detection and attribution of changes in 20th century land precipitation. *Geophysical Research Letters*, **31 (10)**, 110203.

Lary, D. J., 1997: Catalytic destruction of stratospheric ozone. *Journal of Geophysical Research: Atmospheres*, **102 (D17)**, 21 515–21 526.

Lawrence, B. N., V. L. Bennett, J. Churchill, M. Juckes, P. Kershaw, S. Pascoe, S. Pepler, M. Pritchard, and A. Stephens, 2013: Storing and manipulating environmental big data with JASMIN. *Big Data, 2013 IEEE International Conference on*, IEEE, 68–75.

Lenferna, A., R. Russotto, A. Tan, S. Gardiner, and T. Ackerman, 2017: Relevant climate response tests for stratospheric aerosol injection: A combined ethical and scientific analysis. *Earth's Future*, **5 (6)**, 577–591.

Liou, K.-N., 2002: *An introduction to atmospheric radiation*, Vol. 84. Academic press.

Llewellyn, E. J., N. D. Lloyd, D. A. Degenstein, R. L. Gattinger, S. V. Petelina, A. E. Bourassa, J. T. Wiensz, E. V. Ivanov, I. C. McDade, B. H. Solheim, and Coauthors, 2004: The OSIRIS instrument on the Odin spacecraft. *Canadian Journal of Physics*, **82 (6)**, 411–422.

Lott, F. C., P. A. Stott, D. M. Mitchell, N. Christidis, N. P. Gillett, L. Haimberger, J. Perlwitz, and P. W. Thorne, 2013: Models versus radiosondes in the free atmosphere: A new detection and attribution analysis of temperature. *Journal of Geophysical Research: Atmospheres*, **118 (6)**, 2609–2619.

MacMartin, D. G., K. Caldeira, and D. W. Keith, 2014: Solar geoengineering to limit the rate of temperature change. *Philosophical Transactions of the Royal Society of London A: Mathematical, Physical and Engineering Sciences*, **372 (2031)**, 20140 134.

MacMartin, D. G., B. Kravitz, S. Tilmes, J. H. Richter, M. J. Mills, J.-F. Lamarque, J. J. Tribbia, and F. Vitt, 2017: The climate response to stratospheric aerosol geoengineering can be tailored using multiple injection locations. *Journal of Geophysical Research: Atmospheres*, **122 (23)**, 12,574–12,590, 2017JD026868.

Massonnet, F., T. Fichefet, H. Goosse, C. M. Bitz, G. Philippon-Berthier, M. M. Holland, and P.-Y. Barriat, 2012: Constraining projections of summer Arctic sea ice. *The Cryosphere*, **6 (6)**, 1383.

McClellan, J., D. W. Keith, and J. Apt, 2012: Cost analysis of stratospheric albedo modification delivery systems. *Environmental Research Letters*, **7 (3)**, 034 019.

McElroy, C. T., C. R. Nowlan, J. R. Drummond, P. F. Bernath, D. V. Barton, D. G. Dufour, C. Midwinter, R. B. Hall, A. Ogyu, A. Ullberg, and Coauthors, 2007: The ACE-MAESTRO instrument on SCISAT: description, performance, and preliminary results. *Applied Optics*, **46 (20)**, 4341–4356.

McKeen, S. A., S. C. Liu, and C. S. Kiang, 1984: On the chemistry of stratospheric SO2 from volcanic eruptions. *Journal of Geophysical Research: Atmospheres*, **89 (D3)**, 4873–4881.

Mears, C. A., and F. J. Wentz, 2009: Construction of the Remote Sensing Systems V3. 2 atmospheric temperature records from the MSU and AMSU microwave sounders. *Journal of Atmospheric and Oceanic Technology*, **26 (6)**, 1040–1056.

Meehl, G. A., and C. Tebaldi, 2004: More intense, more frequent, and longer lasting heat waves in the 21st century. *Science*, **305 (5686)**, 994–997.

Meeks, M. L., and A. E. Lilley, 1963: The microwave spectrum of oxygen in the Earth's atmosphere. *Journal of Geophysical Research*, **68 (6)**, 1683–1703.

Mercer, A. M., D. W. Keith, and J. D. Sharp, 2011: Public understanding of solar radiation management. *Environmental Research Letters*, **6 (4)**, 044 006.

Mitchell, D., C. Heaviside, S. Vardoulakis, C. Huntingford, G. Masato, B. P. Guillod, P. Frumhoff, A. Bowery, D. Wallom, and M. Allen, 2016: Attributing human mortality during extreme heat waves to anthropogenic climate change. *Environmental Research Letters*, **11 (7)**, 074 006.

Mitchell, J. F. B., D. J. Karoly, G. C. Hegerl, F. W. Zwiers, M. R. Allen, J. Marengo, V. Barros, M. Berliner, G. Boer, T. Crowley, and Coauthors, 2001: Detection of climate change and attribution of causes. *Climate Change 2001: The Scientific Basis. Contribution of Working Group I to the Third Assessment Report of the Intergovernmental Panel on Climate Change*, J. T. Houghton, Y. Ding, D. J. Griggs, M. Noguer, P. J. van der Linden, X. Dai, K. Maskell, and C. A. Johnson, Eds., Cambridge University Press, Cambridge, United Kingdom and New York, NY, USA.

Moore, J. C., A. Grinsted, X. Guo, X. Yu, S. Jevrejeva, A. Rinke, X. Cui, B. Kravitz, A. Lenton, S. Watanabe, and Coauthors, 2015: Atlantic hurricane surge response to geoengineering. *Proceedings of the National Academy of Sciences*, **112 (45)**, 13 794–13 799.

Morice, C. P., J. J. Kennedy, N. A. Rayner, and P. D. Jones, 2012: Quantifying uncertainties in global and regional temperature change using an ensemble of observational estimates: The HadCRUT4 data set. *Journal of Geophysical Research: Atmospheres*, **117 (D8)**, d08101.

Moriyama, R., M. Sugiyama, A. Kurosawa, K. Masuda, K. Tsuzuki, and Y. Ishimoto, 2017: The cost of stratospheric climate engineering revisited. *Mitigation and Adaptation Strategies for Global Change*, **22 (8)**, 1207–1228.

Mote, P. W., K. H. Rosenlof, M. E. McIntyre, E. S. Carr, J. C. Gille, J. R. Holton, J. S. Kinnersley, H. C. Pumphrey, J. M. Russell, and J. W. Waters, 1996: An atmospheric tape recorder: The imprint of tropical tropopause temperatures on stratospheric water vapor. *Journal of Geophysical Research: Atmospheres*, **101 (D2)**, 3989–4006.

Myhre, G., D. Shindell, F.-M. Bréon, W. Collins, J. Fuglestvedt, J. Huang, D. Koch, J.-F. Lamarque, D. Lee, B. Mendoza, T. Nakajima, A. Robock, G. Stephens, T. Takemura, and H. Zhang, 2013: Anthropogenic and natural radiative forcing. *Climate Change 2013: The Physical Science Basis. Contribution of Working Group I to the Fifth Assessment Report of the Intergovernmental Panel on Climate Change*, T. F. Stocker, D. Qin, G. K. Plattner, M. Tignor, S. K. Allen, J. Boschung, A. Nauels, Y. Xia, V. Bex, and P. M. Midgley, Eds., Cambridge University Press, Cambridge, United Kingdom and New York, NY, USA.

Nakicenovic, N., J. Alcamo, G. Davis, B. de Vries, J. Fenhann, S. Gaffin, K. Gregory, A. Grübler, T. Y. Jung, and Coauthors, 2000: Summary for Policymakers: Emissions Scenarios. *A Special Report of Intergovernmental Panel on Climate Change Working Group III*, N. Nakicenovic, R. Swart et al., Eds., Cambridge University Press, Cambridge, England.

References

NASA Goddard Earth Science Data and Information Services Center, 2002: Advanced microwave sounding unit-a (amsu-a) instrument guide. URL http://disc.sci.gsfc.nasa.gov/AIRS/documentation/amsu_instrument_guide.shtml, [Online; accessed 22-March-2017].

National Research Council, 2015a: *Climate Intervention: Carbon Dioxide Removal and Reliable Sequestration*. The National Academies Press, Washington, DC, doi:10.17226/18805, URL https://www.nap.edu/catalog/18805/climate-intervention-carbon-dioxide-removal-and-reliable-sequestration.

National Research Council, 2015b: *Climate Intervention: Reflecting Sunlight to Cool Earth*. The National Academies Press, Washington, DC, doi:10.17226/18988, URL https://www.nap.edu/catalog/18988/climate-intervention-reflecting-sunlight-to-cool-earth.

Niemeier, U., and H. Schmidt, 2017: Changing transport processes in the stratosphere by radiative heating of sulfate aerosols. *Atmospheric Chemistry and Physics*, **17 (24)**, 14 871–14 886.

Niemeier, U., H. Schmidt, K. Alterskjæ r, and J. E. Kristjánsson, 2013: Solar irradiance reduction via climate engineering: Impact of different techniques on the energy balance and the hydrological cycle. *Journal of Geophysical Research: Atmospheres*, **118 (21)**, 11,905–11,917.

NOAA National Centers for Environmental information, 2017: Climate at a Glance: Global Time Series. URL http://www.ncdc.noaa.gov/cag/, [Online; accessed 29-August-2017].

Oman, L. D., and A. R. Douglass, 2014: Improvements in total column ozone in GEOSCCM and comparisons with a new ozone-depleting substances scenario. *Journal of Geophysical Research: Atmospheres*, **119 (9)**, 5613–5624.

O'Neill, B. C., C. Tebaldi, D. P. Van Vuuren, V. Eyring, P. Friedlingstein, G. Hurtt, R. Knutti, E. Kriegler, J.-F. Lamarque, J. Lowe, G. A. Meehl, R. Moss, K. Riahi, and B. M. Sanderson, 2016: The Scenario Model Intercomparison Project (ScenarioMIP) for CMIP6. *Geoscientific Model Development*, **9 (9)**, 3461.

Orr, J. C., V. J. Fabry, O. Aumont, L. Bopp, S. C. Doney, R. A. Feely, A. Gnanadesikan, N. Gruber, A. Ishida, F. Joos, and Coauthors, 2005: Anthropogenic ocean acidification over the twenty-first century and its impact on calcifying organisms. *Nature*, **437 (7059)**, 681–686.

Osborn, T., 2017: Tim Osborn: HadCRUT4 global temperature graphs. URL https://crudata.uea.ac.uk/~timo/diag/tempdiag.htm, [Online; accessed 29-August-2017], Climate Research Unit, University of East Anglia.

Pall, P., T. Aina, D. A. Stone, P. A. Stott, T. Nozawa, A. G. J. Hilberts, D. Lohmann, and M. R. Allen, 2011: Anthropogenic greenhouse gas contribution to flood risk in England and Wales in autumn 2000. *Nature*, **470 (7334)**, 382.

Pan, X., M. den Elzen, N. Höhne, F. Teng, and L. Wang, 2017: Exploring fair and ambitious mitigation contributions under the Paris Agreement goals. *Environmental Science & Policy*, **74**, 49–56.

Parker, A., 2014: Governing solar geoengineering research as it leaves the laboratory. *Philosophical Transactions of the Royal Society of London A: Mathematical, Physical and Engineering Sciences*, **372 (2031)**, 20140173.

Parker, D. E., H. Wilson, P. D. Jones, J. R. Christy, and C. K. Folland, 1996: The impact of Mount Pinatubo on world-wide temperatures. *International Journal of Climatology*, **16 (5)**, 487–497.

Phipps, S. J., L. D. Rotstayn, H. B. Gordon, J. L. Roberts, A. C. Hirst, and W. F. Budd, 2011: The CSIRO Mk3L climate system model version 1.0–Part 1: Description and evaluation. *Geoscientific Model Development*, **4 (2)**, 483–509.

Phipps, S. J., L. D. Rotstayn, H. B. Gordon, J. L. Roberts, A. C. Hirst, and W. F. Budd, 2012: The CSIRO Mk3L climate system model version 1.0-part 2: Response to external forcings. *Geoscientific Model Development*, **5 (3)**, 649.

Pidgeon, N., A. Corner, K. Parkhill, A. Spence, C. Butler, and W. Poortinga, 2012: Exploring early public responses to geoengineering. *Philosophical Transactions of the Royal Society of London A: Mathematical, Physical and Engineering Sciences*, **370 (1974)**, 4176–4196, doi:10.1098/rsta.2012.0099.

Pidgeon, N., K. Parkhill, A. Corner, and N. Vaughan, 2013: Deliberating stratospheric aerosols for climate geoengineering and the SPICE project. *Nature Climate Change*, **3 (5)**, 451.

Pierce, J. R., D. K. Weisenstein, P. Heckendorn, T. Peter, and D. W. Keith, 2010: Efficient formation of stratospheric aerosol for climate engineering by emission of condensible vapor from aircraft. *Geophysical Research Letters*, **37 (18)**, l18805.

Pitari, G., E. Mancini, V. Rizi, and D. T. Shindell, 2002: Impact of future climate and emission changes on stratospheric aerosols and ozone. *Journal of the Atmospheric Sciences*, **59 (3)**, 414–440.

Pitari, G., V. Aquila, B. Kravitz, A. Robock, S. Watanabe, I. Cionni, N. D. Luca, G. D. Genova, E. Mancini, and S. Tilmes, 2014: Stratopsheric ozone response to sulfate geoengineering: results from the Geoengineering Model Intercomparison Project (GeoMIP). *Journal of Geophysical Research: Atmospheres*, **119**, 2629–2653.

Prather, M., 1992: Catastrophic loss of stratospheric ozone in dense volcanic clouds. *Journal of Geophysical Research: Atmospheres*, **97 (D9)**, 10 187–10 191.

Preston, C. J., 2013: Ethics and geoengineering: reviewing the moral issues raised by solar radiation management and carbon dioxide removal. *Wiley Interdisciplinary Reviews: Climate Change*, **4 (1)**, 23–37.

Randles, C. A., S. Kinne, G. Myhre, M. Schulz, P. Stier, J. Fischer, L. Doppler, E. Highwood, C. Ryder, B. Harris, and Coauthors, 2013: Intercomparison of shortwave radiative transfer schemes in global aerosol modeling: results from the AeroCom Radiative Transfer Experiment. *Atmospheric Chemistry and Physics*, **13 (5)**, 2347–2379.

Rasch, P. J., P. J. Crutzen, and D. B. Coleman, 2008a: Exploring the geoengineering of climate using stratospheric sulfate aerosols: The role of particle size. *Geophysical Research Letters*, **35 (2)**, l02809.

References

Rasch, P. J., S. Tilmes, R. P. Turco, A. Robock, L. Oman, C.-C. J. Chen, G. L. Stenchikov, and R. R. Garcia, 2008b: An overview of geoengineering of climate using stratospheric sulphate aerosols. *Philosophical Transactions of the Royal Society A: Mathematical, Physical and Engineering Sciences*, **366 (1882)**, 4007–4037.

Rayner, S., C. Heyward, T. Kruger, N. Pidgeon, C. Redgwell, and J. Savulescu, 2013: The Oxford Principles. *Climatic Change*, **121 (3)**, 499–512.

Reichler, T., M. Dameris, and R. Sausen, 2003: Determining the tropopause height from gridded data. *Geophysical Research Letters*, **30 (20)**, 2042.

Reynolds, R. W., 1993: Impact of mount pinatubo aerosols on satellite-derived sea surface temperatures. *Journal of climate*, **6 (4)**, 768–774.

Riahi, K., S. Rao, V. Krey, C. Cho, V. Chirkov, G. Fischer, G. Kindermann, N. Nakicenovic, and P. Rafaj, 2011: Rcp 8.5—a scenario of comparatively high greenhouse gas emissions. *Climatic Change*, **109 (1-2)**, 33.

Ribes, A., S. Planton, and L. Terray, 2013: Application of regularised optimal fingerprinting to attribution. Part I: method, properties and idealised analysis. *Climate dynamics*, **41 (11-12)**, 2817–2836.

Ricchiazzi, P., S. Yang, C. Gautier, and D. Sowle, 1998: Sbdart: A research and teaching software tool for plane-parallel radiative transfer in the earth's atmosphere. *Bulletin of the American Meteorological Society*, **79 (10)**, 2101.

Richter, J. H., S. Tilmes, M. J. Mills, J. J. Tribbia, B. Kravitz, D. G. MacMartin, F. Vitt, and J.-F. Lamarque, 2017: Stratospheric dynamical response and ozone feedbacks in the presence of SO2 injections. *Journal of Geophysical Research: Atmospheres*, **122 (23)**, 12,557–12,573, 2017JD026912.

Rind, D., R. Suozzo, N. K. Balachandran, and M. J. Prather, 1990: Climate change and the middle atmosphere. part i: The doubled CO2 climate. *Journal of the Atmospheric Sciences*, **47 (4)**, 475–494.

Robock, A., 2014: Chapter 7 stratospheric aerosol geoengineering. *Geoengineering of the Climate System*, The Royal Society of Chemistry, 162–185.

Robock, A., L. Oman, and G. L. Stenchikov, 2008: Regional climate responses to geoengineering with tropical and Arctic SO2 injections. *Journal of Geophysical Research: Atmospheres*, **113 (D16)**, d16101.

Rogelj, J., M. Den Elzen, N. Höhne, T. Fransen, H. Fekete, H. Winkler, R. Schaeffer, F. Sha, K. Riahi, and M. Meinshausen, 2016: Paris agreement climate proposals need a boost to keep warming well below 2 c. *Nature*, **534 (7609)**, 631–639.

Rupp, D. E., P. W. Mote, N. L. Bindoff, P. A. Stott, and D. A. Robinson, 2013: Detection and attribution of observed changes in northern hemisphere spring snow cover. *Journal of Climate*, **26 (18)**, 6904–6914.

Sanford, T., P. C. Frumhoff, A. Luers, and J. Gulledge, 2014: The climate policy narrative for a dangerously warming world. *Nature Climate Change*, **4 (3)**, 164–166.

Santer, B. D., J. J. Hnilo, T. M. L. Wigley, J. S. Boyle, C. Doutriaux, M. Fiorino, D. E. Parker, and K. E. Taylor, 1999: Uncertainties in observationally based estimates of temperature change in the free atmosphere. *Journal of Geophysical Research: Atmospheres*, **104 (D6)**, 6305–6333.

Santer, B. D., J. F. Painter, C. A. Mears, C. Doutriaux, P. Caldwell, J. M. Arblaster, P. J. Cameron-Smith, N. P. Gillett, P. J. Gleckler, J. Lanzante, and Coauthors, 2013: Identifying human influences on atmospheric temperature. *Proceedings of the National Academy of Sciences*, **110 (1)**, 26–33.

Sato, M., 2006: Forcings in GISS climate model: Stratospheric aerosol optical thickness. URL https://data.giss.nasa.gov/modelforce/strataer/, [Online; accessed 01-August-2017].

Sato, M., J. E. Hansen, M. P. McCormick, and J. B. Pollack, 1993: Stratospheric aerosol optical depths, 1850–1990. *Journal of Geophysical Research: Atmospheres*, **98 (D12)**, 22 987–22 994.

Schmidt, G. A., 2017: GISS Surface Temperature Analysis (GISTEMP). URL https://data.giss.nasa.gov/gistemp/, [Online; accessed 29-August-2017], National Aeronautics and Space Administration Goddard Institute for Space Studies.

Schmidt, G. A., M. Kelley, L. Nazarenko, R. Ruedy, G. L. Russell, I. Aleinov, M. Bauer, S. E. Bauer, M. K. Bhat, R. Bleck, and Coauthors, 2014: Configuration and assessment of the GISS ModelE2 contributions to the CMIP5 archive. *Journal of Advances in Modeling Earth Systems*, **6 (1)**, 141–184.

Schoeberl, M. R., P. K. Bhartia, E. Hilsenrath, and O. Torres, 1993: Tropical ozone loss following the eruption of mt. pinatubo. *Geophysical research letters*, **20 (1)**, 29–32.

Senior, C. A., T. Andrews, C. Burton, R. Chadwick, D. Copsey, T. Graham, P. Hyder, L. Jackson, R. McDonald, J. Ridley, and Coauthors, 2016: Idealized climate change simulations with a high-resolution physical model: HadGEM3-GC2. *Journal of Advances in Modeling Earth Systems*, **8 (2)**, 813–830.

Shepherd, J. G., 2009: *Geoengineering the climate: science, governance and uncertainty*. Royal Society.

Shiogama, H., M. Watanabe, Y. Imada, M. Mori, M. Ishii, and M. Kimoto, 2013: An event attribution of the 2010 drought in the South Amazon region using the MIROC5 model. *Atmospheric Science Letters*, **14 (3)**, 170–175.

Sioris, C. E., C. D. Boone, P. F. Bernath, J. Zou, C. T. McElroy, and C. A. McLinden, 2010: Atmospheric Chemistry Experiment (ACE) observations of aerosol in the upper troposphere and lower stratosphere from the Kasatochi volcanic eruption. *Journal of Geophysical Research: Atmospheres*, **115 (D2)**, d00L14.

Slangen, A., J. A. Church, X. Zhang, and D. Monselesan, 2014: Detection and attribution of global mean thermosteric sea level change. *Geophysical Research Letters*, **41 (16)**, 5951–5959.

Spearman, C., 1904: The proof and measurement of association between two things. *The American journal of psychology*, **15 (1)**, 72–101.

References

Stenchikov, G., A. Robock, V. Ramaswamy, M. D. Schwarzkopf, K. Hamilton, and S. Ramachandran, 2002: Arctic oscillation response to the 1991 Mount Pinatubo eruption: Effects of volcanic aerosols and ozone depletion. *Journal of Geophysical Research: Atmospheres*, **107 (D24)**, ACL 28–1–ACL 28–16, 4803.

Stenchikov, G. L., I. Kirchner, A. Robock, H.-F. Graf, J. C. Antuna, R. G. Grainger, A. Lambert, and L. Thomason, 1998: Radiative forcing from the 1991 Mount Pinatubo volcanic eruption. *Journal of Geophysical Research: Atmospheres*, **103 (D12)**, 13 837–13 857.

Stjern, C. W., H. Muri, L. Ahlm, O. Boucher, J. N. S. Cole, D. Ji, A. Jones, J. Haywood, B. Kravitz, A. Lenton, J. C. Moore, U. Niemeier, S. J. Phipps, H. Schmidt, S. Watanabe, and J. E. Kristjánsson, 2018: Response to marine cloud brightening in a multi-model ensemble. *Atmospheric Chemistry and Physics*, **18 (2)**, 621–634.

Stott, P. A., 2003: Attribution of regional-scale temperature changes to anthropogenic and natural causes. *Geophysical Research Letters*, **30 (14)**, 1728.

Stott, P. A., M. R. Allen, and G. S. Jones, 2003a: Estimating signal amplitudes in optimal fingerprinting. Part II: application to general circulation models. *Climate dynamics*, **21 (5-6)**, 493–500.

Stott, P. A., N. P. Gillett, G. C. Hegerl, D. J. Karoly, D. A. Stone, X. Zhang, and F. Zwiers, 2010: Detection and attribution of climate change: a regional perspective. *Wiley Interdisciplinary Reviews: Climate Change*, **1 (2)**, 192–211.

Stott, P. A., G. S. Jones, and J. F. B. Mitchell, 2003b: Do models underestimate the solar contribution to recent climate change? *Journal of Climate*, **16 (24)**, 4079–4093.

Stott, P. A., D. J. Karoly, and F. W. Zwiers, 2017: Is the choice of statistical paradigm critical in extreme event attribution studies? *Climatic Change*, 1–8.

Stott, P. A., J. F. B. Mitchell, M. R. Allen, T. L. Delworth, J. M. Gregory, G. A. Meehl, and B. D. Santer, 2006: Observational constraints on past attributable warming and predictions of future global warming. *Journal of Climate*, **19 (13)**, 3055–3069.

Stott, P. A., S. F. B. Tett, G. S. Jones, M. R. Allen, W. J. Ingram, and J. F. B. Mitchell, 2001: Attribution of twentieth century temperature change to natural and anthropogenic causes. *Climate Dynamics*, **17 (1)**, 1–21.

Sun, Y., X. Zhang, F. W. Zwiers, L. Song, H. Wan, T. Hu, H. Yin, and G. Ren, 2014: Rapid increase in the risk of extreme summer heat in Eastern China. *Nature Climate Change*, **4 (12)**, 1082.

Sütterlin, B., and M. Siegrist, 2017: Public perception of solar radiation management: the impact of information and evoked affect. *Journal of Risk Research*, **20 (10)**, 1292–1307.

Svoboda, T., K. Keller, M. Goes, and N. Tuana, 2011: Sulfate aerosol geoengineering: the question of justice. *Public Affairs Quarterly*, **25 (3)**, 157–179.

Taylor, K. E., and C. Doutriaux, 2010: CMIP5 model output requirements: file contents and format, data structure and metadata. URL http://cmip-pcmdi.llnl.gov/cmip5/docs/CMIP5_output_metadata_requirements.pdf, [Online; accessed 23-March-2017].

Taylor, K. E., R. J. Stouffer, and G. A. Meehl, 2012: An overview of CMIP5 and the experiment design. *Bulletin of the American Meteorological Society*, **93 (4)**, 485–498.

Tett, S. F. B., G. S. Jones, P. A. Stott, D. C. Hill, J. F. B. Mitchell, M. R. Allen, W. J. Ingram, T. C. Johns, C. E. Johnson, A. Jones, D. L. Roberts, D. M. H. Sexton, and M. J. Woodage, 2002: Estimation of natural and anthropogenic contributions to twentieth century temperature change. *Journal of Geophysical Research: Atmospheres (1984–2012)*, **107 (D16)**, ACL–10.

Thomason, L. W., and G. Taha, 2003: SAGE III aerosol extinction measurements: Initial results. *Geophysical Research Letters*, **30 (12)**, 1631.

Thomson, A. M., K. V. Calvin, S. J. Smith, G. P. Kyle, A. Volke, P. Patel, S. Delgado-Arias, B. Bond-Lamberty, M. A. Wise, L. E. Clarke, and J. A. Edmonds, 2011: RCP4. 5: a pathway for stabilization of radiative forcing by 2100. *Climatic change*, **109 (1-2)**, 77–94.

Thorne, P. W., 2001: Advancing climate change detection and attribution studies in the free atmosphere. Ph.D. thesis, University of East Anglia.

Thuillier, G., M. Hersé, D. Labs, T. Foujols, W. Peetermans, D. Gillotay, P. C. Simon, and H. Mandel, 2003: The solar spectral irradiance from 200 to 2400 nm as measured by the SOLSPEC spectrometer from the Atlas and Eureca missions. *Solar Physics*, **214 (1)**, 1–22.

Tilmes, S., R. R. Garcia, D. E. Kinnison, A. Gettelman, and P. J. Rasch, 2009: Impact of geoengineered aerosols on the troposphere and stratosphere. *Journal of Geophysical Research: Atmospheres*, **114 (D12)**, d12305.

Trenberth, K. E., and A. Dai, 2007: Effects of Mount Pinatubo volcanic eruption on the hydrological cycle as an analog of geoengineering. *Geophysical Research Letters*, **34 (15)**, l15702.

United Nations Framework Convention on Climate Change, 2017: The paris agreement. URL http://unfccc.int/paris_agreement/items/9485.php, [Online; accessed 30-August-2017].

Vanhellemont, F., D. Fussen, N. Mateshvili, C. Tétard, C. Bingen, E. Dekemper, N. Loodts, E. Kyrölä, V. Sofieva, J. Tamminen, A. Hauchecorne, J.-L. Bertaux, F. Dalaudier, L. Blanot, O. Fanton d'Andon, G. Barrot, M. Guirlet, T. Fehr, and L. Saavedra, 2010: Optical extinction by upper tropospheric/stratospheric aerosols and clouds: GOMOS observations for the period 2002–2008. *Atmospheric Chemistry and Physics*, **10 (16)**, 7997–8009.

Vaughan, N. E., and T. M. Lenton, 2011: A review of climate geoengineering proposals. *Climatic change*, **109 (3-4)**, 745–790.

Vermote, E., N. E. Saleous, Y. Kaufman, and E. Dutton, 1997: Data pre-processing: Stratospheric aerosol perturbing effect on the remote sensing of vegetation: Correction method for the composite NDVI after the Pinatubo eruption. *Remote Sensing Reviews*, **15 (1-4)**, 7–21.

Vernier, J.-P., L. W. Thomason, J.-P. Pommereau, A. Bourassa, J. Pelon, A. Garnier, A. Hauchecorne, L. Blanot, C. Trepte, D. Degenstein, and F. Vargas, 2011: Major influence of tropical volcanic eruptions on the stratospheric aerosol layer during the last decade. *Geophysical Research Letters*, **38 (12)**, 112807.

References

Vuuren, D. P., E. Stehfest, M. G. J. Elzen, T. Kram, J. Vliet, S. Deetman, M. Isaac, K. K. Goldewijk, A. Hof, A. M. Beltran, and Coauthors, 2011: Rcp2. 6: exploring the possibility to keep global mean temperature increase below 2 c. *Climatic Change*, **109 (1-2)**, 95–116.

Wang, W., and C.-Z. Zou, 2014: AMSU-A-only atmospheric temperature data records from the lower troposphere to the top of the stratosphere. *Journal of Atmospheric and Oceanic Technology*, **31 (4)**, 808–825.

Watanabe, S., T. Hajima, K. Sudo, T. Nagashima, T. Takcmura, H. Okajima, T. Nozawa, H. Kawase, M. Abe, T. Yokohata, and Coauthors, 2011: MIROC-ESM 2010: model description and basic results of CMIP5-20c3m experiments. *Geoscientific Model Development*, **4 (4)**, 845–872.

Welch, B. L., 1947: The generalization of student's' problem when several different population variances are involved. *Biometrika*, **34 (1/2)**, 28–35.

Wibeck, V., A. Hansson, J. Anshelm, S. Asayama, L. Dilling, P. M. Feetham, R. Hauser, A. Ishii, and M. Sugiyama, 2017: Making sense of climate engineering: a focus group study of lay publics in four countries. *Climatic Change*, 1–14.

Wigley, T. M. L., 2006: A combined mitigation/geoengineering approach to climate stabilization. *Science*, **314 (5798)**, 452–454.

Wilcox, L. J., P. Yiou, M. Hauser, F. C. Lott, G. J. van Oldenborgh, I. Colfescu, B. Dong, G. Hegerl, L. Shaffrey, and R. Sutton, 2017: Multiple perspectives on the attribution of the extreme European summer of 2012 to climate change. *Climate Dynamics*, 1–19.

Winker, D. M., J. Pelon, J. A. Coakley Jr., S. A. Ackerman, R. J. Charlson, P. R. Colarco, P. Flamant, Q. Fu, R. M. Hoff, C. Kittaka, and Coauthors, 2010: The CALIPSO mission: A global 3D view of aerosols and cloud. *Bulletin of the American Meteorological Society*, **91 (9)**, 1211–1230.

World Meteorological Organization, 1957: Meteorology—a three-dimensional science: second session of the commission of Aerology. *WMO Bulletin*, **IV**, 134–138.

World Meteorological Organization Radiation Commission, 1986: IAMAP (1986), A preliminary cloudless standard atmosphere for radiation computation, WCP-112, WMO/TD-No. 24. *World Meteorological Organization*.

Xia, L., P. J. Nowack, S. Tilmes, and A. Robock, 2017: Impacts of stratospheric sulfate geoengineering on tropospheric ozone. *Atmospheric Chemistry and Physics*, **17 (19)**, 11 913–11 928.

Xia, L., A. Robock, S. Tilmes, and R. R. Neely III, 2016: Stratospheric sulfate geoengineering could enhance the terrestrial photosynthesis rate. *Atmospheric Chemistry and Physics*, **16 (3)**, 1479–1489.

Yu, X., J. C. Moore, X. Cui, A. Rinke, D. Ji, B. Kravitz, and J. Yoon, 2015: Impacts, effectiveness and regional inequalities of the GeoMIP G1 to G4 solar radiation management scenarios. *Global and Planetary Change*, **129**, 10–22.

Zhao, L., Y. Yang, W. Cheng, D. Ji, and J. C. Moore, 2017: Glacier evolution in high-mountain asia under stratospheric sulfate aerosol injection geoengineering. *Atmospheric Chemistry and Physics*, **17 (11)**, 6547–6564.

Appendix A

Supplementary information

A.1 List of models used

Model name	Modelling group	Output used
ACCESS1.0 ACCESS1.3	Commonwealth Scientific and Industrial Research Organization (CSIRO) and Bureau of Meteorology (BOM), Australia	RCP4.5
BCC-CSM1.1 BCC-CSM1.1(m)	Beijing Climate Center, China Meteorological Administration	RCP4.5
BNU-ESM	College of Global Change and Earth System Science, Beijing Normal University	G4, RCP4.5, piControl
CanESM2	Canadian Centre for Climate Modelling and Analysis	G4, RCP4.5, piControl
CCSM4	National Center for Atmospheric Research	RCP4.5
CESM1(BGC) CESM1(CAM5)	Community Earth System Model Contributors	RCP4.5

CESM1(WACCM)

CMCC-CM CMCC-CMS	Centro Euro-Mediterraneo per I Cambiamenti Climatici	RCP4.5
CNRM-CM5	Centre National de Recherches Météorologiques / Centre Européen de Recherche et Formation Avancée en Calcul Scientifique	RCP4.5
CSIRO-Mk3.6.0	Commonwealth Scientific and Industrial Research Organization in collaboration with Queensland Climate Change Centre of Excellence	G4, RCP4.5, piControl
EC-EARTH	EC-EARTH consortium	RCP4.5
FIO-ESM	The First Institute of Oceanography, SOA, China	RCP4.5
GFDL-CM3 GFDL-ESM2G GFDL-ESM2M	NOAA Geophysical Fluid Dynamics Laboratory	RCP4.5
GISS-E2-H GISS-E2-R	NASA Goddard Institute for Space Studies	RCP4.5 RCP4.5, piControl
HadGEM2-AO	National Institute of Meteorological Research/Korea Meteorological Administration	RCP4.5
HadGEM2-CC HadGEM2-ES	Met Office Hadley Centre (additional HadGEM2-ES realizations contributed by Instituto Nacional de Pesquisas Espaciais)	RCP4.5 G4, RCP4.5, piControl
INM-CM4	Institute for Numerical Mathematics	RCP4.5
IPSL-CM5A-LR IPSL-CM5A-MR	Institut Pierre-Simon Laplace	RCP4.5

IPSL-CM5B-LR		
MIROC-ESM	Japan Agency for Marine-Earth Science and Technology, Atmosphere and Ocean Research	G4, RCP4.5, piControl
MIROC-ESM-CHEM	Institute (The University of Tokyo), and National Institute for Environmental Studies	RCP4.5
MIROC5	Atmosphere and Ocean Research Institute (The University of Tokyo), National Institute for Environmental Studies, and Japan Agency for Marine-Earth Science and Technology	RCP4.5
MPI-ESM-MR MPI-ESM-LR	Max-Planck-Institut für Meteorologie (Max Planck Institute for Meteorology)	RCP4.5
MRI-CGCM3	Meteorological Research Institute	RCP4.5
NorESM1-M NorESM1-ME	Norwegian Climate Centre	RCP4.5

Table A.1 GeoMIP and CMIP5 model output used in this thesis and the modelling groups that provided them.

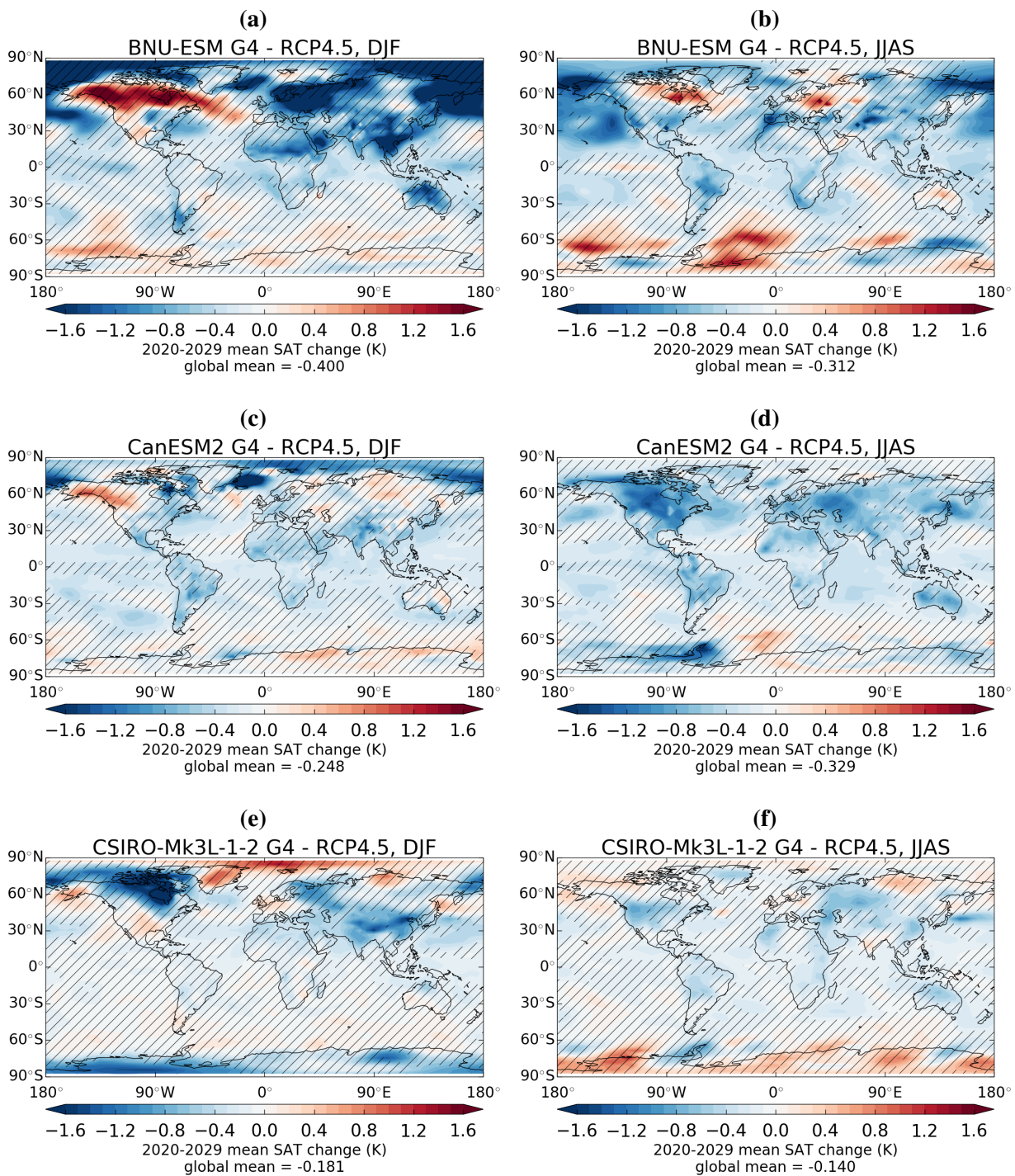## A.2   Seasonal temperature diagnostics of the G4 scenario

Figure A.1 Maps of ensemble-mean, seasonal-mean SAT changes in G4 relative to RCP4.5, averaged over the period 2020–2029. The left panel shows changes in boreal winter (December-January-February, or DJF), whereas the right panel shows changes in boreal summer (June-July-August-September, or JJAS). The top panel shows changes simulated by BNU-ESM, the middle panel shows changes simulated by CanESM2, and the bottom panel shows changes simulated by CSIRO-Mk3L-1-2. Hatching indicates areas where the plotted changes are statistically insignificant from internal variability.
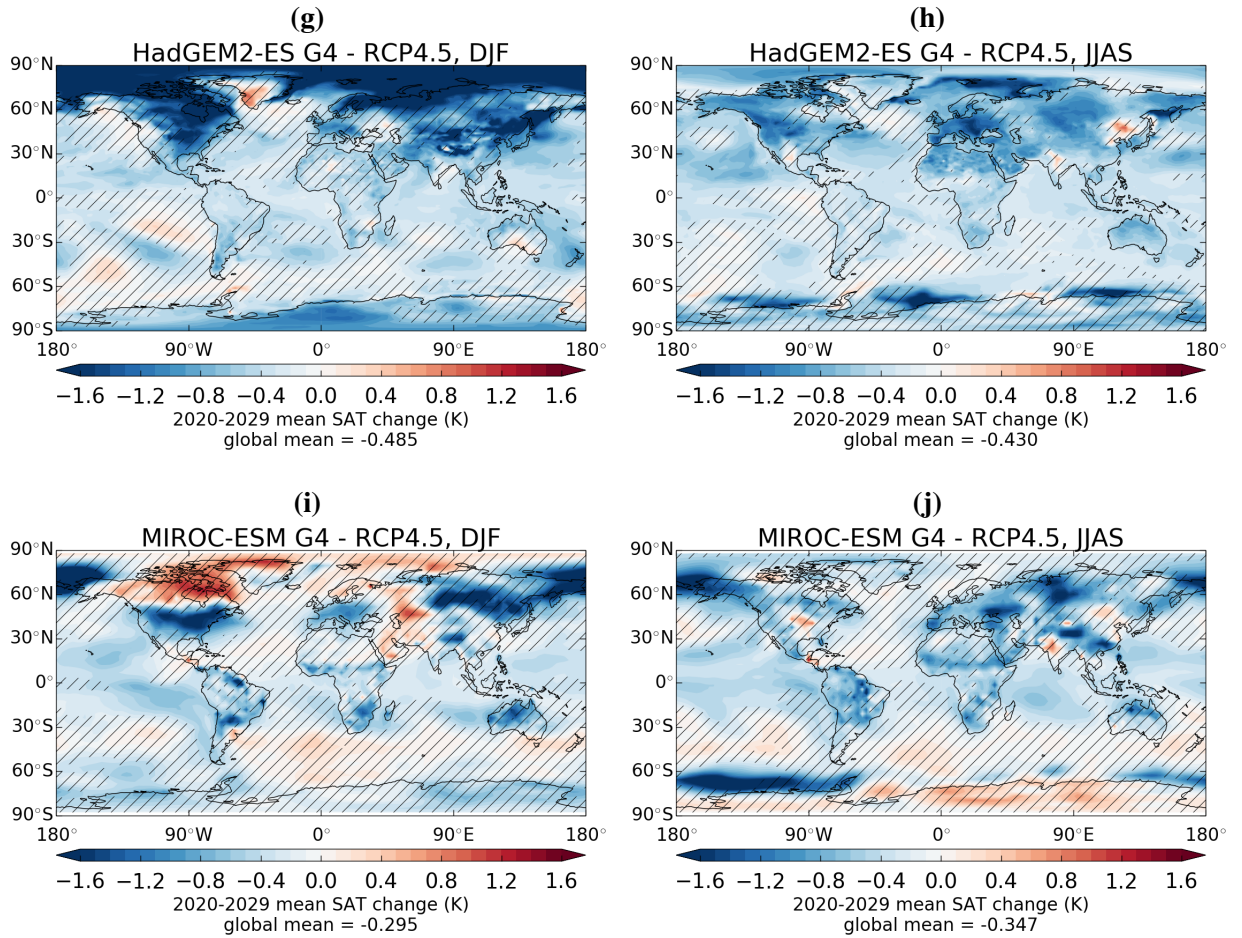
Figure A.1 continued from the previous page, but for (top panel) HadGEM2-ES and (bottom panel) MIROC-ESM.